

In-medium short-range dynamics of nucleons: Recent theoretical and experimental advances



Claudio Ciofi degli Atti¹

Departamento de Física, Centro de Estudios Subatómicos, Universidad Técnica Federico Santa María, Casilla 110-V, Valparaíso, Chile

ARTICLE INFO

Article history:

Accepted 17 June 2015

Available online 2 July 2015

editor: A. Schwenk

Keywords:

NN interactions

Many-body theories

Momentum distributions and
spectral functions

Short-range correlations

ABSTRACT

The investigation of in-medium short-range dynamics of nucleons, usually referred to as the study of short-range correlations (SRCs), is a key issue in nuclear and hadronic physics. As a matter of fact, even in the simplified assumption that the nucleus could be described as a system of protons and neutrons interacting via effective nucleon-nucleon (NN) interactions, several non trivial problems arise concerning the description of in-medium (NN short-range dynamics, namely: (i) the behavior of the NN interaction at short inter-nucleon distances in medium cannot be uniquely constrained by the experimental NN scattering phase shifts due to off-shell effects; (ii) by rigorous renormalization group (RG) techniques entire families of phase equivalent interactions differing in the short-range part can be derived; (iii) the in-medium NN interaction may be, in principle, different from the free one; (iv) when the short inter-nucleon separation is of the order of the nucleon size, the question arises of possible effects from quark and gluon degrees of freedom. For more than fifty years, experimental evidence of SRCs has been searched by means of various kinds of nuclear reactions, without however convincing results, mainly because the effects of SRCs arise from non observable quantities, like, e.g., the momentum distributions, and have been extracted from observable cross sections where short- and long-range effects, effects from nucleonic and non nucleonic degrees of freedom, and effects from final state interaction, could not be unambiguously separated out. Recent years, however, were witness of new progress in the field: from one side, theoretical and computational progress has allowed one to solve *ab initio* the many-nucleon non relativistic Schrödinger equation in terms of realistic NN interactions, obtaining realistic microscopic wave functions, unless the case of parametrized wave functions used frequently in the past, moreover the development of advanced treatments of FSI effects resulted in a robust theoretical framework for the analysis and the interpretations of experimental data; at the same time, and more importantly, new results appeared in the experimental sector thanks to the increase of the resolution at which nuclei can at present be investigated, reaching a scale of the order of the nucleon dimensions and covering kinematical regions less affected by FSI and non nucleonic degrees of freedom. As a result the model dependence of the extracted information on SRCs could be reduced and the link between the short-range dynamics predicted by a given NN interaction and the experimental data became more reliable.

© 2015 Elsevier B.V. All rights reserved.

E-mail address: ciofi@pg.infn.it.

¹ On leave from INFN, Sezione di Perugia, Department of Physics, University of Perugia, Via. A. Pascoli, I-06122 Perugia, Italy.

Contents

1.	Introduction.....	3
2.	The strong force and the nuclear many-body problem.....	4
2.1.	From a field theoretical approach to a potential description of nuclei.....	4
2.1.1.	The main features of free realistic NN interactions.....	5
2.1.2.	NN interaction from effective field theories (EFT).....	6
2.1.3.	Renormalization group soft interactions.....	6
2.2.	Methods of solution of the nuclear many-body problem.....	7
2.2.1.	The two-nucleon problem.....	7
2.2.2.	The three- and four-nucleon systems.....	8
2.2.3.	Complex nuclei.....	8
3.	Nuclear wave functions in configuration space and theoretical prediction of short-range correlations.....	11
3.1.	Many-body wave functions and spin-isospin independent and dependent density matrices.....	11
3.2.	The effect of SRCs on the number of spin-isospin pairs in nuclei.....	13
3.3.	Two-nucleon densities and theoretical evidence of the universal character of short-range correlations.....	15
4.	Short-range correlations in momentum space: one- and two-nucleon momentum distributions.....	16
4.1.	Two-nucleon SRCs in momentum space: introduction.....	16
4.2.	The one-nucleon and two-nucleon momentum distributions: general formulae.....	17
4.3.	The one-nucleon momentum distribution (1NMD) and its correlation structure.....	20
4.4.	The spin-isospin structure of the one-nucleon momentum distributions.....	22
4.5.	The momentum distribution of nuclei vs the deuteron momentum distributions.....	22
4.6.	The proton and neutron momentum distributions in ${}^3\text{He}$ and ${}^3\text{H}$	23
4.7.	On the effects of the three-nucleon force on the one-nucleon momentum distributions.....	24
4.8.	The two-nucleon momentum distributions (2NMD).....	24
5.	Short-range correlations in momentum space: one- and two-nucleon spectral functions.....	27
5.1.	The one-nucleon (hole) spectral function.....	27
5.1.1.	The momentum sum rule.....	29
5.1.2.	The Koltun sum rule.....	29
5.2.	Many-body calculations of the one-nucleon spectral function.....	29
5.2.1.	Mean-Field and Fermi gas spectral functions.....	29
5.2.2.	Microscopic spectral functions of the three-nucleon systems.....	29
5.2.3.	Microscopic spectral function of nuclear matter.....	31
5.2.4.	Model spectral functions for complex nuclei.....	32
5.3.	Saturation of the momentum sum rule: link between high momenta and high removal energies.....	35
5.4.	The spectral function and the ground-state energy of nuclei.....	37
5.5.	On the effects of three-nucleon correlations on the hole spectral function.....	38
5.6.	Two-nucleon spectral function.....	39
6.	Experimental investigation of short-range correlations.....	39
6.1.	Inclusive electron scattering off nuclei.....	39
6.1.1.	The Plane Wave Impulse Approximation (PWIA).....	41
6.1.2.	The general features of the quasi elastic (q.e.) inclusive cross section in PWIA.....	42
6.2.	The scaling properties of the inclusive cross section: Y-scaling.....	43
6.2.1.	Extracting the nucleon momentum distributions of complex nuclei from y scaling.....	48
6.2.2.	The scaling variable $Y = y_{CW} \equiv y_2$	49
6.3.	The scaling properties of the inclusive cross section: the cross section ratio vs the Bjorken scaling variable.....	53
6.4.	The final state interaction (FSI) in inclusive scattering.....	55
6.5.	The exclusive $A(e, e'N)X$ and $A(e, e'N_1N_2)X$ processes and SRCs.....	59
6.5.1.	The Final state Interaction in $A(e, e'p)X$	62
6.5.2.	The process $A(e, e'N_1N_2)X$	69
7.	The relevance of short-range correlations in various fields.....	73
7.1.	Deep inelastic lepton–nucleus scattering and the EMC effect.....	73
7.2.	High energy diffractive hadron–nucleus and nucleus–nucleus scattering.....	75
7.3.	Neutrino physics.....	78
8.	Summary and outlook.....	79
	Acknowledgments.....	81
	References.....	82

1. Introduction

Unveiling short-range nucleon dynamics in nuclei is a fundamental and challenging task. It is fundamental because the details of the short-range behavior of nuclei are related to various key aspects of physics, like e.g. [1]: (i) the role of quark and gluon degrees of freedom in nuclei; (ii) the limits of validity of the mean-field (MF) model, which is very successful in explaining many low-energy properties of nuclei [2,3]; (iii) the properties of matter at high densities, e.g. in compact stellar objects and in relativistic heavy ion scattering; (iv) the possible change of nucleon properties in nuclei (EMC-like effects), that are expected to occur when two nucleons approach a relative distance comparable with their dimensions; (v) the details of the response of nuclear matter when probed at relativistic energies, e.g. in hadron and lepton scattering off nuclei and in nucleus–nucleus scattering. It is challenging because the nucleus is an extremely complicated many-body system composed of A nucleons (N) (Z protons (p) and N neutrons (n)) which, in turn, are also many-body systems, composed of quarks (q) and gluons (g). Since q and g are the basic elements of the strong interaction governed by quantum-chromo-dynamics (QCD), it is natural to try to describe nuclear properties in terms of them, a task, however, which nowadays not only is outside the conceptual and computational possibilities of nuclear physics but, to some extent, might also be unnecessary for the explanation of many nuclear properties. As a matter of fact, there are many examples in physics when various kinds of many-body systems can be described in terms of effective components interacting via effective potentials. In case of nuclei, such a picture would correspond to a description in terms of structureless nucleons interacting via effective two-body potentials which explains NN scattering data. Several realistic NN interactions (called hereafter *bare NN interactions*), describing a large wealth of experimental data on NN scattering (in particular about 4000 phase shifts reproduced with a $\chi/\text{datum} \simeq 1$), have been produced by various groups. Assuming that the nucleus could be to a large extent considered as a non relativistic system, one can try therefore to describe nuclear properties in terms of the solution of the many-body non-relativistic Schrödinger equation. Unfortunately the practical realization of this project meets severe difficulties for various reasons, like, e.g.: (i) the reduction of a field theoretical approach to a potential one leads to Hamiltonians which include many-body forces that are experimentally unknown; (ii) realistic interactions are very repulsive at short inter-nucleon distances, perturbation theory cannot be used to solve the Schrödinger equation and *ad hoc* methods have to be devised to treat the many-nucleon systems; (iii) whereas the long-range behavior of the NN interaction can be constrained by field theory via boson exchange, the short-range part cannot, and it is usually described in terms a strong repulsive core containing various form factors leading to different short-range behaviors; (iv) elastic on-shell scattering cannot determine the details of the NN interaction in medium, because two nucleons that experience interaction with surrounding partners are off-the-energy shell, with off-shell effects expected to be particularly relevant at short inter-nucleon distances. To sum up, the short-range structure of nuclei is not well known and a possible way to study it would be the comparison of accurate solutions of the many-body Schrödinger equation, obtained with realistic interactions, with proper experimental data. Such a program implies, from one side, a reliable treatment of bound systems of interacting nucleons and, more importantly, from the other side, the identification of proper experimental data which could provide unambiguous information on in-medium short-range dynamics. This is not easy task, since signals from SRCs are mainly provided by the detection of nucleon high momentum components that not only represent only a small part of the nuclear wave function, but also because momentum distributions, i.e. the wave functions in momentum space, are not observable quantities, and have to be *extracted* from observable cross sections and therefore might always be affected by model assumptions [4]. It is precisely for this reason that in the past various attempts to investigate high momentum components in nuclei were not very successful: the model dependence of the extraction generated by competing relevant effects (e.g. final state interactions and the effects from non nucleonic degrees of freedom) masked to a large extent the effects from SRCs. It is mainly for this reason that, although the importance of studying in-medium short range dynamics was stressed more than fifty years ago [5,6], it was only recently that their investigation was placed on robust grounds thanks to relevant experimental and theoretical advances. From the theoretical side: (i) impressive computational progress allowed one to integrate exactly (*ab initio*) the many-body Schrödinger equation for $A \leq 12$, even in presence of strong repulsive short-range interactions, with progress going on to extend these calculations to heavier nuclei; (ii) approximate but still realistic many-body approaches have been developed which allowed one to perform reliable calculations of various kinds of one- and two-nucleon densities and momentum distributions; (iii) relevant progress in the theory of nuclear reactions reduced the model dependence of the extraction of the momentum distributions from various scattering processes of leptons and hadrons off nuclei probed at high resolution (high Q^2). At the same time, a new wave of experiments performed at increasing resolution are providing novel and important information on SRCs.

It should be stressed here that in recent years renormalization group (RG) techniques are being largely applied to produce families of different phase-equivalent soft NN potentials obtained by properly evolving bare phenomenological NN potentials, [7–9]. These soft interactions, which turn out to be very successful in the description of low-energy properties of nuclei, produce ground-state wave functions exhibiting a very low amount SRCs. In order to avoid misunderstanding, it should be clarified that this does not imply the absence of SRCs in nuclei, because within any RG approach, all necessary operators have to be properly evolved, which means that within a discussion of SRCs the problem is faced of evolving, besides the Hamiltonian, also those operators that are linked to high resolution quantities, e.g. the high momentum component operators generating SRCs. This is no easy task but progress is also appearing in this direction [10,11].

The aim of the present report is to critically review this field, also in view of the interpretation of on going and planned theoretical and experimental activities. In order to make the Report accessible to people not directly involved in this topic, in

Section 2 an elementary presentation of the basic approaches that are being used to solve the non relativistic many-nucleon approach is presented; in Section 3 a short, but exhaustive review, of the various many-body calculations concerning the nuclear wave function in configuration space is provided, and the universal character of the short-range behavior of the two-body density distributions, obtained within different many-body techniques and realistic interactions, is illustrated; the nuclear wave function in momentum space is discussed in Section 4, where the one- and two-nucleon momentum distributions are presented, considering for the latter both the relative (*rel*) and the center-of-mass (*c.m.*) distributions of *pn*, *pp* and *nn* correlated pairs; in Section 5 the one- and two-nucleon spectral functions, the basic quantities entering various types of reactions induced by lepton and hadron probes, are introduced, several sum rules, like the momentum and energy sum rules, are discussed, and a new topic, namely the factorization properties exhibited by the nuclear wave function in configurations characterized by *high* values of the relative momentum and, at the same time, *low* values of the *c.m.* momentum of a NN pair, are demonstrated; finally, realistic microscopic spectral functions for few-nucleon systems and nuclear matter, as well as model spectral functions for complex nuclei, are critically analyzed; recent experimental investigations of SRCs are reviewed in Section 6, discussing, in particular, inclusive and exclusive lepton scattering off nuclei, stressing the role played by the final state interaction and its treatment based upon advanced Glauber-type multiple scattering approaches; the agreement of a class of exclusive experimental data with theoretical predictions is emphasized and, at the same time, some open problems of theoretical character in the interpretation of inclusive experimental data are stressed; the role played by a realistic treatment of SRCs in a series of processes, like, e.g. deep inelastic scattering and the EMC effect, high-energy diffractive hadron–nucleus and nucleus–nucleus scattering and, eventually, neutrino nucleus processes, are briefly illustrated in Section 7; finally, the Summary and Outlook are presented in Section 8. Several aspects of SRCs have been recently the object of various review papers [12–16]; our review is aimed at updating these works both from the theoretical and the experimental points of views, as well as at presenting our point of view on the subject.

2. The strong force and the nuclear many-body problem

2.1. From a field theoretical approach to a potential description of nuclei

A description of nuclei in terms of quark and gluon degrees of freedom (d.o.f.) implies the solution of a **non** perturbative QCD problem, a very difficult and yet unsolved task. However, as in the case of various many-body systems composed of particles having an internal structure, many-nucleon systems could in principle be viewed as systems of point-like particles interacting via proper effective potentials. However, the reduction of a field theoretical problem to a non-relativistic potential description generates two-, three-..., *A*-body interactions, so that the general potential energy operator that should in principle be considered assumes the following form

$$\widehat{V}(\mathbf{x}_1, \mathbf{x}_2, \mathbf{x}_3, \dots, \mathbf{x}_A) = \sum_{n=2}^A \widehat{v}_n(\mathbf{x}_1, \dots, \mathbf{x}_n), \quad (2.1)$$

where $\mathbf{x}_i \equiv \{\mathbf{r}_i, \mathbf{s}_i, \mathbf{t}_i\}$ denotes the nucleon generalized coordinate that includes spatial, spin and isospin coordinates. It has been estimated many years ago [17] that the relative strength between two- and *n*-body interactions should obey the following qualitative relation

$$(n\text{-body potential}) \simeq \left(\frac{v_N}{c}\right)^{(n-2)} \times (\text{two-body potential}), \quad (2.2)$$

where v_N denotes the average nucleon velocity in a nucleus and c the velocity of light. Taking as an upper limit $v_N \simeq 0.1c$, one is led to the conclusion that the two-nucleon interaction is the dominant one. Though such a statement is qualitatively correct, it is nowadays well established that three-nucleon potentials have to be considered in order to explain the ground-state energy of light nuclei [18–20] (for a recent review on three- and many-nucleon forces see Refs. [21,22]). Therefore, in a first, realistic approach, the non-relativistic Schrödinger equation assumes the following form

$$\left[\sum_i \frac{\hat{\mathbf{p}}_i^2}{2m_N} + \sum_{i < j} \widehat{v}_2(\mathbf{x}_i, \mathbf{x}_j) + \sum_{i < j < k} \widehat{v}_3(\mathbf{x}_i, \mathbf{x}_j, \mathbf{x}_k) \right] \Psi_A^f(\{\mathbf{x}\}_A) = E_A^f \Psi_A^f(\{\mathbf{x}\}_A), \quad (2.3)$$

where $\{\mathbf{x}\}_A \equiv \{\mathbf{x}_1, \mathbf{x}_2, \mathbf{x}_3, \dots, \mathbf{x}_A\}$ denotes the set of *A* generalized coordinates (the spatial coordinates satisfying the condition $\sum_{i=1}^A \mathbf{r}_i = 0$) and *f* denotes the complete set of quantum numbers of state *f*, and in what follows we will be mainly interested in the ground-state wave function $\Psi_A^{f=0} \equiv \Psi_0 \equiv \Psi_A$ and the ground state energy $E_A^0 \equiv E_0 \equiv E_A$. Once the interactions are fixed, Eq. (2.3) should be solved *ab initio*, i.e. exactly, or at least without any significant approximation which could mask or distort the main features of Ψ_0 . By comparing with available experimental data, like e.g. ground-state energies and radii, charge distributions, form factors, etc., it would be possible in principle to assess the limits of validity of Eq. (2.3) and to look for its improvements by considering, e.g., relativistic effects, possible deviations of bound-nucleon properties from the free ones, the effects of non-nucleonic degrees of freedom, etc. It is well known that the solution of Eq. (2.3) represents a formidable computational task because bare realistic potentials obtained from the analysis of NN

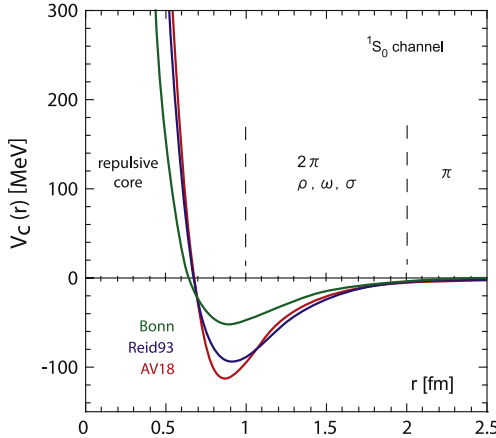


Fig. 1. The radial shape of the interaction in the 1S_0 channel corresponding to three different NN potentials: RSC [24], Bonn [25] and AV18 [30]. Source: Reprinted from [9].

© 2013, by Institute of Physics.

experimental data [23] exhibit a very complicated structure. In the case of few-nucleon systems ($A = 2, 3, 4$) Eq. (2.3) can be solved *ab initio*, and, as previously mentioned, a first result on its validity has already been obtained, namely it turns out that if only two-nucleon interactions are considered, the binding energy of few-nucleon systems is only $\simeq 90\%$ of the experimental value, with the remaining $\simeq 10\%$ provided by phenomenological three-nucleon interactions [18–20]. The latter, however, cannot be obtained experimentally and have to be parametrized by reproducing the binding energy of the few-nucleon systems, introducing, by this way, a certain degree of ambiguity, since different phenomenological two-nucleon potentials require different phenomenological three-nucleon interactions.²

2.1.1. The main features of free realistic NN interactions

The most common realistic interactions that will be recalled in the present Report are the Reid soft core (RSC) [24], Bonn [25], Paris [26], Nijmegen [27] interactions, and the family of Argonne interactions, namely the AV6, AV8, AV $'$, [28], AV14 [29] and the AV18 [30] interactions. All of them exhibit the following basic features³:

1. they depend upon the relative orbital angular momentum L , the total spin S and total isospin T , with the Pauli principle imposing that $L + S + T$ be an odd number;
2. in state 1S_0 they are attractive between spin-aligned nucleons at distances larger than $r \gtrsim 0.7$ fm, reaching a maximum value at $r \simeq 0.9$ fm; beyond this distance they decrease exponentially and becomes strongly repulsive at $r \lesssim 0.5$ –0.6 fm as required by the change of sign of the experimental phase shift; the attractive, long range part is constrained by field theory in terms of pion and other boson exchange [31] as illustrated in Fig. 1 [32] (see also Ref. [33]).
3. to a large extent they are charge-independent, which means that once the Coulomb interaction is removed, they do not depend upon whether the nucleons are neutrons or protons. The introduction of the isotopic spin T allows one to describe a two-nucleon state in a simple way, via the projection T_3 of the isospin of the pair, which assumes the values $T_3 = 1$ for a pp pair, $T_3 = -1$ for a nn pair, and $T_3 = 0$ for a pn pair;
4. in states with $S = 1$ they have a tensor character, i.e. they depend upon the angle between the direction of the spin of the two nucleons and the direction of their relative distance. The tensor force leads to the binding of the deuteron and to the mixing of the deuteron orbital momentum states $L = 0$ and $L = 2$.

The family of Argonne interactions, that will be frequently referred to in this Report, can be represented in the following form

$$v(\mathbf{x}_i, \mathbf{x}_j) = \sum_{p=1}^m v^{(p)}(r_{ij}) \mathcal{O}_{ij}^{(p)}, \quad (2.4)$$

where $r_{ij} = |\mathbf{r}_i - \mathbf{r}_j|$ is the relative distance of nucleons i and j and $\mathcal{O}_{ij}^{(p)}$ a proper operators. The most advanced interaction, the AV18, corresponds to $m = 18$, with the main eight components being

$$\begin{aligned} \mathcal{O}_{ij}^{(1)} &= 1, & \mathcal{O}_{ij}^{(2)} &= \sigma_i \cdot \sigma_j, & \mathcal{O}_{ij}^{(3)} &= \tau_i \cdot \tau_j, & \mathcal{O}_{ij}^{(4)} &= (\sigma_i \cdot \sigma_j)(\tau_i \cdot \tau_j), \\ \mathcal{O}_{ij}^{(5)} &= S_{ij}, & \mathcal{O}_{ij}^{(6)} &= S_{ij}\tau_i \cdot \tau_j, & \mathcal{O}_{ij}^{(7)} &= (\mathbf{L} \cdot \mathbf{S})_{ij}, & \mathcal{O}_{ij}^{(8)} &= (\mathbf{L} \cdot \mathbf{S})_{ij}\tau_i \cdot \tau_j. \end{aligned} \quad (2.5)$$

² Chiral interactions, to be briefly presented in Section 2.1.2 reduce the ambiguities in the definition of many-nucleon forces.

³ From now on the spectroscopic notation for the quantum numbers of a pair of nucleons will be used, namely $^{2S+1}L_J$, where L is the relative orbital momentum of the pair, S and T the total spin and isospin of the pair and J the total angular momentum allowed by the vector coupling $\mathbf{J} = \mathbf{L} + \mathbf{S}$. The usual spectroscopic notations for the orbital momentum are used, namely $L = S, P, D, \dots$

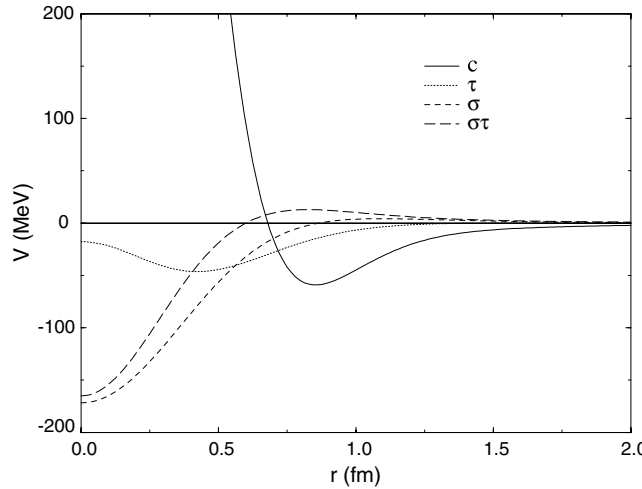


Fig. 2. Central, isospin, spin, and spin-isospin components of the potential AV18 [30]. The central potential has a peak value of 2031 MeV at $r = 0$.
Source: Reprinted from [30].

© 1995, by the American Physical Society.

Here $S_{ij} = 3(\hat{\mathbf{r}}_{ij} \cdot \sigma_i)(\hat{\mathbf{r}}_{ij} \cdot \sigma_j) - \sigma_i \cdot \sigma_j$ is the tensor operator, and $(\mathbf{L} \cdot \mathbf{S})_{ij}$ is the spin-orbit operator where $\mathbf{L} = \mathbf{r}_{ij} \times \pi_{ij}$ with $\pi_{ij} = -i(\partial/\partial \mathbf{r}_{ij})$ and $\mathbf{S} = \frac{1}{2}(\sigma_i + \sigma_j)$. The Coulomb potential is included in Eq. (2.4) with $v^{(p)}(r_{ij}) = e^2/r_{ij}$ and $\mathcal{O}_{ij}^{(p)} = P_{i\pi}P_{j\pi}$ where $P_{i\pi}$ is 1 for protons and 0 for neutrons. The potential V8' which includes only the first eight components of V8 is also frequently used. The first radial components of the V8 interaction are shown in Fig. 2. All NN interactions reproduce, by definition, the two-nucleon scattering states, as well as the static properties of the deuteron (binding energy, root mean square radius and quadrupole moment). As for the phenomenological models of 3N interactions, most of them are based on meson-exchange mechanism, a prototype being the Fujita–Miyazawa model, where a pion is exchanged by nucleon “1” and “2”, followed by a creation of an excited state of the latter, which decays by emitting a pion which is absorbed by nucleon “3”.

2.1.2. NN interaction from effective field theories (EFT)

Chiral (χ) perturbation theory (ChPT) is an EFT of QCD which allows one to construct low energy interactions in a model independent way and where two- and many-nucleon forces arise in a consistent and systematic way. A central role of NN EFT interactions is playing by the concept of resolution, according to which: a probe of wavelength λ can resolve details of a system within a linear scale $R \gg \lambda$, or, equivalently, in momentum space, a probe carrying a momentum q can provide information on momentum scale $p \leq q$. Following this principle, EFT are based upon an expansion in terms of the quantity Q/Λ_χ , where Q is the soft ($\simeq m_\pi$) momentum scale at which the nucleus is probed (the resolution of the probe) and Λ_χ is the high (hard) momentum cut-off beyond which EFT is no longer valid. In EFT NN interactions the short-range part is expressed in terms of contact interactions and the long-range part is expressed in terms of the exchange of one, two, etc. pion exchange. EFT NN interactions are able to explain NN phase shifts up to energy of about 200 MeV and though not exhibiting the hard core of phenomenological realistic interactions, are still hard enough [34–37] to make the direct solution of the Schrödinger equation still a difficult task. In Fig. 3 the local projection⁴

$$\bar{V}_\lambda(r) = \int_0^\infty r'^2 dr' V_\lambda(r, r') \quad (2.6)$$

in the 3S_1 state of the chiral N3LO(500 MeV) interaction [34] is compared with the AV18 potential.

2.1.3. Renormalization group soft interactions

The presence of strong repulsive core in realistic NN interactions, as well as in EFT interactions, creates severe difficulties in the solution of the Schrödinger equation. As it will be shown, the exact solution of the latter in terms of realistic bare NN interactions can be obtained only for $A \leq 12$. At the same time, the necessity in various field of the computed values of the ground and excited states of heavier nuclei led to the flourishing of many-body approaches based on effective soft NN interactions which allowed high precision diagonalization of the nuclear many-body Hamiltonian. The renormalized soft interactions are obtained from the original realistic bare interaction (e.g. the AV18 one) by rigorous procedures based upon, e.g., various similarity group transformations (see [7,9]) that produce phase equivalent soft interactions. These approaches

⁴ The chiral potentials and their evolved part are non local.

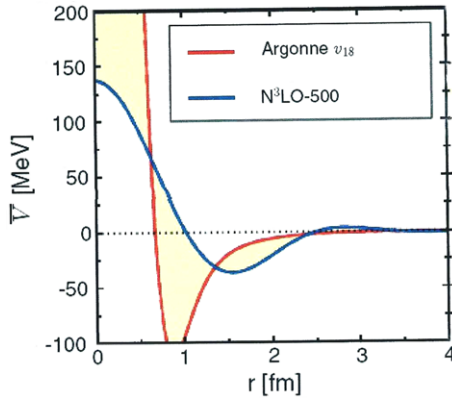


Fig. 3. Comparison [38] of the central part (S-wave) of the AV18 interaction with the local projected EFT interaction N³LO-500 of Ref. [34]. The yellow highlighted parts represent the difference between the two interactions. (For interpretation of the references to color in this figure legend, the reader is referred to the web version of this article.)

Source: Adapted from [38].

© 2003, by the American Physical Society.

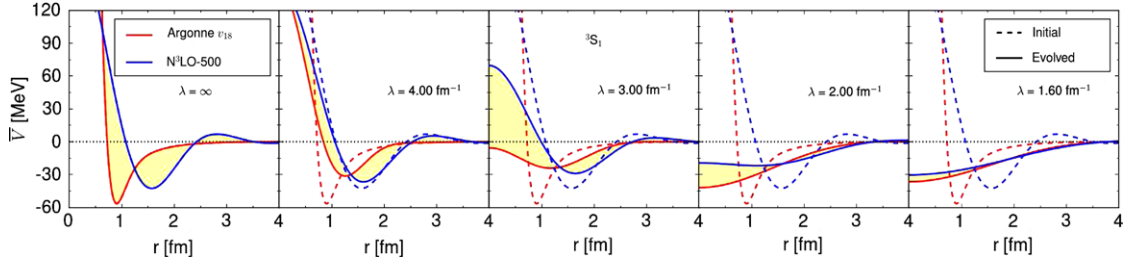


Fig. 4. Local projection of AV18 and N3LO (500 MeV) potentials in ³S₁ channel [34] at different resolutions [38]. The dashed lines show the matrix elements of the initial unevolved potentials. Here λ is the parameter governing the resolution.

Source: Reprinted from [38].

© 2003, by the American Physical Society.

are based upon the application of unitary transformations of the original interaction $v \rightarrow \tilde{v}_\lambda = \hat{U}_\lambda v \hat{U}_\lambda^\dagger$. An example is shown in Fig. 4, representing the evolution of the chiral N3LO(500) interaction at various resolution scales. It should again be stressed that these soft interactions are phase equivalent to the realistic ones but with the short-range repulsive core appreciably decreasing with decreasing resolution λ . Therefore, the many-body wave function, solution of the evolved Schrödinger equation that they produce, exhibits a very low degree of SRCs, unlike what happens, as it will be shown in detail, when bare realistic interactions are used in the Schrödinger equation. This does not mean that the expectation value of the momentum operator $\hat{n}(k) = a_k^\dagger a_k$ does not exhibit high momentum components. As a matter of fact, being the renormalization group transformation a unitary one, we have $\Psi_\lambda = U_\lambda \Psi_0$ and $\hat{O}_\lambda = U_\lambda \hat{O}^0 U_\lambda^\dagger$, so that [10,11],

$$\langle \Psi_0^\lambda | \hat{n}^\lambda(k) | \Psi_0^\lambda \rangle = \langle \Psi_0 | \hat{n}(k) | \Psi_0 \rangle \quad (2.7)$$

and the high momentum components do not disappear but are taken care of by the momentum operator.

2.2. Methods of solution of the nuclear many-body problem

Several exhaustive monographs on the nuclear many-body problems exist in the literature (see e.g. [39–41]). A variety of approaches for the solution of the non relativistic Schrödinger equation has been developed and is being extensively applied; since in this Report results obtained within these approaches will be discussed, a concise review of them will be presented, with particular emphasis of those methods that allow a direct solution of the Schrödinger equation in terms of realistic NN interactions.

2.2.1. The two-nucleon problem

The two-nucleon problem can be solved exactly by direct numerical integration of the Schrödinger equation. The deuteron wave function describing a state with $J = 1$ and projection M , orbital momentum $L = 0$ and 2, spin $S = 1$ and isospin $T = 0$, has the following form

$$\Psi_{1M}(r) = \phi_0(r) Y_{00}(\Omega_r) \chi_{1M}(s_1 s_2) \xi_{00}(t_1 t_2) + \phi_2(r) [Y_2(\omega_r) \otimes \chi_1(s_1 s_2)]_{1M} \xi_{00}(t_1 t_2). \quad (2.8)$$

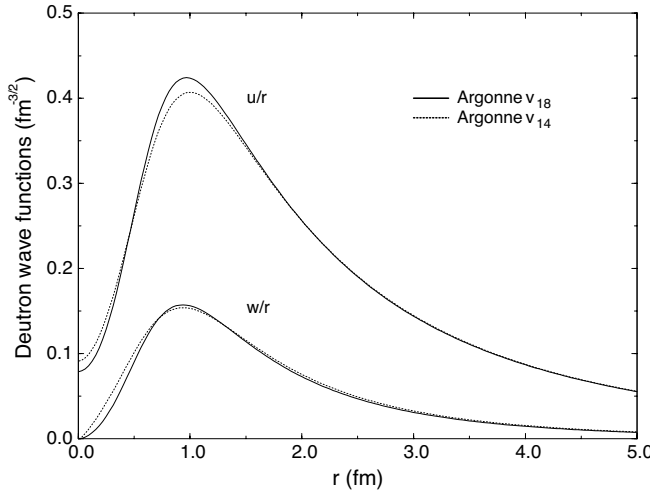


Fig. 5. The deuteron wave functions corresponding to AV14 [29] and AV18 [30] interactions.
Source: Reprinted from [30].
© 1995, by the American Physical Society.

Here $r = |\mathbf{r}_1 - \mathbf{r}_2|$ is the two-nucleon relative distance, ϕ_0 and ϕ_2 are the radial relative wave functions in $L = 0$ and $L = 2$ angular momentum states, $Y_{0(2)}$ are the corresponding spherical harmonics, and χ_{SM_S} and ξ_{TM_T} are the spin and isospin wave functions of the pair. Fig. 5 shows the deuteron wave functions $u(r) = \phi_0(r)/r$ and $w(r) = \phi_2(r)/r$ with $\phi_0(0) = \phi_2(0) = 0$ corresponding to the AV14 and AV18 interactions. The following features are worth being stressed: (i) the suppression at $r \lesssim 1$ fm (the *correlation hole*) due to the repulsive core, and (ii) the maximum at $r \simeq 1$ fm, whose position and magnitude is governed by the cooperation of the strong attractive tensor force and the short-range repulsion. Different NN interactions exhibiting different central-to-tensor interaction strength produce different short-range behaviors of the deuteron wave function. It will be shown that the correlation hole is a general feature of any nucleus and the investigation of SRCs is the investigation of the effects that it produces on momentum distributions.

2.2.2. The three- and four-nucleon systems

Ab initio solutions of the Schrödinger equation in the case of $A = 3$ and 4 are currently being obtained via the Faddeev [42] and Faddeev-Yakubovsky [43] approaches (a useful monograph on the subject is given in [44]), as well as by many other techniques [45–55] (for an exhaustive review see [56]). All of these methods produce similar results, which is evidence that the Schrödinger equation for the few-body systems can be solved *ab initio* with any type of two-nucleon interaction. As a matter of fact a benchmark calculation of the binding energy of three- and four-body nuclei [45], performed with different many-body approaches, produces practically undistinguishable results as far as ground-state properties are concerned. The results of Ref. [45] not only prove the convergence of the various methods, but also demonstrate that realistic NN interactions produce underbinding which can be removed by the introduction of phenomenological three-nucleon forces.

2.2.3. Complex nuclei

Obtaining *ab initio* solutions of the Schrödinger equation for complex nuclei ($A > 4$) is a very difficult task when bare realistic interactions are used. All difficulties arise from the short-range repulsion that makes matrix elements of the two nucleon interaction to diverge, so that usual perturbation theory cannot be used. Nonetheless, several reliable approaches have been worked out during the last decade, at least as far as the calculation of ground-state properties and not to high values of A are concerned. Most of these approaches have in common, as the zero-th order approximation, the mean-field (MF) approach describing the independent motion of nucleons [2,3].

1. The MF approach

The underlying assumption of this approach in its simplest form (the independent particle (IP) model) is the independent motion of nucleons in a mean nuclear field $U(\mathbf{x}_i)$. Such an assumption reduces the many-body problem to an effective one-body problem defined by the Schrödinger equation determining the single particle (s.p.) wave functions (ϕ_α) and energy (ϵ_α) in state α , viz

$$\left[-\frac{\hbar^2}{2m_N} \hat{\nabla}_i^2 + U(\mathbf{x}_i) \right] \phi_\alpha(\mathbf{x}_i) = \epsilon_\alpha \phi_\alpha(\mathbf{x}_i). \quad (2.9)$$

In case of a spherically symmetric potential, $U(\mathbf{x}_i) = U(r_i)$ one has $\alpha = \{n, l, m, s_3, t_3\}$, and, accordingly

$$\phi_\alpha(\mathbf{x}_i) = \varphi_{nlm}(\mathbf{r}_i) \chi_{\sigma_i}^{1/2} \xi_{t_i}^{1/2}. \quad (2.10)$$

The ground-state wave function Φ_0 of a nucleus A is the antisymmetrized product of $\phi_\alpha(\mathbf{x}_i)$, i.e. a Slater determinant

$$\Phi_0(\{\mathbf{x}_i\}_A) = \frac{1}{\sqrt{A!}} \det\{\phi_{\alpha_i}(\{\mathbf{x}_i\})\}, \quad (2.11)$$

in which all single-particle states below the last occupied state (the Fermi state α_F) are fully occupied, according to Pauli principle. It is clear that the IP wave function (Eq. (2.11)) cannot be considered a correct solution of the Schrödinger equation if the two-nucleon interaction is strongly singular at short distances. In this case, without loss of generality, the solution of the Schrödinger equation can be represented as an expansion of a complete set of Slater determinants as follows

$$\Psi_0(\{\mathbf{x}_i\}_A) = \sum_{n=0}^{n_{\max}} c_n \Phi_n(\{\mathbf{x}_i\}_A), \quad (2.12)$$

where a generic Slater determinant $\Phi_n(1, 2, \dots, A)$ in the expansion includes all possible n particle–n hole (np–nh) excitations created by the NN interaction, so that $c_m \equiv c_{mp-mh}$. The first state describes the IP motion, and the square of the generic coefficient $|c_{mp-mh}|^2$, that includes the redistribution of A particles in all possible Slater determinants having mp–mh excitations, is a measure of the effects of NN correlations. An advanced shell model is the one where nucleons in a partly occupied shell, with the closed shell considered as an inert core, are allowed to interact by an effective residual interaction. In such a model the ground state is described by a wave function representing a superposition of few Slater determinants describing virtual low-energy excitations of nucleons in the open shell. Such a wave function, describing long range correlations (LRC) is only a small part of the fully correlated wave function where all nucleons, including those in closed shells, are subject to the bare interaction, with resulting p–h excitations to states much higher than the Fermi level, i.e. with high values of n_{\max} in Eq. (2.12). Due to the success of the shell model in explaining many ground- and excited-state properties of nuclei, it is expected that the largest component of the expansion (2.12) will be given by the Slater determinant corresponding to the IP model, provided the MF is chosen or obtained in the proper way by realistic procedures.

2. The no-core shell model (NCSM) approach

The NCSM [57] is a very general approach to the many-nucleon problem. It is based upon the diagonalization of the many-body Hamiltonian in a large shell-model basis of the type of Eq. (2.12). The application of this method to the three- and four-nucleon systems is very successful and produce value of the ground-state binding energies comparable with other methods, but in case of complex nuclei it is impracticable in presence of strong repulsive interactions, because the number of possibilities to redistribute A nucleons in p–h states is very large, so that the use of high dimensional basis is required and the convergence is difficult to reach. The method is very successful when using soft effective interactions of various types, where the singularity of the NN interaction is smoothed out. Calculations are usually performed in a finite model space in the harmonic-oscillator (HO) basis. The transformation from the realistic Hamiltonian to an effective one, exhibits many-body effective forces whose effect decreases with enlargement of the basis functions. The NCSM approach, employed with renormalized soft interactions, has allowed the calculation of low energy properties of nuclei with extremely high accuracy.

3. The G matrix approach

The G-matrix or Brueckner–Bethe–Goldstone (BBG) approach [58–61] is based upon an effective well-behaved interaction, the G-matrix, which incorporates the effects of the short-range repulsion, without containing it explicitly, so that perturbation theory can in principle be applied. The G matrix describing the interaction of nucleons “i” and “j” in the medium is defined by the following integral equation

$$G_{ij}(\omega) = v_2(ij) + v_2(ij) \frac{Q_{ij}}{e_{ij}(\omega)} G_{ij}(\omega) \quad (2.13)$$

which is the result of the summation of ladder diagrams representing the action of the two-nucleon interaction to all orders, in a way similar to what one does in scattering problems; in-medium effects are taken care of via: (i) the Pauli projection operator Q_{ij} , which forbids scattering into occupied states, and (ii) the energy denominator $e_{ij}(\omega) = \omega - h_0(i) - h_0(j)$, where ω is the unknown starting energy and $h_0(j)$ the free particle Hamiltonian. The in-medium two-body wave function is the Bethe–Goldstone (BG) wave function

$$\Psi_{ij}^{BG}(\omega) = \Phi_0(ij) + \frac{Q_{ij}}{e_{ij}(\omega)} v_2(ij) \Psi_{ij}^{BG}(\omega), \quad (2.14)$$

with $G(ij)$ and $\Psi_{ij}^{BG}(ij)$ linked by the following relation

$$v_2(ij) \Psi_{ij}^{BG}(\omega) = G_{ij}(\omega) \Phi_0(ij), \quad (2.15)$$

where $\Phi_0(ij)$ is the two-body independent particle (unperturbed) wave function. The BG wave function Ψ_{ij}^{BG} differs from $\Phi_0(ij)$ at short separations where it is strongly suppressed. Eq. (2.15) implies that the action the G matrix on the BG wave function is equivalent to the action of the bare NN interaction on the BG wave function; since the latter tends to zero at

short internucleon distances, matrix elements of $G(ij)$, e.g. the energy shift given by the first order perturbation theory $\Delta E = \langle \Phi_0(ij) | v_2(ij) | \Psi_0(ij) \rangle = \langle \Phi_0(ij) | G(ij) | \Phi_0(ij) \rangle$ is finite. In first order of perturbation theory the wave function of the nucleus, usually called Brueckner–Hartree–Fock wave function, is a Slater determinant, but already at second order the wave function exhibits 2p–2h excitations, i.e. SRCs. The application of the method to finite nuclei is complicated by several points linked, in particular, to the summation of the bare NN interaction over all ladder diagrams and the choice of the starting energy, so that the method is nowadays employed mainly to the calculation of equation of state of infinite nuclear or neutron matter where the unperturbed wave function is known [61].

4. The coupled cluster approach

In this approach [62–64] the ground-state function $|\Psi_0\rangle$ is obtained from a reference MF state $|\Phi_0\rangle$ by a similarity transformation which introduces particle–hole excitations by the action of a particle–hole unitary operator \hat{T} as follows

$$|\Psi_0\rangle = e^{\hat{T}} |\Phi_0\rangle, \quad (2.16)$$

leading to

$$E_0 = \langle \Psi_0 | \hat{H} | \Psi_0 \rangle = \langle \Phi_0 | \bar{\hat{H}} | \Phi_0 \rangle, \quad (2.17)$$

with

$$\bar{\hat{H}} = e^{-\hat{T}} \hat{H} e^{\hat{T}}. \quad (2.18)$$

In other words the zero-th order wave function is the MF one and the ground-state energy is calculated perturbatively by the effective Hamiltonian $\bar{\hat{H}}$. Recent applications using softened NN potentials can be found in Refs. [63,64].

5. The correlated basis function approach.

In this method the problems arising from the repulsive core are cured by using a trial function of the form [65]

$$\Psi_0(\{\mathbf{x}\}_A) = \hat{F}(\{\mathbf{x}\}_A) \Phi_0(\{\mathbf{x}\}_A), \quad (2.19)$$

where \hat{F} is a correlation operator which reflects the properties of the two-body interaction, so that, acting on the mean-field wave function Φ_0 , a many-body wave function $\Psi_0(\{\mathbf{x}\}_A)$ is generated that has finite matrix elements of singular two-body interactions. In case of purely central two-body interactions with hard core repulsion of radius r_c , such that $v_2(r_{ij} \leq r_c) = \infty$, the symmetric correlation operator has the well known Jastrow form [66]

$$\hat{F}_J(\{\mathbf{x}\}_A) = \prod_{i < j} f_C(r_{ij}), \quad (2.20)$$

where the correlation functions $f_C(r_{ij})$ (C stands for *central*) satisfies the conditions

$$f_C(r_{ij} \leq r_c) = 0 \quad f_C(r_{ij} > r_c) \simeq 1, \quad (2.21)$$

with the second condition simply expressing the fact that far from the core region the wave function is well represented by the mean-field two-body relative wave function. When realistic NN interactions of the type Eq. (2.4) are considered, e.g. the V8 one, the correlation operator assumes the form

$$\hat{F}(\{\mathbf{x}\}_A) = \hat{S} \prod_{i < j} \left[\sum_{p=1}^8 f^p(r_{ij}) \hat{O}_{ij}^p \right], \quad (2.22)$$

where the operators \hat{O}_{ij}^p are the same appearing in the two-nucleon interaction (Eq. (2.4)) and $f^p(r_{ij})$ represents the correlation function associated to the corresponding operator. Since the operators \hat{O}_{ij}^p do not commute between themselves, the full correlation operator has to be symmetrized, which is taken care of by the operator \hat{S} . The radial functions $f^p(r_{ij})$ can be determined through functional minimization of the expectation value of the Hamiltonian

$$\langle \hat{H} \rangle = \frac{\langle \Psi_0 | \hat{H} | \Psi_0 \rangle}{\langle \Psi_0 | \Psi_0 \rangle} = E_V \geq E_0, \quad (2.23)$$

leading to Euler–Lagrange equation for $f^p(r)$ which satisfy the conditions

$$f^{p=1}(r) = f_c(r) \rightarrow 1 \text{ at } r \geq d \quad (2.24)$$

$$f^{p>1}(r) \rightarrow 0 \text{ as } r \rightarrow \infty, \quad (2.25)$$

where d , the healing distance, represents the distance beyond which the two body correlated wave function $\psi(12)$ heals to the uncorrelated one $\phi(12)$. The evaluation of Eq. (2.23) is no easy task due to the presence of many-particle integrations

and its exact evaluation is only possible for small values of A . For large values of A , proper cluster expansions have been developed [65–72] which allows one to express the expectation value of a given operator \hat{O} in the following form

$$\langle \hat{O} \rangle = \frac{\langle \Psi_0 | \hat{O} | \Psi_0 \rangle}{\langle \Psi_0 | \Psi_0 \rangle} = \langle \Phi_0 | \hat{O} | \Phi_0 \rangle_{MF} + \langle \hat{O} \rangle_2 + \langle \hat{O} \rangle_3 + \dots, \quad (2.26)$$

where $\langle \hat{O} \rangle_n$ represents the contribution from clusters of n correlated nucleons. In this report we will frequently refer to the linked cluster expansion approach of Ref. [68], which is a generalization to realistic interactions of the method developed in Refs. [67,71] for central interactions. In this approach each term of Eq. (2.26) can be expressed in terms of well defined Yvon–Mayer diagrams [73].

6. The variational Monte Carlo and the Green function Monte Carlo approaches

The variational Monte Carlo (VMC) method [50,74] makes use of the correlated wave function Eq. (2.19) to evaluate the full expectation value of the Hamiltonian by Monte Carlo integration, avoiding the use of cluster expansions. Thus the VMC method is fully *ab initio* but still keeps the limits of the variational approach, in that only the upper limit of the energy is available. Moreover, the calculation of the momentum distributions represents a difficult computational task and are limited, at present, to the case of $A \leq 12$. The exact value of the ground-state wave function can be obtained by the Green Function Monte Carlo (GFMC) approach [75,76]. Here the ground state energy and wave functions of a nucleus A can be projected out from a sufficiently realistic trial function Ψ_T (e.g. the VMC trial function implemented by $3N$ correlation functions). It can be shown that the exact ground state wave function Ψ_0 can be obtained by evaluating path integrals of the form:

$$\Psi_0 = \lim_{\tau \rightarrow \infty} \Psi(\tau), \quad (2.27)$$

with

$$\Psi(\tau) = e^{-(H-E_0)\tau} \Psi_T, \quad (2.28)$$

$$= [e^{-(H-E_0)\Delta\tau}]^n \Psi_T, \quad (2.29)$$

where $\tau = it$ is the “imaginary time”. In configuration space one has

$$\Psi(\tau) = e^{-(H-E_0)\tau} \Psi_T = \int d\mathbf{R} d\mathbf{R}' | \mathbf{R} \rangle G(\mathbf{R}\mathbf{R}', \tau) \langle \mathbf{R}' | \Psi \rangle, \quad (2.30)$$

where G is the Green function and \mathbf{R} denotes the full set of coordinates. The GFMC method is the one that can be used to generate exact ground-state wave functions and energies with bare realistic interactions. However computational difficulties has limited up to now its application to the calculation of ground and excited states energies and densities of light nuclei ($A \leq 12$) and no calculations up to now could be performed of the momentum distributions. GFMC is an exact method and therefore, whenever possible, approximate, but still realistically enough approaches, should always have the GFMC method as a landmark. Up to now GFMC calculations have been mostly performed with bare realistic interactions of the Argonne family, but first calculations with chiral effective potentials, properly transformed to local ones, begin to appear [77].

3. Nuclear wave functions in configuration space and theoretical prediction of short-range correlations

3.1. Many-body wave functions and spin-isospin independent and dependent density matrices

It is now firmly established that unlike the shell-model wave function, describing the independent motion of nucleons in a mean field, the many-body wave function resulting from the solution of the Schrödinger equation with realistic bare interactions exhibits a rich correlation structure, featuring central, spin-isospin and tensor correlations. The main feature of these short-range (with respect to the NN average distance) correlations is that the probability density to find two nucleons located at relative distances $r_{12} \equiv |\mathbf{r}_1 - \mathbf{r}_2| \lesssim 1\text{--}1.5$ fm is strongly suppressed with respect to the MF two-nucleon distribution exhibiting the maximum value at $r \simeq 0$. This is the *correlation hole* already encountered in the deuteron wave function. The features and magnitudes of these SRCs depend upon the spin and isospin of the interacting pair, generating a difference between pp and pn distributions, as well as upon the value of their relative and center-of-mass coordinates. SRCs in momentum space are characterized by high momentum components such that at $k_{rel} \geq 2\text{--}3 \text{ fm}^{-1}$ the nuclear wave function is totally governed by SRCs. In this section it will be shown that microscopic calculations of the two-nucleon density distribution of nuclei performed *ab initio*, or within approximate, but still realistic many-body approaches, predict a correlation hole exhibiting a universal character in that, apart from trivial normalization factors, it is almost independent of the nucleus mass and, moreover, in the spin-isospin state $(ST) = (10)$ is similar to the deuteron one. Particle dynamics in many-body systems is described by density matrices (DM). The diagonal DM is the modulus squared of the ground-state wave function $|\Psi_0(\{\mathbf{x}_i\}_A)|^2$ integrated over a certain number of variables, e.g. $\mathbf{x}_{n+1}, \mathbf{x}_{n+2}, \dots, \mathbf{x}_A$, so that it represents the probability density to find in the nucleus particles $1, 2, \dots, n$ with generalized coordinates $\mathbf{x}_1, \mathbf{x}_2, \dots, \mathbf{x}_n$; non-diagonal density matrices, in turn, describe density fluctuations and are given by the integral of the product $\Psi_0^*(\{\mathbf{x}_i\}_A) \Psi_0(\{\mathbf{x}'_i\}_A)$

integrated over e.g. $\mathbf{x}_{n+1} \delta(\mathbf{x}_{n+1} - \mathbf{x}'_{n+1})$, $\mathbf{x}_{n+2} \delta(\mathbf{x}_{n+2} - \mathbf{x}'_{n+2})$, ..., $\mathbf{x}_A \delta(\mathbf{x}_A - \mathbf{x}'_A)$, and represent the density probability to find nucleons $1, 2, \dots, n$ with generalized coordinates $\mathbf{x}_1, \mathbf{x}_2, \dots, \mathbf{x}_n$ and $\mathbf{x}'_1, \mathbf{x}'_2, \dots, \mathbf{x}'_n$. These DMs are spin-isospin dependent, and if the spin-isospin coordinates are integrated out, the spin-isospin independent DMs are obtained. The spin-isospin independent A -body DM is nothing but the square of the A -body wave function⁵

$$\rho(\mathbf{r}_1, \mathbf{r}_2, \dots, \mathbf{r}_A) = |\Psi_0(\mathbf{r}_1, \mathbf{r}_2, \dots, \mathbf{r}_A)|^2 \delta\left(\sum_{i=1}^A \mathbf{r}_i\right) \quad (3.1)$$

where the *delta*-function results from the requirement of translational invariance according to which only $A - 1$ radial coordinates are linearly independent (in what follows the *delta*-function will be omitted for ease of presentation). In this Report particular attention will be paid to the one-nucleon and two-nucleon diagonal and non diagonal DMs, defined, respectively, as follows

$$\rho_1(\mathbf{r}_1) = \int \prod_{j=2}^A d\mathbf{r}_j |\Psi_0(\mathbf{r}_1, \mathbf{r}_2, \dots, \mathbf{r}_A)|^2, \quad (3.2)$$

$$\rho_1(\mathbf{r}_1; \mathbf{r}'_1) = \int \prod_{j=2}^A d\mathbf{r}_j \Psi_0^*(\mathbf{r}_1, \mathbf{r}_2, \dots, \mathbf{r}_A) \Psi_0(\mathbf{r}'_1, \mathbf{r}_2, \dots, \mathbf{r}_A), \quad (3.3)$$

$$\rho_2(\mathbf{r}_1, \mathbf{r}_2) = \int \prod_{j=3}^A d\mathbf{r}_j |\Psi_0(\mathbf{r}_1, \mathbf{r}_2, \dots, \mathbf{r}_A)|^2, \quad (3.4)$$

$$\rho_2(\mathbf{r}_1, \mathbf{r}_2; \mathbf{r}'_1, \mathbf{r}'_2) = \int \prod_{j=3}^A d\mathbf{r}_j \Psi_0^*(\mathbf{r}_1, \mathbf{r}_2, \mathbf{r}_3, \dots, \mathbf{r}_A) \Psi_0(\mathbf{r}'_1, \mathbf{r}'_2, \mathbf{r}_3, \dots, \mathbf{r}_A), \quad (3.5)$$

obeying the following condition

$$\int \rho_2(\mathbf{r}_1, \mathbf{r}_2) d\mathbf{r}_1 = \rho_1(\mathbf{r}_1) \quad (3.6)$$

and normalization

$$\int \rho_1(\mathbf{r}_1) d\mathbf{r}_1 = A \quad \int \rho_2(\mathbf{r}_1, \mathbf{r}_2) d\mathbf{r}_1 d\mathbf{r}_2 = \frac{A(A-1)}{2}. \quad (3.7)$$

Introducing the relative (*rel*) and center-of-mass (*c.m.*) coordinates

$$\mathbf{r}_{\text{rel}} = \mathbf{r}_1 - \mathbf{r}_2 \equiv \mathbf{r} \quad \mathbf{R}_{\text{c.m.}} = \frac{1}{2} (\mathbf{r}_1 + \mathbf{r}_2) \equiv \mathbf{R}, \quad (3.8)$$

the 2BDM can be expressed in terms of \mathbf{r}_{rel} and $\mathbf{R}_{\text{c.m.}}$ and, the separate *rel* and *c.m.* densities can be defined as follows

$$\rho_{\text{rel}}(\mathbf{r}) = \int \rho_2(\mathbf{r}, \mathbf{R}) d\mathbf{R} \quad \rho_{\text{c.m.}}(\mathbf{R}) = \int \rho_2(\mathbf{r}, \mathbf{R}) d\mathbf{r}. \quad (3.9)$$

The majority of processes to be considered in this Report depends upon the density matrices just defined. However also processes will be discussed which require the knowledge of the full A -body density matrix [78,79]

$$\begin{aligned} & |\Psi_0(\mathbf{r}_1, \mathbf{r}_2, \dots, \mathbf{r}_A)|^2 \delta\left(\sum_{i=1}^A \mathbf{r}_i\right) \\ &= \prod_{j=1}^A \rho_1(\mathbf{r}_j) + \sum_{i < j} \Delta(\mathbf{r}_i, \mathbf{r}_j) \prod_{k \neq i,j} \rho_1(\mathbf{r}_k) + \sum_{(i < j) \neq (k < l)} \Delta(\mathbf{r}_i, \mathbf{r}_j) \Delta(\mathbf{r}_k, \mathbf{r}_l) \prod_{m \neq i,j,k,l} \rho_1(\mathbf{r}_m) + \dots \end{aligned} \quad (3.10)$$

Here $\Delta(\mathbf{r}_i, \mathbf{r}_j)$, is two-nucleon contraction

$$\Delta(\mathbf{r}_1, \mathbf{r}_2) = \rho_2(\mathbf{r}_1, \mathbf{r}_2) - \rho_1(\mathbf{r}_1) \rho_1(\mathbf{r}_2), \quad (3.11)$$

and the relation

$$\int d\mathbf{r}_1 \Delta(\mathbf{r}_1, \mathbf{r}_2) = \int d\mathbf{r}_2 \Delta(\mathbf{r}_1, \mathbf{r}_2) = 0, \quad (3.12)$$

⁵ In what follows we will often call DMs simply *densities*.

trivially follows. Eq. (3.10) includes unlinked products of two-, three-, four-, etc, two-nucleon contractions, representing two-nucleon correlations, plus all possible unlinked products of three-body contractions, describing three-nucleon correlations, four-body contractions, describing four-body correlations, and so on.⁶ When all terms up to A -body correlations are written down explicitly, all lowest order correlations cancel out. In a single Slater determinant approach, all two- and higher order DMs differ from zero only because of statistical correlations, whereas in a system of interacting particles dynamical correlations, generated by the details of the NN interactions, introduce appreciable changes in the structure of DMs. DMs can be generalized to make them dependent upon the relative orbital momentum L , the spin S , and the isospin T , of the NN pair. The non diagonal spin-isospin dependent two-nucleon density matrix has the following form

$$\rho_{(ST)}^{N_1 N_2}(\mathbf{r}_1, \mathbf{r}_2; \mathbf{r}'_1, \mathbf{r}'_2) = \int \Psi_0^*(\tilde{\mathbf{x}}_1, \tilde{\mathbf{x}}_2, \dots, \tilde{\mathbf{x}}_A) \sum_{i < j} \hat{\rho}_{ij}^{(ST)}(\mathbf{r}_1, \mathbf{r}_2; \mathbf{r}'_1, \mathbf{r}'_2) \Psi_0(\tilde{\mathbf{x}}'_1, \tilde{\mathbf{x}}'_2, \dots, \tilde{\mathbf{x}}'_A) \prod_{i=1}^A d\tilde{\mathbf{x}}_i d\tilde{\mathbf{x}}'_i, \quad (3.13)$$

with the non diagonal two-nucleon spin-isospin dependent density matrix operator being

$$\hat{\rho}_{ij}^{(ST)}(\mathbf{r}_1, \mathbf{r}_2; \mathbf{r}'_1, \mathbf{r}'_2) = \hat{P}_{ij}^S \hat{P}_{ij}^T \delta(\tilde{\mathbf{r}}_i - \mathbf{r}_1) \delta(\tilde{\mathbf{r}}_j - \mathbf{r}_2) \delta(\mathbf{r}'_i - \tilde{\mathbf{r}}'_1) \delta(\mathbf{r}'_j - \tilde{\mathbf{r}}'_2) \prod_{k \neq \{i,j\}}^A \delta(\tilde{\mathbf{r}}_k - \tilde{\mathbf{r}}'_k) \prod_{n=1}^A \delta_{s_{3n} s'_{3n}} \delta_{t_{3n} t'_{3n}}, \quad (3.14)$$

where $\hat{P}_{ij}^{T=1} = (3 + \tau_i \cdot \tau_j)/4$ and $\hat{P}_{ij}^{T=0} = (1 - \tau_i \cdot \tau_j)/4$, are the isospin projector operators (with the same form for the spin operators). The explicit expressions for other spin-dependent matrices and operators can be found e.g. in Ref. [80]. The two-nucleon spin-isospin dependent density matrix is linked to the number of pairs in nucleus A in state (ST) , $N_{(ST)}^A$, by the trivial relation

$$\int \rho_{(ST)}^{N_1 N_2}(\mathbf{r}_1, \mathbf{r}_2) d\mathbf{r}_1 d\mathbf{r}_2 = N_{(ST)}^{N_1 N_2} \quad \sum_{N_1 N_2} N_{(ST)}^{N_1 N_2} = N_{(ST)}^A, \quad (3.15)$$

with

$$\sum_{(ST)} N_{(ST)}^A = \frac{A(A-1)}{2} \equiv N_A. \quad (3.16)$$

Note that, as previously stressed, we are considering for ease of presentation ground state wave functions with zero total angular momentum, $J = 0$, and in case of $J \neq 0$ the various quantities have to be averaged over the projections M_J . Many ground-state properties of nuclei can be expressed in terms of density matrices. For example, in the case of a pure central interaction $V(\mathbf{r}_1, \dots, \mathbf{r}_A) = \sum_{i < j} v(r_{ij})$ the expectation value of the Hamiltonian has the form

$$E_A^{(0)} \equiv E_0 = -\frac{\hbar^2}{2m_N} \int d\mathbf{r}_1 [\nabla_1 \cdot \nabla_{1'} \rho(\mathbf{r}_1, \mathbf{r}'_1)]_{\mathbf{r}_1=\mathbf{r}'_1} + \frac{A(A-1)}{2} \int d\mathbf{r}_1 d\mathbf{r}_2 v(r_{12}) \rho_2(\mathbf{r}_1, \mathbf{r}_2), \quad (3.17)$$

whereas if spin-isospin dependent interactions are considered, one has

$$E_A^{(0)} \equiv E_0 = -\frac{\hbar^2}{2m_N} \int d\mathbf{r}_1 [\nabla_1 \cdot \nabla_{1'} \rho(\mathbf{r}_1, \mathbf{r}'_1)]_{\mathbf{r}_1=\mathbf{r}'_1} + \sum_p \int d\mathbf{r}_1 d\mathbf{r}_2 v^{(p)}(r_{12}) \rho_2^{(p)}(\mathbf{r}_1, \mathbf{r}_2), \quad (3.18)$$

where the summation over p runs over all different components of the two-nucleon interaction.

3.2. The effect of SRCs on the number of spin-isospin pairs in nuclei

SRCs have been shown to affect the number of NN pairs in various spin-isospin states $N_{(ST)}^{N_1 N_2}$ given by Eq. (3.15). This quantity has been calculated in various papers, e.g. in Refs. [81–83] for $A \leq 16$, in Ref. [55] for $A \leq 4$, in Ref. [80], for $A = 3, 4, 12, 16$ and 40 , and in Refs. [84,85] for NN pairs in $L = 0$. The results of various calculations are presented in Tables 1 and 2. In a full independent-particle (IP) shell model the number of pairs in (ST) states in case of s-shell nuclei can readily be obtained. As a matter of fact in $A = 3$ and 4 nuclei the relative orbital momentum of all pairs is zero, so that only two (ST) states survive, namely the (10) and (01) ones. A pn pair can be either in (10) state, with probability $3/4$, or in (01) state, with probability $1/4$, whereas a $pp(nn)$ pair can only be in (01) state, with probability 1 . Therefore the total number of pairs in a given (ST) state is $N_{(10)}^3 = 3/2$ and $N_{(01)}^3 = 3/2$, in ${}^3\text{He}$, and $N_{(10)}^4 = N_{(01)}^4 = 3$, in ${}^4\text{He}$. In $A > 4$ nuclei also the states (11) and (00) , associated with odd values of L , can contribute. In Ref. [81] a general approach to calculate, within the IP model, the number of pairs in various (ST) states, based upon counting even and odd pairs in spatial configurations corresponding to a given Young tableaux, has been given, and explicit formulas can be found there. When the IP model picture is released and a full many-body approach with interacting nucleons is considered, odd values of the relative orbital momentum appear

⁶ An unlinked product is defined as a product of contractions having no indexes in common.

Table 1

The effects of SRCs on the number of pairs $N_{(ST)}^A$ (Eq. (3.15)) in nuclei ${}^3\text{He}$, ${}^4\text{He}$, ${}^{16}\text{O}$ and ${}^{40}\text{Ca}$ calculated within the Independent Particle Model (IPM) and various realistic many-body short-range correlated wave functions. Only pairs in relative $L = 0$ motion, considered to be the most prone to SRCs, were considered in Ref. [84].

Source: Reprinted from [80].

© 2013, by the American Physical society.

Nucleus	(ST)			
	(10)	(01)	(00)	(11)
${}^2\text{H}$	1	–	–	–
${}^3\text{He}$	IPM	1.50	1.50	–
	SRC [80]	1.488	1.360	0.013
	SRC [82]	1.50	1.350	0.01
	SRC [55]	1.489	1.361	0.011
${}^4\text{He}$	IPM	3	3	–
	IPM(Os states) [84]	3	3	–
	SRC [80]	2.99	2.57	0.01
	SRC [82]	3.02	2.5	0.01
${}^{16}\text{O}$	SRC [55]	2.992	2.572	0.08
	IPM	30	30	6
	IPM(Os states) [84]	20	18	–
	SRC [80]	29.8	27.5	6.075
${}^{40}\text{Ca}$	SRC [82]	30.05	28.4	6.05
	IPM	165	165	45
	IPM(Os states) [84]	90	20	–
	SRC [80]	165.18	159.39	45.10
				410.34

Table 2

The same as in Table 1 for nuclei ${}^3\text{He}$, ${}^4\text{He}$, ${}^6\text{Li}(1^+)$, ${}^7\text{Li}(\frac{3}{2}^-)$, ${}^8\text{Be}(0^+)$, ${}^9\text{Be}(\frac{3}{2}^-)$, ${}^{10}\text{B}(3^+)$ calculated in Ref. [83] with both independent pair (IP = IPM in Table 1) and correlated (cor = SRC in Table 1). All calculations within the VMC approach with the AV18 NN interaction plus 3N UIX force.

Source: Reprinted from [83].

© 2014, by the American Physical society.

Nucleus	Ψ	N_{01}	N_{11}	N_{10}	N_{00}
${}^3\text{He}(\frac{1}{2}^+)$	IP	1.5	0.0	1.5	0.0
	cor	1.36	0.14	1.49	0.01
${}^4\text{He}(0^+)$	IP	3.0	0.0	3.0	0.0
	cor	2.54	0.46	2.99	0.01
	[AV18]	2.60	0.40	2.99	0.01
	[AV18(4)]	2.99	0.01	2.99	0.01
${}^6\text{Li}(1^+)$	[AV18(J)]	3.00	0.00	3.00	0.00
	IP	4.5	4.5	5.5	0.5
${}^7\text{Li}(\frac{3}{2}^-)$	cor	4.05	4.95	5.47	0.53
	IP	6.75	6.75	6.75	0.75
${}^8\text{Be}(0^+)$	cor	6.12	7.38	6.74	0.76
	IP	9.0	9.0	9.0	1.0
${}^9\text{Be}(\frac{3}{2}^-)$	cor	8.07	9.93	8.98	1.02
	IP	10.5	13.5	10.5	1.5
${}^{10}\text{B}(3^+)$	cor	9.56	14.44	10.48	1.52
	IP	12.0	18.0	13.0	2.0
		11.17	18.83	12.95	2.05

also in $A = 3$ and 4 nuclei so that: (i) the states (00) and (11) are generated in ${}^3\text{H}$, ${}^3\text{He}$, and ${}^4\text{He}$ and (ii) the amount of various (ST) states in complex nuclei is changed. Thanks to isospin conservation, the number of states (01) is decreased in favor of states (11) and the number of deuteron-like states (10) is also decreased in favor of the state (00). In Ref. [80] the values of $N_{(ST)}^A$, for the three- and four-nucleon systems, have been obtained using the wave functions of Refs. [48,49] corresponding to the AV18 and AV8' interactions, respectively, whereas for complex nuclei the cluster expansion of Ref. [68], which includes two-, three- and four-body cluster contributions has been adopted. In Ref. [82] $N_{(ST)}^A$ has been calculated for ${}^3\text{He}$, ${}^4\text{He}$, ${}^6\text{Li}$, ${}^7\text{Li}$, and ${}^{16}\text{O}$ using variational VMC wave functions and various Argonne interactions; in Ref. [55] $N_{(ST)}^A$ has been obtained for nuclei ${}^3\text{He}$, ${}^3\text{H}$ and ${}^4\text{He}$ using wave functions resulting from the correlated Gaussian basis approach [52] and the V8' interaction. Very recently, the number of correlated pairs in ${}^3\text{He}$, ${}^4\text{He}$, ${}^6\text{Li}$, ${}^7\text{Li}$, ${}^8\text{Be}$, ${}^9\text{Be}$ and ${}^{10}\text{Be}$ has been calculated, within the VMC method using the AV18 interactions and Urbana UIX three-nucleon interactions [83]. In Refs. [84,85] the number of pairs in $L = 0$ state has been evaluated through the Periodic Table using phenomenological correlated wave functions. The results of these calculations, clearly show that: (i) there is satisfactory general agreement between the results of Ref. [80]

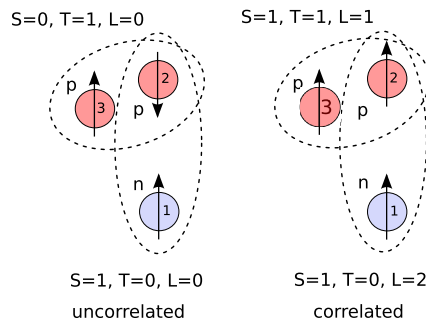


Fig. 6. The three-body mechanism as suggested in Refs. [82,55].

Source: Reprinted from [55].

© 2011, by the American Physical society.

and the ones of Refs. [82,55,83], and (ii) when the IP model picture is released and NN correlations are taken into account, the value of $N_{(10)}^A$ is practically unchanged, whereas the number of pairs in the (01) state is decreased in favor of the state (11). The reason for that was nicely explained in Refs. [55,82]: it is due to some kind of many-body effects induced by tensor correlations between particles “2” and “3”, generating a spin flip of particle “2”, and giving rise to the state (11) between particles “2” and “1”. This is schematically shown in Fig. 6.

3.3. Two-nucleon densities and theoretical evidence of the universal character of short-range correlations

Two-nucleon DMs of nuclei $A = 3, 4, 12, 16$ and 40 have been calculated by various groups using ground-state wave functions resulting from the direct solution of the Schrödinger equation with realistic bare NN interactions. In case of few-nucleon systems ($A = 3, 4$), *ab initio* solutions have been obtained within different equivalent methods: the Faddeev approach [47], the expansion of the ground state wave function in a complete set of basis functions [48,54,55], the ATMS method [49] and the VMC method [50,82,83]. In Fig. 7 the results of Ref. [54] obtained using a wave function expressed in terms of a Gaussian basis and the V8' interaction are shown for ${}^2\text{H}$, ${}^3\text{H}$, ${}^3\text{He}$, ${}^4\text{He}$, and ${}^4\text{He}^*$ in correspondence of the various components of the interaction. It can be seen that:

1. the correlation hole is present in all spin-isospin states;
2. the dominant states are the (10) central (C_1) and tensor (C_T) states;
3. apart from a normalization factor, generally the densities behave very similarly at short range and reach their maxima at $r \simeq 1$ fm.

The latter point is also illustrated by the results shown in Fig. 8 (Left), obtained *ab initio* in Ref. [55] using wave functions and two-nucleon interactions as in Ref. [54]: it can be seen that the correlation hole has the same spatial extent in $A = 2, 3$ and 4 . In the same figure (Right) the results of *ab initio* calculations for nuclei with $A = 2, 4, 6, 16$ are shown. In Fig. 9 the two body densities of ${}^{12}\text{C}$, ${}^{16}\text{O}$ and ${}^{40}\text{Ca}$ are shown together with the separate densities of $p-p$ and $p-n$ pairs. It can be seen that the correlation hole found in $A = 3, 4$ is clearly visible in complex nuclei as well, moreover:

1. at short separations the correlation hole appears to be the same for all values of A , which leads to the non trivial conclusion that at short ranges the two-nucleon motion is not affected by the presence of the other particles; this is what has been called in Ref. [55] universality of SRCs in few-nucleon system that can be extended to complex nuclei as well;
2. at large separation the asymptotic of the two-nucleon densities for different nuclei is different due to the different binding energy (for details see Ref. [54]).

Finally, Fig. 10 clearly illustrates the large overshooting of the correlated two-nucleon density generated by the attractive tensor force acting between a proton–neutron pair. To sum up, calculations with bare realistic interactions show that, apart from an obvious normalization factor depending upon the different number of pairs in different nuclei, the relative two-nucleon density $\rho_{rel}(r)$ and its spin-isospin components $\rho_{ST}^{N_1 N_2}(r)$ at $r \lesssim 1.5$ fm exhibit similar correlation holes, generated by the cooperation of the short-range repulsion and the intermediate-range tensor attraction of the NN interaction, with the tensor force governing the overshooting at $r \simeq 1.0$ fm. The correlation hole is universal, in that it is almost independent of the mass A of the nucleus. These results also demonstrate that different many-body approaches, ranging from the VMC to proper cluster expansion methods predict essentially the same behavior of the correlation hole. In order to ascertain whether these features can have an experimental confirmation, one has first of all to shift to momentum space, expecting: (i) an increase of nucleon high-momentum components in the ground-state wave function, (ii) peculiar momentum configurations that are missing in a mean-field description. Very recently the GFMC approach has been applied for the first time with a local version of a chiral NN interaction to the calculation of ${}^4\text{He}$ properties [77]. The results for

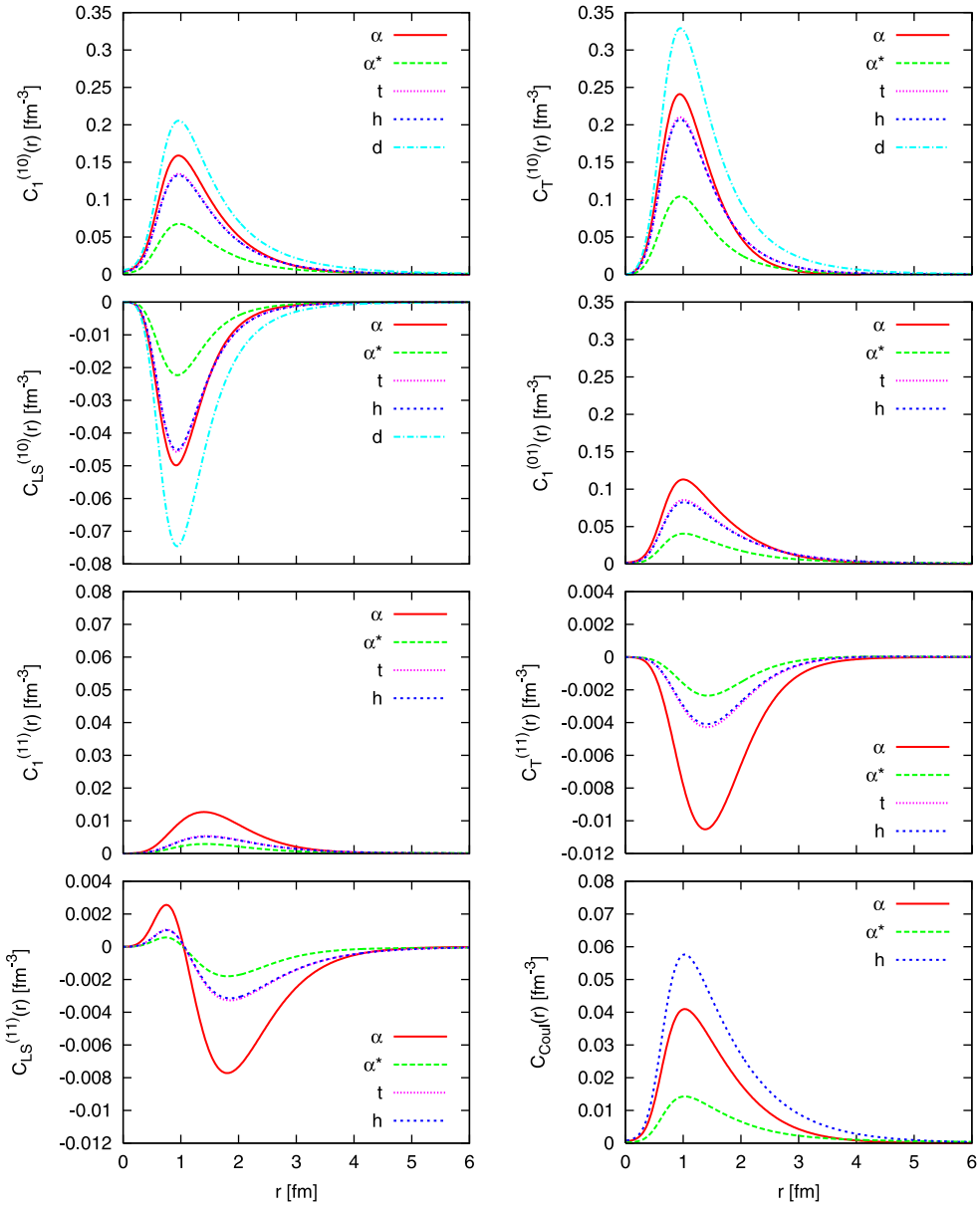


Fig. 7. The two-nucleon relative distribution in various spin-isospin states in ^2H , ^3H , ^3He and $^4\text{He}^*$ obtained from the calculation within the Gaussian expansion method [54] with the AV8' interaction.

Source: Reprinted from [54].

© 2009, by the American Physical Society.

the two-body density in $T = 1$ state, shown in Fig. 11, exhibits, as expected a correlation hole much softer than the one predicted by the AV18 interaction. It would be interesting to produce the momentum distribution within such an approach.

4. Short-range correlations in momentum space: one- and two-nucleon momentum distributions

4.1. Two-nucleon SRCs in momentum space: introduction

SRCs considerably increase the high-momentum content of the one-body momentum distributions through the term $\sum_{n=2}^{\infty} c_n \Phi_{npnh}$ in Eq. (2.12), i.e. via the population of $np-nh$ states with momentum much higher than the Fermi momentum $k_F \simeq 1.4 \text{ fm}^{-1}$. SRCs, moreover, generate peculiar wave function configurations that are missing in a MF description [12].

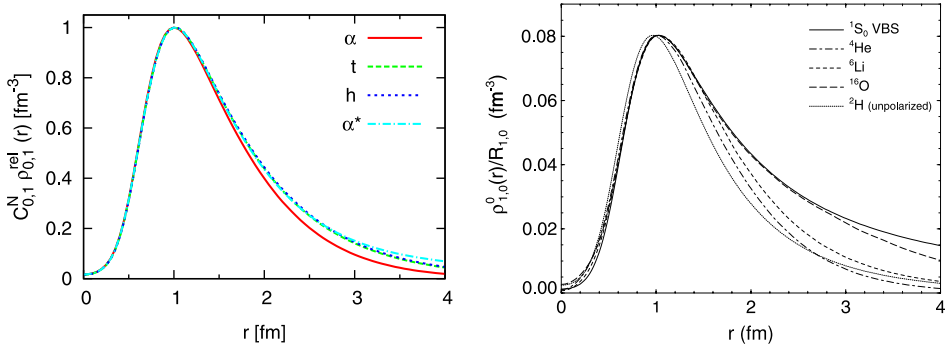


Fig. 8. (Left): the two-nucleon relative distribution in state (ST) = (01) for ^3H , ^3He and ^4He obtained *ab initio* [55] with the AV8 interaction. All distributions are normalized to $r = 1$ fm. (Right): two-nucleon densities of ^2H , ^4He , ^6Li , ^{16}O shown together with the virtual state 1S_0 of the AV18 interaction (the analog of the deuteron in the (ST) = (0, 1) channel) obtained in Ref. [82] within the VMC method and the AV18 interaction.

Source: (Left) Reprinted from [55]. © 2011, by the American Physical Society. (Right) Reprinted from [82]. © 1996, by the American Physical Society.

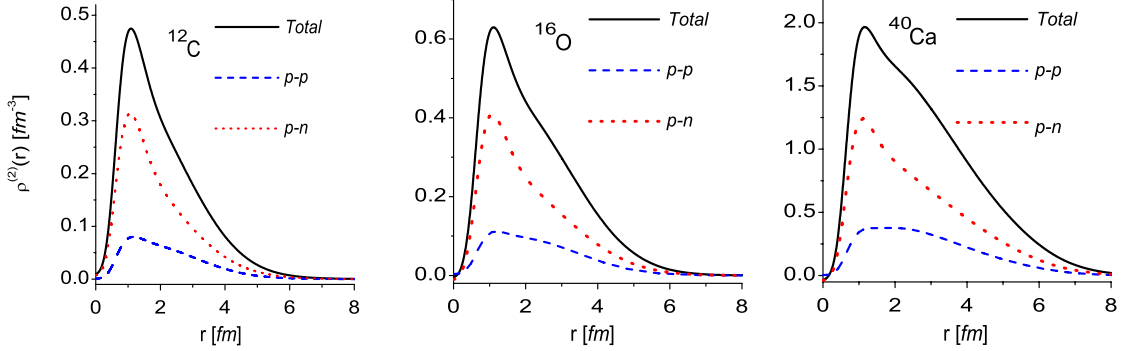


Fig. 9. The relative two-nucleon density distribution ($\rho_{\text{rel}} \equiv \rho^{(2)}$) (Eq. (3.9)) of ^{12}C , ^{16}O , and ^{40}Ca calculated within the linked cluster expansion and the AV6 interaction [86]. The proton-neutron ($p-n$) and proton-proton ($p-p$) contributions are also shown. The various curves are normalized to the corresponding numbers of NN pairs of the given type.

Source: After Ref. [86].

As a matter of fact, since in a nucleus momentum conservation requires that⁷

$$\sum_{i=1}^A \mathbf{k}_i = 0, \quad (4.1)$$

a nucleon with high momentum \mathbf{k}_1 in a MF configuration is expected to be balanced by the rest of the $(A - 1)$ nucleons, i.e.

$$\mathbf{k}_1 \simeq - \sum_{i=2}^A \mathbf{k}_i \quad \mathbf{k}_i \simeq \frac{\mathbf{k}_1}{A - 1}, \quad (4.2)$$

whereas in a 2NSRC configuration one should have

$$\mathbf{k}_1 \simeq -\mathbf{k}_2 \quad \mathbf{K}_{A-2} = \sum_{i=3}^A \mathbf{k}_i \simeq 0. \quad (4.3)$$

Therefore two-nucleon short-range correlations (2N-SRCs) can be defined as those configurations of a pair of nucleons characterized by *high* values of the relative momentum and *small* values of the center-of-mass momentum. The quantitative meaning of such a statement will be discussed later on.

4.2. The one-nucleon and two-nucleon momentum distributions: general formulae

The spin-isospin-independent one-nucleon momentum distribution (1NMD) of a nucleon N_1 is defined as follows

$$n_A^{N_1}(\mathbf{k}_1) = \frac{1}{(2\pi)^3} \int d\mathbf{r}_1 d\mathbf{r}'_1 e^{i\mathbf{k}_1 \cdot (\mathbf{r}_1 - \mathbf{r}'_1)} \rho_A^{N_1}(\mathbf{r}_1, \mathbf{r}'_1), \quad (4.4)$$

⁷ Through this report the momentum of nucleon i in the nucleus will be denoted by \mathbf{k}_i whereas in the continuum it will be denoted by \mathbf{p}_i .

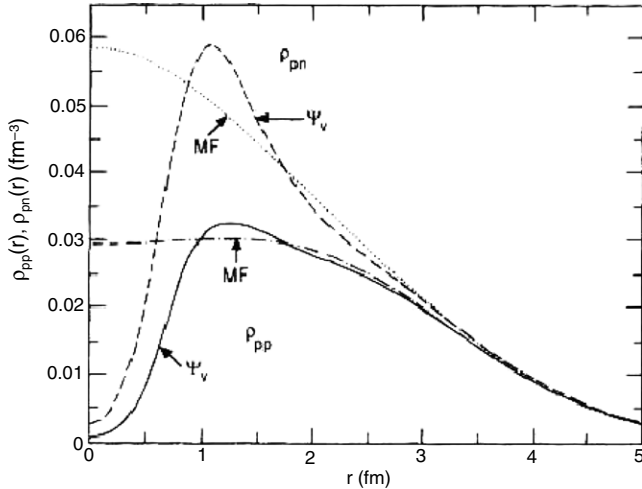


Fig. 10. The correlated variational Monte Carlo (ψ_v) proton-neutron (pn) and proton-proton (pp) two-nucleon relative distributions of ^{16}O calculated in Ref. [87] using the AV14 interaction [29] and the VMC method, compared with the MF distributions.

Source: Reprinted from [87].

© 1992, by the American Physical Society.

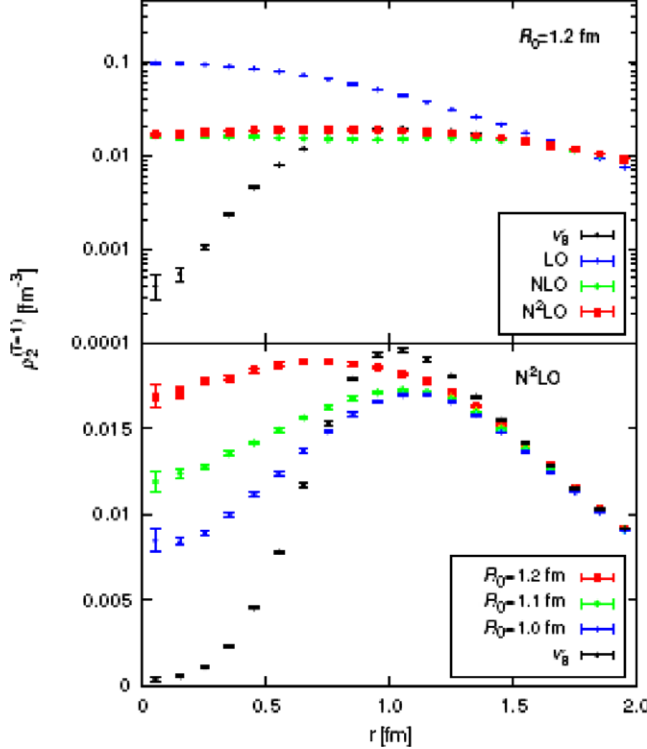


Fig. 11. (Top panel): the results of *ab initio* GFMC calculations of the two-body density in $T = 1$ state in ^4He obtained with a local version of the chiral effective interaction up to next-to-next-to-leading order, compared with the results corresponding to the V8' interaction (black dots). (Bottom panel): dependence of the GFMC results upon the cut off parameter R_0 appearing in the regulator adopted to obtain a local interaction from the non-local chiral potential (for details see Ref. [77]).

Source: Reprinted from [77].

with $N_1 = \{p, n\}$ and normalization

$$\int n_A^{p(n)}(\mathbf{k}_1) d\mathbf{k}_1 = \int \rho_A^{p(n)}(\mathbf{r}_1) d\mathbf{r}_1 = Z(N), \quad (4.5)$$

where $\rho_A^{N_1}$ is normalized to the number of nucleons of the type N_1 (in case of isoscalar nuclei $N_p = N_n = A/2$ and the label N_1 will be omitted). The spin independent two-nucleon momentum distributions (2NMD) is defined as follows

$$n_A^{N_1 N_2}(\mathbf{k}_1, \mathbf{k}_2) = \frac{1}{(2\pi)^6} \int d\mathbf{r}_1 d\mathbf{r}_2 d\mathbf{r}'_1 d\mathbf{r}'_2 e^{i\mathbf{k}_1 \cdot (\mathbf{r}_1 - \mathbf{r}'_1)} e^{i\mathbf{k}_2 \cdot (\mathbf{r}_2 - \mathbf{r}'_2)} \rho_2^{N_1 N_2}(\mathbf{r}_1, \mathbf{r}_2; \mathbf{r}'_1, \mathbf{r}'_2). \quad (4.6)$$

Here the following relation

$$n^{N_1}(\mathbf{k}_1) = \int n^{N_1 N_2}(\mathbf{k}_1, \mathbf{k}_2) d\mathbf{k}_2, \quad (4.7)$$

trivially holds. By introducing the relative and *c.m.* momenta

$$\mathbf{k}_{rel} = \frac{1}{2}(\mathbf{k}_1 - \mathbf{k}_2) \equiv \mathbf{k} \quad \mathbf{K}_{CM} = \mathbf{k}_1 + \mathbf{k}_2 \equiv \mathbf{K}, \quad (4.8)$$

one obtains

$$\begin{aligned} n(\mathbf{k}_1, \mathbf{k}_2) &= n(\mathbf{k}_{rel}, \mathbf{K}_{CM}) = n(k_{rel}, K_{CM}, \theta) \\ &= \frac{1}{(2\pi)^6} \int d\mathbf{r} d\mathbf{r}' d\mathbf{R} d\mathbf{R}' e^{-i\mathbf{K} \cdot (\mathbf{R} - \mathbf{R}')} e^{-i\mathbf{k} \cdot (\mathbf{r} - \mathbf{r}')} \rho_2(\mathbf{r}, \mathbf{r}'; \mathbf{R}, \mathbf{R}'), \end{aligned} \quad (4.9)$$

where θ is the angle between \mathbf{k}_{rel} and $\mathbf{K}_{c.m.}$. Different types of 2NMDs can therefore be defined:

1. the 2NMD of back-to-back nucleons $\mathbf{k}_2 = -\mathbf{k}_1$, $\mathbf{K}_{c.m.} = 0$ (like in the deuteron)

$$n(\mathbf{k}_{rel}, \mathbf{K}_{CM} = 0) = \frac{1}{(2\pi)^6} \int d\mathbf{r} d\mathbf{r}' e^{-i\mathbf{k} \cdot (\mathbf{r} - \mathbf{r}')} \rho_2(\mathbf{r}, \mathbf{r}'), \quad (4.10)$$

where

$$\rho_2(\mathbf{r}, \mathbf{r}') = \int \rho_2(\mathbf{r}, \mathbf{r}'; \mathbf{R}, \mathbf{R}') d\mathbf{R} d\mathbf{R}' \quad (4.11)$$

2. the relative two-body and *c.m.* MDs

$$n_{rel}(\mathbf{k}) = \int n(\mathbf{k}, \mathbf{K}) d\mathbf{K} \quad n_{c.m.}(\mathbf{K}) = \int n(\mathbf{k}, \mathbf{K}) d\mathbf{k}. \quad (4.12)$$

3. the total 2NMD given by Eq. (4.9).

All formulae above have been generalized [80] to the spin-isospin representation as follows: using the spin-isospin dependent DMs presented in Section 3, the two-body spin-isospin dependent momentum distribution of a pair of nucleons in state (*ST*) can be introduced, namely

$$n_{(ST)}^{N_1 N_2}(\mathbf{k}_1, \mathbf{k}_2) = \frac{1}{(2\pi)^6} \int d\mathbf{r}_1 d\mathbf{r}_2 d\mathbf{r}'_1 d\mathbf{r}'_2 e^{i\mathbf{k}_1 \cdot (\mathbf{r}_1 - \mathbf{r}'_1)} e^{i\mathbf{k}_2 \cdot (\mathbf{r}_2 - \mathbf{r}'_2)} \rho_{N_1 N_2}^{(ST)}(\mathbf{r}_1, \mathbf{r}_2; \mathbf{r}'_1, \mathbf{r}'_2). \quad (4.13)$$

By summing Eq. (4.13) over *T* and *S*, the spin-isospin averaged 2NMD is obtained

$$n_A^{(N_1 N_2)}(\mathbf{k}_1, \mathbf{k}_2) = \sum_{(ST)} n_{(ST)}^{(N_1 N_2)}(\mathbf{k}_1, \mathbf{k}_2) = \frac{1}{(2\pi)^6} \int d\mathbf{r}_1 d\mathbf{r}'_1 d\mathbf{r}_2 d\mathbf{r}'_2 e^{i\mathbf{k}_1 \cdot (\mathbf{r}_1 - \mathbf{r}'_1)} e^{i\mathbf{k}_2 \cdot (\mathbf{r}_2 - \mathbf{r}'_2)} \rho_A^{(N_1 N_2)}(\mathbf{r}_1, \mathbf{r}_2; \mathbf{r}'_1, \mathbf{r}'_2), \quad (4.14)$$

where

$$\rho_A^{(N_1 N_2)}(\mathbf{r}_1, \mathbf{r}_2; \mathbf{r}'_1, \mathbf{r}'_2) = \sum_{(ST)} \rho_{(ST)}^{(N_1 N_2)}(\mathbf{r}_1, \mathbf{r}_2; \mathbf{r}'_1, \mathbf{r}'_2). \quad (4.15)$$

The 2NMD obeys the following normalization

$$\int n_{(ST)}^{N_1 N_2}(\mathbf{k}_1, \mathbf{k}_2) d\mathbf{k}_1 d\mathbf{k}_2 = \int \rho_{(ST)}^{N_1 N_2}(\mathbf{r}_1, \mathbf{r}_2) d\mathbf{r}_1 d\mathbf{r}_2 = N_{(ST)}^{N_1 N_2}, \quad (4.16)$$

and

$$\int n_A(\mathbf{k}_1, \mathbf{k}_2) d\mathbf{k}_2 d\mathbf{k}_1 = \int \rho_A(\mathbf{r}_1, \mathbf{r}_2) d\mathbf{r}_1 d\mathbf{r}_2 = \frac{A(A-1)}{2}. \quad (4.17)$$

A recent systematic analysis of realistic calculations of $n_A(k)$ for $A = 2, 3, 4, 16$, and 40 has been presented in Ref. [80] and for $A \leq 12$ in Ref. [83]. The momentum distributions of medium-weight nuclei have been previously obtained by different groups. The results for ^{16}O , shown in Fig. 12(a), are aimed at illustrating the convergence of different approaches performed with similar NN interactions, whereas the results presented in Fig. 12(b) shows that the high-momentum part of $n_A(\mathbf{k}_1)$ of different nuclei exhibits a qualitative universal scaling behavior. This point will be discussed on a more quantitative level in Section 4.5.

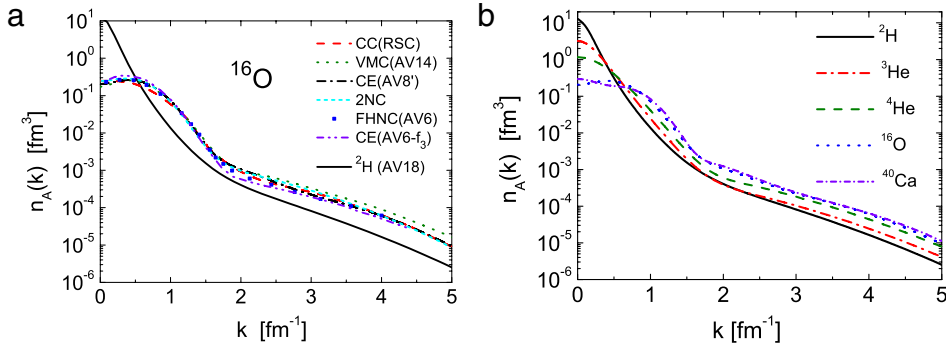


Fig. 12. (a) The proton momentum distribution in ^{16}O calculated with different NN interactions and theoretical approaches. CC: RSC interaction and the Coupled Cluster approach [88]; VMC: AV14 interaction and the VMC approach [87]; FHNC: AV8 interaction and the Fermion Hypernetted Chain approach [72]; CE: AV8' interaction and the linked cluster expansion approach [68]; CE: AV6 interaction and the linked cluster expansion approach within the f_3 approximation (only three correlation functions f_1 , f_4 and f_6 are taken into account) [89]. 2NC: The phenomenological two-nucleon correlation model of Ref. [114]. Similar distributions have been obtained within the BBG approach [90,91]. The full line denotes the deuteron momentum distributions corresponding to the AV18 interaction [30]. (b) The proton momentum distribution of different nuclei calculated within different many-body approaches and equivalent NN interactions, namely the AV18 one [30], in the case of ^2H and ^3He , and the AV8' one, in the case of ^4He , ^{16}O , and ^{40}Ca . Note that in this and in the following figures all distributions are normalized to one i.e. they represent the *per nucleon* momentum distributions. Note, moreover, for isoscalar nuclei $n^p(\mathbf{k}) = n^n(\mathbf{k}) = n_A(\mathbf{k})/2$. $|\mathbf{k}_1| \equiv |\mathbf{k}| \equiv k$.

Source: Adapted from [80].

© 2013, by the American Physical Society.

4.3. The one-nucleon momentum distribution (1NMD) and its correlation structure

Recently the 1NMDs have been systematically calculated within well defined many-body approaches and interactions, namely *ab initio* solutions and the AV18 interaction for $A = 3, 4$ [80], the linked-cluster expansion and the AV8' interaction [80], and the VMC with the Argonne AV18 two-nucleon plus the Urbana UIX three-nucleon interactions in Ref. [83]. In Ref. [80] a detailed illustration of the SRC and spin-isospin structure of nuclei has been presented, whose most relevant aspects will be illustrated in what follows. The ground-state wave function Ψ_0 , solution of Eq. (2.3) describes both MF and correlated nucleon motions. The latter, in turn, includes both long-range (LR) and short-range (SR) correlations; LRCs manifest themselves mostly in open shell nuclei, and are responsible for configuration mixing resulting in partial occupation of states which are empty in a simple independent particle model, with small effects, however, on high-momentum components; SRCs, on the contrary, generate high virtual particle-hole excitations even in closed-shell nuclei, and strongly affect the high-momentum content of the wave function. However there is a region of transition where the two types of correlations overlap. Therefore, assuming that the momentum distributions could be extracted from some experimental data, we have to figure out a clear cut way to disentangle the momentum content generated by the MF and LRCs from the one arising from SRCs. Denoting by $\{\lvert \psi_f^{A-1} \rangle\}$ the complete set of eigenfunctions of nucleus $(A-1)$ described by the same Hamiltonian of nucleus A , and using the completeness relation

$$\sum_{f=0}^{\infty} \lvert \Psi_{A-1}^f \rangle \langle \Psi_{A-1}^f \rvert = 1, \quad (4.18)$$

the 1NMD can be written as follows [92]

$$n_A(\mathbf{k}_1) = n_{gr}(\mathbf{k}_1) + n_{ex}(\mathbf{k}_1), \quad (4.19)$$

where

$$(2\pi)^3 n_{gr}(\mathbf{k}_1) = \sum_{f=0, \sigma_1} \left| \int e^{i\mathbf{k}_1 \cdot \mathbf{r}_1} d\mathbf{r}_1 \int \chi_{\frac{1}{2}\sigma_1}^\dagger \Psi_{A-1}^f(\{\mathbf{r}_i\}_{A-1})^\dagger \Psi_0(\mathbf{r}_1, \{\mathbf{r}_i\}_{A-1}) \prod_{i=2}^A d\mathbf{r}_i \right|^2, \quad (4.20)$$

and

$$(2\pi)^3 n_{ex}(\mathbf{k}_1) = \sum_{f \neq 0, \sigma_1} \left| \int e^{i\mathbf{k}_1 \cdot \mathbf{r}_1} d\mathbf{r}_1 \int \chi_{\frac{1}{2}\sigma_1}^\dagger \Psi_{A-1}^f(\{\mathbf{r}_i\}_{A-1})^\dagger \Psi_0(\mathbf{r}_1, \{\mathbf{r}_i\}_{A-1}) \prod_{i=2}^A d\mathbf{r}_i \right|^2. \quad (4.21)$$

In Eq. (4.21) the sum over f stands also for an integral over the continuum final states that are present in Eq. (4.18). Thus the momentum distribution can be expressed through the overlap integrals between the ground-state wave function Ψ_0 of nucleus A and the wave function $\Psi_{(A-1)}^f$ of the state f of nucleus $(A-1)$. The separation of the momentum distributions in n_{gr} and n_{ex} is particularly useful for $A = 3, 4$ nuclei, when the excited states of $(A-1)$ are in the continuum. For complex nuclei, where many discrete hole excited states are present, it is more convenient to use another representation where the

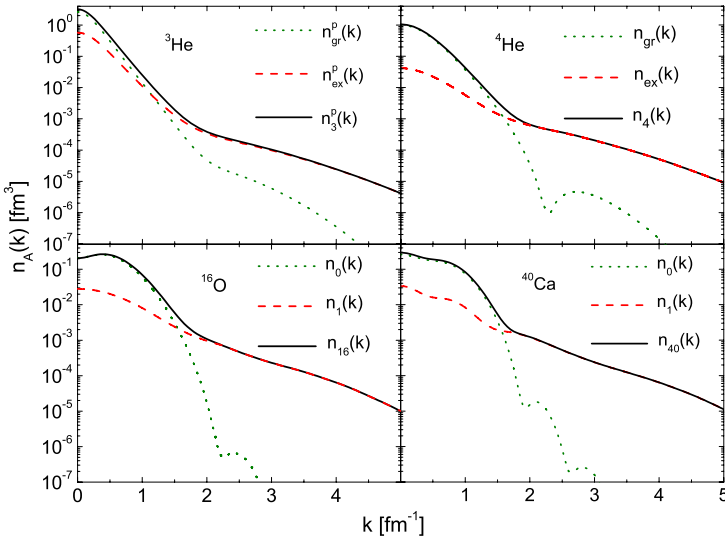


Fig. 13. The proton momentum distribution $n_A^p(k_1) \equiv n_A(k)$ and its separation into the uncorrelated and correlated contributions, Eqs. (4.19)–(4.24), in $A = 3$ (wave function from Ref. [48], AV18 interaction), $A = 4$ (wave function from Ref. [49], AV8' interaction), $A = 16$ (wave functions from Ref. [68], AV8' interaction), and $A = 40$ (wave function from Ref. [68], AV8' interaction). The values of the probabilities $\mathcal{P}_{gr(0)}^p = 4\pi \int k^2 dk n_{gr}^p(k)$ and $\mathcal{P}_{ex(1)}^p = 4\pi \int k^2 dk n_{ex}^p$, Eq. (4.26), are listed in Table 3 and the partial probabilities, Eq. (4.28), in Table 4.

Source: Reprinted from [80].

© 2013, by the American Physical Society.

particle–hole structure of the realistic solutions of Eq. (2.3) is explicitly exhibited by Eq. (2.12). Within such a representation, one has [93,111]

$$n_A(\mathbf{k}_1) = n_0(\mathbf{k}_1) + n_1(\mathbf{k}_1), \quad (4.22)$$

where

$$(2\pi)^3 n_0(\mathbf{k}_1) = \sum_{f \leq F, \sigma_1} \left| \int e^{i\mathbf{k}_1 \cdot \mathbf{r}_1} d\mathbf{r}_1 \int \chi_{\frac{1}{2}\sigma_1}^\dagger \Psi_{A-1}^f(\{\mathbf{r}_i\}_{A-1})^\dagger \Psi_0(\mathbf{r}_1, \{\mathbf{r}_i\}_{A-1}) \prod_{i=2}^A d\mathbf{r}_i \right|^2, \quad (4.23)$$

$$(2\pi)^3 n_1(\mathbf{k}_1) = \sum_{f > F, \sigma_1} \left| \int e^{i\mathbf{k}_1 \cdot \mathbf{r}_1} d\mathbf{r}_1 \int \chi_{\frac{1}{2}\sigma_1}^\dagger \Psi_{A-1}^f(\{\mathbf{r}_i\}_{A-1})^\dagger \Psi_0(\mathbf{r}_1, \{\mathbf{r}_i\}_{A-1}) \prod_{i=2}^A d\mathbf{r}_i \right|^2. \quad (4.24)$$

The summation over f in Eq. (4.23) includes all the discrete shell-model levels below the Fermi level in $(A - 1)$ (“hole states” of A), and in Eq. (4.24) it includes all the discrete and continuum states above the Fermi level created by SRCs. In a fully uncorrelated MF approach, one has

$$n_A(\mathbf{k}_1) = n_0(\mathbf{k}_1) = \sum_{\alpha \leq F} |\phi_\alpha(\mathbf{k}_1)|^2 \quad n_1(\mathbf{k}_1) = 0. \quad (4.25)$$

The modulus squared of the overlap integral represents the weight of the ground and excited virtual states of $(A - 1)$ in the ground state of A , so that the quantities

$$\mathcal{P}_{gr(0)} = \int_0^\infty n_{gr(0)}(\mathbf{k}_1) d\mathbf{k}_1 \quad \mathcal{P}_{ex(1)} = \int_0^\infty n_{ex(1)}(\mathbf{k}_1) d\mathbf{k}_1, \quad (4.26)$$

with

$$\mathcal{P}_{gr(0)} + \mathcal{P}_{ex(1)} = 1, \quad (4.27)$$

yield, respectively, the probability to find a MF and a correlated nucleon in the range $0 \leq k_1 \leq \infty$, therefore they can be assumed to represent the MF and SRC total probabilities. It is clear that both low- and high-momentum components contribute to mean-field and correlated momentum distributions but, as it should be expected, $n_{gr(0)}$ ($n_{ex(1)}$) should get contribution mainly from low (high) momentum components. This is clearly illustrated in Fig. 13, where the proton momentum distributions of $A = 3, 4, 16$, and 40 nuclei are shown with the separation into the MF and correlation contributions: it can be seen that, starting from $k \gtrsim 2 \text{ fm}^{-1}$, the momentum distributions are dominated by the correlated part, but around $k \simeq 1.5 \text{ fm}^{-1}$, LRC may play a non negligible role. The calculated values of $\mathcal{P}_{gr(0)}$ and $\mathcal{P}_{ex(1)}$ for several nuclei

Table 3

The proton MF, $\mathcal{P}_{gr(0)}^p = \int d\mathbf{k}_1 n_{gr(0)}^p(\mathbf{k}_1)$, and SRC, $\mathcal{P}_{ex(1)}^p = \int d\mathbf{k}_1 n_{ex(1)}^p(\mathbf{k}_1)$, probabilities, Eq. (4.26), in various nuclei obtained from AV18 and AV8' interactions.

Source: Reprinted from [80].

© 2013, by the American Physical Society.

Mean Field and SRC Probabilities			
Nucleus	Potential	\mathcal{P}_{gr}	\mathcal{P}_{ex}
${}^3\text{He}$ [48]	AV18 [30]	0.677	0.323
${}^4\text{He}$ [49]	RSC [24] V8' [28]	0.8	0.2
Nucleus	Potential	\mathcal{P}_0	\mathcal{P}_1
${}^{16}\text{O}$ [68]	V8' [28]	0.8	0.2
${}^{40}\text{Ca}$ [68]	V8' [28]	0.8	0.2

Table 4

The values of the proton partial probability, Eq. (4.28), for ${}^3\text{He}$, ${}^4\text{He}$, ${}^{16}\text{O}$ and ${}^{40}\text{Ca}$, calculated for different values of the momentum k_1^- (in fm $^{-1}$) with $k_1^+ = \infty$.

Source: Reprinted from [80].

© 2013, by the American Physical Society.

k_1^-	${}^2\text{H}$	${}^3\text{He(p)}$		${}^4\text{He}$		${}^{16}\text{O}$	${}^{40}\text{Ca}$		
	\mathcal{P}	\mathcal{P}_{gr}	\mathcal{P}_{ex}	\mathcal{P}_{gr}	\mathcal{P}_{ex}	\mathcal{P}_0	\mathcal{P}_1	\mathcal{P}_0	
0.0	1.0	0.7	0.3	0.8	0.2	0.8	0.2	0.8	0.2
0.5	0.3	0.3	0.2	0.5	0.1	0.7	0.2	0.7	0.2
1.0	0.08	0.03	0.07	0.1	0.1	0.2	0.1	0.2	0.1
1.5	0.06	0.005	0.04	0.008	0.08	0.008	0.1	0.01	0.1
2.0	0.04	0.002	0.02	$7 \cdot 10^{-4}$	0.06	$6 \cdot 10^{-4}$	0.06	$3 \cdot 10^{-4}$	0.07

are listed in Table 3. Assuming that $n_0^{N_1}$ and $n_1^{N_1}$ could be obtained from some measurable cross section, it might well be that only a limited range of momenta is available experimentally, in which case it is useful to define the partial probabilities

$$\mathcal{P}_{0(1)}(k_1^\pm) = 4\pi \int_{k_1^-}^{k_1^+} n_{0(1)}(\mathbf{k}_1) k_1^2 d\mathbf{k}_1, \quad (4.28)$$

i.e. the probability to observe a MF or a correlated nucleon with momentum in the range $k_1^- \leq k_1 \leq k_1^+$. The calculated values of $\mathcal{P}_{0(1)}^{N_1}(k_1^\pm)$ are given in Table 4.

4.4. The spin-isospin structure of the one-nucleon momentum distributions

By introducing the spin-isospin dependent half-diagonal density matrix, $\rho_{(ST)}^{N_1 N_2}(\mathbf{r}_1, \mathbf{r}_2, \mathbf{r}'_1)$, the one-body momentum distribution can be expressed in terms of its various spin-isospin components as follows [80]

$$n_A(\mathbf{k}_1) = \sum_{(ST)} n_A^{(ST)}(\mathbf{k}_1) = \int d\mathbf{r}_1 d\mathbf{r}'_1 e^{i\mathbf{k}_1 \cdot (\mathbf{r}_1 - \mathbf{r}'_1)} \sum_{(ST)} \int d\mathbf{r}_2 \rho_{(ST)}^{N_1 N_2}(\mathbf{r}_1, \mathbf{r}_2; \mathbf{r}'_1). \quad (4.29)$$

The half-diagonal density $\rho_{(ST)}^{N_1 N_2}(\mathbf{r}_1, \mathbf{r}_2; \mathbf{r}'_1)$ has been calculated in Ref. [80] for $A = 3, 4, 16$ and 40 , and the various spin-isospin contributions to $n_A(k)$ have been obtained as shown in Fig. 14. It appears that: (i) the contribution from the (00) state is negligible, both in few-nucleon systems and complex nuclei; (ii) the contribution from the (11) state in ${}^3\text{He}$ and ${}^4\text{He}$ is small, both at low and large values of k , but it plays a relevant role in the region $1.5 \lesssim k \lesssim 2.5 \text{ fm}^{-1}$; (iii) in the proton distribution of ${}^3\text{He}$ the (01) contribution is important everywhere except in the region $1.5 \lesssim k \lesssim 3 \text{ fm}^{-1}$; (iv) in complex nuclei, in agreement with the results shown in Table 3, the (11) state (odd relative orbital momenta) plays a dominant role, both in the independent particle model and in many-body approaches which include SRCs. These results are in general agreement with the VMC results obtained in Ref. [83] for $A \leq 12$.

4.5. The momentum distribution of nuclei vs the deuteron momentum distributions

It would appear from Fig. 12(b), that at $k \gtrsim 1.5\text{--}2 \text{ fm}^{-1}$ the momentum distribution in $A \geq 3$ nuclei would be nothing but the rescaled deuteron momentum distribution. Such a possibility has been quantitatively investigated in Ref. [80] by plotting the ratio $R_{A/D}^N(k) = n_A^N(k)/n_D(k)$. The results are presented in Fig. 15(a), which shows the proton ratio for $A \geq 3$, and in Fig. 15(b), which shows the proton and neutron ratios in ${}^3\text{He}$. The linear scale demonstrates that, starting from $k \gtrsim 2 \text{ fm}^{-1}$, the ratio $R_{A/D}^N(k)$ is not constant but appreciably increases with k . The reasons for such an increase are manifold, namely [80]:

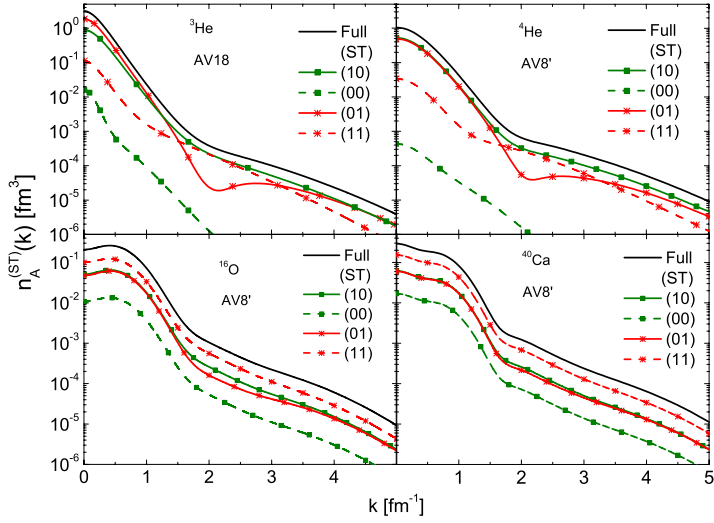


Fig. 14. The various spin-isospin contributions to the proton distributions in ${}^3\text{He}$, ${}^4\text{He}$, ${}^{16}\text{O}$ and ${}^{40}\text{Ca}$ (Eq. (4.29)). Wave functions as in Fig. 13. The integrals of the various curves provide the probability for one nucleon (the full line is normalized to one) to belong to a pair with different values of the total spin and isospin (ST).

Source: Reprinted from [80].

© 2013, by the American Physical Society.

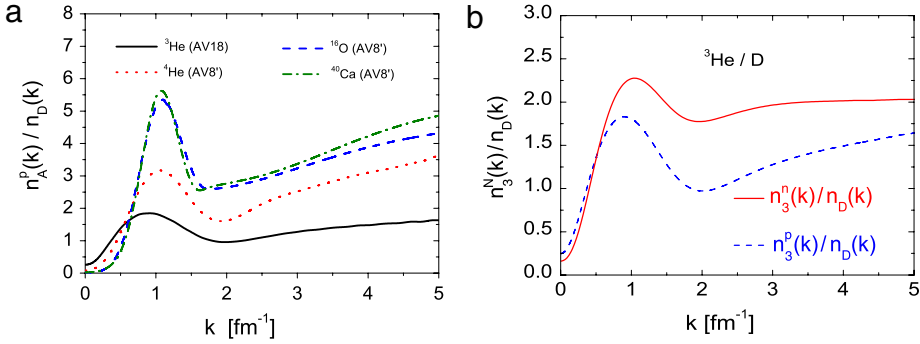


Fig. 15. (a) The ratio $n_A^p(k)/n_D(k)$ of the proton momentum distribution in nucleus A, to the deuteron momentum distribution. (b) The proton and neutron ratios in ${}^3\text{He}$. Wave functions as in Fig. 13.

Source: Reprinted from [80].

© 2013, by the American Physical Society.

(i) the role of the states $(ST) = (01)$ and (11) , that are missing in the deuteron; (ii) the *c.m.* motion of a pair in a nucleus, that, unlike what happens in the deuteron, is not zero; (iii) the different role played by pp and pn SRCs. In order to better understand the last point, in Ref. [80] the proton and neutron momentum distributions in ${}^3\text{He}$ have been analyzed in detail.

4.6. The proton and neutron momentum distributions in ${}^3\text{He}$ and ${}^3\text{H}$

The different behavior of the proton and neutron momentum ratios shown in Fig. 15(a), can be understood in terms of SRCs as follows [80]. A pn pair can be either in deuteron-like (10) state with probability $3/4$, or in (01) state, with probability $1/4$; a pp (nn) pair can only be in (01) state with probability one.⁸ As illustrated in the cartoon shown in Fig. 16, in ${}^3\text{He}$ the proton momentum distribution is affected by 2NSRCs acting in one pn and one pp pairs; in the former pair the deuteron-like state (10) is three times larger than the (01) state, whereas in the latter pair the deuteron-like state is totally missing; on the contrary, the neutron distribution is affected by SRCs acting in two proton-neutron pairs, with a pronounced dominance of the deuteron-like state (10) ; therefore, one expects that around $k \simeq 2 \text{ fm}^{-1}$, where np SRCs dominate over pp SRCs, $n_3^n/n_D \simeq 2$ and $n_3^p/n_D \simeq 1$, which is indeed confirmed by the results presented in Fig. 17, where the various spin-isospin ratios $R_{A/D}^{N,(ST)}(k) = n_A^{N,(ST)}(k)/n_D(k)$ are presented, as well as in Fig. 18 where the proton and neutron distributions in ${}^3\text{He}$ are

⁸ This is strictly true in the independent particle picture. SRCs slightly change these probability according to the results presented in Tables 1 and 2 without, however, affecting the correctness of our argument.

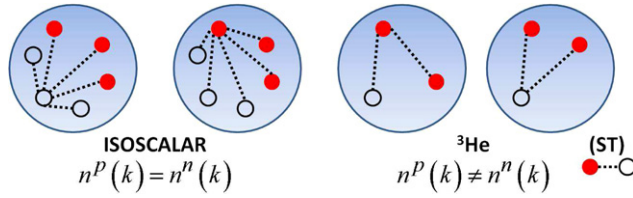


Fig. 16. The number of pn and pp pairs affecting the high-momentum components of the nucleon momentum distributions. In isoscalar nuclei $n^p(k) = n^n(k)$, whereas in non isoscalar nuclei, e.g. in ${}^3\text{He}$, $n^p(k) \neq n^n(k)$ because the proton and the neutron are correlated with different nucleon pairs (Full (open) dots denote protons (neutrons)).

Source: Reprinted from [80].

© 2013, by the American Physical Society.

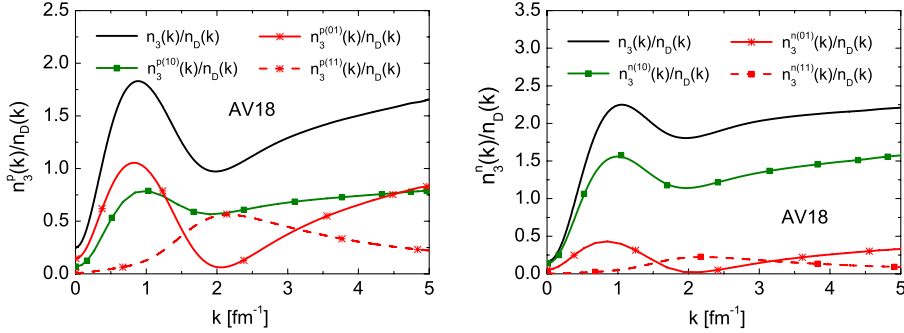


Fig. 17. The spin–isospin components of the proton (Left) and neutron (Right) ratios $n_A^N(k)/n_D(k) = \sum_{ST} n_3^{N(ST)}(k)/n_D(k)$ in ${}^3\text{He}$.

Source: Reprinted from [80].

© 2013, by the American Physical Society.

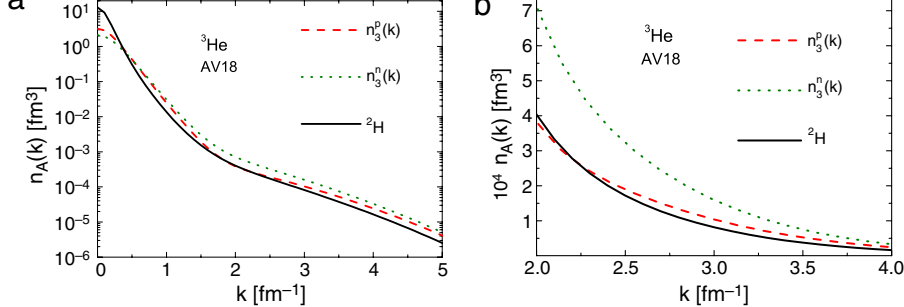


Fig. 18. The proton and neutron momentum distribution in ${}^3\text{He}$ normalized to one on log (a) and linear (b) scales. Wave function from Ref. [48]. AV18 interaction.

Source: Reprinted from [80].

© 2013, by the American Physical Society.

shown. It can be seen that the momentum distribution of the minority nucleon component (n in ${}^3\text{He}$ and p in ${}^3\text{H}$) is always larger than the one of the majority nucleon components and more similar to the deuteron momentum distribution.

4.7. On the effects of the three-nucleon force on the one-nucleon momentum distributions

In the results so far illustrated the nuclear Hamiltonian contained only two-nucleon interaction, so that it is legitimate to ask oneself about the possible effects from three-nucleon force on the 1NMD. This is nicely illustrated in Ref. [83] in the case of ${}^4\text{He}$ (see Fig. 19). It appears that the, unlike the case of the ground-state energy, the 1NMD are practically unaffected by the three-body force model used in Ref. [83]. It is expected that only a short-range 3N force could affect the high momentum components, which does not seem the case of the Urbana UIX case.

4.8. The two-nucleon momentum distributions (2NMD)

The 2NMDs represent the ideal tool to learn about SRCs and, particularly, about their relative and center-of-mass dependences and their spin–isospin structure. Recently several calculations [94–98,83] have appeared concerning: (i) the

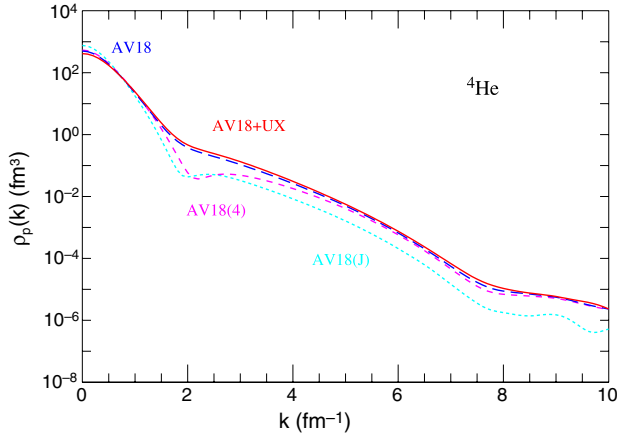


Fig. 19. (Color online) The proton momentum distribution in ${}^4\text{He}$ is shown for the AV18 + UX Hamiltonian by the red solid line, and for AV18 alone by the blue long-dash line; simplified calculations for AV18 using only a central Jastrow correlation (J) are shown by the cyan short-dash line, and including spin-isospin (but no tensor) correlations are indicated by the magenta dash line.

Source: Reprinted from [83].

© 2013, by the American Physical Society.

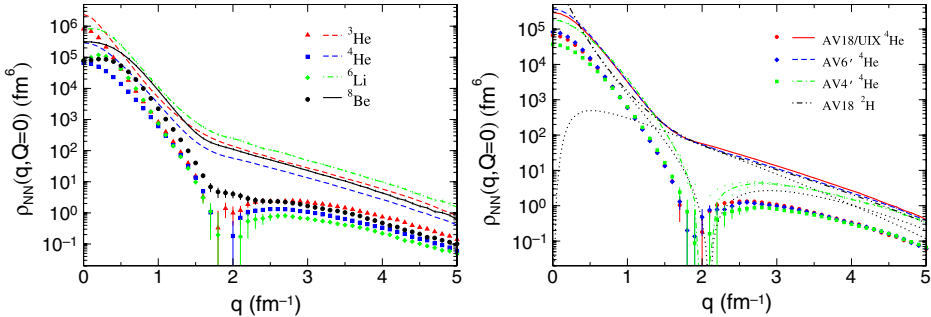


Fig. 20. (Left): the relative momentum distribution of pp and pn pairs in ${}^3\text{He}$, ${}^4\text{He}$, ${}^6\text{Li}$ and ${}^8\text{Be}$ plotted vs $k_{rel} \equiv q$, in correspondence of $K_{CM} \equiv Q = 0$ (Eq. (4.10)), calculated within the VMC method using the AV18 interaction plus Argonne UIX 3N forces. (Right): the relative momentum distribution of pp and pn pairs in ${}^3\text{He}$ corresponding to $K_{CM} = 0$ and different NN interactions.

Source: Reprinted from [94].

© 2006, by the American Physical Society.

2NMD at $K_{c.m.} = 0$, i.e. Eq. (4.10); (ii) the relative and c.m. 2NMDs, Eq. (4.12); (iii) the full 2NMD, Eq. (4.9); (iv) the spin-isospin dependent 2NMD, Eq. (4.13). The nuclei considered in these calculations were ${}^3\text{He}$, ${}^4\text{He}$, ${}^6\text{Li}$, ${}^8\text{Be}$, ${}^{12}\text{C}$, ${}^{16}\text{O}$ and ${}^{40}\text{Ca}$. The results of Ref. [94], performed within the VMC approach, shown in Fig. 20, demonstrate: (i) the relevance of the tensor force in determining the momentum distribution of pn pairs at $k_{rel} \geq 1.5 \text{ fm}^{-1}$ (see also Ref. [99]); (ii) the similarity of the momentum distribution for different light nuclei at $k_{rel} \geq 2 \text{ fm}^{-1}$, independently of the form of the two-nucleon interactions provided they have the same tensor/central ratio strength; (iii) the small effects from 3N force of the UIX type at high momenta, as in the case of the 1NMD (cf. Fig. 19). In Refs. [97,83], the full k_{rel} and $K_{c.m.}$ dependences of $n(k_{rel}, K_{CM}, \theta)$ (Eq. (4.9)) has been investigated for different values of $K_{c.m.}$ and θ . The results of Ref. [97], presented in Fig. 21 show that, as previously found in Ref. [94], at small values of k_{rel} the pn and pp momentum distributions do not appreciably differ, with their ratio being closer to the ratio of the pn to pp pairs, whereas at $1.0 \lesssim k_{rel} \lesssim 4.0 \text{ fm}^{-1}$ the dominant role of tensor correlations makes the pn distributions much larger than pp distribution, with the node exhibited by the latter filled up by the D wave in the pn two-body density. From Fig. 21 it can be seen that:

(i) starting from a given value of k_{rel} which increases with increasing values of $K_{c.m.}$ and which equals to $k_{rel} \simeq 1.5$ when $K_{c.m.} = 0$, the pn distribution changes its slope and becomes close to the deuteron distribution;

(ii) in the region $k_{rel} \gtrsim 2 \text{ fm}^{-1}$, $K_{c.m.} \lesssim 1 \text{ fm}^{-1}$, n^{NN} becomes θ -independent,⁹ which means that $n^{NN}(k_{rel}, K_{c.m.}, \theta)$ factorizes, i.e. $n^{NN}(k_{rel}, K_{c.m.}, \theta) \simeq n_{rel}^{NN}(k_{rel})$ which represents a configuration with high relative and low c.m. momenta;

(iii) the relative momentum distribution, which reflects the local short-range properties of nuclei, exhibits very mild A-dependence at $k_{rel} \gtrsim 1.5\text{--}2.0 \text{ fm}^{-1}$ and for pn pairs it can be represented as the rescaled deuteron momentum distribution;

⁹ Such an independence has been checked in a wide range of angles.

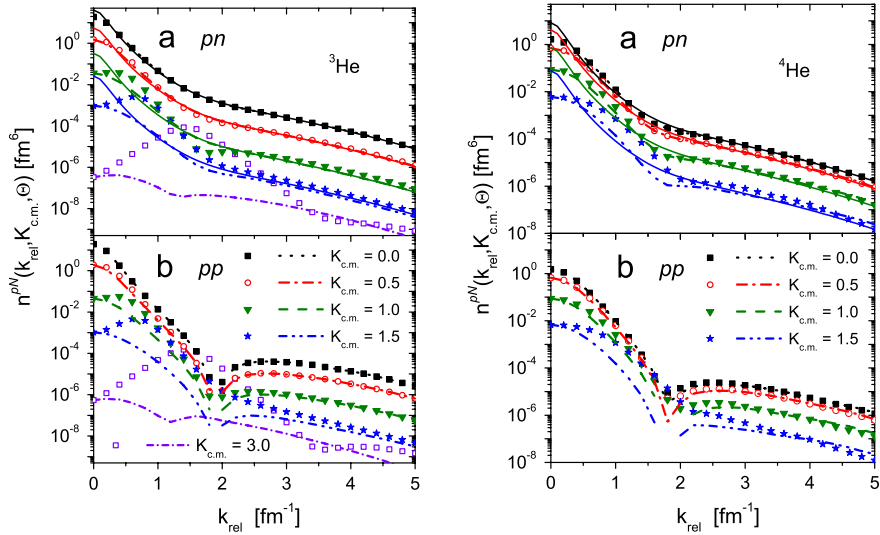


Fig. 21. (Color online) (Left): the two-nucleon momentum distributions of pn (a) and pp (b) pairs in ${}^3\text{He}$ normalized to one, vs. the relative momentum k_{rel} , for fixed values of the c.m. momentum $K_{\text{c.m.}}$ and two orientations of them: $\mathbf{k}_{\text{rel}} \parallel \mathbf{K}_{\text{c.m.}}$ (broken curves) and $\mathbf{k}_{\text{rel}} \perp \mathbf{K}_{\text{c.m.}}$ (symbols). The continuous curves for the pn pair represent the deuteron momentum distribution rescaled by the c.m. momentum distribution $n_{\text{c.m.}}^{pn}(K_{\text{c.m.}}) = \int n^{pn}(\mathbf{k}_{\text{rel}}, \mathbf{K}_{\text{c.m.}}) d\mathbf{k}_{\text{rel}}$ (see text). ${}^3\text{He}$ wave function from Ref. [48] and AV18 interaction [30]. (Right): the same as (Left) but for ${}^4\text{He}$. Correlated variational wave function from [49] and AV8' interaction [28].

Source: Reprinted from [97].

© 2006, by the American Physical Society.

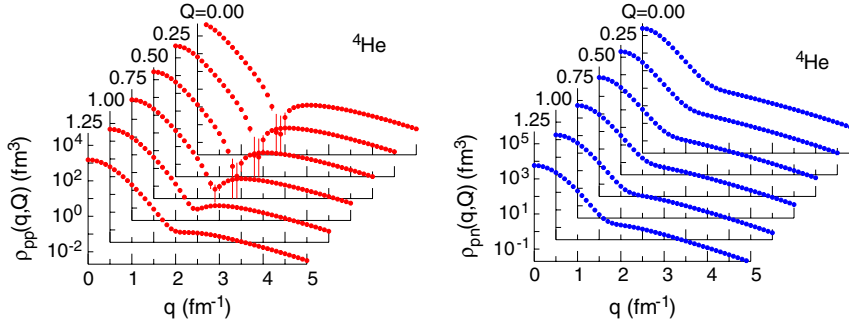


Fig. 22. (Color online) The proton–proton, (Left), and proton–neutron, (Right), momentum distributions in ${}^4\text{He}$ averaged over the directions of $\mathbf{q} = \mathbf{k}_{\text{rel}}$ and $\mathbf{Q} = \mathbf{K}_{\text{c.m.}}$ as a function of q for several fixed values of Q from 0 to 1.25 fm^{-1} .

Source: Reprinted from [83].

© 2013, by the American Physical Society.

(iv) the c.m. momentum distribution $n_{\text{c.m.}}^{NN}$ at low c.m. momenta ($K_{\text{c.m.}} \lesssim 1.0–1.5 \text{ fm}^{-1}$) can be associated to the mean field average kinetic energy and approximated by a Gaussian, in agreement with the results of Ref. [114] and the experimental finding on ${}^4\text{He}$ and ${}^{12}\text{C}$ to be discussed in Section 6;

(v) at high values of the c.m. momentum, of the same order of the (large) relative momentum, more than two particles can be locally correlated, with a resulting strong dependence upon the angle and the breaking down of factorization, as clearly shown in Fig. 21 for $K_{\text{c.m.}} = 3 \text{ fm}^{-1}$.

The above behaviors are quite general and characterize also complex nuclei. Recent results obtained within the VMC approach with the AV18 interaction (see Fig. 22), confirm the general trend previously obtained in Ref. [97], in particular that the momentum distributions $n_{\text{c.m.}}^{NN}(k_{\text{rel}}, K_{\text{c.m.}})$ plotted vs. k_{rel} at fixed values of $K_{\text{c.m.}}$ decreases with increasing value of $K_{\text{c.m.}}$ with the dip in the pp distribution filled in by the c.m. motion. Concerning heavier nuclei, in Fig. 23 the momentum distribution of a back-to-back pn pair in $A = 3, 4, 12, 16, 40$ is compared with the deuteron momentum distribution, and the qualitative A -independence of the momentum distribution of a deuteron-like pair in nuclei and its similarity with the deuteron momentum distribution shows up very clearly, with the differences with the latter due to the motion of the c.m. in the in-medium pair. To sum up, the 2NMD provide a clear physical picture of the motion of a pair of nucleons embedded in the nuclear medium. In the region $2 \lesssim k_{\text{rel}} \lesssim 5 \text{ fm}^{-1}$, $K_{\text{c.m.}} \lesssim 1 \text{ fm}^{-1}$, the motion of NN pairs is governed by 2NSRCs, characterized by a decoupling of the c.m. and relative motions which, for a pn pair, is described by the deuteron momentum

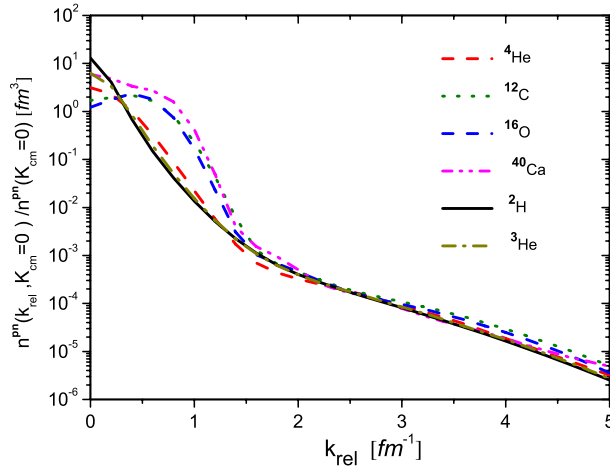


Fig. 23. The momentum distribution for a back-to-back proton–neutron pair illustrating that, unlike the case of the single nucleon momentum distribution, a scaling to the deuteron momentum distributions really occur for the pn momentum distributions in heavier nuclei. Calculations within the linked cluster expansion of Ref. [98] and AV8' interaction.
Source: Adapted reprinted from [98].

distribution. As for the *c.m.* momentum distribution, apart from the weakly bound three-nucleon system, it is governed by the average kinetic energy associated to the independent particle motion and provide most of the A dependence. The experimental investigation of these feature will provide the 3D structure of the two-nucleon momentum distributions that are the basic quantities providing information on in-medium two-nucleon dynamics.

5. Short-range correlations in momentum space: one- and two-nucleon spectral functions

5.1. The one-nucleon (hole) spectral function

Extracting the momentum distribution from measurable cross sections is a difficult task, not only because of the underlying model dependence of the extraction itself, but also because there are no experimental data that, even within the most extreme approximation, will directly depend upon the momentum distribution. To clarify this point let us consider the reaction $A(e, e'N)X$, i.e. the process in which in the initial state an electron is impinging on the target nucleus A and, in the final state, the scattered electron and a nucleon N are detected in coincidence, with the residual nucleus $X = (A - 1)$ left in the energy state E_{A-1}^f ; in the simplified assumption (the Plane Wave Impulse Approximation (PWIA)) that the detected nucleon, with momentum \mathbf{k}_1 in the initial state was knocked out by a direct interaction γ^*N and has left the nucleus with momentum $\mathbf{p}_N = \mathbf{k}_1 + \mathbf{q}$ without interacting with the medium, the cross section of the process is not proportional to the one-nucleon momentum distribution $n_A(|\mathbf{k}_1|)$ but to the hole Spectral Function $P_A(\mathbf{k}_1, E)$, representing the joint probability that when a nucleon with momentum \mathbf{k}_1 is removed instantaneously from the ground state of the nucleus A , the nucleus $(A - 1)$ is left in the excited state $E_{A-1}^* = E - E_{min}$, where E is the so called *removal energy* and $E_{min} = M_{A-1} + m_N - M_A = |E_A| - |E_{A-1}|$, E_A and E_{A-1} being the (negative) ground-state energy of nuclei A and $A - 1$, respectively. The hole spectral function, which takes into account the fact that nucleons in nuclei have not only a momentum distribution, but also a distribution in energy, is trivially related to a well defined many-body quantity, namely the two-points Green's function (see e.g. [41]). For an extended system like nuclear matter, realistic calculations in terms of the Green's function have been performed by various authors (see Section 5.2.3). However for nuclei with $A > 3$ no *ab initio* calculations of the spectral function exist to date, unlike what happens for the momentum distributions, thanks to the recent progress reached by the solution of the many-body problem, which allowed one to obtain *ab initio* non diagonal one-body density matrices, as illustrated in the previous sections. The focus in this section is mainly on a critical discussion of model spectral functions for finite nuclei and, to this end, it is appropriate to use the following well-known representation of the spectral function

$$P_A(\mathbf{k}_1, E) = \frac{1}{2J+1} \sum_{M,\sigma} \langle \Psi_A^{JM} | a_{\mathbf{k}_1\sigma}^\dagger \delta(E - (\hat{H} - E_A)) a_{\mathbf{k}_1\sigma} | \Psi_A^{JM} \rangle \quad (5.1)$$

$$= \frac{1}{2J+1} \sum_{M,\sigma} \sum_f \left| \langle \Psi_{A-1}^f | a_{\mathbf{k}_1\sigma} | \Psi_A^M \rangle \right|^2 \delta(E - (E_{A-1}^f - E_A)) \quad (5.2)$$

$$= \frac{1}{2J+1} (2\pi)^{-3} \sum_{M,\sigma} \sum_f \left| \int d\mathbf{r}_1 e^{i\mathbf{k}_1 \cdot \mathbf{r}_1} G_f^{M\sigma}(\mathbf{r}_1) \right|^2 \delta(E - (E_{A-1}^f - E_A)), \quad (5.3)$$

where $a_{\mathbf{k}_1\sigma}^\dagger$ ($a_{\mathbf{k}_1\sigma}$) is the creation (annihilation) operator of a nucleon with momentum \mathbf{k}_1 and spin σ and \hat{H} the intrinsic Hamiltonian for A interacting nucleons. Eq. (5.3) has been obtained using the completeness relation for the eigenstates states of $(A - 1)$, $\sum_f |\Psi_{A-1}^f\rangle \langle \Psi_{A-1}^f| = 1$, and the quantity $G_f^{M\sigma}(\mathbf{r}_1)$ in Eq. (5.3) is the overlap integral

$$G_f^{M\sigma}(\mathbf{r}_1) = \langle \chi_\sigma^{1/2}, \Psi_{A-1}^f(\{\mathbf{r}\}_{A-1}) | \Psi_A^{JM}(\mathbf{r}_1, \{\mathbf{r}\}_{A-1}) \rangle, \quad (5.4)$$

between Ψ_A^{JM} and the discrete and continuum eigenfunctions Ψ_{A-1}^f (with eigenvalue $E_{A-1}^f = E_{A-1} + E_{A-1}^{f*}$) of the system $(A - 1)$. In what follows the angle integrated spectral functions depending upon $k \equiv |\mathbf{k}_1|$ will be considered, with normalization

$$4\pi \int P_A(k, E) k^2 dkdE = 1. \quad (5.5)$$

The very definition of $P_A(k, A)$ (5.3) leads to the following general form for the spectral function [92]

$$P_A(k, E) = P_{gr}(k, E) + P_{ex}(k, E), \quad (5.6)$$

where

$$P_{gr}(k, E) = (2\pi)^{-3} (2J + 1)^{-1} \sum_{M,\sigma} \left| \int e^{i\mathbf{k}_1 \cdot \mathbf{r}_1} G_{gr}^{M\sigma}(\mathbf{r}_1) d\mathbf{r}_1 \right|^2 \delta(E - E_{min}), \quad (5.7)$$

and

$$P_{ex}(k, E) = (2\pi)^{-3} (2J + 1)^{-1} \sum_{M,\sigma} \sum_{f \neq 0} \left| \int e^{i\mathbf{k}_1 \cdot \mathbf{r}_1} G_f^{M\sigma}(\mathbf{r}_1) d\mathbf{r}_1 \right|^2 \delta(E - E_{A-1}^f). \quad (5.8)$$

Here $P_{gr}(k, E)$ yields the probability distribution that the final $(A - 1)$ system is left in its ground state, and $P_{ex}(k, E)$ the probability distribution that the final $(A - 1)$ system is left in the excited state with excitation energy $E_{A-1}^* = E - E_{min}$.¹⁰ Eq. (5.12) holds for any value of A , but for a complex nucleus, as in the case of the momentum distributions, it is useful to adopt the representation in which the ground state of the $(A - 1)$ system and its excited states, i.e. one-hole excitations, are explicitly separated from more complex configurations, e.g. one-particle–two-hole states, which can be reached when two-particle–two-hole states in the target nucleus are considered. One has, accordingly, [93]¹¹

$$P_A(k, E) = P_0(k, E) + P_1(k, E), \quad (5.9)$$

where

$$\begin{aligned} P_0(k, E) &= (2\pi)^{-3} (2J + 1)^{-1} \sum_{M,\sigma} \sum_{\alpha} \left| \int e^{i\mathbf{k}_1 \cdot \mathbf{r}_1} G_{\alpha}^{M\sigma}(\mathbf{r}_1) d\mathbf{r}_1 \right|^2 \delta(E - |\epsilon_{\alpha}|) \\ &= A^{-1} \sum_{\alpha} A_{\alpha} n_{\alpha}(k) \delta(E - |\epsilon_{\alpha}|), \end{aligned} \quad (5.10)$$

and

$$P_1(k, E) = (2\pi)^{-3} (2J + 1)^{-1} \sum_{M,\sigma} \sum_{f \neq \alpha} \left| \int e^{i\mathbf{k}_1 \cdot \mathbf{r}_1} G_f^{M\sigma}(\mathbf{r}_1) d\mathbf{r}_1 \right|^2 \delta(E - E_1^f). \quad (5.11)$$

Here $n_{\alpha}(k)$ is the hole state momentum distribution with single particle (sp) energy ϵ_{α} and nucleon number A_{α} ($\sum_{\alpha} A_{\alpha} = A$), the sum over α runs only over hole states of the target, and $E_1^f \equiv E_{A-1}^* + E_{min}$. Eqs. (5.8) and (5.11) clearly display the role of NN correlations: as a matter of fact, it can clearly be seen that, if the target ground-state wave function, Ψ_A^{JM} , and the wave functions of the final $(A - 1)$ system, Ψ_{A-1}^f , are described by one Slater determinant, $P_1(|\mathbf{k}|, E)$ (and $n_1(|\mathbf{k}|)$) will be vanishing. On the other hand, if two-particle–two-hole admixtures generated in nucleus A by correlations are considered in the ground state of A , $P_1(|\mathbf{k}|, E)$ (and $n_1(|\mathbf{k}|)$) will differ from zero due to the coupling of Ψ_A^{JM} to one-particle–two-hole states which are present in Ψ_{A-1}^f .

¹⁰ It should be stressed that the separation (5.6) also trivially results from the analytic structure of the two-point Green's function. Since the momentum distributions and the spectral function are related by the momentum sum rule (see Section 5.1.1), the separation of the momentum distributions (4.19) into a mean field and a correlation contributions is theoretically fully justified also within a formalism based upon the two-point Green's function.

¹¹ A fully equivalent notation would be $P_A(k, E) = P_{MF}(k, E) + P_{SRC}(k, E)$.

5.1.1. The momentum sum rule

Using the definition of the momentum distribution provided by Eq. (4.24) and the completeness relation for the states of $(A - 1)$, one readily obtains the *momentum sum rule* [92]

$$n_A(k) = \int_{E_{\min}}^{\infty} P_A(k, E) dE = n_{\text{gr}(0)}(|\mathbf{k}|) + n_{\text{ex}(1)}(|\mathbf{k}|). \quad (5.12)$$

5.1.2. The Koltun sum rule

The knowledge of the Spectral Function and the momentum distributions allows one to calculate the mean kinetic, $\langle T \rangle$, and removal, $\langle E \rangle$, energies. In fact, using the momentum sum rule (Eq. (5.12)) one obtains

$$\langle T \rangle = \int d^3k dE \left(\frac{\mathbf{k}^2}{2m_N} \right) P_A(|\mathbf{k}|, E) = \int d^3k \left(\frac{\mathbf{k}^2}{2m_N} \right) n_A(|\mathbf{k}|) = \langle T_{0(\text{gr})} \rangle + \langle T_{1(\text{ex})} \rangle, \quad (5.13)$$

$$\langle E \rangle = \int d^3k dE P_A(|\mathbf{k}|, E) = \langle E_{0(\text{gr})} \rangle + \langle E_{1(\text{ex})} \rangle. \quad (5.14)$$

These quantities are linked to the total energy per particle $|\epsilon_A| = \frac{|E_A|}{A}$ through a model independent relation (the *Koltun sum rule* [100]), which reads

$$|\epsilon_A| = \frac{|E_A|}{A} = \frac{1}{2} \left\{ \langle E \rangle - \langle T \rangle \frac{A-2}{A-1} \right\}, \quad (5.15)$$

if the Hamiltonian contains only two-body density-independent forces, and

$$|\epsilon_A| = \frac{1}{2} \left\{ \langle E \rangle - \langle T \rangle \frac{A-2}{A-1} + \langle V_3 \rangle \right\}, \quad (5.16)$$

if also a three-body interaction V_3 is present.

5.2. Many-body calculations of the one-nucleon spectral function

Calculations of the spectral function for three-nucleon systems and nuclear matter are possible within various many-body techniques (Faddeev and Faddeev–Yakubovsky equations, Brueckner–Bethe–Goldstone and the method of correlated basis functions) because the full energy spectrum of the three-nucleon systems is known (it is the complete set of bound and scattering states of the two-nucleon system), and in case of nuclear matter the knowledge of the unperturbed single particle states facilitates the calculation within different many-body schemes. Unfortunately, for finite nuclei only model spectral functions can be developed. Before briefly discussing many-body calculations, let us recall the form of the spectral function for simple systems.

5.2.1. Mean-Field and Fermi gas spectral functions

Within the MF approximation ($P_1(k, E) = 0$), the spectral function is

$$P_0^{\text{MF}}(|\mathbf{k}|, E) = A^{-1} \sum_{\alpha} A_{\alpha} n_{\alpha}^{\text{MF}}(|\mathbf{k}|) \delta(E - |\epsilon_{\alpha}|). \quad (5.17)$$

Here the main difference between $n_{\alpha}^{\text{MF}}(k)$ and $n_{\alpha}(k)$ appearing in Eq. (5.10), concerns their normalization, i.e. the hole state occupation probability $S_{\alpha} = \int n_{\alpha}(k) d^3k$; in fact, $S_{\alpha}^{\text{MF}} = 1$ for $\alpha \leq F$, and $S_{\alpha}^{\text{MF}} = 0$, for $\alpha > F$, whereas, because the presence ground-state correlations, one has $S_{\alpha} < 1$ for $\alpha \leq F$ and $S_{\alpha} > 0$ for $\alpha > F$. For symmetrical nuclear matter described by a non interacting Fermi gas (FG) the spectral function can be cast in the following form

$$P_0^{\text{FG}}(|\mathbf{k}|, E) = \frac{3}{4\pi k_F^3} \Theta(k_F - |\mathbf{k}|) \delta \left(E + \frac{|\mathbf{k}^2|}{2m_N} \right) \quad (5.18)$$

where the Θ function makes the spectral function equal to zero for $|\mathbf{k}| \geq k_F$, with the Fermi momentum $k_F = 1.36 \text{ fm}^{-1}$ at density $\rho = 0.16 \text{ N/fm}^3$.

5.2.2. Microscopic spectral functions of the three-nucleon systems

For $A = 3$, the overlap integral, Eq. (5.4), assumes the form

$$G_f^{M\sigma}(\mathbf{r}_1) = \langle \chi_{\sigma}^{1/2}, \Psi_2^f(\mathbf{r}_{23}) | \Psi_3^{1/2M}(\mathbf{r}_{23}, \rho) \rangle, \quad (5.19)$$

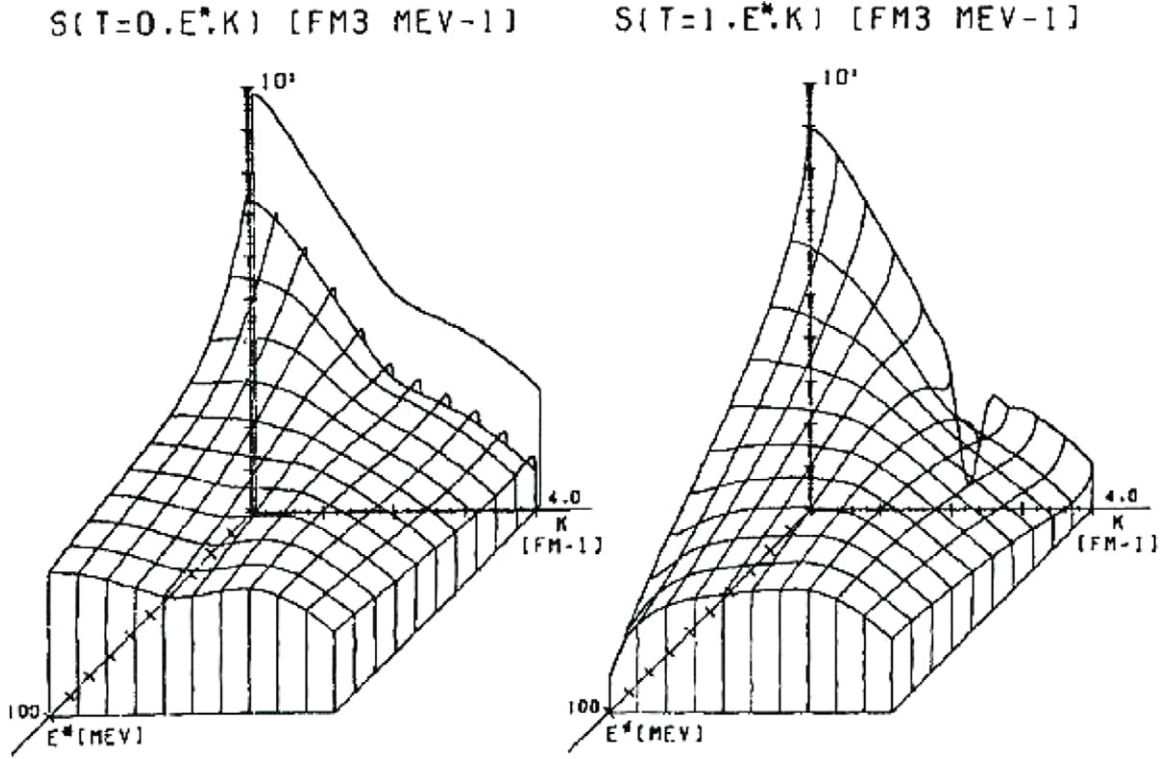


Fig. 24. The proton spectral function of ${}^3\text{He}$ obtained from the solution of Faddeev equations with the Paris NN interaction. The left and right spectral functions correspond to different values of the isospin of the spectator pn pair, namely $T = 0$ (left) and $T = 1$ (right).

Source: Reprinted from [103].

© 1983, by Elsevier.

where $\mathbf{r}_{23} = \mathbf{r}_2 - \mathbf{r}_3$, $\rho = \mathbf{r}_1 - (\mathbf{r}_2 + \mathbf{r}_3)/2$ are the Jacobi coordinates in the three-nucleon system and ψ_2^f is the bound or continuum wave function of the two-nucleon interacting system (the *spectator pair*). Exact three-nucleon spectral functions have been obtained by several groups [101–105] in terms of *ab initio* realistic wave functions for the ground state of $A = 3$ and the ground- and continuum states of $A = 2$. The proton spectral function of ${}^3\text{He}$ obtained in Ref. [103] obtained with three-body Faddeev wave functions and the Paris interaction, is shown in Fig. 24 for the channels $T = 0$ and $T = 1$ of the spectator interacting pn pair. In the (Left) figure, the proton spectral function P_{gr} corresponding to two-body break-up (2BBU) channel



is clearly seen at the value of the removal energy (one-nucleon threshold energy $E_{th}^{(1)}$)

$$E = E_{th}^{(1)} = |E_3| - |E_2| = 5.5 \text{ MeV}, \quad (5.21)$$

whereas at $E > E_{th}$ a continuum spectrum due to SRCs, and described by $P_{ex}(k, E = E_{th}^{(2)} + E_2^*)$, can be seen where $E_{th}^{(2)} = |E_3|$ is the two-body threshold energy, and

$$E_2^* = \frac{|\mathbf{k}_2 - \mathbf{k}_3|^2}{m_N}, \quad (5.22)$$

represents the intrinsic excitation energy of the two-nucleon system in the continuum, which is nothing but the relative kinetic energy of the pn pair in the three-body-break-up (3BBU) channel



A careful inspection at Fig. 24 reveals that in the region of the 3BBU channel, at high values of momenta and removal energies, peaks located at $E = E_{th}^{(2)} + E_2^* \simeq |\mathbf{k}_1|^2/(4m_N)$ can be seen. It will be shown in what follows that the spectral functions of all nuclei should exhibit a strong $E - k_1$ correlation represented by peaks located at

$$E \simeq \frac{A-2}{A-1} \frac{k_1^2}{2m_N}, \quad (5.24)$$

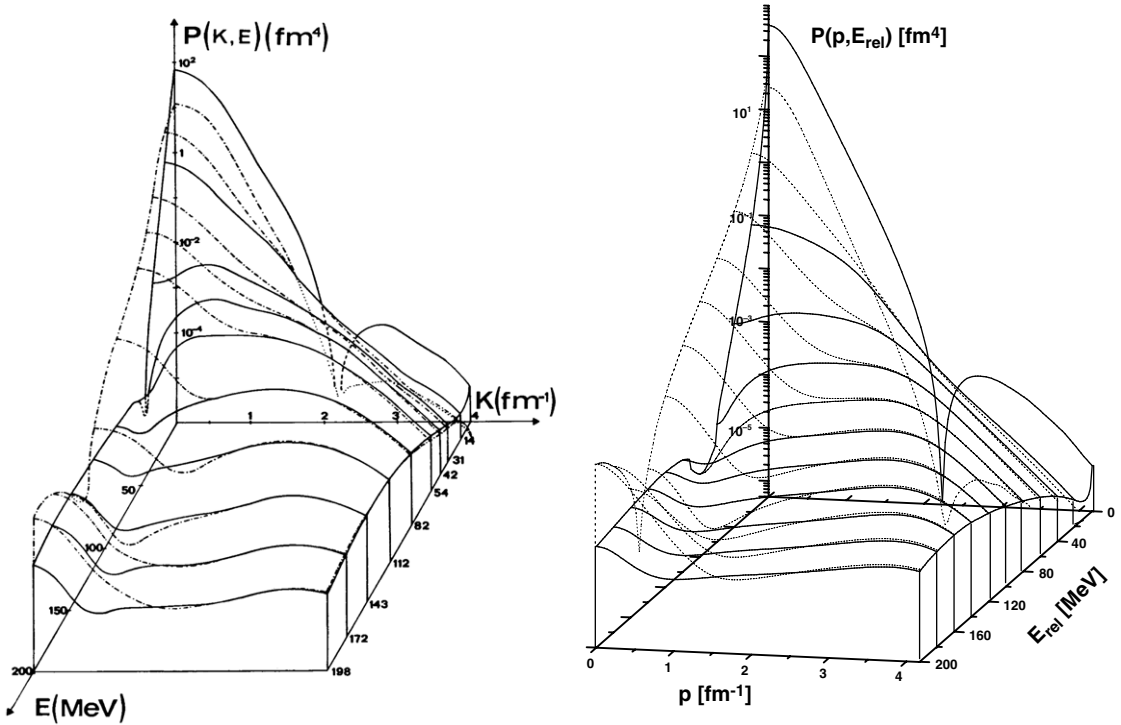


Fig. 25. (Left): Neutron spectral function in ${}^3\text{He}$ corresponding to the channel ${}^3\text{He} \rightarrow n + (pp)$ including (full line) and disregarding (dot-dashed line) the interaction in the spectator pp pair (after Ref. [102], RSC interaction). (Right): The same as in (Left) but for the spectral function of Ref. [105] corresponding to the wave function of Ref. [104] and the AV18 interaction. In this figure $k = p$, $E_{\text{rel}} = E_2^*$.
Source: Reprinted from [102] and [105]. © 1980 and 1985, by APS.

independently of the realistic NN interaction and the method of solution of the Schrödinger equation; it will also be demonstrated that the experimental observation of these peaks represents evidence of SRCs in their basic configuration, namely the one in which $\mathbf{k}_1 \simeq -\mathbf{k}_2$ and $\mathbf{K}_{A-2} = \sum_{i=3}^A \mathbf{k}_i \simeq 0$. Another general and relevant feature of the spectral function is related to the final state interaction in the spectator pair. This is clearly seen in Fig. 25, which shows (dotted lines) the neutron spectral functions of ${}^3\text{He}$ calculated with the RSC (Left) and AV18 (Right) interactions within the Plane Wave Approximation (PWA), when the final pp pair in the continuum is described by a plane wave, and when the final state interaction in the pp pair is taken exactly into account (full line). This figure demonstrates a very interesting feature, namely that near the correlation peaks the PWA and the exact calculation practically coincide. To conclude, let us also recall that by assuming isospin invariance, the neutron (proton) spectral function in ${}^3\text{He}$ equals the proton (neutron) spectral function in ${}^3\text{H}$ and that the integral of the proton and neutron spectral functions of ${}^3\text{He}$ and ${}^3\text{H}$ give the momentum distributions shown in Fig. 18 in Section 4.5.

5.2.3. Microscopic spectral function of nuclear matter

When the NN interaction is turned on, the spectral function of nuclear matter assumes the general structure given by Eq. (5.9). The uncorrelated part becomes

$$P_0^{\text{NM}}(|\mathbf{k}|, E) = \frac{3}{4\pi k_F^3} Z(|\mathbf{k}|) \delta(E + e(|\mathbf{k}|)), \quad (5.25)$$

where $Z(|\mathbf{k}|)$ is the hole strength playing the same role as the partial occupation probability in the mean-field spectral function, $e(|\mathbf{k}|)$ is the hole single particle energy spectrum and k_F the Fermi momentum (in absence of NN correlations $e(|\mathbf{k}|) = \mathbf{k}^2/2m_N$, $Z(|\mathbf{k}|) = \Theta(k_F - |\mathbf{k}|)$ and the usual Fermi gas spectral function (Eq. (5.18)) is recovered). The spectral functions of nuclear matter has been calculated in Refs. [106,107,116] within the Brueckner–Bethe–Goldstone theory and in Ref. [108] within the theory of correlated basis functions. In the calculation within the BBG theory a central quantity is the nucleon self-energy $M(k, E) = V(k, E) + iW(k, E)$ which in general is expressed in terms matrix elements of the Brueckner G matrix. The spectral function of nuclear matter calculated in Ref. [108] is shown in Fig. 26 and a widespread strength involving high values of momenta and energies associated to 2h-1p configurations resulting from ground-state 2p-2h excitations generated by SRCs, can be observed. Recently, a spectral function of nuclear matter has also been obtained within the Giessen–Boltzmann–Uehling–Uhlenbeck (GiBUU) transport theory [109]. In the next section it will be shown that also the spectral function of nuclear matter exhibits the correlation peaks located at $E \simeq k^2/2m_N$.

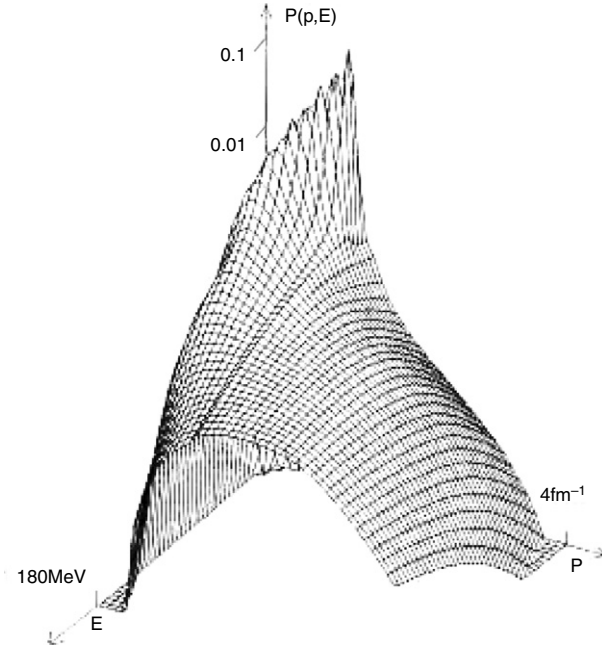


Fig. 26. The spectral function of nuclear matter obtained in Ref. [108] within the method of correlated basis functions. In this Figure $p = k$.
Source: Reprinted from Ref. [173].
© 1989, by Elsevier.

5.2.4. Model spectral functions for complex nuclei

For finite nuclei, the theoretical calculation of the discrete and continuum spectrum of ($A - 1$) interacting particles represent a formidable many-body problem. Even for a light nucleus as ^4He , the channels that contribute to the spectral function are all possible states of three interacting nucleons including the continuum, i.e. systems whose theoretical treatment is far from being solved, particularly at medium and high energies and momenta which are necessary for the study of SRCs. The use of model approaches for the spectral function is unavoidable. Let us present a review of several current models.

In Ref. [110] the Spectral Function of ^4He has been obtained assuming plane waves for the continuum three body states; in Ref. [111], a simple Spectral Function for complex nuclei has been proposed in which only the average excitation energy of the final nuclear system is considered, *viz* Eq. (5.6) with $P_{\text{ex}}(|\mathbf{k}|, E) = n_{\text{ex}}(|\mathbf{k}|)\delta(E - \bar{E}_{\text{ex}})$ for ^4He , and Eq. (5.9) with $P_1(|\mathbf{k}|, E) = n_1(|\mathbf{k}|)\delta(E - \bar{E}_1)$ for complex nuclei. Realistic models for complex nuclei have been developed essentially within two approaches: (i) the local density approximation [112], and (ii) the convolution model of Refs. [113,114].

5.2.4(a) The local density approximation (LDA)

This model spectral function has been obtained in Ref. [112] and widely applied in the calculation of lepton scattering off nuclei. We will follow the derivation given there. In coordinate space, the spectral function is

$$P_A(\mathbf{r}_1, \mathbf{r}_{1'}, E) = \sum_f \langle \Psi_A^0 | a_{\mathbf{r}_1}^\dagger | \Psi_A^f \rangle \langle \Psi_A^f | a_{\mathbf{r}_{1'}} | \Psi_A^0 \rangle \delta(E - E_{A-1}^f + E_A), \quad (5.26)$$

and its integral over the energy yields the non-diagonal one-body density matrix

$$\rho(\mathbf{r}_1, \mathbf{r}_{1'}) = \int P_A(\mathbf{r}_1, \mathbf{r}_{1'}, E) dE. \quad (5.27)$$

Eq. (5.26) can be expressed in terms of the coordinates $\mathbf{r} = \mathbf{r}_1 - \mathbf{r}_{1'}$ and $\mathbf{R} = [\mathbf{r}_1 + \mathbf{r}_{1'}]/2$ and the usual spectral function is obtained by Fourier transforming in \mathbf{r} and integrating in \mathbf{k}

$$P_A(k, E) = \int d\mathbf{R} \int e^{i\mathbf{k}\cdot\mathbf{r}} P_A(\mathbf{R}, \mathbf{r}, E) d\mathbf{r}. \quad (5.28)$$

As in the case of the momentum distributions, one has

$$P_A(\mathbf{R}, \mathbf{r}, E) = P_0(\mathbf{R}, \mathbf{r}, E) + P_1(\mathbf{R}, \mathbf{r}, E), \quad (5.29)$$

with the MF part given by

$$P_0(\mathbf{R}, \mathbf{r}, E) = \sum_\alpha \phi_\alpha(\mathbf{r}') \phi_\alpha(\mathbf{r}_1) \delta(E - E_\alpha); \quad (5.30)$$

and the correlated part expressed in terms of the correlated spectral function of nuclear matter [108] using the LDA, obtaining

$$P_1(\mathbf{R}, \mathbf{r}, E) = \rho(\mathbf{R}) P_1^{NM}(\rho(\mathbf{R}), \mathbf{r}, E) \quad (5.31)$$

where $P_1^{NM}(\rho(\mathbf{R}), \mathbf{r}, E)$ is calculated at a density $\rho(\mathbf{R})$ equal to the density of the final nucleus. Once (5.31) is obtained in a reasonable interval of variables, Eq. (5.28) can be used to obtain the final spectral function $P_A(k, E)$.

5.2.4(b) The convolution model

The convolution model, widely used in the calculation of various scattering processes related to SRCs, originated from the observation [12] that, as explained in Section 4.1, at high values of the nucleon momentum and removal energy, the spectral function should be mainly governed by the process in which the high momentum $\mathbf{k}_1 \equiv \mathbf{k}$ of a nucleon (the *hard* nucleon) is balanced only by the momentum $\mathbf{k}_2 \simeq -\mathbf{k}$ of another nucleon, with the remaining ($A - 2$) nucleons (the *soft* nucleons) acting as spectators with total momentum $\mathbf{K}_{A-2} \simeq 0$. Energy conservation for such a configuration is

$$E_{A-1}^* + E_{A-1}^R \simeq \frac{\mathbf{k}^2}{2m_N}, \quad (5.32)$$

where $E_{A-1}^R \approx \frac{\mathbf{k}^2}{2(A-1)m_N}$ is the recoil energy of the ($A - 1$) system, whose intrinsic excitation energy would be therefore

$$E_{A-1}^* \approx \frac{(A-2)\mathbf{k}^2}{2(A-1)m_N}. \quad (5.33)$$

Such a picture, which is based on the simplified assumption that the system ($A - 2$) is at rest, leads to a spectral function P_1 in the form of a delta function $\delta(E - E_1(|\mathbf{k}|))$, with $E_1(|\mathbf{k}|) = \frac{(A-2)\mathbf{k}^2}{2(A-1)m_N} + E_{thr}^{(2)}$ with the two-nucleon threshold energy being $E_{thr}^{(2)} = |E_A| - |E_{A-2}|$. The motion of ($A - 2$) with momentum $\mathbf{K}_{c.m.} = -\mathbf{K}_{A-2} \equiv -\mathbf{k}_3 \neq 0$ was taken into account in Ref. [114] within the following assumptions :

(i) the initial wave function of a nucleus A describing the configuration with two strongly short-range correlated nucleons exhibits a factorized form

$$\Psi_A^0(\{\mathbf{r}_i\}_A) = \hat{\mathcal{A}} \left[\chi(\mathbf{y}) \Phi(\mathbf{x}) \otimes \Psi_{A-2}^{f_{A-2}}(\{\mathbf{r}_i\}_{A-2}) \right], \quad (5.34)$$

where

$$\mathbf{x} = \mathbf{r}_1 - \mathbf{r}_2 \quad \mathbf{y} = \mathbf{r}_3 - \frac{1}{2}(\mathbf{r}_1 + \mathbf{r}_2), \quad (5.35)$$

are the relative and *c.m.* Jacobi coordinates of the correlated pair composed by nucleon “1” and “2”; (ii) the final-state wave function of the ($A - 1$) system is

$$\Psi_{A-1}^f(\{\mathbf{r}_i\}_{A-1}) = \hat{\mathcal{A}} \left[e^{i(\mathbf{k}_2 \cdot \mathbf{r}_2)} \otimes \Psi_{A-2}^f(\{\mathbf{r}_i\}_{A-2}) \right]; \quad (5.36)$$

(iii) the removal energy is

$$\begin{aligned} E &= |E_A| + E_{A-1}^f = |E_A| - |E_{A-2}| + \frac{\mathbf{t}^2}{2\mu} \\ &= E_{thr} + \frac{A-2}{2m_N(A-1)} \left[\mathbf{k} + \frac{A-1}{A-2} \mathbf{k}_3 \right]^2, \end{aligned} \quad (5.37)$$

where $\mathbf{t}^2/(2\mu)$ represents the kinetic energy of particle “2” and “particle 3” (i.e. ($A - 2$)) (with momentum $\mathbf{k}_3 = -(\mathbf{k}_1 + \mathbf{k}_2) = -\mathbf{K}_{A-2}$). Within these assumptions, the correlated part of the spectral function P_1 becomes ($\mathbf{k} \equiv \mathbf{k}_1$)

$$P_1^{N_1}(|\mathbf{k}|, E) = \sum_{N_2=n,p} \int d\mathbf{k}_3 \delta \left(E - E_{thr} - \frac{A-2}{2m_N(A-1)} \left(\mathbf{k} + \frac{A-1}{A-2} \mathbf{k}_3 \right)^2 \right) n_{rel}^{N_1 N_2} \left(\left| \mathbf{k} + \frac{1}{2} \mathbf{k}_3 \right| \right) n_{CM}^{N_1 N_2}(|\mathbf{k}_3|). \quad (5.38)$$

Eq. (5.38) satisfies the momentum (Eq. (5.12)) and energy (Eq. (5.16)) sum rules and, being expressed in terms of many-body quantities $n_{rel}^{N_1 N_2}$ and $n_{CM}^{N_1 N_2}$, contains no adjustable parameters. A comparison of Eq. (5.38) with *ab initio* spectral function of ${}^3\text{He}$ and realistic many-body spectral function of Nuclear Matter shows a very good agreement, as illustrated in Fig. 27. As a matter of fact, it can be seen that the k -dependence of the peak position, the mean removal energy and the full width at half maximum (FWHM) of the correlation peak are in excellent agreement with microscopic calculations. Such an agreement is a demonstration that in principle any microscopic calculation of the spectral function should produce in the correlation region a convolution formula as the one given by Eq. (5.38). It has indeed been shown [116] that a convolution formula, resulting

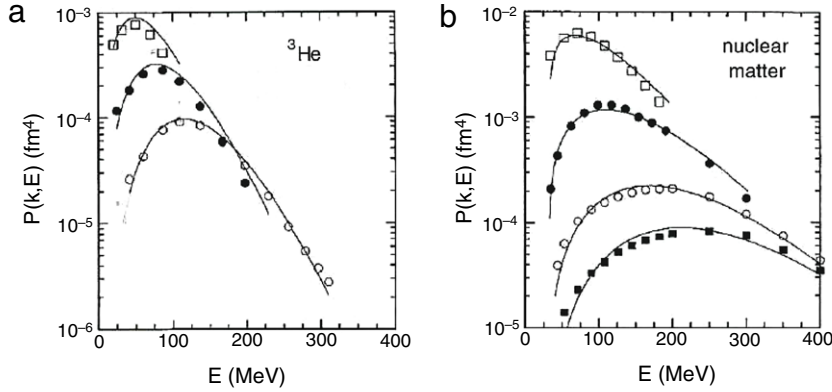


Fig. 27. The proton spectral function of ${}^3\text{He}$ (a) and Nuclear Matter (b) vs the removal energy E for various values of the proton momentum $k \equiv |\mathbf{k}|$. For ${}^3\text{He}$ the squares, full dots, and open dots correspond to $k = 2.2, 2.8$, and 3.5 fm^{-1} , respectively. For Nuclear Matter the squares, full dots, and open dots correspond to $k = 1.5, 2.2$, and 3.0 fm^{-1} , respectively. The solid lines are the prediction of the 2N convolution model of Ref. [114] (Eq. (5.38)) whereas the squares, full dots, and open dots correspond to the microscopic calculations of Ref. [102] for ${}^3\text{He}$ and Ref. [112] for Nuclear Matter.
Source: Reprinted from Ref. [114]. © by the American Physical Society.

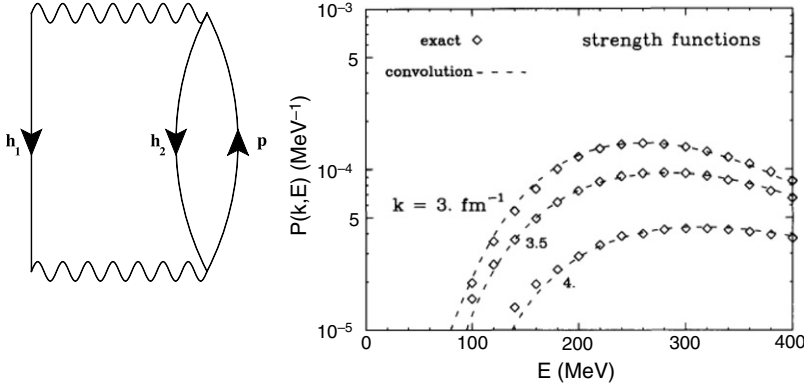


Fig. 28. (Left): the diagram of the BBG expansion considered in the calculation of the spectral functions of nuclear matter at high values of k and E . (Right): the exact BBG nuclear matter spectral function (diamonds) vs E in correspondence of three values of $k = 3, 3.5, 4 \text{ fm}^{-1}$ compared with the BBG convolution model Eq. (5.43) (dashed line). (After [116]).
Source: Reprinted from Ref. [116].

© 1996, by Elsevier.

from the factorization of the ground-state wave function of the target nucleus at large values of the pair momentum can be obtained within the BBG theory of Nuclear Matter. Let us briefly illustrate this important result. In nuclear matter the spectral function corresponding to the nucleon self-energy $M(k, E) = V(k, E) + iW(k, E)$ is obtained from the single particle Green function \mathcal{G} in the following form [60]

$$P_A(k, E) = -\frac{1}{\pi} \text{Im} \mathcal{G}(k, E) = \frac{1}{\pi} \frac{W(k, E)}{(-E - k^2/2m_N - V(k, E))^2 + W(k, E)^2}. \quad (5.39)$$

As we have seen in the previous chapters, the correlation region corresponds to high values of k and E . In this region one can assume

$$E + \frac{k^2}{2m_N} \gg |V(k, E)|, |W(k, E)|, \quad (5.40)$$

and Eq. (5.39) can be approximated as follows [116]

$$P_A(k, E) \simeq \frac{1}{\pi} \frac{W(k, E)}{(E + k^2/2m_N)^2}. \quad (5.41)$$

The major contribution to SRCs arises from 2p–2h excitations in the ground-state wave functions, i.e. in 1p–2h excitations in the final state represented by the diagram shown in Fig. 28; accordingly, the imaginary part of the self energy

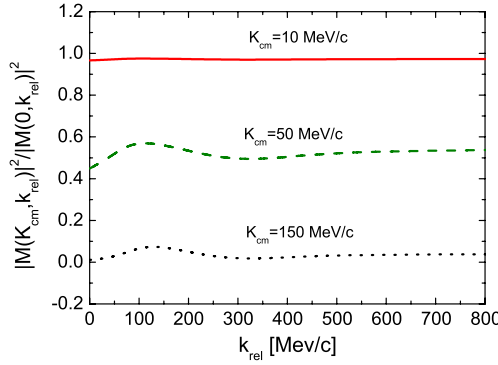


Fig. 29. The ratio R (Eq. (5.44)) in ${}^3\text{He}$. Three-nucleon wave functions from Ref. [48]. AV18 interaction [30].

Source: Reprinted from [117].

© 2011, by Springer.

becomes [60]

$$\begin{aligned} W(k, E) &= \frac{1}{2} \sum_{h_1 h_2 p} \text{Im} \frac{|\langle kp | G(e(h_1) + e(h_2)) | h_1 h_2 \rangle_a|^2}{E - e(p) + e(h_1) + e(h_2) - i\eta} \\ &= \sum_{h_1 h_2 p} |\langle kp | G(e(h_1) + e(h_2)) | h_1 h_2 \rangle_a|^2 \delta(-E + e(p) - e(h_1) - e(h_2)) \end{aligned} \quad (5.42)$$

leading to the following convolution integral for the spectral function of nuclear matter [116]

$$P_A(k_1, E) = \frac{\pi^2 \rho}{16} \int \frac{d^3 \mathbf{K}_{c.m.}}{(2\pi)^3} n_{\text{rel}} \left(\left| \mathbf{k}_1 - \frac{1}{2} \mathbf{K}_{c.m.} \right| \right) n_{c.m.}^{FG}(K_{c.m.}) \delta \left(E - E_{\text{thr}}^{(2)} - \frac{1}{2 m_N} (\mathbf{K}_{c.m.} - \mathbf{k}_1)^2 \right), \quad (5.43)$$

i.e. precisely the convolution model of Ref. [114]. Further confirmation of the correctness of the convolution model, has been provided by the demonstration [117] that *ab initio* three-nucleon ground-state wave functions Ψ_0 in momentum space at high values of the relative momentum and low values of the *c.m.* momentum factorize, as clearly demonstrated by the calculation of the two-body momentum distribution discussed in Section 4.8. As a matter of fact, by considering for ${}^3\text{He}$ the following ratio

$$R = \frac{|\Psi_0(\mathbf{K}_{c.m.}, \mathbf{k}_{\text{rel}})|^2}{|\Psi_0(\mathbf{K}_{c.m.} = 0, \mathbf{k}_{\text{rel}})|^2} \equiv \frac{|M(\mathbf{K}_{c.m.}, \mathbf{k}_{\text{rel}})|^2}{|M(\mathbf{K}_{c.m.} = 0, \mathbf{k}_{\text{rel}})|^2}, \quad (5.44)$$

as a function of $|\mathbf{k}_{\text{rel}}|$ at constant values of $|\mathbf{K}_{c.m.}|$, it is trivial to conclude that if factorization of Ψ_0 holds, i.e. $|\Psi_0(\mathbf{K}_{c.m.}, \mathbf{k}_{\text{rel}})|^2 \simeq n_{c.m.}(K_{c.m.}) n_{\text{rel}}(k_{\text{rel}})$ the ratio becomes a constant

$$R \simeq \frac{n_{c.m.}(K_{c.m.})}{n_{c.m.}(K_{c.m.} = 0)} = \text{constant}. \quad (5.45)$$

Using *ab initio* three-nucleon wave functions from Ref. [19] corresponding to the AV18 interaction, the ratio (5.44) has been calculated in Ref. [117]. The results, shown in Fig. 29, demonstrate that factorization indeed occurs starting, as expected, at a value of k_{rel} which increases with increasing values of $K_{c.m.}$, in agreement with the results for the 2N momentum distributions presented in Fig. 21. Similar results have been obtained for ${}^4\text{He}$. To sum up, it turns out that the 2N convolution model stands on solid grounds resulting from a general property of the many-body wave function, namely its factorization, at high values of momenta and removal energy, into relative and center-of-mass coordinates; this property appears to be a universal one, since it holds both for nuclear matter and few-nucleon systems. To get more insight in the structure of the spectral function of complex nuclei, it would be useful to compare the two spectral functions predicted by the LDA and the convolution model. A comparison already exists for the momentum distribution of ${}^{16}\text{O}$, shown in Fig. 30. It appears that the convolution and the LDA models qualitatively agree up $k \simeq 3 \text{ fm}^{-1}$, but at higher momenta the LDA momentum distribution exhibits a damping at $k \gtrsim 3 \text{ fm}^{-1}$. The same behavior appears to hold for the Gold nucleus.

5.3. Saturation of the momentum sum rule: link between high momenta and high removal energies

In Ref. [92] the saturation of the momentum sum rule (Eq. (5.12)) has been investigated using the microscopic spectral function of ${}^3\text{He}$ described in the previous section. To this end the following quantity has been considered

$$n_A(E_f, k) = 4\pi \int_{E_{\text{min}}}^{E_f} P_A(k, E) dE \equiv n_f(k), \quad (5.46)$$

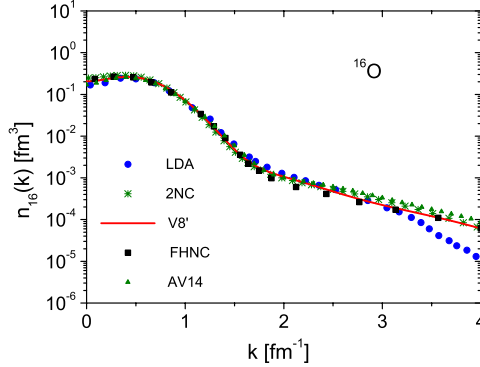


Fig. 30. A comparison between various microscopic calculations of the momentum distributions of ^{16}O . LDA: momentum distribution obtained [118] by integrating the LDA spectral function of Ref. [112]; 2NC: two-nucleon correlation model of Ref. [114]; V8': linked cluster expansion of Ref. [80] with interaction V8'; FHNC: fermion hypernetted chain of Ref. [72] with V8' interaction; AV14: Variational Monte Carlo of Ref. [87] with AV14 interaction.

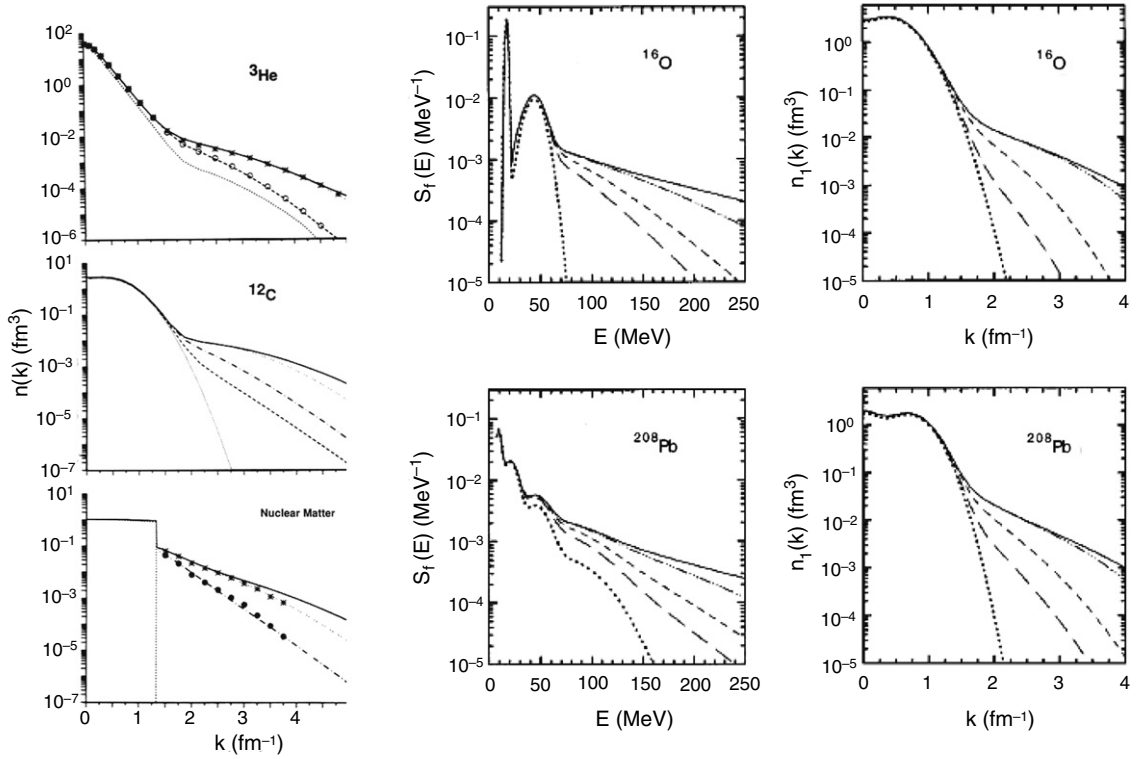


Fig. 31. (Left): the saturation of the momentum sum rule (Eq. (5.46)) in ^3He , ^{12}C and Nuclear matter. Here, the dotted lines represent $n_0(k)$ whereas the dashed, dot-dashed, double-dotted and full lines represent the sum of n_0 plus the integral of P_1 , with the upper limit of integration in ^{12}C equal to $E_{max} = 50, 100, 300 \text{ MeV}$ and ∞ , respectively; for ^3He and nuclear matter the same quantities are represented by the circles, full circles, stars and the full line. Calculations for ^3He have been performed with the *ab initio* spectral function of Ref. [102], for complex nuclei with the model spectral function of Ref. [114] and for Nuclear Matter with the many-body spectral function of Ref. [108]. (Right): the saturation of the energy and momentum sum rule for ^{16}O and ^{208}Pb within the two-nucleon convolution model [114]. The long dashed, dashed, dot-dashed and solid lines represent Eqs. (5.46) and (5.47) integrated up to $k_f = 1.5, 2.0, 3.0, \infty \text{ fm}^{-1}$, and $E_f = 50, 100, 300, \infty \text{ MeV}$.

Source: (Left) Reprinted from Refs. [92,114]. © 1990, by APS. (Right) Reprinted from Ref. [114]. © 1996, by APS.

by varying the upper limit of integration until saturation of the momentum distribution is reached. The results are shown in Fig. 31. In Refs.[111,114] this analysis has been extended to ^{12}C , ^{16}O , ^{208}Pb and Nuclear matter also considering the energy sum rule, i.e. the quantity

$$S_A(k_f, E) = 4\pi \int_0^{k_f} P_A(k, E) k^2 dk \equiv S_f(E). \quad (5.47)$$

Table 5

The normalization $\mathcal{P}_{gr(0)}(\mathcal{P}_{ex(1)})$ (Eq. (4.26)), the mean kinetic, $\langle T \rangle$, and removal, $\langle E \rangle$, energies, and the energy per nucleon $|\epsilon_3|$ for Helium-3, calculated with the spectral function of Ref. [105] and the Pisa group wave function [48] corresponding to the AV18 interaction [30]. The state $f = gr$ corresponds to the spectator proton-neutron system in the ground state (the deuteron), whereas the state $f = ex$ corresponds to the proton-neutron system in the continuum. *per nucleon* = (2 proton + neutron)/3 and $3 \times |\epsilon_3| = |E_3| \approx 7.7$ MeV is the value computed in Ref. [48].

Source: Reprinted from [119].

© 2013, by the American Physical Society.

	Norm, \mathcal{P}			$\langle T \rangle$ (MeV)			$\langle E \rangle$ (MeV)			$ \epsilon_3 $ (MeV)		
	gr	ex	tot.	gr	ex	tot.	gr	ex	tot.	gr	ex	tot.
Proton	0.65	0.35	1	4.67	8.60	13.27	3.72	6.81	10.53	0.69	1.26	1.95
Neutron	0	1	1	0	17.69	17.69	0	16.33	16.33	0	3.74	3.74
per nucleon	–	–	1	3.11	11.63	14.74	2.48	9.99	12.47	0.46	2.09	2.55

Table 6

The same as in Table 5 but for the deuteron and complex nuclei. The results for $A = 2$ correspond to the AV18 interaction and the ones for complete nuclei to the Spectral Function of Ref. [114].

Source: Reprinted from Ref. [119].

© 2007, by the American Physical Society.

A	\mathcal{P}_0	\mathcal{P}_1	$\langle T \rangle_0$ (MeV)	$\langle T \rangle_1$ (MeV)	$\langle T \rangle$ (MeV)	$\langle E \rangle_0$ (MeV)	$\langle E \rangle_1$ (MeV)	$\langle E \rangle$ (MeV)	$ \epsilon_A (\epsilon_A^{exp})$ (MeV)
D	1.0	–	–		11.10			2.22	1.11
^{12}C	0.8	0.2	13.54	18.92	32.50	18.40	26.75	45.15	7.82 (7.7)
^{16}O	0.8	0.2	11.22	19.73	31.95	19.42	27.23	46.65	8.88 (8.0)
^{40}Ca	0.8	0.2	13.39	20.45	33.85	21.28	28.57	49.85	8.44 (8.5)
^{56}Fe	0.8	0.2	11.45	21.26	32.71	20.00	29.11	49.11	8.49 (8.8)
^{208}Pb	0.8	0.2	14.27	24.41	39.13	18.53	34.80	53.33	7.19 (7.9)

The results, shown in Fig. 31, demonstrate that:

1. the momentum distribution for $k \gtrsim 2 \text{ fm}^{-1}$ is entirely determined by the three-body channel configuration in the ground state wave function, i.e. by ground-state correlations;
2. although the components of the wave function with removal energy $E \gtrsim 50 \text{ MeV}$ have probability less than three percent, they have large effects on the high momentum part of $n(k)$;
3. high momentum components are strictly linked to high removal energies;
4. the experimental investigation of the full high momentum (removal energy) part of the spectral function always implies the investigation of full high removal energy (momentum) components, which makes such an investigation a difficult task.

To sum up, the high momentum components in a nucleus are always associated with high virtual excitations of the spectator ($A - 1$) system, i.e., to the integral of $P_1(k, E)$ for high values of E much higher than typical shell-model removal energies; these very high excitations are absent in any mean field approach, where the behavior of the momentum distributions is governed by the size of the system and by the values of the single particle energies; this is the reason why, at high values of k , the mean field momentum distributions are orders of magnitude less than the momentum distributions for correlated nucleons. The link between high momentum components and high values of the removal energies can be qualitatively explained in terms of the two-nucleon correlation mechanism in which the high momentum components of a nucleon are generated by its hard interaction with a single nucleon, whereas the remaining ($A - 2$) nucleons (the *soft* nucleons) move in the mean field with a center-of-mass momentum $\mathbf{K}_{A-2} \approx 0$; for a heavy nucleus, for which recoil energy can be disregarded, the excitation energy of the ($A - 1$) system is therefore centered at $E_{A-1}^{f*} \approx \mathbf{k}^2/2m_N$, which, e.g. at $k \approx 3 \text{ fm}^{-1}$, equals $E_{A-1}^{f*} \approx 200 \text{ MeV} \gg \langle E_{MF} \rangle \approx 20\text{-}30 \text{ MeV}$. Such a picture predicts similar behavior of the high momentum part of $n(|\mathbf{k}|)$ independently of A , in agreement with microscopic calculations of the momentum distributions in terms of realistic NN interactions discussed in Section 4.

5.4. The spectral function and the ground-state energy of nuclei

The Koltun sum rule (Eqs. (5.15) and (5.16)) allows one to obtain the value of $\langle E \rangle$ even if the full spectral function is unknown: it is sufficient to know only $n_A(k)$ (which yields $\langle T \rangle$) and ϵ_A . Conversely, the knowledge of the spectral function allows one to calculate $\langle T \rangle$ and $\langle E \rangle$ obtaining the value of $|\epsilon_A|$. Following Refs. [114] and [119], in Tables 5 and 6 the values of $\langle E \rangle$ and $\langle T \rangle$ predicted by many-body calculations are listed. In case of ^3He realistic spectral functions have been used, whereas for ^4He and heavier nuclei the 2NC convolution model has been used to calculate the value of $|\epsilon_A|$ and it can be seen, as originally stressed in Ref. [114], that acceptable values are obtained.

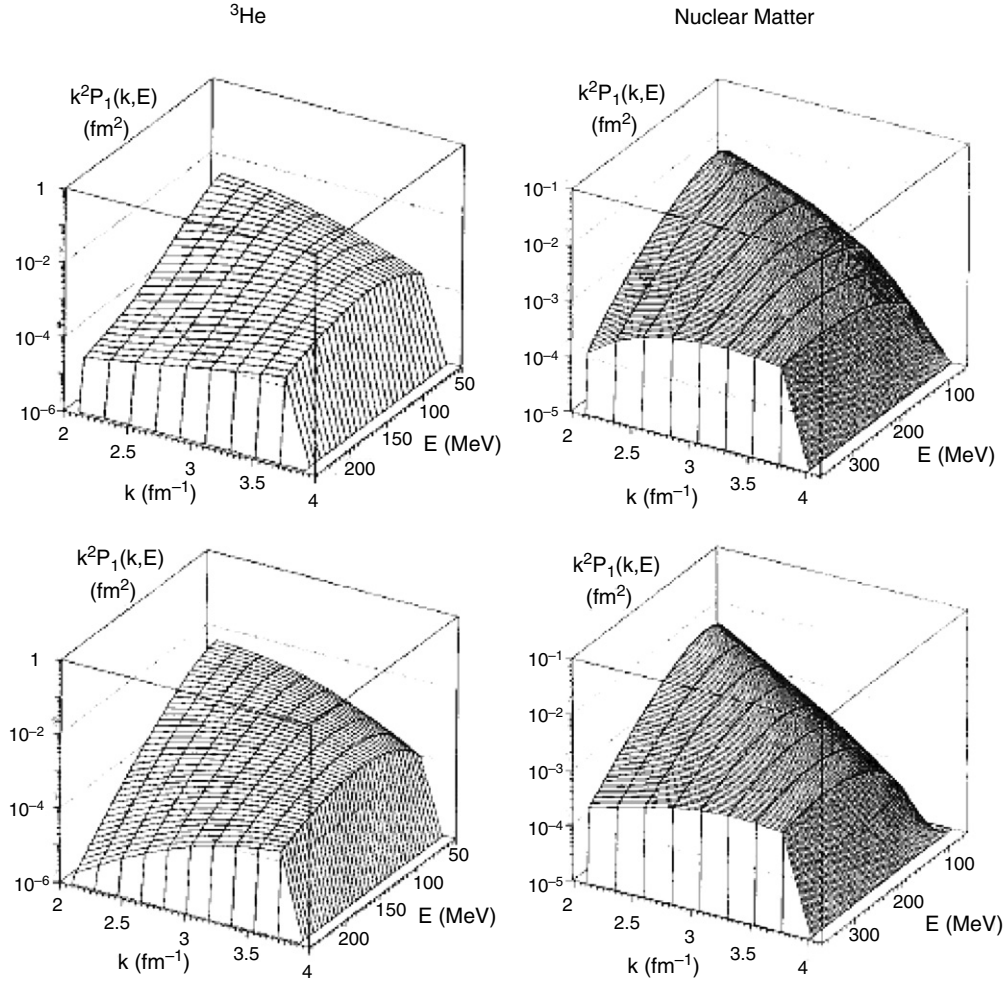


Fig. 32. Momentum and removal energy dependences of the nucleon spectral function $k^2 P_1(k, E)$ for ${}^3\text{He}$ (left panel) and Nuclear Matter (right panel). The top figures show the microscopic spectral functions [102,112], whereas the bottom figures represent the predictions of the 2N convolution model [114]. Source: Adapted from Ref. [114].

© 1996, by APS.

5.5. On the effects of three-nucleon correlations on the hole spectral function

In Fig. 32 the spectral functions of ${}^3\text{He}$ and nuclear matter predicted by the 2N convolution model are compared with the results of microscopic many-body approaches. It can be seen that unlike the case of nuclear matter, for ${}^3\text{He}$ an appreciable difference between the 2N convolution model and the *ab initio* calculations occurs at high values of removal energy and momenta, far from the correlation peaks located at $E \simeq k^2/(4m_N)$. The origin of such a disagreement should probably be ascribed to the effects of three-nucleon (3N) correlations. As a matter of fact the *ab initio* calculation contains both 3N- and 2N-correlations, whereas the convolution model contains only the latter. In case of nuclear matter, on the contrary, both spectral functions are mainly based upon SRCs due to 2p–2h correlations. A more detailed analysis of the ${}^3\text{He}$ spectral functions has been performed in Ref. [120]. There it is stressed that the *ab initio* and the 2N convolution model spectral functions of ${}^3\text{He}$ differ not only by the presence in the former of 3N-correlations, but also by the FSI of the spectator pair which is present in the former and missing in the latter. However as it appears in Fig. 25, the region around the correlation peaks is only slightly affected by the FSI in the spectator pair. This is even more clearly shown in Fig. 33 (Left panel), where the *ab initio* spectral functions of ${}^3\text{He}$ with and without the FSI in the spectator pair are compared: it can be seen that, apart from the region of very low excitation energy, the two spectral functions are practically identical in a large interval of energy. Therefore in this interval it is very meaningful to compare the *ab initio* spectral function with the one predicted by the 2N convolution model and ascribe the differences between them to the effects of three nucleon SRCs. This is illustrated in Fig. 33 (Right panel), where the red highlighted area represents the surface delimited by the difference between the *ab initio* and the 2N convolution model spectral functions. It can be seen that 3N-SRCs represent only a small contribution (of the order of 1–2 percent) to the spectral function and, consequently, to the nucleon momentum distributions.

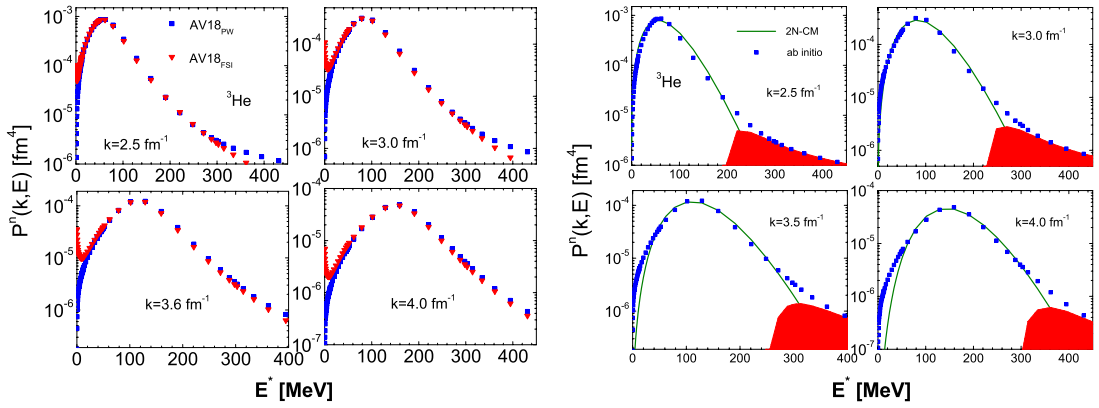


Fig. 33. (Left panel): the microscopic neutron spectral function of ${}^3\text{He}$ corresponding to the AV18 interaction [105] and to different values of the momentum k (red triangles). The blue squares give the same quantity with the pp rescattering in the spectator pair removed. (Right panel): comparison of the neutron spectral function of ${}^3\text{He}$ obtained within the 2N-convolution model [114] (green full line) with the *ab initio* spectral function [105] with the pp rescattering in the final state removed (blue squares of (Left panel)). The two spectral functions in the right panel differ thus only by the presence of three-nucleon correlations in the *ab initio* spectral function, lacking in the 2N-convolution model. The highlighted red areas are the ones delimited by the difference between the *ab initio* and the 2N-Convolution Model spectral functions and represent the effects of three-nucleon SRCs. (For interpretation of the references to color in this figure legend, the reader is referred to the web version of this article.)

Source: Adapted from Ref. [120].

5.6. Two-nucleon spectral function

The most interesting quantity, as far as SRCs are concerned, is the two-nucleon momentum distributions, that in PWIA might in principle be extracted from the $A(e, e'2N)X$ process, when two nucleons are knocked out from the nucleus A and are detected with momenta \mathbf{p}_1 and \mathbf{p}_2 in coincidence with the scattered electron, with the nucleus ($A - 2$) left in the energy state E_{A-2}^f . The measurable missing momentum and energy are in this case the $\mathbf{p}_m = \mathbf{q} - \mathbf{p}_1 - \mathbf{p}_2$ and $E_m = \nu - T_{p_1} - T_{p_2} - T_{A-2} = E_{A-2}^f$. The two-nucleon emission process $A(e, e'N_1N_2)X$ the PWIA cross section will depend upon the two-nucleon spectral function

$$\begin{aligned} P_A^{N_1N_2}(\mathbf{k}_1, \mathbf{k}_2, E^{(2)}) &= \langle \Psi_0 | a_{\mathbf{k}_2}^\dagger a_{\mathbf{k}_1}^\dagger \delta(E - (\hat{H}_{A-2} - E_A)) a_{\mathbf{k}_1} a_{\mathbf{k}_2} | \Psi_0 \rangle \\ &= \sum_f \left| \int e^{-i\mathbf{k}_1 \cdot \mathbf{r}_1 - i\mathbf{k}_2 \cdot \mathbf{r}_2} d\mathbf{r}_1 d\mathbf{r}_2 \langle \Psi_f^{(A-2)}(\{\mathbf{r}\}_{A-2}) | \Psi_0(\mathbf{r}_1, \mathbf{r}_2 \{\mathbf{r}\}_{A-2}) \rangle \delta(E^{(2)} - (E_{A-2}^f - E_A)) \right|. \end{aligned} \quad (5.48)$$

Summing over the final states of ($A - 2$) the *two-nucleon momentum sum rule*

$$n_A^{N_1N_2}(\mathbf{k}_1, \mathbf{k}_2) = \int dE^{(2)} P_A^{N_1N_2}(\mathbf{k}_1, \mathbf{k}_2, E^{(2)}) = n_A^{N_1N_2}(k_{rel}, K_{c.m.}, \Theta), \quad (5.49)$$

is obtained. The two-nucleon Spectral Functions has been obtained within many body theories in Ref. [121] for finite nuclei, in Ref. [122] for nuclear matter, and in Ref. [212] for ${}^3\text{He}$.¹² Assuming a strict 2N correlation model ($\mathbf{k}_1 = -\mathbf{k}_2, \mathbf{K}_{c.m.} = 0$ [12]) the two-nucleon spectral function becomes [115]

$$P_A^{N_1N_2}(\mathbf{k}_1, \mathbf{k}_2, E^{(2)}) = \frac{n_{rel}^{N_1N_2}(\frac{\mathbf{k}_1 - \mathbf{k}_2}{2})}{4\pi} \times \delta(\mathbf{k}_1 + \mathbf{k}_2) \delta(E^{(2)} - E_{th}^{(2)}), \quad (5.50)$$

whereas within the 2N convolution model one has

$$P_A^{N_1N_2}(\mathbf{k}_1, \mathbf{k}_2, E^{(2)}) = \frac{n_{rel}^{N_1N_2}(\frac{\mathbf{k}_1 - \mathbf{k}_2}{2})}{4\pi} \frac{n_{c.m.}^{N_1N_2}(\mathbf{k}_1 + \mathbf{k}_2)}{4\pi} \delta(E^{(2)} - E_{th}^{(2)}), \quad (5.51)$$

which leads to the factorized 2NMD when integrated over the removal energy.

6. Experimental investigation of short-range correlations

6.1. Inclusive electron scattering off nuclei

Electron scattering off nuclei has played and continue to play a fundamental role in the study of the structure of hadrons (see e.g. [123–128]) thanks to the following properties of the electromagnetic interaction (i) the interaction of the probe

¹² Eq. (5.48) has been called *vector spectral function* in Ref. [212] and a similar quantity has been called *decay function* in Ref. [12].

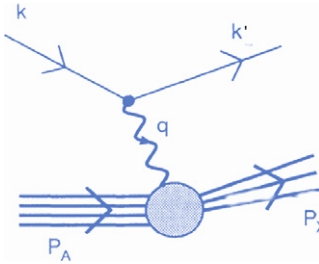


Fig. 34. The Feynman diagram in the one-photon-exchange (OPE) approximation describing electron–nucleus interaction in inclusive $A(e, e')X$ scattering when only the scattering electron is detected. $k \equiv \{\epsilon, \mathbf{k}\}$ and $k' \equiv \{\epsilon', \mathbf{k}'\}$ denote the four-vectors of the incoming and scattered electron, respectively, $q \equiv \{q_0, \mathbf{q}\}$ the four-momentum of the exchanged virtual photon γ^* , $P_A \equiv \{P_A^0, \mathbf{P}_A\}$ and $P_X \equiv \{P_X^0, \mathbf{P}_X\}$ the four-momenta of the initial and final nuclei.

with the nucleus is well described by quantum electro-dynamics (QED); (ii) the internal “working” of nucleons and nuclei can be seen without disturbing the latter with the probe itself; (iii) the momentum and energy transfers can be varied independently. Recent progress in the investigation of SRCs became possible thanks to: (i) the high resolution of hadron and electron probes, characterized by a wave length of the order, or even less, than the nucleon dimension, (ii) the high intensity beams, (iii) multi-coincidence experiments. The Feynman diagram describing the one-photon-exchange approximation of inclusive scattering of electrons off nucleus A is shown in Fig. 34. The following invariant quantities can be used to characterize the process: (i) the squared 4-momentum transfer

$$-q^2 = \mathbf{q}^2 - q_0^2 = 4\epsilon \epsilon' \sin^2 \frac{\theta}{2} \equiv Q^2 > 0; \quad (6.1)$$

(ii) the squared invariant mass of the final hadronic state:

$$W_X^2 = (P_A + q)^2 = P_A^2 + 2P_A \cdot q + q^2; \quad (6.2)$$

(iii) the quantity

$$\nu = \frac{P_A \cdot q}{M_A}, \quad (6.3)$$

which, in the lab system, is nothing but the energy transfer

$$\nu = q_0 = \epsilon - \epsilon'. \quad (6.4)$$

Using general symmetry principles, e.g. Lorentz and time reversal invariance, parity and current conservations, the inclusive cross section in the lab system is a function of two response (or structure) functions $W_{1(2)}$ depending upon two independent kinematical variables, e.g. the energy transfer ν and the four-momentum transfer Q^2 , as follows:

$$\frac{d^2\sigma}{d\epsilon' d\Omega'} = \sigma_{Mott} \left\{ W_2^A(\nu, Q^2) + 2 \tan^2 \frac{\theta}{2} W_1^A(\nu, Q^2) \right\}, \quad (6.5)$$

where

$$\sigma_{Mott} = \frac{\alpha^2 \cos^2 \frac{\theta}{2}}{4\epsilon^2 \sin^4 \frac{\theta}{2}}, \quad (6.6)$$

is the *Mott* cross section describing scattering off a point-like hadron and α is the fine-structure constant. The two functions $W_{1(2)}^A$, describe the structure of the target and can be chosen to depend, besides ν and Q^2 , upon other sets of two independent variables, e.g.

$$(W^2 = (P_A + q)^2, Q^2), \quad (6.7)$$

$$\left(x_B = \frac{Q^2}{2m_N \nu}, Q^2 \right), \quad (6.8)$$

$$(Y, Q^2), \quad (6.9)$$

where x_B is the Bjorken scaling variable [132] and Y any function (to be discussed later on) of $|\mathbf{q}|$ and ν . The nuclear responses $W_{1(2)}^A(\nu, Q^2)$ have the following form

$$W_{1(2)}(\nu, Q^2) = \sum_{f \neq 0} |\langle \Psi_A^f | \hat{J}_{1(2)} | \Psi_A^0 \rangle|^2 \cdot \delta(\nu - \varepsilon_i + \varepsilon_f), \quad (6.10)$$

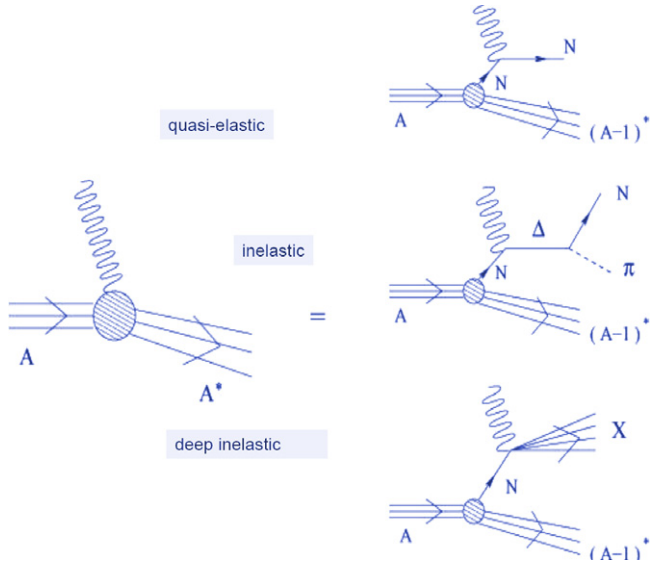


Fig. 35. The exact γ -nucleus vertex in the left panel approximated by the PWIA depicted in the right panel in terms of quasi-elastic scattering, inelastic scattering and deep-inelastic scattering on nucleon N . The four-momentum of the struck nucleon N before interaction is $k \equiv (k_0, \mathbf{k})$, and the one of the produced hadron (N, Δ, X) is $p_X \equiv (p_X^0, \mathbf{p}_X)$.

where $\varepsilon_{i(f)}$ are initial (final) total energies of the process, $\Psi_A^0(E_A^{(0)})$ and $\Psi_A^f(E_A^{(f)})$ the eigenfunctions (eigenvalues) corresponding to the ground (0) and excited (f) states of the nuclear Hamiltonian i.e.

$$\hat{H}|\Psi_A^f\rangle = E_A^f|\Psi_A^f\rangle \quad (6.11)$$

and $\hat{J}_{1(2)}$ is the nuclear current operator composed of one- and two-body parts

$$\hat{J}_{1(2)} = \sum_i \hat{J}_{1(2)}(i) + \sum_{ij} \hat{J}_{1(2)}(ij). \quad (6.12)$$

Within a realistic many-body approach the one-body part couples to both the mean-field and the 2p-2h ground-state configurations originating from SRCs, and the two-body part couples also to meson exchange currents (MEC) (for a comprehensive review see [129]). It has been argued (see e.g. a detailed discussion in [13]) that at high values of Q^2 and $x_B > 1$ the effects from MEC should be small, though non negligible (a few examples will be given later on); in this respect, it should be pointed out that recent many-body calculations (see [130] and [131] and references therein quoted) demonstrate that SRCs appreciably increase the contribution of the interference term between the one- and two-body currents, strongly enhancing the full transition amplitude providing, by this way, a further evidence of the importance of short-range effects and stressing, at the same time, the necessity of using realistic models for both current operators and wave functions.

6.1.1. The Plane Wave Impulse Approximation (PWIA)

At high values of the momentum transfer when $\lambda = 1/\sqrt{Q^2} \ll R_A$ (R_A characterizes the size of nucleus A), an approximation which is useful to understand the basic physics of the process is the so called *plane wave impulse approximation* (PWIA), according to which the virtual photon interacts with a bound, off-the-energy-shell nucleon, that, after interaction, is: (i) either left in the ground state (*quasi-elastic* scattering) or, (ii) it is excited in the state $|X_N\rangle$ (*inelastic* and *deep inelastic (DIS)* scattering). The basic approximation of the PWIA is the assumption that the hadronic state created in the γ^*N interaction is leaving the nucleus without interacting with the nucleons (*the spectators nucleons*) of the nucleus $(A - 1)$, as depicted in Fig. 35. In the Laboratory system the kinematics of the process is therefore described by the following 4-vectors ($\mathbf{k}_1 \equiv \mathbf{k}$)

$$P_A \equiv (M_A, 0), \quad (6.13)$$

$$k \equiv (k_0, \mathbf{k}), \quad (6.14)$$

$$P_{A-1} \equiv ((\mathbf{k}^2 + M_{A-1}^{f2})^{1/2}, -\mathbf{k}), \quad (6.15)$$

$$p_X \equiv ((\mathbf{p}_X^2 + m_X^2)^{1/2}, \mathbf{p}_X). \quad (6.16)$$

Here k_0 is the energy of the off-the-energy-shell bound nucleon

$$k_0 = M_A - (\mathbf{k}^2 + M_{A-1}^{f2})^{1/2}, \quad (6.17)$$

with $M_{A-1}^f = M_{A-1} + E_{A-1}^*$. In PWIA the nuclear response functions $W_{1(2)}^A$ can be expressed in terms of the nucleon responses $W_{1(2)}^N$ as follows (see e.g. [133–135])

$$W_1(2)^{A,i}(\nu, Q^2) = Z \int d\mathbf{k} \int dE P_A^p(|\mathbf{k}|, E) \left[C_{1(2)} W_1^{p,i}(\bar{Q}^2, \bar{W}, k^2) + D_{1(2)} W_2^{p,i}(\bar{Q}^2, \bar{W}, k^2) \right] \\ + (\text{the same for neutrons}), \quad (6.18)$$

where $i = \{qe, in, dis\}$ stand for *quasi-elastic*, *inelastic* and *deep inelastic scattering*. The elastic nucleon structure functions are related to the nucleon charge and magnetic form factors, and the inelastic and deep inelastic structure functions can be parametrized from the experimental data on inelastic and deep inelastic scattering off the nucleon (see e.g. [136]), the coefficients $C_{1(2)}$ and $D_{1(2)}$ depend upon the way off-shell effects are taken into account and the barred quantities are used to mean that Q^2 and W^2 effectively include off-shell effects (see [133–135]). Note moreover that in Eq. (6.18) k^2 denotes the squared four-momentum of the bound nucleon.¹³ To sum up, the cross section in PWIA has the following form

$$\frac{d^2\sigma}{d\nu' d\Omega'} = \frac{d^2\sigma^{qe}}{d\nu' d\Omega'} + \frac{d^2\sigma^{in}}{d\nu' d\Omega'} + \frac{d^2\sigma^{dis}}{d\nu' d\Omega'}. \quad (6.20)$$

The theoretical calculation of the responses (Eq. (6.10)) implies the knowledge of the nuclear current and the complete set of final states $|\Psi_A^f\rangle$ which makes the calculation prohibitive (except for the trivial case of the two, and, to some extent, three-body and four-body systems). It should be stressed that if the δ -function were absent in Eq. (6.10) then the completeness of final states would allow one to replace the sum $\sum_f |\Psi_A^f\rangle \langle \Psi_A^f|$ by unity thus getting rid of the final states. Nonetheless, even in the presence of the δ -function, the response function can be represented as a ground state expectation value of a complicated operator. This can be achieved by using the equation of motion formalism, leading to¹⁴

$$W_C^A(\nu, \mathbf{q}) = \int_{-\infty}^{+\infty} \frac{dt}{2\pi} e^{i(\nu - \frac{\mathbf{q}^2}{2m_N})t} \langle \Psi_0 | \sum_{i,j=1}^Z \hat{Q}_i \hat{Q}_j e^{-i(H-E_A^{(0)} - \frac{\hat{\mathbf{p}}_i \cdot \mathbf{q}}{m_N})t} | \Psi_0 \rangle, \quad (6.21)$$

where \hat{Q} is the nucleon charge operator. In order to understand in a more formal way the approximation underlying the PWIA and its possible improvements, it is useful to rewrite the nuclear Hamiltonian in the following way¹⁵

$$\hat{H} = \sum_i \frac{\hat{\mathbf{p}}_i^2}{2m_N} + \hat{V}(\mathbf{r}_1 \dots \mathbf{r}_A) = H_{A-1} + \sum_{j \neq 1} v(1, j) + \frac{\mathbf{p}_1^2}{2m_N}, \quad (6.22)$$

where H_{A-1} contains the nucleons that did not interact with the probe. The PWIA corresponds to neglecting in Eq. (6.21) the interaction term containing $v(1j)$ appearing in the Hamiltonian (cf. Eq. (6.22)).

6.1.2. The general features of the quasi elastic (q.e.) inclusive cross section in PWIA

In PWIA the q.e. differential cross section at high values of momentum transfer can be expressed in the following general form (see e.g. [134,149]) (note that in what follows the notations $|\mathbf{k}| \equiv k$ and $|\mathbf{q}| \equiv q$ will be used)

$$\sigma_2^A(q, \nu) \equiv \frac{d^2\sigma(q, \nu)}{d\nu' d\Omega'} \quad (6.23)$$

$$= \sum_{N=1}^A \int dE \int d^3k P_A^N(k, E) \sigma_{eN}(q, k, \nu, E) \delta(\nu + M_A - E_N(p_N) - E_{A-1}(p_{A-1})) \quad (6.24)$$

$$= 2\pi \sum_{N=1}^A \int_{E_{\min}}^{E_{\max}(q, \nu)} dE \int_{k_{\min}(q, \nu, E)}^{k_{\max}(q, \nu, E)} k dk \left| \frac{\partial \nu}{k \partial \cos \alpha} \right|^{-1} \sigma_{eN}(q, k, \nu, E) P_A^N(k, E) \quad (6.25)$$

$$\simeq [Zs_{ep} + Ns_{en}] \left| \frac{\partial \nu}{k \partial \cos \alpha} \right|^{-1} F_A(q, \nu), \quad (6.26)$$

¹³ Deep inelastic scattering is usually described in terms of the following structure functions

$$F_1(x_B, Q^2) = m_N W_1(x_B, Q^2) \quad F_2(x_B, Q^2) = \nu W_1(x_B, Q^2). \quad (6.19)$$

¹⁴ For ease of presentation let us consider only the Coulomb response W_C^A .

¹⁵ Without any loss of generality only two-nucleon forces will be considered.

where it has been considered, without loss of generality, the case of an isoscalar nucleus for which $P_A^p = P_A^n \equiv P_A$ and the error one does in taking the kinematical factor out of the integral is at most few percent at the values of momentum transfer considered in available experiments at high values of Q^2 (see for details Ref. [149]). The quantity

$$F_A(q, \nu) = 2\pi \int_{E_{\min}}^{E_{\max}(q, \nu)} dE \int_{k_{\min}(q, \nu, E)}^{k_{\max}(q, \nu, E)} P_A(k, E) k dk, \quad (6.27)$$

is the q.e. structure function reflecting the structure of the nucleus if the PWIA holds. The limits of integrations, fixed by energy conservation, are given explicitly in Ref. [149]. The quantities appearing in the energy conserving δ -function are $E_N(p_N) = [m_N^2 + (\mathbf{k} + \mathbf{q})^2]^{1/2}$, $E_{A-1}(P_{A-1}) = [M_{A-1}^{f2} + \mathbf{k}^2]^{1/2}$, $\cos \alpha = \mathbf{k} \cdot \mathbf{q}/(k q)$ and the quantity $|\frac{\partial \nu}{k \partial \cos \alpha}|$ results from the integration of Eq. (6.25) over $\cos \alpha$. It has been shown that at high values of q or Q^2 , the dependence of Eq. (6.24) upon k and E is practically contained only in the spectral function, so that σ_{eN} and $|\frac{\partial \nu}{k \partial \cos \alpha}|$ can safely be replaced by their values calculated at $k_{\min}(q, \nu, E_{\min})$ and E_{\min} and taken out of the integral obtaining Eq. (6.26) (the estimated error is only 2–3 percent). Concerning the explicit expressions of E_{\max} , k_{\max} and k_{\min} , which are given in [149]), the following remark is in order: at fixed values of ν , E_{\max} and k_{\max} rapidly increase with q in such a way that they can be replaced by infinity, also in view of the rapid fall-off of the spectral functions with k and E ; on the contrary, k_{\min} decreases with increasing values of q . Therefore, the following model independent statement holds: *the PWIA structure function (6.27) plotted vs q at fixed values of ν has to increase until it reach its constant asymptotic limit. Any other way of reaching the asymptotic limit, e.g. from top, would be clear evidence of the breaking down of the PWIA, and a clear evidence of FSI effects.* Thus, at high resolution, the behavior of the structure function is essentially governed by the value of k_{\min} which is obtained from the following equation

$$\nu + M_A = \sqrt{m_N^2 + (q \pm k_{\min})^2} + \sqrt{(M_{A-1} + E_{A-1}^f)^2 + k_{\min}^2}, \quad (6.28)$$

where the positive and negative signs in front of k_{\min} correspond to the right ($\nu < \nu_0$) and to the left ($\nu > \nu_0$) parts of the q.e. peak where $\nu = \nu_0 \simeq Q^2/(2m_N)$, $x_B \simeq 1$. Let us now analyze the most peculiar feature of the experimental data and their comparison with the PWIA.

Many experimental data on q.e. cross sections have been collected at different energy and momentum transfer (for an exhaustive review on q.e. scattering see Ref. [137]). In Fig. 36 the experimental inclusive cross section off ${}^3\text{He}$ and its comparison with the PWIA calculation is shown in correspondence of several increasing values of Q^2 . The following general features of the cross section can be observed:

1. at $\nu \simeq Q^2/2m_N A$ ($x_B \simeq A$), elastic scattering from the entire nucleus occurs (the elastic peak is not visible at these high values of Q^2 because of the rapid drop off of the elastic nucleon form factor with Q^2);
2. at $\nu \simeq Q^2/2m_N \equiv \nu_0$ ($x_B \simeq 1$) quasi-elastic scattering from a bound nucleon almost at rest is the dominant process;
3. at $\nu > \nu_0$ ($x_B < 1$), nucleon degrees of freedom can be excited and particle production and deep inelastic scattering almost exhaust the cross section.

Therefore the q.e. region with $\nu < \nu_0$, $x_B > 1$ is the correct region to look for SRCs since there nucleon's d.o.f. and high momentum components of the wave functions dominate for the reasons just explained. In Fig. 37 the separate contributions from the MF (P_0) and SRC (P_1) parts of the spectral function are compared with the experimental data. It can be seen that at transferred energy $\nu \simeq Q^2/(2m_N)$ ($x_B \simeq 1$) scattering from uncorrelated nucleons dominates whereas at low transferred energy ($x_B > 1$) SRCs provide the leading contribution to the cross section. The results presented in the previous figures have been obtained with the spectral function of the two-nucleon convolution model, without adjusting any parameter, but the same general quantitative features can be found using, the *ab initio* spectral function of ${}^3\text{He}$ and the microscopic LDA spectral function of nuclear matter as shown in Fig. 38. Even for complex nuclei the convolution model and the LDA spectral functions provide similar results (cf. Refs. [141,137]).

6.2. The scaling properties of the inclusive cross section: Y-scaling

It was shown in Ref. [145] that by introducing a proper kinematical quantity, function of q and ν , the *scaling variable* $Y = Y(q, \nu)$, the structure functions of quasi elastic (q.e.) inclusive scattering in the asymptotic limit of high momentum transfer, become a function of only the variable, Y , and not of the two independent variables, q and ν , i.e. the structure functions scale in Y , and it can easily be related to the nucleon momentum distributions. Unfortunately in that paper non-relativistic kinematics, non interacting nucleons and the PWIA have been used, so that the simple relation between Y -scaling and the momentum distribution had no practical impact. Nevertheless the paper was very seminal and triggered an intense activity aimed at investigating the possible usefulness of scaling relations within a realistic treatment of the nucleus, based on the use of relativistic kinematics and the inclusion of FSI effects. Recently, new data on q.e. inclusive scattering have renewed the interest in finding scaling relations which might be useful to get information on SRCs. In what follows we will critically review these attempts. A popular scaling variable is the one denoted by y [146–152], which is obtained by placing in the energy conservation, Eq. (6.26), $k = y$, $\mathbf{k} \cdot \mathbf{q}/kq = \pm 1$ and, most importantly, $E_{A-1}^* = 0$, which means that y is the solution of the following equation

$$\nu + M_A = \sqrt{m_N^2 + (q + y)^2} + \sqrt{M_{A-1}^2 + y^2}. \quad (6.29)$$

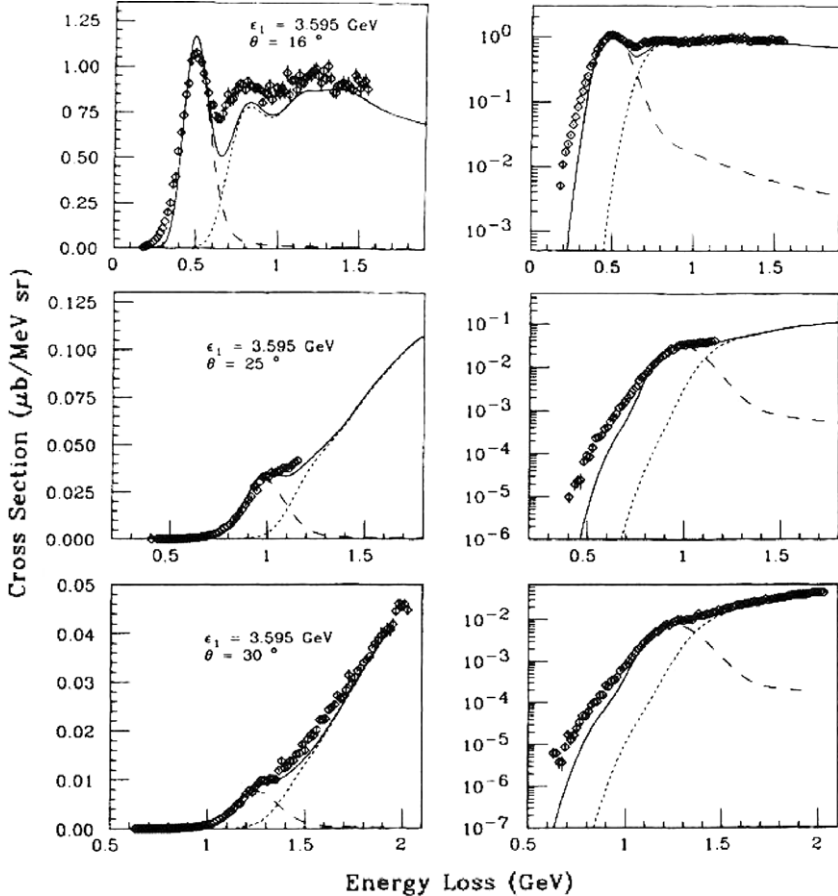


Fig. 36. The experimental cross section of the inclusive process ${}^3\text{He}(e, e')X$ compared with theoretical calculations performed in PWIA using the *ab initio* three-nucleon spectral function of Ref. [102]. Cross sections are shown in linear (left panel) and log (right panel) scales in correspondence of different electron scattering angles (θ) and fixed initial electron energy (ϵ_1). The average value of the squared momentum transfer Q^2 in the three considered cases is $Q^2 \simeq 1, \simeq 2, \simeq 3 (\text{GeV}/c)^2$, in correspondence of $\theta = 16^\circ, 25^\circ, 30^\circ$, respectively. At the lowest value of Q^2 the *quasi elastic* peak (1st term of Eq. (6.20)) with $v = v_0 \simeq Q^2/2m_N, x_B \simeq 1$, is the dominant contribution; with increasing values of the transferred energy and momentum the *inelastic* and *deep inelastic* channels (2nd and 3rd terms of Eq. (6.20)) are excited mostly in the region $v > v_0, x_B < 1$. The region of interest for the study of short-range nucleon dynamics is the *quasi-elastic* region characterized by $v < v_0$ and $x_B > 1$. The dashed and dotted curves represent, respectively, the *quasi-elastic* and the *inelastic* contributions, and the full line their sum. It can be seen from the right panel that at $x_B > 1$ the PWIA systematically underestimates the experimental data. This is a general A-independent effect, as shown in detail in Fig. 37. Experimental data from [138].
Source: Reprinted from [134].

© 1992, by the American Physical Society.

By comparison with Eq. (6.28) one gets

$$|y| = k_{\min}(q, v, E_{\min}), \quad (6.30)$$

which is nothing but the *minimum momentum of a bound nucleon having the minimum value of the removal energy* $E = E_{\min}$, with $y < 0$ ($x_B > 1$) and $y > 0$ ($x_B < 1$) corresponding respectively to $v < v_0$ and $v > v_0$. The q.e. structure function (Eq. (6.27)) assumes now the following form

$$F_A(q, y) = 2\pi \int_{E_{\min}}^{\infty} dE \int_{k_{\min}(q, y, E)}^{\infty} P_A(k, E) k dk, \quad (6.31)$$

where the dependence upon q and y is governed by the q dependence of k_{\min} . The theoretical PWIA structure (scaling) function (6.31) can be compared with the corresponding experimental quantity defined as [149]¹⁶

$$F_A^{ex}(q, y) = \frac{\sigma_2^{ex}(q, y)}{[Zs_{ep} + Ns_{en}]} \times \left| \frac{\partial v}{k \partial \cos \alpha} \right|. \quad (6.32)$$

¹⁶ The proper definition and the physical meaning of y has been discussed in detail in Ref. [149] whereas in Refs. [150,151] k_{\min} has been improperly interpreted as the minimum longitudinal ($k_{\perp} = 0$) momentum of the bound nucleon and, accordingly, the definition of the scaling function reflected the erroneous assumption that $k_{\perp} = 0$ and the comparison with the experimental data (where $k_{\perp} \neq 0$) where misleading. The role of k_{\perp} was clarified in Ref. [149] and in Ref. [152] the proper definition of y has been eventually adopted.

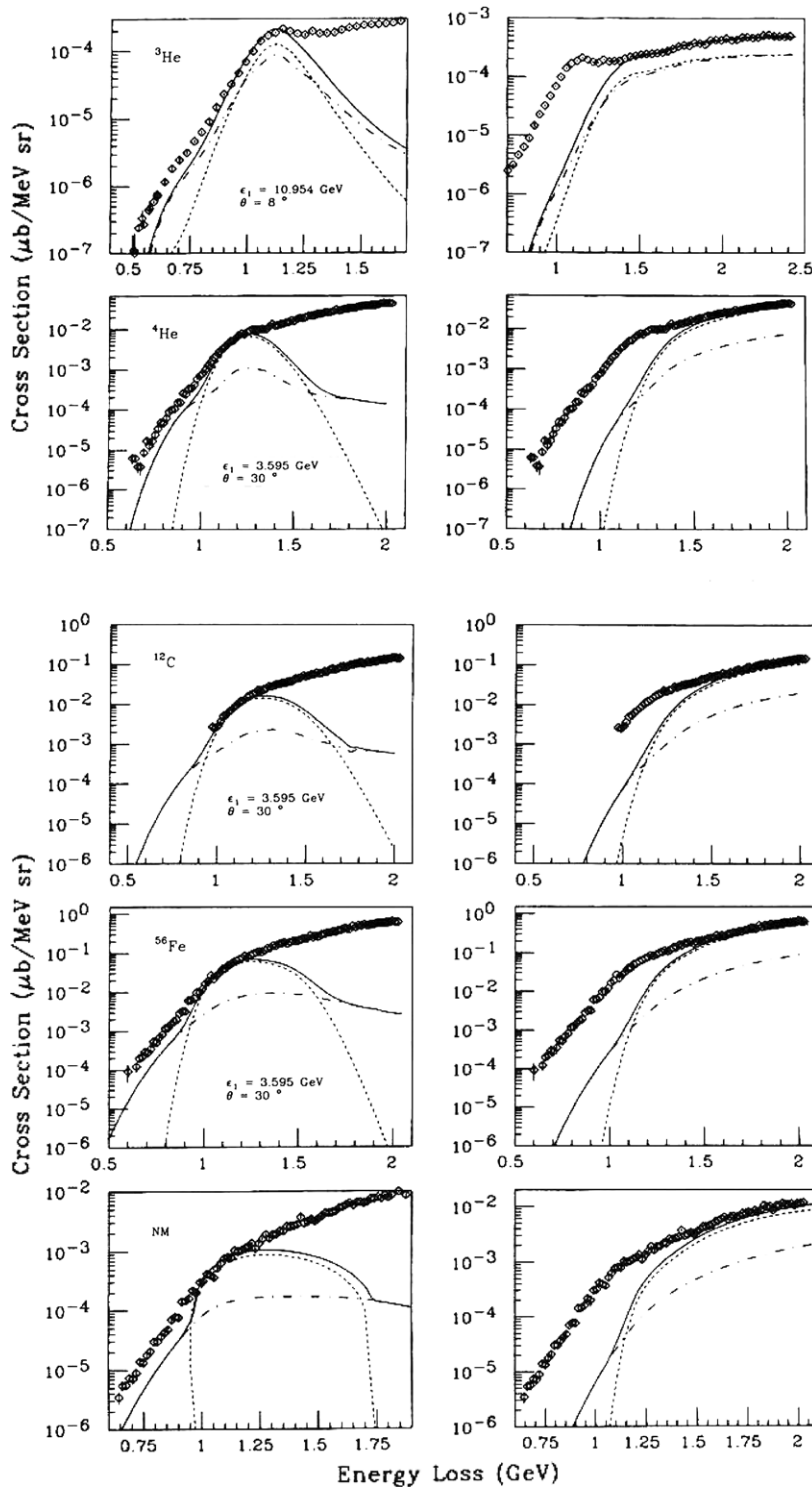


Fig. 37. The same as in Fig. 36 but with a separate illustrations of quasi-elastic (left panel) and inelastic (right panel) contributions in nuclei ${}^3\text{He}$, ${}^4\text{He}$, ${}^{12}\text{C}$, ${}^{16}\text{O}$, ${}^{56}\text{Fe}$ and Nuclear Matter at values of $Q^2 \simeq 2 (\text{GeV}/c)^2$ for ${}^3\text{H}$ and $Q^2 \simeq 3 (\text{GeV}/c)^2$ for the other nuclei. Parameter-free calculation from Ref. [134] using for complex nuclei the two-nucleon convolution model of the spectral function. Experimental data from Refs. [138,139]. Source: Reprinted from Ref. [134].

© 1992, by the American Physical Society.

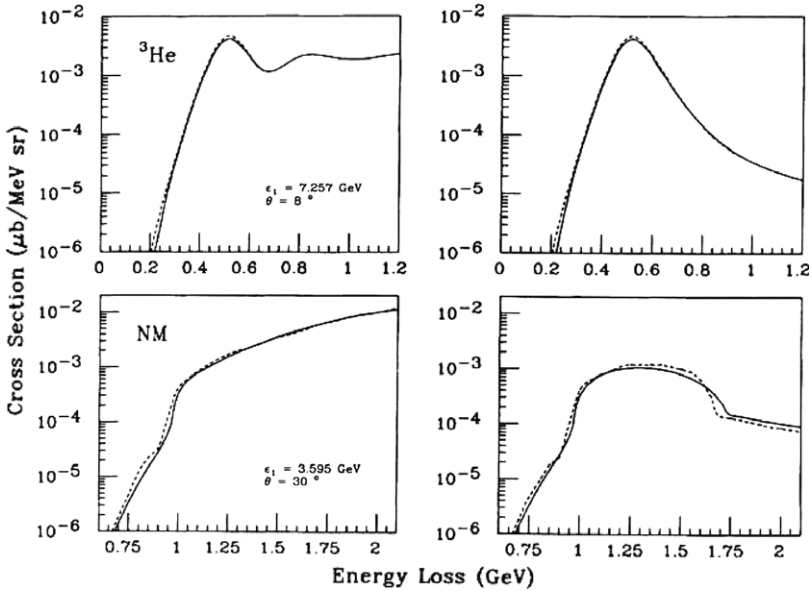


Fig. 38. The PWIA quasi-elastic cross section in ^3He (top panel) and Nuclear Matter (bottom panel) calculated in Ref. [134] using two different spectral functions, namely: (i) the *ab initio* spectral functions of ^3He [102] and the microscopic spectral function of nuclear matter [108] (dotted lines), and (ii) the 2N convolution model spectral function of Ref. [114] (full lines) for both nuclei. The left panel shows the full inclusive cross section (quasi elastic plus inelastic) (cf. Eq. (6.20)), whereas the right panel shows only the quasi elastic contribution (cf. Eq. (6.20)).

Source: Reprinted from [134].

© 1992, by the American Physical Society.

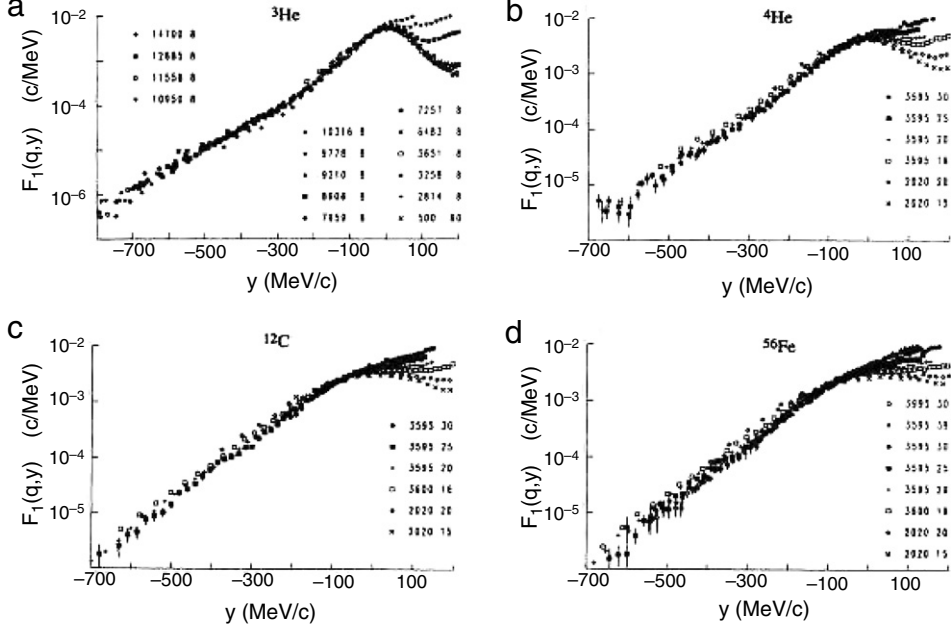


Fig. 39. The experimental scaling function (6.31) of ^3He , ^4He , ^{12}C and ^{56}Fe obtained in Ref. [149] from q.e. data [138,140,137]. The insets denote the value of the incident electron energy and the electron scattering angle which correspond to different values of the three-momentum q and energy v .

Source: Reprinted from [151].

© 1991, by the American Physical Society.

In Refs. [147–149] the experimental scaling functions (6.32) for nuclei in the range $2 \leq A \leq 56$ have been obtained by plotting all available experimental data on q.e. cross sections corresponding to different values of v and q^2 leading to the same value of y . Some of them are shown in Fig. 39. These plots demonstrate that at $y < 0$ ($x_B > 1$) the available data group together, whether at $y > 0$ ($x_B < 1$) they are largely spread out, so it would appear that at $y > 0$ scaling is grossly violated

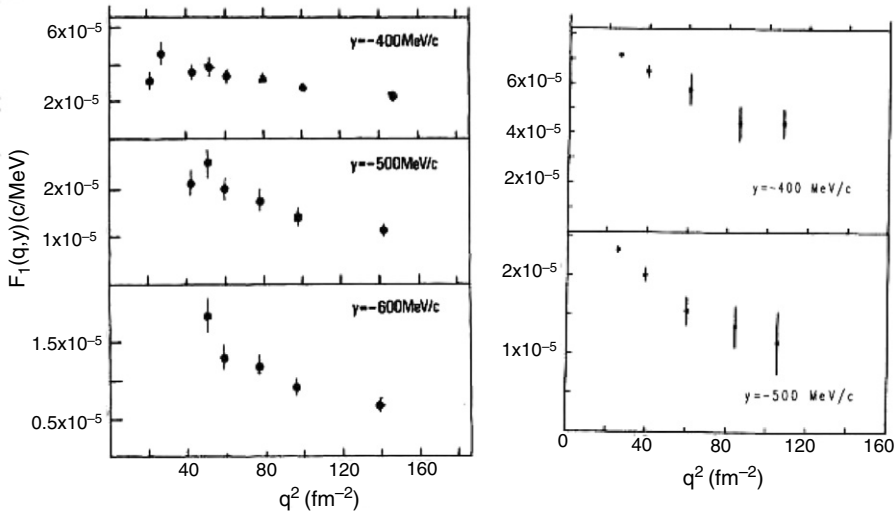


Fig. 40. The ^2H (Left) and ^{56}Fe (Right) experimental scaling function $F_1^{\exp}(q, y) \equiv F_1(q, y)$ (Eq. (6.32)) at high negative values of y illustrating its decrease with increasing values of the square of the three-momentum transfer q^2 . The decreasing behavior of F_1 with increasing q^2 represents a model independent proof of the breaking down of the PWIA.

Source: Reprinted from [147] and [149]. © 1987 and 1991, by the American Physical Society.

whereas at $y < 0$ it is satisfied. Whereas the first statement is certainly true, the second one is not fully true, because, as stressed in Ref. [147], the occurrence of scaling cannot be ascertained on a *log scale*. As a matter of fact same of the scaling functions plotted on a *linear scale* in Fig. 40 clearly show that at large negative values of y scaling is violated and only at the largest value of the momentum transfer the constant asymptotic value seems to be reached. Note, moreover, that the approach of scaling from the top is clear, model independent demonstration of the breaking down of the PWIA, since this, as previously explained, has to approach the constant behavior from the bottom due to the decrease (increase) of k_{\min} (k_{\max}) with q^2 [149]. For a deuteron target $E = E_{\min} = 2.22 \text{ MeV}$, so that the spectral function is entirely determined by the nucleon momentum distribution $n(k)$, since $P(k, E) = n_D(k)\delta(E - E_{\min})$; as a result $k_{\min} = |y|$ for any value of $|\mathbf{q}| \equiv q$ and the deuteron structure function (6.31) reduces in the absence of FSI to the *longitudinal momentum distribution*

$$f_D(y) = 2\pi \int_{|y|}^{\infty} n_D(k) k dk, \quad (6.33)$$

which can be inverted to obtain the momentum distributions by a simple derivative

$$n_D(k) = -\frac{1}{2\pi y} \frac{df_D(y)}{dy}, \quad k = |y|. \quad (6.34)$$

The experimental scaling function of deuteron shown in Fig. 40(Left) demonstrate the presence of FSI but this, given a two-body interaction, can be readily and exactly calculated. This has been done in Ref. [153]; the results are shown by the dashed line in Fig. 41 (Left). Thus by removing the effects of the FSI, the longitudinal momentum distribution of the deuteron $f_D(y)$ has been obtained (Fig. 41 (Right)) and the momentum distribution have been accordingly obtained by Eq. (6.34) and shown in (Fig. 42 (Left)). Following a similar procedure, the momentum distribution of the deuteron was recently obtained from a large set of new q.e. data on y -scaling [154] which allowed one to obtain n_D with higher precision but still in agreement with the results of Ref. [147]. The comparison with theoretical momentum distributions of the deuteron, obtained from non-relativistic wave functions corresponding to the RSC [24] and Paris [26] interactions, is impressive. It appears therefore that up to $k \approx 600 \text{ MeV}/c$ a non-relativistic description of the two-body system is in agreement with the experimental data.

It has been demonstrated [146, 149] that y -scaling also occurs in complex nuclei, since

$$\lim_{|\mathbf{q}| \rightarrow \infty} F_A(|\mathbf{q}|, y) = F_A(y) = 2\pi \int_{E_{\min}}^{\infty} dE \int_{k_{\min}^{\infty}(y, E)}^{\infty} P_A(k, E) k dk. \quad (6.35)$$

However the scaling function $F_A(y)$ is not related to the momentum distribution, as in the case of deuteron, but to the spectral function, whose removal energy dependence, introduces, besides FSI, further scaling violation. For this reason $F_A(y)$, the asymptotic scaling function, differs from the *longitudinal momentum distribution*

$$f_A(y) = 2\pi \int_{|y|}^{\infty} n_A(k) k dk. \quad (6.36)$$

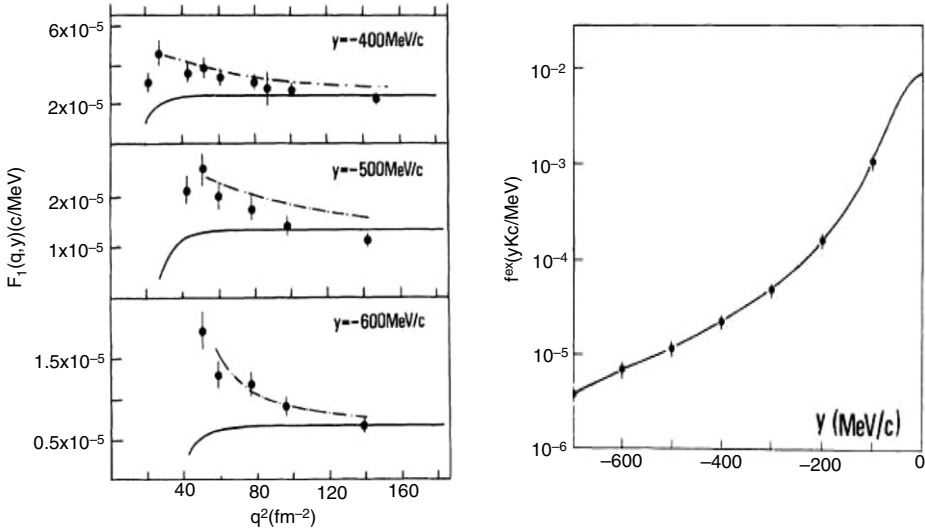


Fig. 41. (Left): the experimental scaling function of the deuteron (see Fig. 40) compared with the PWIA (full line) and the exact calculation which includes the FSI of the pn pair in the continuum [153] (dashed line). (Right): the asymptotic scaling function of the deuteron (Eq. (6.33)) extracted from the inclusive cross sections in Ref. [147].

Source: Reprinted from [147].

© 1984, by the American Physical Society.

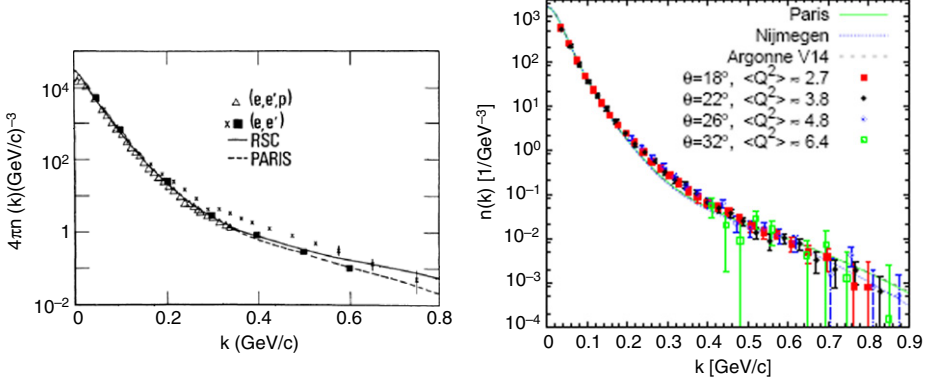


Fig. 42. (Left): the momentum distribution of ${}^2\text{H}$ (Eq. (6.33)) extracted from y -scaling in Ref. [147] (squares); triangles denote the momentum distribution obtained in Ref [153] from the experimental data on exclusive process ${}^2\text{H}(e, e'p)$ [155]; crosses denote the distribution obtained in Ref. [156] using inclusive experimental data [157] without correcting for FSI effects. The theoretical curves represent the momentum distributions obtained with the RSC and Paris interactions, respectively. (Right): the deuteron momentum distributions extracted from recent high statistic experimental data on inclusive scattering at different values of Q^2 and electron scattering angle θ [154].

Source: (Left) Reprinted from [147]. © 1984, by the American Physical Society. (Right) Reprinted from [154]. © 2012, by the American Physical Society.

Therefore, unlike the deuteron case, in case of complex nuclei we can only obtain from the data the scaling function $F(q, y)$, and in order to extract the momentum distributions a recipe is necessary to get, first, the asymptotic scaling function $F_A(y)$, and from this the momentum distribution.

6.2.1. Extracting the nucleon momentum distributions of complex nuclei from y scaling

A recipe, defined “an ingenious procedure” in Ref. [158], has been worked out in Refs. [148,149] as follows. Let us consider the most general case of Y scaling, i.e. Eq. (6.31) written in terms of the general scaling variable $Y = Y(q, v)$. It is trivial to show that, by adding and subtracting a proper term, the structure function (6.31) can be cast in the following general form [149,167]

$$F_A(q, Y) = 2\pi \int_{E_{min}}^{\infty} dE \int_{k_{min}(q, Y, E)}^{\infty} k dk P_A(k, E) = f_A(Y) - B_A(q, Y), \quad (6.37)$$

where

$$f_A(Y) = 2\pi \int_{|Y|}^{\infty} n_A(k) k dk \quad (6.38)$$

represents the *longitudinal momentum distribution* of nucleus A, and

$$B_A(q, Y) = 2\pi \int_{E_{min}}^{\infty} dE \int_{|Y|}^{k_{min}(q, Y, E)} k dk P_1(k, E), \quad (6.39)$$

is the so called *binding correction*, which, through $k_{min}(q, Y, E)$, is governed by the continuum energy spectrum of the final $(A - 1)$ system, unlike $f_A(Y)$, which is integrated over all excited states of $(A - 1)$. The quantities $n_A(k)$ and $f_A(Y)$ are linked by the relation

$$n_A(k) = [df_A(Y)/dY]/[2\pi Y], \quad k = |Y|, \quad (6.40)$$

so that if $f_A(Y)$ could be extracted from the experimental data, $n_A(k)$ could be determined. Up to now, everything was completely general and independent of the specific form of the scaling variable Y. Let us now consider $Y = y$ (Eq. (6.29)). In this case, because of FSI, the quantity $F_A(y)$ can be reached only in the asymptotic limit. In Ref. [148,149] $F_A(y)$ has been obtained by extrapolating to $q \rightarrow \infty$ the available values of $F_{ex}^A(q, y)$, on the basis that FSI can be represented as a power series in $1/q$ and dies out at large q^2 , a conclusion which has been reached by various authors (see e.g. [159,160]), i.e.

$$F_A(q, y) = F_A(y) + F_{(-1)}(y)/q + [F_{(-2)}(y)/q^2 + F_{(-3)}(y)/q^3 + \dots], \quad (6.41)$$

where the first, q -independent term, represents the asymptotic scaling function, and the other, q -dependent terms, include the effects from FSI. At high momentum transfer the terms $F_{(-n)}(y)/q^n$, with $n \geq 2$, go rapidly to zero and it is therefore expected that the effects from FSI are entirely described by the linear term in $1/q$, $F_{(-1)}(y)$. The asymptotic scaling function free from FSI effects has been obtained plotting the experimental scaling function vs. $1/q$ for fixed values of y , and by fitting them with a linear behavior they have been extrapolated to $1/q = 0$. Unfortunately, this is not the whole story since one has also to get rid of the scaling violation due to binding effects. These have been evaluated theoretically within the spectral function of Ref. [114] and $n_{ex(1)}^A(k)$ has been obtained as $n_A(k) = d[F_A(y) + B_A(y)/dy]/[2\pi y]$, $k = |y|$ introducing at this stage a model dependence of the approach. The large errors (up to 60%–70% at high momenta) in the extracted momentum distributions are mainly due to the lack of experimental data at high momentum transfer, that affected the extrapolation procedure of the scaling function. In spite of these errors, the extracted momentum distributions at $k \gtrsim 1.5 - 2 \text{ fm}^{-1}$ turned out to be larger by orders of magnitude than the predictions of the mean field approaches, and in qualitative agreement with realistic many-body calculations which include SRCs. The results are shown in Figs. 43 and 44 where they are compared with various theoretical calculations. These extracted momentum distribution cannot reveal the details of the high momentum components predicted by different NN interactions, but they confirm, for the first time and for complex nuclei, the experimental order of magnitude difference with the MF predictions and the observation of the similarity of the momentum distribution of deuteron and complex nuclei. In order to reduce the model dependence related to the scaling violation introduced by nuclear binding, it has been suggested in Ref. [164] to use a different scaling variable, by stressing that the necessity to introduce appreciable theoretical corrections related to nuclear binding has to be ascribed, to a large extent, to the use of the variable y . As a matter of fact it is clear that a scaling variable can be considered a useful one to the extent of which it has a well defined physical meaning and it can effectively incorporate relevant physical effects of the process under investigation. In this sense the variable y is a very poor one. This is illustrated in the next Subsection, where the more realistic variable proposed in Ref. [164] will be introduced.

6.2.2. The scaling variable $Y = y_{CW} \equiv y_2$

As previously stressed, the scaling variable y represents the minimum momentum component of nucleons *having the minimum value of the removal energy*. This is an unavoidable defect of this variable, because the removal energy is very different for weakly bound, shell-model nucleons ($E_{A-1}^* \sim 0\text{--}20 \text{ MeV}$) and strongly bound, correlated nucleons ($E_{A-1}^* \sim 50\text{--}200 \text{ MeV}$). This leads to the unpleasant situation that at large values of $|y|$ the scaling function is not related to the momenta of strongly correlated nucleons, i.e. those nucleons that almost entirely exhaust the behavior of the scaling function. In order to establish a global link between high momentum components and experimental data, the latter should be analyzed in terms of a scaling variable which could be related, at least on the average, to momenta of both weakly bound and strongly bound nucleons, so as to minimize scaling violation due to binding effects. The approach of Ref. [164–166], recently revisited and improved in Ref. [167–169], shows that this is possible by introducing a scaling variable which properly includes the momentum dependence of the average excitation energy of the nucleus $(A - 1)$ generated by correlations. The mean excitation energy for a given value of k is given by

$$\langle E_{A-1}^*(k) \rangle = \frac{4\pi}{n_1(k)} \int P_1^A(k, E_{A-1}^*) E_{A-1}^* dE_{A-1}. \quad (6.42)$$

This quantity, resulting from realistic Spectral Function for Nuclear Matter and ${}^3\text{He}$, is presented in Fig. 45 (Left), where it can be seen that it practically coincides with the predictions of the Spectral Function of the two-nucleon convolution model of Ref. [114], according to which

$$E_{A-1}^*(\mathbf{k}, \mathbf{K}_{CM}) = \frac{A-2}{A-1} \frac{1}{2m_N} \left[\mathbf{k} - \frac{A-1}{A-2} \mathbf{K}_{CM} \right]^2. \quad (6.43)$$

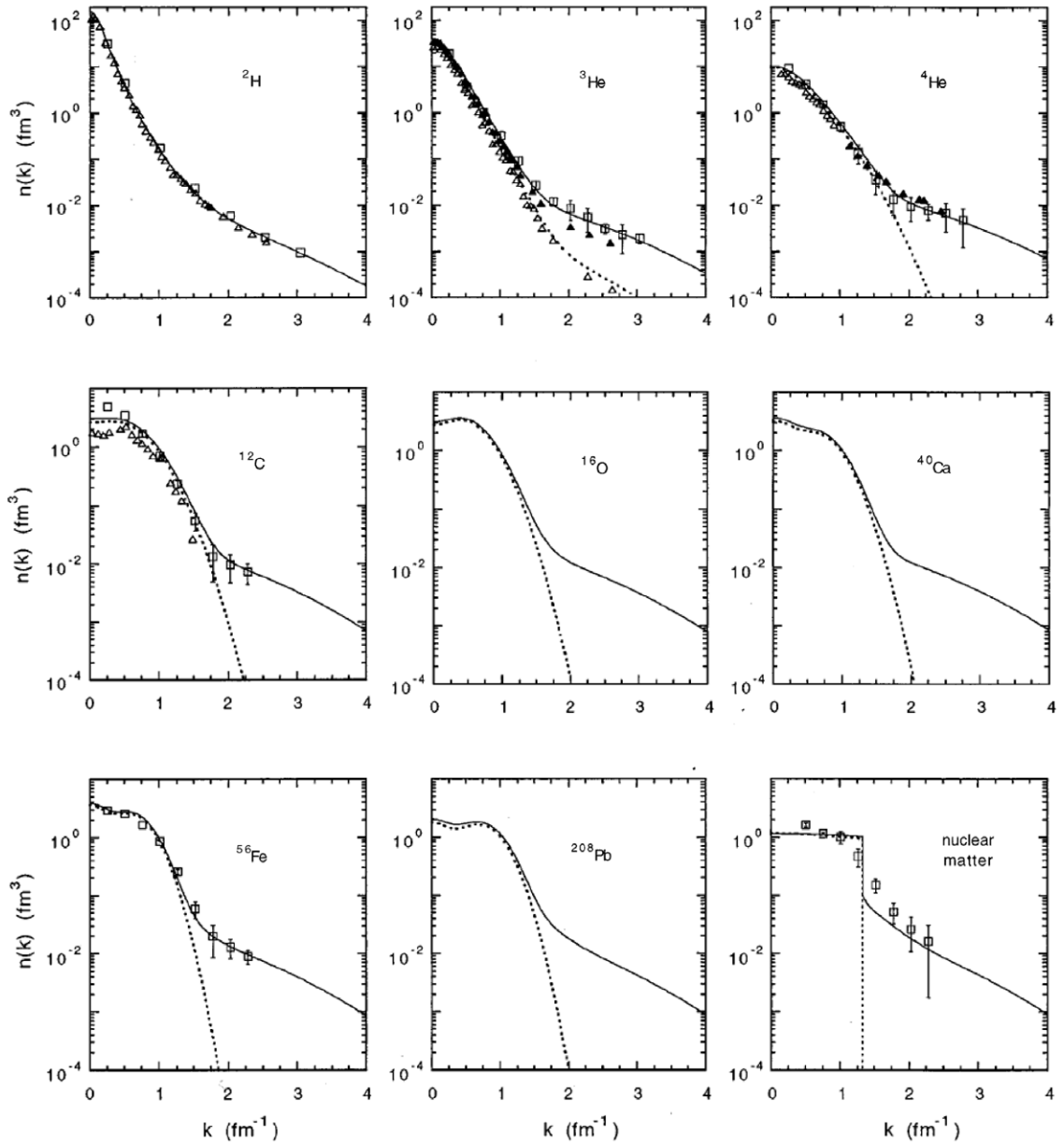


Fig. 43. The momentum distributions of nuclei extracted from y -scaling in Refs. [147–149] with theoretical calculations from various groups (see Ref. [149] for original references). The experimental data obtained from Y -scaling (open squares) are plotted together with data (triangles) obtained from the exclusive process $A(e, e'p)X$ [161–163] to be discussed later on. For ${}^3\text{He}$ both n_{gr} and n_{ex} are shown.

Source: Reprinted from [149]. © by the American Physical Society.

Placing Eq. (6.43) in Eq. (6.42) one obtains

$$\langle E_{A-1}^*(k) \rangle = \frac{A-2}{A-1} T_N + b_A - c_A |\mathbf{k}|, \quad (6.44)$$

where $T_N = (\sqrt{m_N^2 + k^2} - m_N)$, and b_A and c_A arise from the CM motion of the pair ($b_{NM} = 37.3$ MeV and $c_{NM} = 0.04$, for nuclear matter, and $b_3 = -2.94$ MeV $c_3 = -0.03$ for ${}^3\text{He}$). By replacing in Eq. (6.29) $y \rightarrow y_{CW}$, and $M_{A-1} \rightarrow M_{A-1}^* = M_{A-1} + \langle E_{A-1}^*(k) \rangle - \langle E_{gr} \rangle$, a 4th order equation for the new scaling variable y_{CW} is obtained, which, in contrast to previous work [164–166], has been solved numerically in Ref. [167]; this, together with the relativistic extension of the definition of

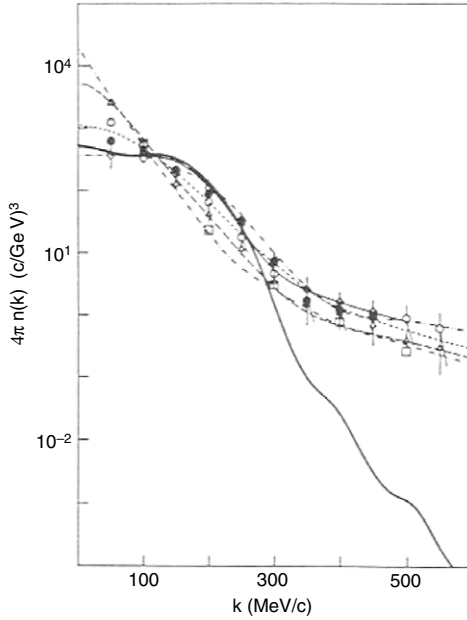


Fig. 44. A graphical summary of the nucleon momentum distributions extracted from y -scaling. Full dots: deuteron; triangles: ${}^3\text{He}$; open dots: ${}^4\text{He}$; open squares: ${}^{12}\text{C}$; crosses: ${}^{56}\text{Fe}$. The extracted momentum distributions are compared with results of many-body calculations and the Hartree–Fock result for ${}^{56}\text{Fe}$ (for reference to the original work see [149]).

Source: Reprinted from [149].

© 1991, by the American Physical Society.

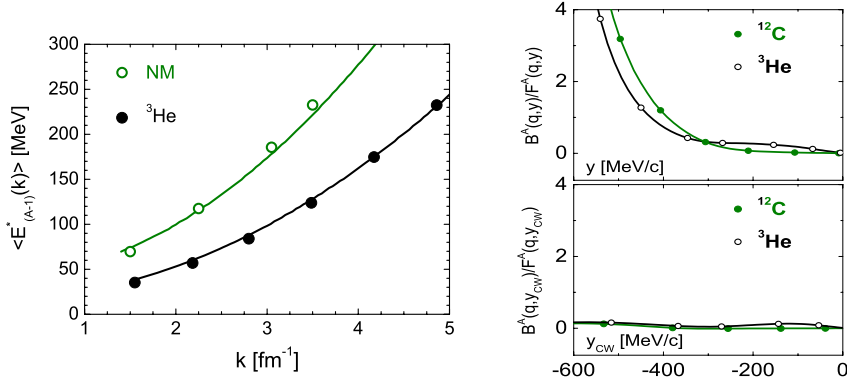


Fig. 45. (Left): the momentum dependence of the average excitation energy of ($A-1$) in ${}^3\text{He}$ and Nuclear Matter. (Right): the ratio of the binding correction (Eq. (6.39)) to the scaling function (Eq. (6.37)) for ${}^3\text{He}$ (open dots) and ${}^{12}\text{C}$ (full dots) calculated with the scaling variable y , representing the minimum momentum of nucleons having the minimum value of the removal energy (upper panel), and with the variable y_{CW} , which effectively includes the average nucleon removal energy via Eq. (6.44) (lower panel).

Source: Reprinted from [167].

© 2009, by the American Physical Society.

the mean excitation energy, is necessary in order to extend y_{CW} to high values.¹⁷ For a large nucleus and not too large values of y_{CW} , one has

$$y_{CW} = -\frac{\tilde{q}}{2} + \frac{\nu_A}{2W_A} \sqrt{W_A^2 - 4m_N^2}, \quad (6.45)$$

Here, $\nu_A = \nu + \tilde{M}_D$, $\tilde{M}_D = 2m_N - E_{th}^{(2)} - b_A + \langle E_{gr} \rangle$, $\tilde{q} = q + c_A \nu_A$ and $W_A^2 = \nu_A^2 - \mathbf{q}^2 = \tilde{M}_D^2 + 2\nu \tilde{M}_D - Q^2$. For the deuteron $y_{CW} = y = -q/2 + (\nu_D/2W_D) \sqrt{W_D^2 - 4m_N^2}$ with $\nu_D = \nu + M_D$ and invariant mass $W_D^2 = \nu_D^2 - \mathbf{q}^2 = M_D^2 + 2\nu M_D - Q^2$,

¹⁷ In previous works [164–166] the 4th order equation has been reduced to an effective 2nd order equation by disregarding several terms which are small only for a heavy nucleus. Note moreover that several misprints, particularly in Ref. [164] are no longer present in Ref. [167]. Let us also stress that all quantities appearing in Eq. (6.44) are not free parameters but results from the average value of $\langle T \rangle$ and $\langle E \rangle$ obtained in many-body calculations.

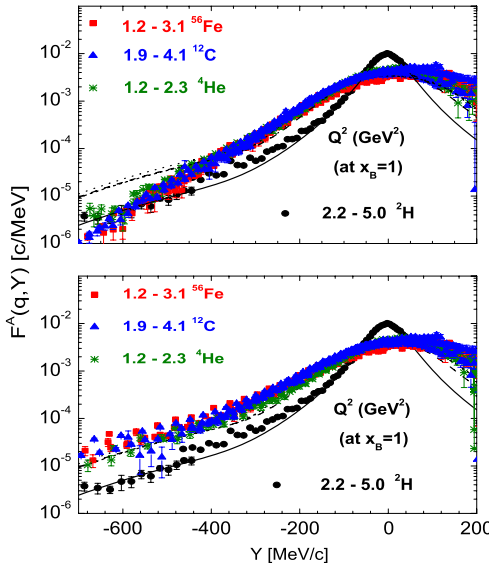


Fig. 46. The experimental scaling function (symbols) for ${}^4\text{He}$, ${}^{12}\text{C}$, and ${}^{56}\text{Fe}$ obtained [167] from the experimental data of Ref. [154,172]. The upper panel shows $F_A(q, Y = y)$ and the lower panel $F_A(q, Y = y_{CW})$. The full, long-dashed, dashed and dotted curves represent the longitudinal momentum distributions $f_A(Y) = 2\pi \int_{|Y|}^{\infty} n_A(k) k dk$ for ${}^2\text{H}$, ${}^4\text{He}$, ${}^{12}\text{C}$ and ${}^{56}\text{Fe}$, respectively, calculated with realistic wave functions.

Source: Reprinted from [167].

© 2009, by the American Physical Society.

for small values of y_{CW} , such that $\frac{A-2}{A-1}(\sqrt{y_{CW}^2 + m_N^2} - m_N) + b_A - c_A|y_{CW}| \ll \langle E_{gr} \rangle$, the variable y , representing the minimal momentum of a weakly bound nucleon, is recovered. Therefore y_{CW} effectively takes into account the k -dependence of E_{A-1}^* , both at low and high values of y_{CW} , and interpolates between the correlated and uncorrelated regions. The scaling function of nucleus A becomes

$$F_A(q, y_{CW}) = 2\pi \int_{|y_{CW}|}^{k_{max}(q, y_{CW})} n_A(k) k dk, \quad (6.46)$$

where the integral over the removal energy no longer appears. Eq. (6.46) can be interpreted as the *scaling function of a nucleon which, at high values of y_{CW} , has removal energy $\langle E_{A-1}^* \rangle$ and is partner of a correlated pair with effective mass M_D* . Thanks to the definition of y_{CW} , binding effects in y_{CW} play a minor role, as clearly illustrated in Fig. 45 which shows that practically $k_{min}(q, v, E) \simeq |y_{CW}|$ and $B^A(q, y_{CW}) \simeq 0$, with two relevant consequences, *viz*: (i) in the asymptotic limit $F_A(q, y_{CW}) \simeq f_A(y_{CW})$ (cf. Eq. (6.37)), and (ii) thanks to (i) it is expected that at high values of y_{CW} , $F^A(q, y_{CW})$ will behave in a way similar to the one of the deuteron and the model dependence of the extraction of the momentum distribution is eliminated. This is fully confirmed by Fig. 46 which, moreover, also shows that whereas $F_A(q, y)$ scales to a quantity which strongly differs from the longitudinal momentum distribution, $F_A(q, y_{CW})$ scales exactly to $f_A(y_{CW})$. This is even better demonstrated in Fig. 47, where the effects of FSI are also illustrated. The left panel shows that: (i) scaling is violated and approached from the top; this is clear signature of the breaking down of the PWIA, which, as previously explained, approaches scaling from the bottom; (ii) the Q^2 dependence of the scaling violation appears to be the same for the deuteron and complex nuclei. To better validate point (ii), in Ref. [167] the scaling functions $F_A(Q^2, y_{CW})$ have been divided by a constant C_A , such as to obtain $F_A(Q^2, y_{CW})/C_A \simeq F^D(Q^2, y_{CW})$. The results are shown in the right panel of Fig. 47 and it can again be seen that at high values of $|y_{CW}|$ all scaling functions scale qualitatively in the same way as the deuteron one. Moreover, the values of the constant C_A are very similar to the values extracted from other types of scaling behaviors, e.g. the scaling of the ratio $R(x_B, Q^2) = 2\sigma_2^A(x_B, Q^2)/A\sigma_2^D(x_B, Q^2)$ [170–172] to be discussed in the next session. FSI has relevant effects on the scaling functions up to $Q^2 \simeq 4\text{--}5 (\text{GeV}/c)^2$ but, most importantly and amazingly, it exhibits a similar Q^2 -dependence in complex nuclei and in the deuteron. Later on other evidences will be presented speaking in favor of a similarity of FSI in complex nuclei and in the deuteron at high values of the momentum transfer. To sum up, a global relativistic scaling variable was proposed which, unlike all previously proposed variables, incorporates the average mean field excitation energy of the $(A-1)$ system, as well as the excitation energy produced by deuteron-like correlated pairs and by their center-of-mass motion in the nucleus. Using such a variable it is possible to establish a more direct link between the scaling function and the momentum distributions of nuclei, without introducing further model dependences related to the removal of binding effects.

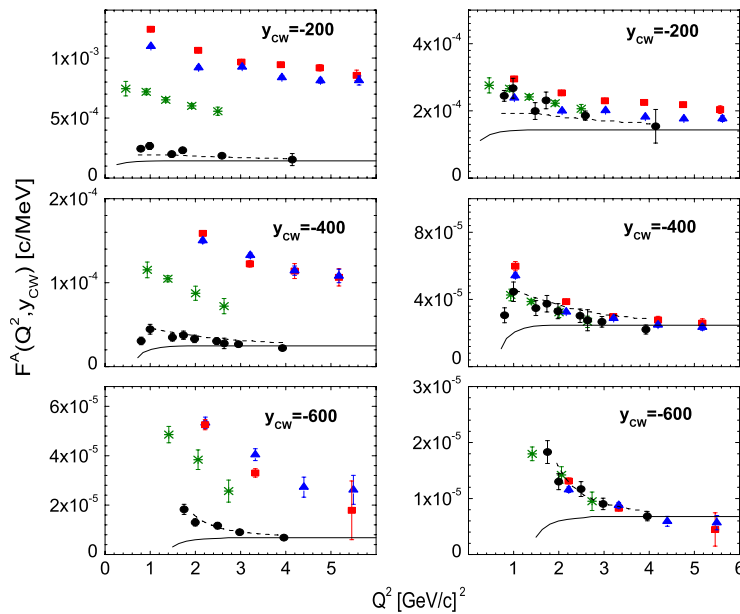


Fig. 47. (Left) The scaling function $F_A(Q^2, y_{CW}) \equiv F^A$ of several nuclei plotted vs. Q^2 at fixed values of y_{CW} (^2H —full dots, ^4He —asterisks, ^{12}C —triangles, ^{56}Fe —squares). (Right) The data for ^4He , ^{12}C and ^{56}Fe shown in the left panel have been divided by the constants $C_4 = 2.7$, $C_{12} = 4.0$ and $C_{56} = 4.6$ for ^4He , ^{12}C and ^{56}Fe , respectively. The theoretical curves refer to ^2H and represent the PWIA results (full) and the results which include the FSI (dashed), both obtained with the AV18 interaction. Scaling variables in MeV/c. The scaling functions have been obtained from the experimental inclusive data from Ref. [154].

Source: Reprinted from Ref. [167].

© 2009, by the American Physical Society.

6.3. The scaling properties of the inclusive cross section: the cross section ratio vs the Bjorken scaling variable

It has been suggested [12] that within the light-cone approach, the inclusive cross sections at proper high values of Q^2 could be represented as an incoherent sum of clusters of correlated nucleons whose number increases with the increase of the Bjorken scaling variable x_B as follows¹⁸

$$\frac{d\sigma}{dx_B dQ^2} \equiv \sigma_A(x_B, Q^2) \simeq \frac{A}{2} a_2(A) \sigma_2(1.5 < x_B < 2, Q^2) + \frac{A}{3} a_3(A) \sigma_3(2 < x_B < 3, Q^2) + \dots, \quad (6.47)$$

where $\sigma_n(x_B, Q^2)$ ($n = 2, 3, \dots, A$) describes the inclusive cross section off a cluster of n correlated nucleons and $a_n(A)$ its weight in the total q.e. cross section off nucleus A . If such an expansion is a correct one, by plotting the ratio

$$r(A, A') = \frac{A'}{A} \frac{\sigma_A(x_B, Q^2)}{\sigma_{A'}(x_B, Q^2)}, \quad (6.48)$$

with $A > A'$, constant values of the ratio (plateaux) should be observed in different regions of x_B , demonstrating the similar structure of SRCs in nuclei A and A' . For example in the case of $A' = 2$ one should observe a plateau in the region $1.5 \lesssim x_B \lesssim 2$ which would indicate that scattering on nucleus A occurred on a pn configuration similar to the deuteron one. The suggestion appears to be an appealing one also in view that, as it has been previously demonstrated, at $x_B > 1.5$ the correlated part of the spectral function plays the major role in q.e. inclusive cross section. Recently these plateaux have been experimentally observed. The first evidence of them has been produced in Ref. [170] by plotting the ratio using for A the inclusive cross section obtained at SLAC for ^3He , ^4He , ^{12}C , ^{27}Al and ^{157}Au in the kinematical region $Q^2 \simeq 1\text{--}3(\text{GeV}/c)^2$, and for A' the cross section for ^2H [138,142–144] (see Fig. 48 referred to the nucleus ^{56}Fe). Experimental data with better statistics for ^3He , ^4He , ^8Be , ^{12}C , ^{63}Cu , ^{56}Fe and ^{197}Au obtained at Jlab have been used to produce ratios using for A' the nuclei of ^3He [171] and ^2H [172], respectively. The results are shown in Fig. 49, where in the (Left) panel three distinct kinematical regions can indeed be observed: (i) the first one, at $x_B \lesssim 1.5$, with a minimum at $x_B \simeq 1$ arises from the coupling of γ^* to mean field nucleons, and its shape is governed by the different behaviors of the magnitude of the q.e. peaks for different nuclei (higher (lower) peaks for lighter (heavier) nuclei); (ii) the second region, at $1.5 \lesssim x_B \lesssim 2$, exhibits a plateau, which is interpreted as due to the coupling of γ^* to a pair of short-range correlated nucleons; (iii) the third region (not visible in Fig. 49 (Right)),

¹⁸ Remember that the maximum value of x_B in a system of n nucleons equals n .

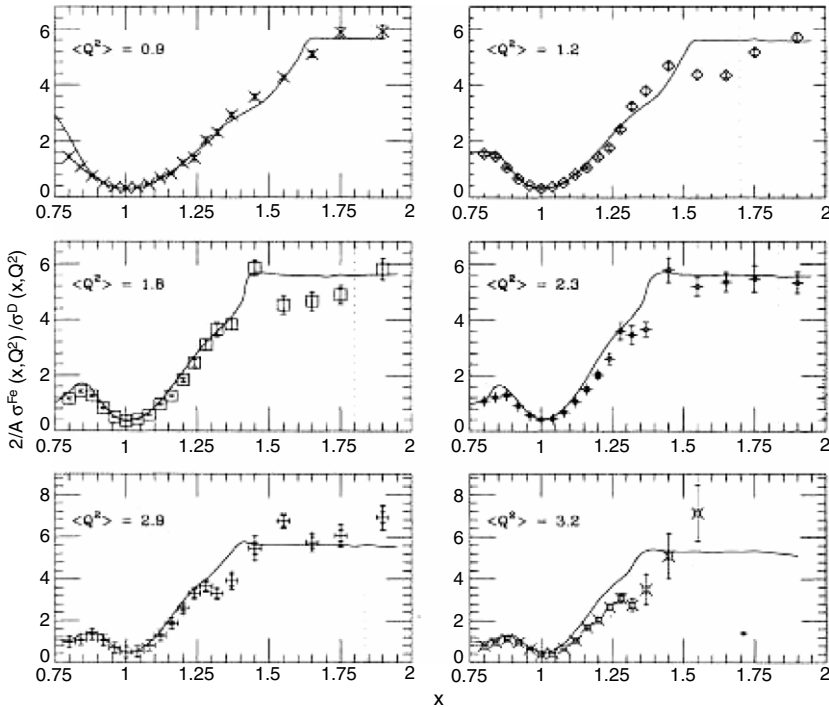


Fig. 48. The ratio of the inclusive cross section off ^{56}Fe to the cross section off ^2He (Eq. (6.48)) produced in Ref. [170] using the experimental data from Refs. [138, 142, 143, 156, 157]. The theoretical curve is discussed in the text.

Source: Reprinted from [170].

© 1993, by the American Physical Society.

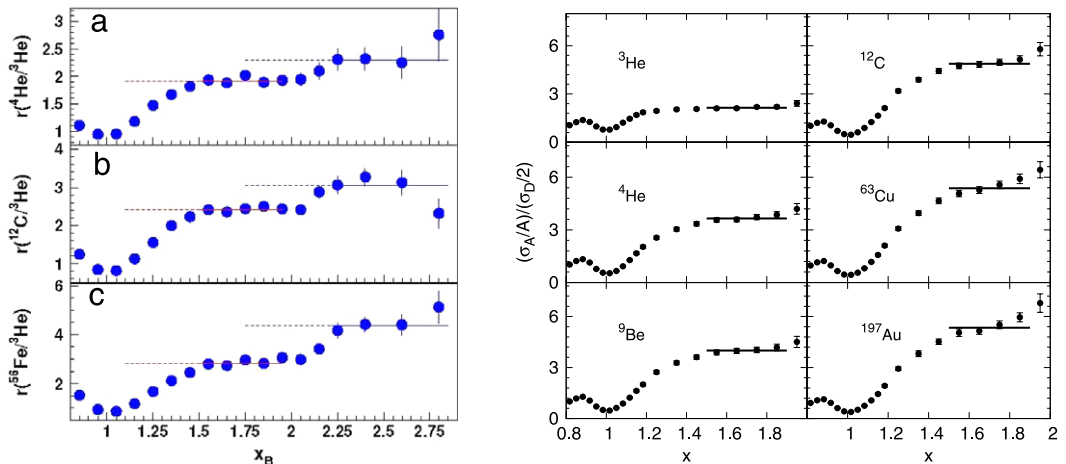


Fig. 49. (Left) The ratio (6.48) obtained at Jlab(CLAS) [171] in correspondence of $A = 4, 12, 56$ and $A' = 3$. The horizontal dotted lines were drawn to highlight the values of the plateaux. (Right): the recent data on Eq. (6.48) obtained at Jlab (E02–019) [172] in correspondence of $A = 3, 4, 9, 12, 63, 197$ and $A' = 2$. The “two-nucleon” plateau is highlighted by the full line.

Source: (Left) Reprinted from [171]. © 2006, by American Physical Society. (Right) Reprinted from [172]. © 2012, by American Physical Society.

at $2.3 \lesssim x_B \lesssim 2.7$, ascribed to the coupling of γ^* to a cluster of three correlated nucleons. The value of the first plateau, ascribed to 2N SRCs, is often denoted by a_2 *viz.*

$$r(A, D) = \frac{2 \sigma_A(1.5 \lesssim x_B \lesssim 2, Q^2)}{A \sigma_D(1.5 \lesssim x_B \lesssim 2, Q^2)} \equiv a_2. \quad (6.49)$$

Table 7 shows the quantity

$$R_{2N}(A) = \frac{r(A, D)}{F_{CM}} \quad (6.50)$$

Table 7

Extracted values of $R_{2N}(A) \equiv R_{2N}$ [172] from SLAC [170] and Jlab(CLAS) [171] data. F_{CM} is a factor introduced [172] in order to correct for the center-of-mass motion of a correlated pair in the nucleus. See Ref. [172] for further detail of the analysis of the experimental data.

Source: Reprinted from Ref. [172].

© 2012, by APS.

A	R_{2N} (E02-019)	SLAC	CLAS	F_{CM}
^3He	1.93 ± 0.10	1.8 ± 0.3	–	1.10 ± 0.05
^4He	3.02 ± 0.17	2.8 ± 0.4	2.80 ± 0.28	1.19 ± 0.05
Be	3.37 ± 0.17	–	–	1.16 ± 0.05
C	4.00 ± 0.24	4.2 ± 0.5	3.50 ± 0.35	1.19 ± 0.05
Cu(Fe)	4.33 ± 0.28	(4.3 ± 0.8)	(3.90 ± 0.37)	1.20 ± 0.05
Au	4.26 ± 0.29	4.0 ± 0.6	–	1.21 ± 0.06
(Q^2)	$\sim 2.7 \text{ GeV}^2$	$\sim 1.2 \text{ GeV}^2$	$\sim 2 \text{ GeV}^2$	
x_{\min}	1.5	–	1.5	
α_{\min}	1.275	1.25	1.22–1.26	

where F_{CM} is a theoretical quantity which is intended to take into account the c.m. of a deuteron-like pn pair in the nucleus. Several interpretation exist in the literature concerning the physical meaning of a_2 going from the *per nucleon probability of $2N$ SRCs in nucleus A with respect to the deuteron*, to the ratio between the momentum distribution of nucleus A to the momentum distributions of the deuteron. The experimental meaning of a_2 is actually the ratio of inclusive cross sections in the region of nucleon momenta sensitive to SRCs. We have however seen that the q.e. cross sections depends upon the spectral functions and not upon the momentum distributions, moreover we have also seen that in the region of the q.e. cross sections sensitive to SRCs the effects of the FSI cannot be disregarded, so that a microscopic interpretation of the quantity a_2 would require a full calculation of the q.e. cross section including FSI effects. Therefore let us first discuss the latter which, apart from the deuteron case, is unavoidably based upon model assumptions.

6.4. The final state interaction (FSI) in inclusive scattering

Unlike what frequently stated in the past, FSIs do affect inclusive quasi-elastic scattering: their presence has been unambiguously inferred from the Q^2 behavior of the Y -scaling function (cf. Fig. 47), as well as by the missing strength exhibited by the inclusive cross at low values of v ($v < v_0, x_B > 1$) (cf. Fig. 36). The theoretical evaluation of FSI in inclusive scattering is in principle a very difficult task since it implies the calculation of the following transition amplitude

$$|T_{f0}|^2 \propto \sum_f \left| \langle \Psi_A^f(1, \dots, A) | \hat{O} | \Psi_A^0(1, \dots, A) \rangle \right|^2 \delta(\varepsilon_0 - \varepsilon_f), \quad (6.51)$$

involving the full energy spectrum of the target nucleus. The quantity (6.51) can be calculated exactly only for the two-body system, whereas for complex nuclei approximations are unavoidable. These, if properly justified, can in principle provide a reasonable approximation for T_{f0} because in particular kinematical ranges not all of the final state wave functions will appreciably contribute to the transition matrix element. Let us briefly illustrate and critically discuss two approximations that have been used to calculate the effects of the FSI in inclusive scattering at high momentum transfer. To this end, let us come back to Eq. (6.24). In Ref. [173] a detailed and systematic calculation of FSI in q.e. scattering off nuclear matter, described by the spectral function of Ref. [108], has been presented. In these calculations, based essentially upon the eikonal approximation and Glauber approach (GA) to multiple scattering, the struck nucleon propagates along a straight trajectory, oriented along the momentum transfer \mathbf{q} and interacts with the other $(A-1)$ nucleons, whose configuration is frozen during the passage of the struck particle.¹⁹ With respect to the original GA, in the approach of Ref. [173], called there *correlated Glauber approach (CGA)*, an important improvement has been worked out, by considering the effects of SRCs in the scattering process, taking into account, to this end, the presence of the correlation hole. Let us show this in a simple way. It is well known that if in the usual GA, where SRCs are neglected, the absorptive imaginary part of the optical potential is obtained in the form

$$W(p) = \frac{\hbar}{2} \rho v(q) \sigma_{NN}(p), \quad (6.52)$$

whereas within the CGA one obtains [173]

$$W(p, z) = \frac{\hbar}{2} \rho v(p) \sigma_{NN}(q) \frac{1}{z} \int_0^z dz' g(z'). \quad (6.53)$$

Here ρ is the nuclear density, $v(p)$ the nucleon velocity, σ_{NN} the NN free total cross section and $g(r_{12})$ is defined by the correlated two-body density $\rho_2(1, 2) = \rho(1)\rho(2)g(r_{12})$ where $g(r_{12})$ takes care of SRCs. The results of the PWIA of the

¹⁹ In a correct Glauber treatment the z-axis should be directed along the momentum of the struck nucleon. It turns out that even at relatively large values of $|\mathbf{q}|$ the choice of the z-axis along \mathbf{q} cannot be justified. See e.g. Ref. [209].

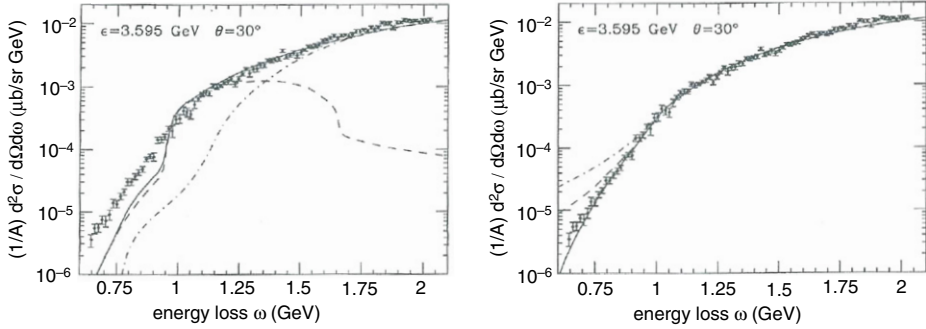


Fig. 50. The inclusive cross section of the scattering of 3.359 GeV electrons off nuclear matter. The experimental data have been obtained in Ref. [140] by extrapolating the experimental data for heavy nuclei and the theoretical calculations, based on the nuclear matter spectral function of Ref. [108] are from Ref. [173]. In the (Left) panel the PWIA results are shown. The dashed line represents the quasi-elastic contribution and the dot-dashed line the inelastic and deep inelastic contributions; the full line is the sum of the two (cf. these results with the ones presented in Figs. 37 and 38). The (Right) panel shows the effects of the FSI. The dot-dashed line results from the usual optical potential treatment of FSI (Eq. (6.52)) and the dashed line from the consideration of the correlation hole amongst the spectator ($A - 1$) nucleons; finally the full line is obtained by replacing the free σ_{NN} cross section by a phenomenological cross section which include the effects of color transparency.

Source: Reprinted from [173].

© 1991, by the American Physical Society.

q.e. cross section for nuclear matter are shown in Fig. 50 (Left) and the strong discrepancy at low ν ($x \gtrsim 1.5$), encountered also in the calculations of q.e. scattering off complex nuclei performed with the convolution model of the spectral function, is evident (cf. Figs. 37 and 38). In the same figure (Right) the results corresponding to the GA and CGA approximations are also shown: it can be seen that GA strongly overestimates the cross section whereas the CGA improves the situation without providing, however, a reasonable agreement with the experimental data at low values of ν . Within the approach of Ref. [173], any effect at low value of ν ($x_B > 1$) that reduces the NN cross section σ_{NN} should also reduce the inclusive cross section. To this end in Ref. [173] the NN cross section has been reduced by introducing the effects of color transparency (CT) (see Section 7), obtaining the good agreement shown by the full line in Fig. 50 (Right). CT is a phenomenon related to the quark structure of nucleons that can hardly be seen in q.e. scattering at these kinematics, where the dominant degrees of freedom are the nucleon ones. The explanation in term CT appears therefore notwithstanding. This has been realized in a following paper [174] where a new, more realistic effect to bring experiments and theory in agreement has been introduced by derivation of an in-medium NN cross section which exhibits a strong reduction with respect to the free one, obtaining an agreement with the experimental data of the same quality as shown in Fig. 50 (right). To sum up, in the approach of Refs. [173, 174] the struck nucleon, a MF or a correlated one, propagates in the medium of correlated frozen nucleons interacting with them with a reduced effective on-shell cross section different from the free NN one. In this connections, it should be pointed out that when in-medium effects are considered, one inevitably is facing the problem related to the fact that at large value of $x_B > 1$ nucleons are far off-shell (see e.g. Refs. [175–177]). It should also be added that when FSI is considered within the GA, unitarity is not satisfied because of the lack of inelastic processes (see Ref. [14] and a clear example of this given in Ref. [178], where the FSI in the process ${}^2\text{H}(e, e')X$ was calculated within the GA and within an exact Schrödinger approach, obtaining rather different results). The second approach to FSI we would like to discuss is from Ref. [179]. It was inspired by the structure of the lepton–nucleus inclusive cross section so far considered, i.e. an incoherent sum of a MF and a SRC contribution. Accordingly, the FSI was split into a MF and a SRC parts. This appears to be also justified by the observation that the FSI of a high momentum nucleon, that was partner in a correlated pair, should in principle differ from the one of a low momentum, mean-field nucleon propagating in a medium of uncorrelated nucleons: in the first case the struck nucleon is more prone to interact with the correlated partner rather than with the ($A - 2$), MF nucleons, whereas a struck MF nucleon will mainly “feel” the average single particle potential. This is somehow equivalent to the argument of Ref. [14] where it has been shown that the distance the struck nucleon should travel before the first interaction is very short for a high momentum correlated nucleon (see Ref. [13] for further discussions on this point). Guided by these arguments two types of FSI have been considered in Ref. [179]: for a strongly deuteron-like correlated pair the FSI was taken care of by the exact solution of the 2N problem in the continuum, by solving the Schrödinger equation with the same NN interaction used to obtain the ground-state wave function, taking into account, moreover, the c.m. motion of the pair; for a MF off-shell nucleon the FSI was assumed to be that generated by an off-shell optical potential. Accordingly, as pictorially represented in Fig. 51, the inclusive cross section has been separated in the correlated and uncorrelated parts as follows

$$\frac{d\sigma}{dx_B dQ^2} = \sigma_0^{(A)}(x_B, Q^2) + \sigma_1^{(A)}(x_B, Q^2), \quad (6.54)$$

where

$$\sigma_0^{(A)}(x_B, Q^2) = |(a) + (d)|^2 \quad \sigma_1^{(A)}(x_B, Q^2) = |(b) + (c)|^2, \quad (6.55)$$

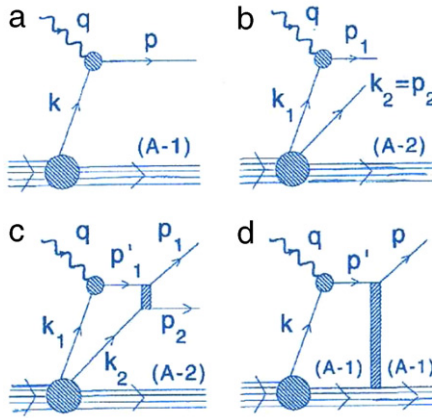


Fig. 51. Cartoons of the various contributions representing the PWIA and the FSI contributions to the q.e. inclusive cross section, according to the model of Ref. [179]. (a) PWIA in the mean field; (b) PWIA in the correlated pair; (c) FSI in the correlated pair; (d) FSI in the mean field.
Source: Reprinted from Ref. [179].

© 1994, by the American Physical Society.

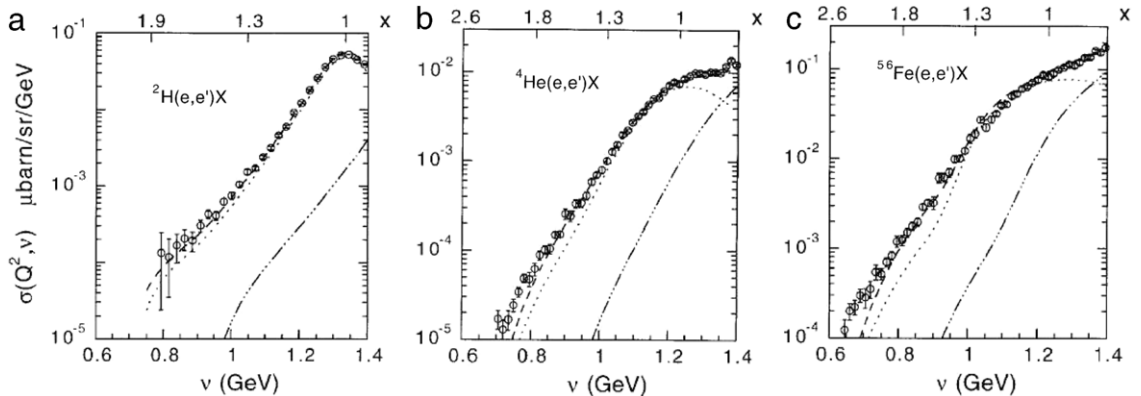


Fig. 52. The effects of the FSI on the inclusive cross section of ${}^2\text{H}$, ${}^4\text{He}$ and ${}^{56}\text{Fe}$ at $Q^2 \simeq 2.3 (\text{GeV}/c)^2$ vs the energy transfer v and the Bjorken scaling variable x_B , according to the model of Ref. [179]. Dotted line: PWIA (Fig. 51, $(|a|^2 + |b|^2)$). Dashed line: the effects of including the FSI between the two nucleons of the correlated pair, described by the exact solution of the continuum Schrödinger equation for two interacting nucleons is included (Fig. 51, $(|a|^2 + |b + d|^2)$). Dot-dashed curve: contribution of inelastic and deep inelastic channels. Experimental data from [157,142].
Source: Reprinted from [179].

© 1994, by Elsevier.

with $\sigma_0^{(A)}(x_B, Q^2)$ describing the scattering from mean-field nucleons and $\sigma_1^{(A)}(x_B, Q^2)$ the scattering from a pair of correlated nucleons. The latter is given by

$$\sigma_1^{(A)} = A\sigma_{\text{Mott}} \sum_{N_1, N_2 = n, p} \int d\mathbf{k}_{CM} n_{CM}^{N_1 N_2}(\mathbf{k}_{CM}) L^{\mu\nu} W_{\mu\nu}^{N_1 N_2}, \quad (6.56)$$

where $L_{\mu\nu}$ is the usual leptonic tensor and

$$W_{\mu\nu}^{N_1 N_2} = \sum_{f_{12}} \sum_{\beta_{12}} [\langle \beta_{12} | j_\mu^{N_1} + j_\mu^{N_2} | f_{12} \rangle]^* \sum_{\beta'_{12}} [\langle \beta'_{12} | j_\nu^{N_1} + j_\nu^{N_2} | f_{12} \rangle] \times \delta[v + k_{CM}^0 - \sqrt{(M_2^{f_{12}})^2 + (\mathbf{k}_{CM} + \mathbf{q})^2}], \quad (6.57)$$

is the hadronic tensor which includes the FSI; here β is the relative wave function of a correlated pair in the nucleus ground state and f_{12} the continuum wave function of the interacting nucleons, i.e. the solution of the Schrödinger equation in the continuum. The quantity (6.56) describes therefore the FSI of an interacting NN pair moving with *c.m.* momentum $\mathbf{K}_{c.m.}$. It should be stressed that $\sigma_1^{(A)}$ is totally free from adjustable parameters. The results of calculations which include FSI only in the correlated pair in σ_1^A , shown in Fig. 52, demonstrate that: (i) the agreement in the deuteron case is excellent, as it should be since when $A = 2$ the above approach is based upon the exact calculation of the transition matrix element between the ground and excited states of the deuteron, and (ii) for a complex nucleus the experimental data in the range $1 < x < 2$,

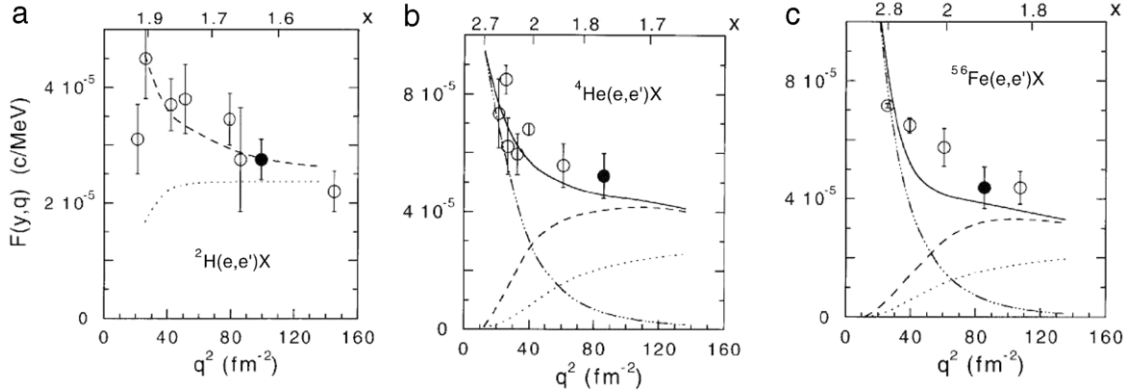


Fig. 53. The effects of the FSI on the scaling function of the inclusive cross section according to the model of Ref. [179]. The value of y is fixed at $y = -0.400$ (GeV/c). Dotted line: PWIA (Fig. 51, $(|a|^2 + |b|^2)$). Dashed line: two-nucleon correlation contribution (Fig. 51, $(|b| + |c|^2)$). Dot-dashed line: Mean Field contribution (Fig. 51, $(|b| + |d|^2)$). Full line: PWIA plus full FSI (Fig. 51, $(|a| + |c|^2 + |b| + |d|^2)$). The experimental points denoted by a full dot, correspond to the kinematics of Fig. 52 with $v = 0.86, 0.82, 0.78$ GeV for ${}^2\text{H}$, ${}^4\text{He}$ and ${}^{56}\text{Fe}$, respectively.

Source: Reprinted from [179].

© 1994, by Elsevier.

are very well explained, whereas at $x > 2$ a missing cross section is still present, which might be ascribed to the lack of three-nucleon correlations in the spectral function that has been used in the calculations. The FSI in the cross section $\sigma_0^{(A)}$ has been described by the multiple scattering of the struck off-shell nucleon in the spectator ($A - 1$) systems composed of MF nucleons, i.e. in terms of the following optical potential

$$V_{opt} = -\rho v_N \sigma_{NN} (i + \alpha) \exp[-\delta(m_N^2 - p'^2)], \quad (6.58)$$

where

$$p'^2 \simeq (v + m_N - E)^2 - (\mathbf{k} + \mathbf{q})^2 \neq m_N^2, \quad (6.59)$$

represents the off-shellness of the struck nucleon affecting V_{opt} . Off-shell effects, as expected from general considerations, reduce the in-medium NN cross by an amount depending on the degree of off-shellness, governed in this approach by the parameter δ ; although this is not an adjustable parameter for single nuclei, but it has a unique value for all nuclei considered, the exponential form of the off-shellness function lacks of deep theoretical justifications, although it was previously advocated in Refs. [175–177]. In Fig. 53 the full calculation of the cross section is shown on the example of the scaling function. It can be seen that off-shell effects brings the distorted MF cross section to zero at $x_B \lesssim 2$, where the effects of FSI is entirely exhausted by the FSI of the initially correlated NN pair. Having described the effects of the FSI in the two models, let us come back to the ratio of inclusive cross sections vs x_B . Here essentially only calculations from three different groups are available. In Ref. [170] an approximate light-cone approach allowed the use of the closure approximation thus reducing the ratios of cross sections to the ratios of the momentum distribution of nuclei A and A'. Approximating the latter with non relativistic momentum distributions with $n_A(k) \simeq C_A n_D(k)$, the coefficient C_A was found and interpreted as the ratio of the momentum distributions in A and A'. It is not surprising that the ratio of the cross section found in y_{CW} scaling (see Section 6.1.2) is similar to the one found in Ref. [170]. In this connection it has to be stressed that the inclusive cross sections, within a non relativistic Schrödinger equation approach depend upon the spectral function and, in the region of $x_B \geq 1$, they are appreciably affected by FSI. The latter has been taken into account, together with the spectral function, in the calculation of the ratios presented in Refs. [180] and [181]. In the first paper the convolution model of the spectral function and the approach to the FSI of ref. [179], respectively, have been adopted. The results pertaining to ${}^{56}\text{Fe}$ are presented in Fig. 54. It can be seen that a plateau is qualitatively reproduced at high values of Q^2 with a value ($\simeq 4.33 \pm 0.28$) which, again, practically coincides with the value ($C_{56} \simeq 4.6$) obtained from recent experimental data (cf. Table 7), but which, at the same time, as in the case of the scaling function (cf. Fig. 47), includes a non negligible contribution from FSIs. The results of Ref. [181], shown in Fig. 55, are based upon the LDA spectral function and the model of FSI of Ref. [173] and, again, the effect of the FSI turns out to be large and, moreover, the x_B behavior, unlike the results of Ref. [180], does not quite remember a plateau, the reason probably being due to the treatment of FSIs. To sum up, from the analysis of the scaling properties of inclusive scattering it appears that: (i) the value of the constant ratio extracted from y -scaling and from the cross section ratio are almost the same; (ii) the separate inclusive cross section off nucleus A and the deuteron are strongly affected by FSI, which is demonstrated in a model independent way by y_{CW} scaling (cf. Fig. 47); (iii) the observed plateaux both in y_{CW} scaling and the cross section ratio, is strong evidence that the FSI in the correlation region is similar in complex nuclei and in the deuteron; (iv) further microscopic calculations seems to be necessary in order to fully clarify the microscopic structure of the quantity a_2 .

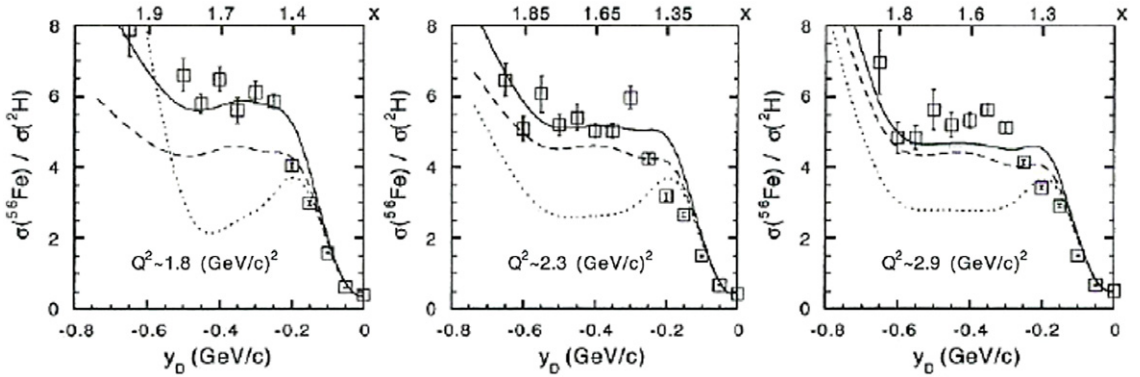


Fig. 54. The effect of SRCs and FSI on the ratio of the inclusive cross sections off ^{56}Fe to the cross section off ^2H at $Q^2 \simeq 1.8, \simeq 2.3, \simeq 2.9 \text{ (GeV}/c)^2$ obtained from an analysis of the experimental data of Refs. [157, 142] and plotted vs. $x_B \equiv x$ and the deuteron scaling variable y_D . Calculations have been performed with the convolution model of the spectral function and a treatment of FSI as in Ref. [179]. Dotted line: PWIA (Fig. 51, $|(a)|^2 + |(b)|^2$); Dashed line: PWIA + two-nucleon rescattering (Fig. 51, $|(a)|^2 + |(b)|^2 + |(c)|^2$). Full line: PWIA+ full FSI (Fig. 51, $|(a) + (d)|^2 + |(b) + (c)|^2$).

Source: Reprinted from [180].

© 1994, by World Scientific.

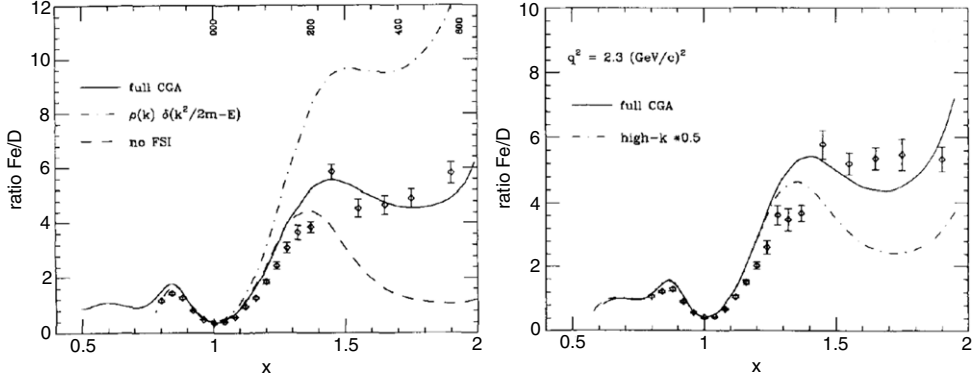


Fig. 55. The ratio of the inclusive cross section off ^{56}Fe to the cross section off ^2H at $Q^2 \simeq 1.8 \text{ (GeV}/c)^2$ (Left) and $\simeq 2.3 \text{ (GeV}/c)^2$ (Right) obtained in Ref. [181] from an analysis of the experimental data of Ref. [157, 142]. Calculations performed within the LDA spectral function and the FSI model of Ref. [173]. The dashed curve in the (Left) panel represents the PWIA and the dot-dashed curve has been obtained within the strict two-nucleon correlation model when $P_A(k, E) = n_A(k)\delta(E - k^2/2m_N)$. Note that the PWIA result is similar to the one of Fig. 54, so that the differences between the full lines in the two figures should be ascribed to the different treatment of FSI. The dot-dashed curve in the (Right) panel has been obtained by reducing by a factor 0.5 the high momentum content of the spectral function. It can be seen that the theoretical ratio does not resemble a plateau at $x_B \equiv x \gtrsim 1.5$ and it is moreover appreciably affected by FSI.

Source: Reprinted from [181].

© 1995, by Elsevier.

6.5. The exclusive $A(e, e'N)X$ and $A(e, e'N_1N_2)X$ processes and SRCs

The exclusive processes in which one or two-nucleons are detected in coincidence with the scattered lepton, i.e. the processes $A(e, e'N)X$ and $A(e, e'N_1N_2)X$, have provided recent information on two-nucleon SRCs. In the $A(e, e'N)X$ process, a bound nucleon N , with momentum \mathbf{k}_1 , acquiring a three-momentum \mathbf{q} transferred by the virtual photon γ^* , makes a transition to the continuum with momentum \mathbf{p}_1 , and the final nucleus X recoils with three-momentum \mathbf{P}_{A-1} and energy $E_{A-1}^f = M_{A-1} + E_{A-1}^*$, where E_{A-1}^* is the intrinsic excitation energy of $(A-1)$. One has

$$\mathbf{q} = \mathbf{p}_1 + \mathbf{P}_{A-1}, \quad (6.60)$$

and momentum and energy conservation read

$$\nu + M_A = \sqrt{\mathbf{p}_1^2 + m_N^2} + \sqrt{\mathbf{P}_{A-1}^2 + (M_{A-1}^f)^2}. \quad (6.61)$$

In the description of the process it is useful to introduce the following measurable kinematical quantities, namely the *missing momentum*

$$\mathbf{p}_m = \mathbf{q} - \mathbf{p}_1 = \mathbf{P}_{A-1}, \quad (6.62)$$

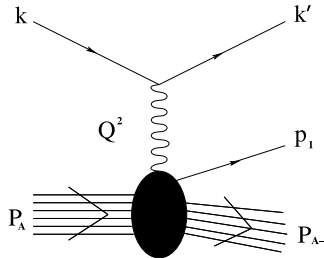


Fig. 56. The Feynman diagram describing the process $A(e, e'p)X$ leading to the cross section (6.64).

and the *missing energy*

$$E_m = \sqrt{P_{A-1}^2} + m_N - M_A = m_N + M_{A-1} - M_A + E_{A-1}^f = E_{\min} + E_{A-1}^f = v - T_p - T_{A-1}. \quad (6.63)$$

In the one-photon-exchange approximation, corresponding to the Feynman diagram of Fig. 56, the differential cross section is given by [133]

$$\frac{d^6\sigma}{d\Omega'd\epsilon' d^3\mathbf{p}_m} = \sigma_{Mott} \sum_{i=1}^4 V_i W_i^A(v, Q^2, \mathbf{p}_m, E_m), \quad (6.64)$$

where $i \equiv \{L, T, LT, TT\}$ are the nuclear structure functions (or nuclear responses) with V_L , V_T , V_{LT} , and V_{TT} being the corresponding kinematical factors. Here L , T , LT and TT denote the longitudinal, transverse, longitudinal-transverse and transverse-transverse contribution to the cross section [133]. As in the case of inclusive scattering, the evaluation of the nuclear responses W_i^A requires the knowledge of both the nuclear vectors $|\alpha_A \mathbf{P}_A\rangle$ and $|\alpha_N \mathbf{p}_1, \alpha_{A-1} \mathbf{P}_{A-1} E_{A-1}^f\rangle$ and the nuclear current operators $\hat{j}_\mu^A(0)$.²⁰ The PWIA approximation (cf. Fig. 35), in which

$$\mathbf{p}_1 = \mathbf{k}_1 + \mathbf{q} \quad \mathbf{p}_m = \mathbf{q} - \mathbf{p}_1 = -\mathbf{k}_1, \quad (6.65)$$

allows one to express the nuclear current operator as sum of one-body nucleon operators with the cross section assuming the following factorized form (for details see, e.g., Ref [133]).

$$\frac{d^6\sigma}{d\epsilon' d\Omega' d\mathbf{p}_m} = \mathcal{K}(v, Q^2, v, \mathbf{p}_m) \sigma_{eN}(\bar{Q}^2, \mathbf{p}_m) P_A^N(|\mathbf{k}_1|, E). \quad (6.66)$$

Here \mathcal{K} is a kinematical factor, $\sigma^{eN}(\bar{Q}^2, \mathbf{p}_m)$ is the cross section describing electron scattering by an off-shell nucleon, whose off-shellness, ($k_1^2 \neq m_N^2$)²¹ is implemented in the nucleon four-momentum $\bar{Q}^2 = \mathbf{q}^2 - \bar{q}_0^2 \quad \bar{q}_0 = q_0 + M_A - \sqrt{(\mathbf{k}_1^2) + (M_{A-1}^f)^2} - \sqrt{\mathbf{k}_1^2 + M_N^2}$.

Thus, unlike the inclusive $A(e, e')X$ case, in exclusive $A(e, e'p)X$ scattering the energy and the momentum of the final $(A-1)$ state are measurable quantities and, consequently, the cross section in PWIA depends directly upon the nucleon spectral function $P_A^N(k, E) = P_0^N(k, E) + P_1^N(k, E)$. As explained in the previous sections, SRCs affect the spectral function in two different ways: (i) a decrease of the MF occupation probability, in P_0^N , and the occupation of states characterized by high values of the removal energy and momenta, in P_1^N , and (ii) the creation of high momentum and high removal energy components. The search for SRCs effects in $A(e, e'p)X$ processes lasted for more than fifty years, with discouraging results, that turned out into optimistic views only recently. To summarize the search for SRCs, we illustrate in Fig. 57 the “history” of the reaction $^{12}\text{C}(e, e'p)X$ [182]. The first pioneering experiment on the reaction $^{12}\text{C}(e, e'p)X$ was performed in 1966 at the electro-synchrotron of the Frascati National Laboratories of the Italian National Institute for Nuclear Physics (INFN) [183]. The energy resolution in the experiment was very low, which resulted in the spectrum shown in Fig. 57 (top panel), where the two maxima located at $E_{^{11}\text{B}^*} \simeq 16$ MeV and $\simeq 36$ MeV were identified, by measuring the angular distributions of the detected protons, as resulting from the knock-out of protons from the $1p$ and $1s$ shells, in agreement with the simplest shell model picture of ^{12}C . Twenty years later a second milestone was represented by an experiment performed at NIKHEF, Holland, where a very narrow interval of removal energy was investigated at very high energy resolution [184], as shown in Fig. 57 (middle panel), demonstrating the limits of the naive shell model by identifying final states of ^{11}B arising from configuration mixing within the unfilled $1p$ shell, e.g. the population of the $1p_{1/2}$ shell, which is empty in the naive single particle shell model. This experiment also provided partial, very qualitative evidence of possible indirect effects from SRCs since the number of p -shell protons participating in the process turned out to be sensibly less than the shell model value, i.e. $Z_{1p} = 4$, and even less of any theoretical prediction based on mean field approaches (cf. Table in Fig. 58). However, in this

²⁰ α_i denotes the set of quantum numbers of the nucleon, the systems A and the system $(A-1)$.

²¹ Here k_1^2 denotes the squared four-momentum of the bound nucleon.

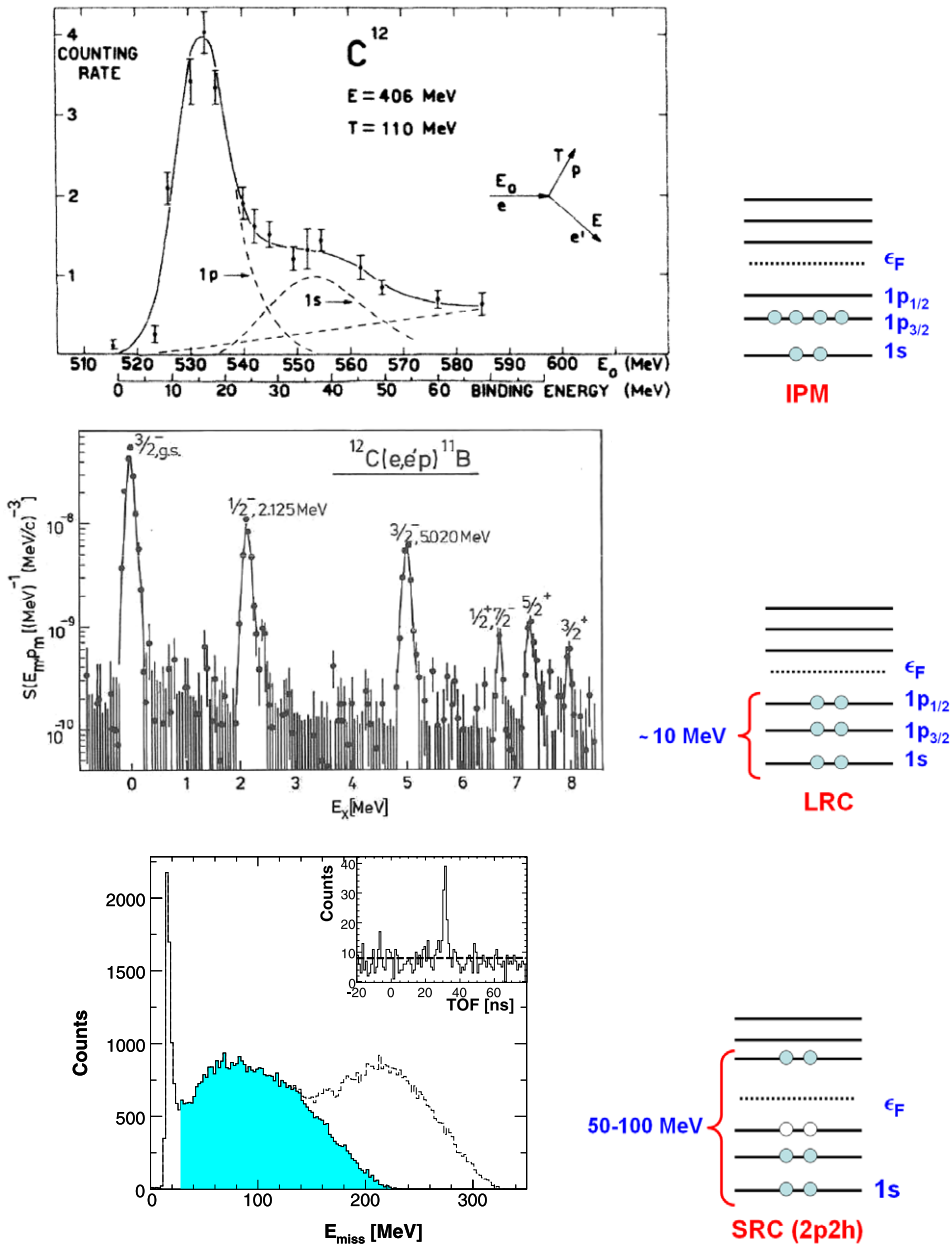
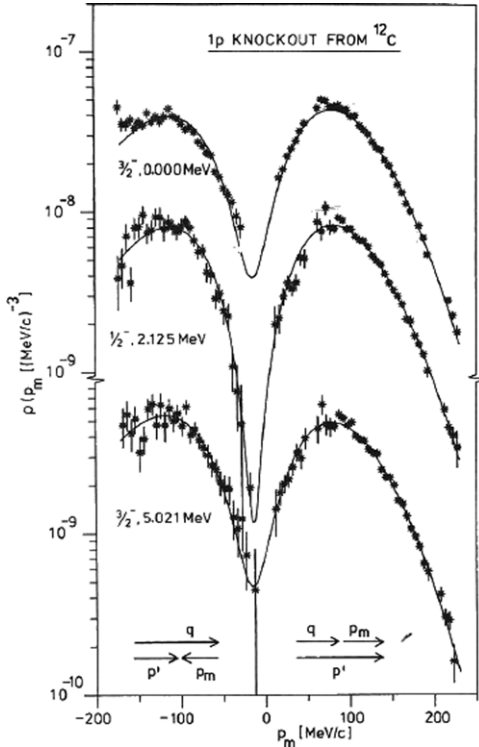


Fig. 57. The process $A(e, e'p)X$ from its birth to present days is illustrated in the figures from top to bottom. Top panel: the first experimental data at low energy resolution obtained in 1966 at the National Frascati Laboratory of INFN, demonstrating the basic shell-model structure of ^{12}C [183]. In the figure the counting rate is plotted vs. the energy of the beam $e \equiv E_0$ and the removal energy $E \equiv \text{Binding energy}$. Middle panel: the NIKHEF high resolution data obtained in 1988 in the range of excitation energy of ^{11}B equal to $0 \leq E_x \equiv E_{11\text{B}}^* \leq 8$ MeV, providing evidence of the spin-orbit single particle potential and the presence of long-range correlations which redistribute the p-shell nucleons within the $p_{3/2}-p_{1/2}$ sub-shells [184]. Bottom panel: the recent data obtained in 2006 at Jlab [249] in the missing energy range $0 < E_m \lesssim 200$ MeV demonstrating the presence of 2p-2h virtual excitations in the ground state of ^{12}C originating from SRCs.

Source: (Top panel) Reprinted from [183]. © 1996, by the American Physical Society. (Middle panel) Reprinted from [184]. © 1988, by Elsevier. (Bottom panel) Reprinted from [249]. © 2006, by the American Physical Society.

connection, it should be stressed that these results have to be taken with due care, because the extraction of the occupation numbers in the analysis of Ref. [184] suffered from several model assumptions, particularly related to the model treatment of the FSI; anyway, the low value of the occupation numbers could in principle also be interpreted as a possible evidence that part of the strength shifted to higher values of removal energies. This work has stimulated, during the following years, extensive experimental studies through the Periodic Table, that provided very important and systematic information on the properties of single particle states in nuclei [187,188], without however furnishing information on the cross section at high

Spectroscopic factors for $^{12}\text{C}(\text{e}, \text{e}'\text{p})$

J^π	E_x (MeV)	Spectroscopic factors			
		Exp. ^a	Th ^b	Th ^c	Th ^d
$3/2^-$	0	1.72	4.0	2.86	2.64
$1/2^-$	2.125	0.26	0	0.75	0.52
$3/2^-$	5.02	0.20	0	0.38	0.47
$\Sigma S_{l=1}$		2.18	4.0	4.00	3.63

Fig. 58. (Left) The angular distributions of the three negative parity levels of the process $^{12}\text{C}(\text{e}, \text{e}'\text{p})^{11}\text{B}$ measured at NIKHEF and shown in Fig. 57. The continuous curves represent a best fit to the experimental data obtained by changing the nucleon occupation number of the p-shell and the radial strength of the optical potential used in the Distorted Wave Born Approximation. (Right) The model values of the spectroscopy factors (occupation numbers) of the process $^{12}\text{C}(\text{e}, \text{e}'\text{p})^{11}\text{B}$ obtained in Ref. [184] by fitting the experimental angular distributions (a). In the table the results of two shell-model calculations including configuration mixing in the p-shell are also shown, namely: (c) [185] and (d) [186] are compared with the experimental results listed in (a), whereas (b) denotes the values predicted by the simple independent particle shell model.

Source: Table reprinted from [184].

© 1988, by Elsevier.

values of the removal energy and momenta. Other twenty years had to pass, and eventually the two-nucleon correlation peak, located at $E \simeq k_1^2/2m_N$ with $k_1 \simeq 2\text{--}3 \text{ fm}^{-1}$ was captured (See Fig. 57) (bottom panel) and the investigation of SRCs could start on more solid grounds. Being the correlation contribution a small part of the strength ($\simeq 20\%$), a very careful evaluation of FSI is necessary before quantitative information on SRCs can be extracted from the experimental data. Therefore a consideration of FSI effects in $A(\text{e}, \text{e}'\text{p})X$ processes is a prerequisite in order to ascribe quantitative values to the strengths at high value of the removal energy, even if the observation of the momentum–energy correlation implied by SRCs represents a convincing evidence of the latter.

6.5.1. The Final state Interaction in $A(\text{e}, \text{e}'\text{p})X$

The treatment of FSI is usually based upon model approaches whose validity sensibly depends upon the kinetic energy of the struck nucleon T_N or, equivalently, upon the value of the four-momentum transfer Q^2 : schematically it can be stated that [189]: (i) at $Q^2 < 1 \text{ GeV}/c$, $T_{kin} \approx 100 \text{ MeV}$ the distorted wave Born approximation (DWBA) describing the motion of the struck proton in an optical potential, is the usual approach to treat FSI; (ii) at very high values of $Q^2 \gtrsim 10 \text{ (GeV}/c)^2$ the parton structure of the nucleon starts playing a role via the QCD effect of color transparency (cf. Section 7), leading to a strong reduction of FSI; (iii) in the range peculiar for the study of SRCs by the process $A(\text{e}, \text{e}'\text{p})X$, $Q^2 \approx 1\text{--}5 \text{ (GeV}/c)^2$ with $T_{kin} \simeq Q^2/(2m_N) \geq 1 \text{ GeV}$, the most appropriate way to treat FSI appears to be the Glauber approach (GA), based upon the eikonal approximation coupled with the rescattering of the struck nucleon on the spectator nucleons [78].²² The application of the GA to the treatment of $A(\text{e}, \text{e}'\text{p})B$ processes is based upon the following assumptions: (i) the NN scattering amplitude is obtained within the eikonal approximation; (ii) the nucleons of the spectator system ($A - 1$) are stationary during the multiple scattering with the struck nucleon (the *frozen approximation*), (iii) the interaction between the struck nucleon with the spectator frozen nucleons occurs only by transferring a perpendicular momentum component. GA has two non trivial advantages in that: (i) it does not contain free parameters, being based upon the use of the experimental values

²² The relationships between the DWIA and the GA are discussed in details in Ref. [189].

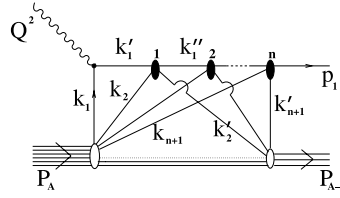


Fig. 59. The Feynman diagrams describing the rescattering in Glauber approximation for the process $A(e, e'p)(A - 1)$. The four-momenta of particle 1 before interaction and in intermediate states are denoted by k_1, k'_1, k''_1 , etc., respectively, and the final momentum by \mathbf{p}_1 . The black oval spots denote the elastic NN scattering matrix f^{NN} .

Source: Reprinted from [206].

© 2005, by the American Physical Society.

characterizing NN scattering processes, and (ii) it can be applied to the treatment of exclusive $A(e, e'p)B$ processes off both complex nuclei and few-nucleon systems, where in the last case, the concept of an optical potential is difficult to justify.

In Refs. [190,191] GA has been formulated in terms of Feynman diagrams; the diagram describing the rescattering in a nucleus A , is shown in Fig. 59. Within the diagrammatic approach GA has been improved by the *generalized eikonal approximation* (GEA) [192–194] in which the frozen approximation is partly removed by taking into account the excitation energy of the $(A - 1)$ system; the main result of GEA is a correction term to the standard profile function of GA, having the form of a longitudinal component of the momentum transfer depending upon the removal energy. The final state wave function in GEA has the following form (see e.g. Ref. [105]).

$$\Psi_f^*(\mathbf{r}_1, \dots, \mathbf{r}_A) = \hat{\mathcal{A}} [S_{GEA}(\mathbf{r}_1, \dots, \mathbf{r}_A) e^{-i\mathbf{p}\mathbf{r}_1} e^{-i\mathbf{p}_{A-1}\mathbf{R}_{A-1}} \Phi_{A-1}^*(\mathbf{r}_2, \dots, \mathbf{r}_A)], \quad (6.67)$$

where $\hat{\mathcal{A}}$ is the anti-symmetrization operator and $\delta_{GEA} = \sum_{n=2}^A \delta_{GEA}^{(n)}$ generates the final state interaction between the struck particle and the $(A - 1)$ nucleon system; in Eq. (6.67) n denotes the order of multiple scattering, with the single scattering term ($n = 1$) given by

$$\delta_{GEA}^{(1)}(\mathbf{r}_1, \dots, \mathbf{r}_A) = 1 - \sum_{i=2}^A \theta(z_i - z_1) e^{i\Delta_z(z_i - z_1)} \Gamma(\mathbf{b}_1 - \mathbf{b}_i), \quad (6.68)$$

where

$$\Gamma(\mathbf{b}) = \sigma_{NN}^{tot}(1 - i\alpha_{NN}) \frac{1}{4\pi B} e^{-\mathbf{b}^2/2B} \quad (6.69)$$

is the usual Glauber profile function and

$$\Delta_z = (q_0/|\mathbf{q}|)E_m, \quad (6.70)$$

E_m being the missing energy related to the excitation energy of $(A - 1)$; due to the presence of Δ_z , the frozen approximation is partly removed and when $\Delta_z = 0$ the GA is recovered (the expression of the n th order contribution $\delta_{GEA}^{(n)}$ is given in Ref. [105,193,194]). It should be stressed that unlike the case of the PWIA, when FSI is taken into account, the cross section does not acquire the factorized form of Eq. (6.66). This is because some of the responses functions W_1 introduce non factorized effects (see Ref. [206] for details). Due to the difficulties to calculate the non factorized cross section, particularly when realistic many-body wave functions are adopted, factorized cross sections within the GA and GEA approximations are often used. The error one does in this case will be discussed later on. The factorized form of the cross section is

$$\frac{d^6\sigma}{d\epsilon' d\Omega' d^3\mathbf{p}_m} = \mathcal{K} \sigma_{eN} P_A^{N(FSI)}(\mathbf{p}_m, E_m), \quad (6.71)$$

which differs from the PWIA cross section (6.66) by the presence of the distorted spectral function

$$P_A^{N(FSI)}(E_m, |\mathbf{p}_m|) = \sum_f |\langle \mathbf{p}_m, \Psi_f^{A-1} | \Psi_0^A \rangle|^2 \delta(E_m - (E_{min} + E_{A-1}^f)), \quad (6.72)$$

where

$$\langle \mathbf{p}_m, \Psi_f^{A-1} | \Psi_0^A \rangle = \int e^{i\mathbf{p}_m \mathbf{r}_1} \hat{S}_A^{GA}(\mathbf{r}_1 \dots \mathbf{r}_A) \Psi_f^{A-1\dagger}(\mathbf{r}_2 \dots \mathbf{r}_A) \Psi_A(\mathbf{r}_1 \dots \mathbf{r}_A) \delta \left(\sum_{j=1}^A \mathbf{r}_j \right) \prod_{i=1}^A d\mathbf{r}_i. \quad (6.73)$$

In GA the final state wave function is obtained from Eq. (6.67) by replacing S_{GEA} with the eikonal Glauber operator

$$\hat{S}_A^{GA}(\mathbf{r}_1, \dots, \mathbf{r}_A) = \prod_{j=2}^A [1 - \theta(z_j - z_1) \Gamma(\mathbf{b}_1 - \mathbf{b}_j)]. \quad (6.74)$$

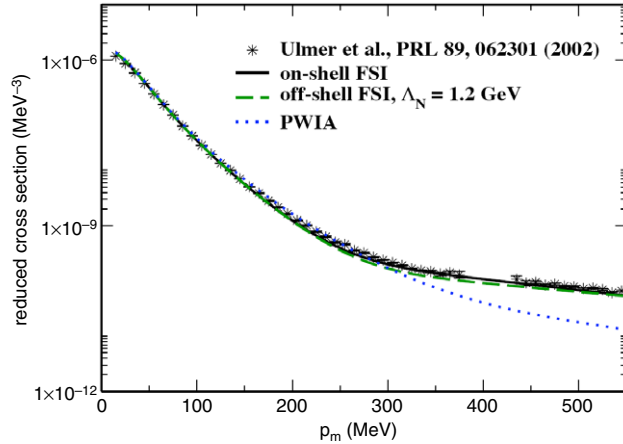


Fig. 60. The missing momentum dependence of the reduced cross section (Eq. (6.75)) of the $D(e, e'p)n$ compared with calculations from Ref. [197] using Bonn interaction and GEA in PWIA (full and dashed lines) and taking into account FSI (dot-dashed line). Experimental data from Ref. [195]. Source: Reprinted from [197].

© 2008, by the American Physical Society.

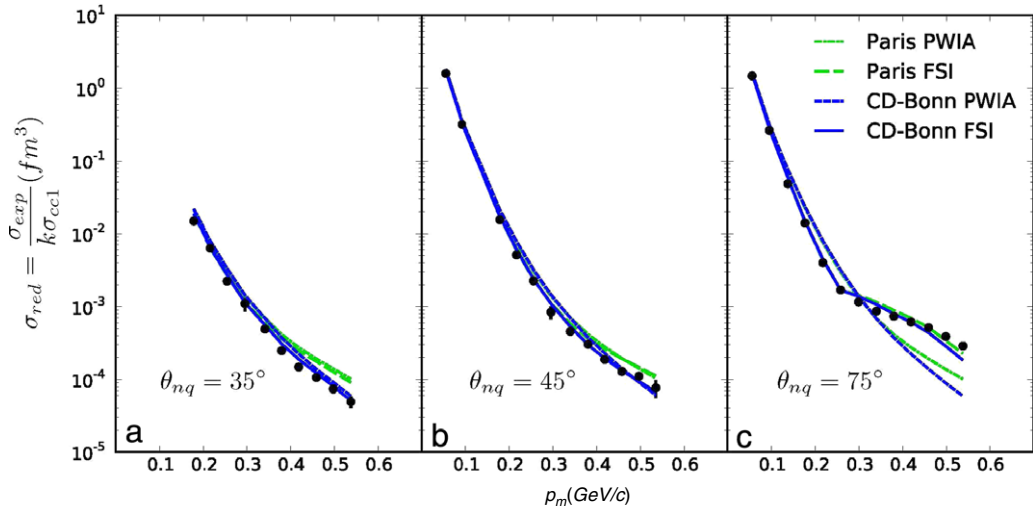


Fig. 61. The missing momentum distribution of the reduced cross section (Eq. (6.75)) of the process $D(e, e'p)n$ measured [196] at fixed $Q^2 = 3.5 \text{ (GeV/c)}^2$ and $0.78 \leq x_B \leq 1.52$, and three values of the neutron recoil angle θ_{nq} , with the smallest recoil angle corresponding to highest values of x_B , where data are expected to be less sensitive to FSIs. Theoretical calculations from [198] using GEA and Bonn and Paris interactions to calculate PWIA and FSI as explained in the inset (c).

Source: Reprinted from [196].

© 2010, by the American Physical Society.

Let us now discuss a series of relevant experiments that have been recently performed mainly on few-nucleon systems:

6.6.1a The process ${}^2\text{H}(e, e'p)n$.

Recent experiments on ${}^2\text{H}(e, e'p)n$ have been performed at Jlab [195,196]. A comparison of theoretical calculations with these experimental data within the GEA have been performed in Refs. [105,198,197] by considering the so called *reduced cross section*

$$\sigma_{red} = \frac{d^4\sigma^{exp}}{d\Omega' d\epsilon' d\Omega_{p_m}} \times [\mathcal{K}\sigma_{eN}(\bar{Q}^2, \mathbf{p}_m)]^{-1}, \quad (6.75)$$

i.e. a quantity that would equal the distorted momentum distribution if the factorized cross section (6.71) is valid.²³ In Fig. 60 the experimental data of Ref. [195] are compared with the results of Ref. [197], whereas in Fig. 61 the experimental

²³ Note that in case of a deuteron target, the distorted spectral function is replaced by the distorted momentum distribution.

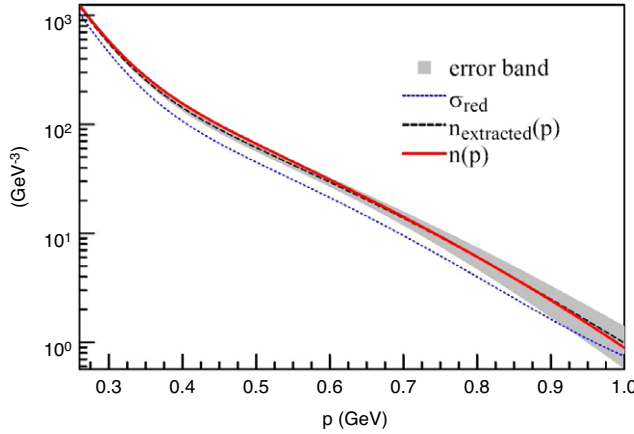


Fig. 62. The pseudoreduced cross section (σ_{red}), the extracted momentum distribution ($n_{\text{extracted}}(p)$) with errors (error band) and the input AV18 momentum distribution ($n(p)$).
Source: Reprinted from [199].

results of Ref. [196] are compared with calculations from Ref. [198]. It can be seen that the reduced cross section is correctly reproduced but at high values of the missing momentum FSI is quite relevant. A possible way to extract the momentum distribution from this type of data reducing the model dependence of the extraction, has been recently proposed in Ref. [199]. There, theoretical momentum distributions generated by a set of different NN interactions [30,25,200–202] have been used to generate pseudo data of the reduced cross section, and a momentum distribution has been extracted and compared with the input one. An example is given in Fig. 62.

6.6.1b The process ${}^3\text{He}(e, e' p)X$.

In the quasi-elastic region, the process ${}^3\text{He}(e, e' p)X$ is characterized by two final state channels: the two-body break-up (2BBU)

$$e + {}^3\text{He} = e' + p + {}^2\text{H}, \quad (6.76)$$

and three-body break-up (3BBU)

$$e + {}^3\text{He} = e' + p + (pn), \quad (6.77)$$

channels, respectively. The factorized cross section is given in this case by [105]

$$\frac{d^n\sigma}{d\epsilon' d\Omega' d\tau_f} = \mathcal{K}(\nu, Q^2, \mathbf{p}_m) \sigma^{eN}(\bar{Q}^2, \mathbf{p}_m) P_3^{N(FSI)}(\mathbf{p}_m, E_m),$$

where $d\tau_f = d\Omega_{p_1}$ ($d\Omega_f = d\Omega_{p_1} dE_m$) for the 2BBU(3BBU) channel, and the corresponding distorted spectral function including FSI, $P_3^{(FSI)}(\mathbf{p}_m, E_m)$, is given by Eq. (6.72) with $(A - 1) = {}^2\text{H}$ and (pn) , respectively. Experiments were performed in Refs. [203–205] and theoretical calculations were performed in Refs. [105,194,198,207–211,213]. Here we will briefly present the results of Refs. [209–211], where both the 2BBU and 3BBU channels have been considered within a unified approach based upon the following major assumptions: (i) initial state correlations (ISC) treated by the use *ab initio* few-body wave functions [48] corresponding to the AV18 interaction; (ii) final state interactions (FSI), treated within GEA with the parameters of the NN scattering amplitudes taken from [214]; (iii) fully unfactorized cross section. In Fig. 63 (Left) we show the cross section for the 2BBU channel calculated in a fully unfactorized approach. The good agreement of a parameter free calculation with experimental data within six order of magnitudes is impressive. It can be seen that the PWIA describes well the data up to $p_m \simeq 300$ MeV/c, but completely fails at higher values of the missing momentum. The experimental data exhibits a trend reminiscent of the elastic proton–nucleus scattering cross section [78], with the slopes abruptly changing with increasing value of the momentum due to the increasing order of rescattering. This is clear sign of FSI effects resulting from the eikonal approach as shown in Fig. 63, with the first change of slope due to single scattering of the struck proton in the final state and the second one to double scattering. In Ref. [213] the second change of slope has been interpreted as evidence of a three-nucleon effect according to which γ^* is absorbed by a nucleon at rest which propagates emitting a pion, which is reabsorbed by the spectator two-nucleon pair. The Glauber-like behavior of the experimental data seems to rule out such a mechanism. The results presented in Fig. 63 (Right) clearly show that treating FSI within the factorization approximation is not legitimate at “negative” (left, $\phi = 0$) values of the missing momentum, unlike what happens for “positive” (right, $\phi = \pi$) values (here ϕ is the azimuthal angle of the detected proton with respect to the momentum transfers \mathbf{q}). The results for the 3BBU channel, presented in Fig. 64, show that: (i) correlation peaks located at $E^* \simeq p_m^2/(4m_N)$ can be seen; (ii) the effects from FSI are very large and overwhelm the PWIA; (iii) FSIs seem to be located only in the interacting pair, since at

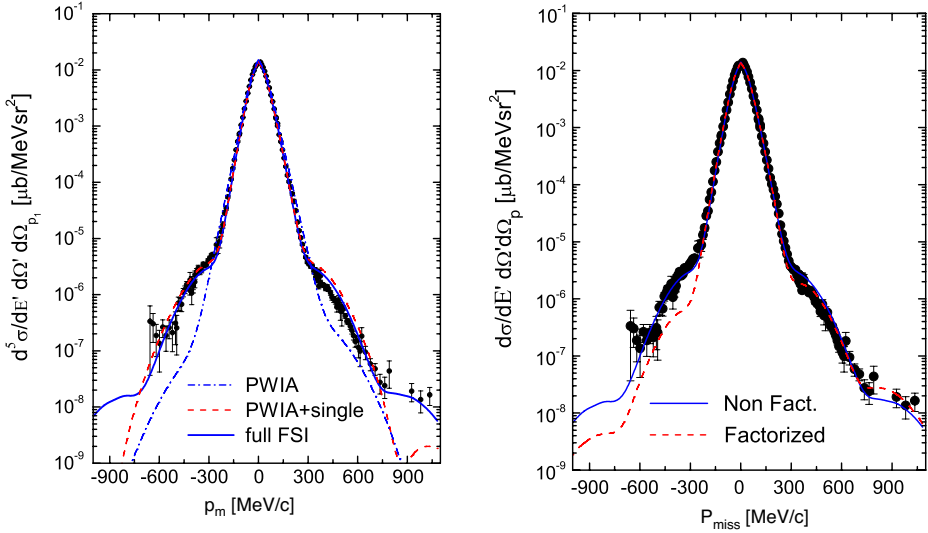


Fig. 63. (Left): the cross section of the process ${}^3\text{He}(e, e'p){}^2\text{H}$ (2BBU channel). Full parameter-free and unfactorized calculation [210] of the cross section using *ab initio* ground-state wave functions of ${}^3\text{He}$ and the generalized eikonal approximation. The dot-dashed curve represents the PWIA, the dashed curve includes single-scattering of the struck proton in the final state and the full curve includes single plus double scattering. (Right): Comparison between the factorized (Eq. (6.77)) and unfactorized calculations. Experimental data from [205]. $\epsilon' = E'$.
Source: Reprinted from [210].

© 2005, by the American Physical Society.

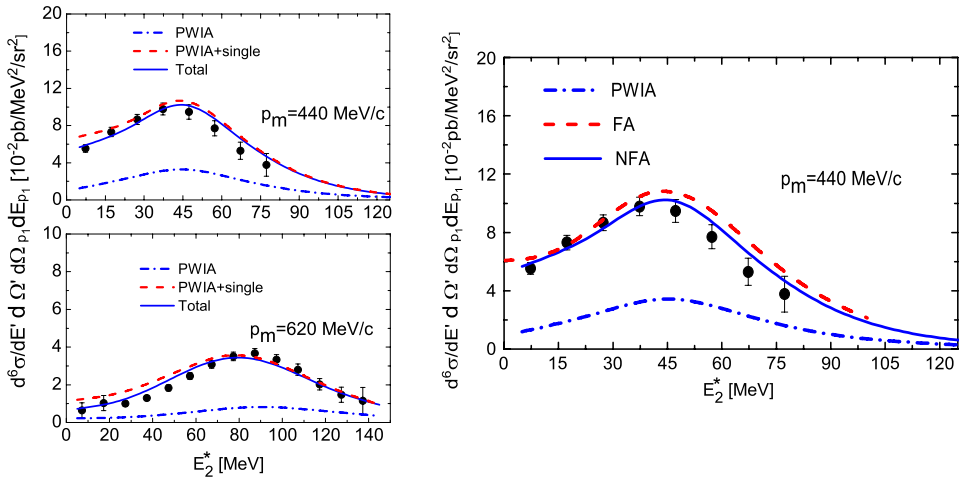


Fig. 64. The cross section of the 3BBU channel ${}^3\text{He}(e, e'p)np$. Full parameter-free and unfactorized calculation [211] of the cross section using *ab initio* ground-state wave functions of ${}^3\text{He}$ and the generalized eikonal approximation. (Left): the dot-dashed curve denotes the PWIA, the dashed curve includes single-scattering and the full curve single plus double scattering of the struck proton in the final state. (Right): comparison between the factorized approximation (FA) and the full unfactorized calculation (NFA). Experimental data from [204].
Source: Reprinted from [211].

© 2010, by the American Physical Society.

the top of the peak only single scattering is relevant; (iv) the factorization approximation appears to be a rather reasonable one in the 3BBU channel.

6.6.1c the process ${}^4\text{He}(e, e'p){}^3\text{H}$

Calculations of the 2BBU channel in ${}^4\text{He}$, i.e. the process ${}^4\text{He}(e, e'p){}^3\text{H}$, have been performed in Refs. [215–219] using *ab initio* realistic wave functions for ${}^4\text{He}$ and ${}^3\text{H}$. The reduced cross section

$$\sigma_{red} = \frac{d^5 \sigma}{d\Omega' d\epsilon' d\Omega_p} (\mathcal{K} \sigma_{ep})^{-1} \equiv n_D(\mathbf{p}_m), \quad (6.78)$$

is presented in Fig. 65 (Left) where it is compared with preliminary JLab data ($CQ\omega 2$) obtained in perpendicular kinematics [220] and it can be seen, as expected, that FSI fills up in a reasonable way the dip in the PWIA cross section.

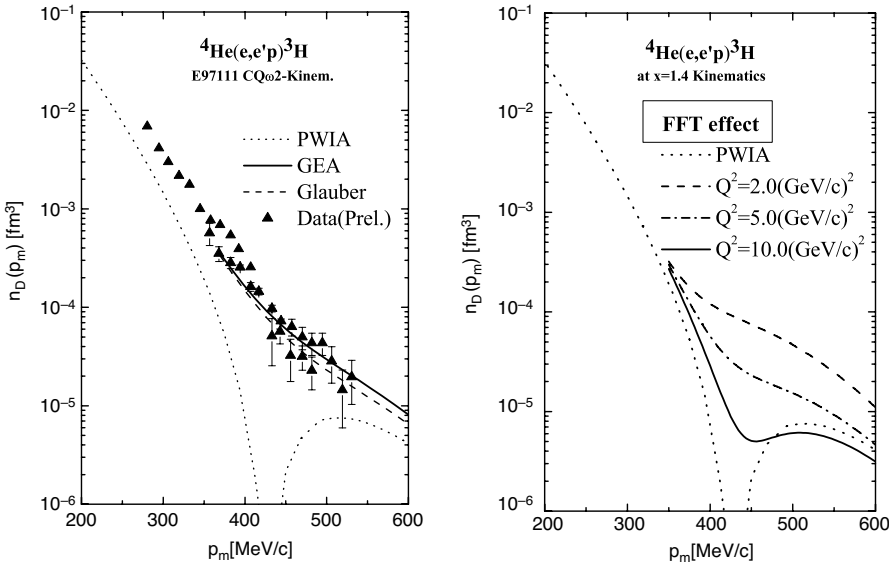


Fig. 65. (Left): the reduced cross section (Eq. (6.78)) of the process ${}^4\text{He}(e, e'p){}^3\text{H}$ at perpendicular kinematics and $x \simeq 1.8$. The solid line shows the results within GEA, whereas the dashed curve corresponds to the conventional GA. Preliminary data from [220]. (Right): the reduced cross section (6) of the process ${}^4\text{He}(e, e'p){}^3\text{H}$ at perpendicular kinematics for various values of Q^2 and $x \simeq 1.4$, calculated taking finite formation time effects into account. Four-body wave functions from Ref. [49].

Source: Reprinted from [215].

© 2008, by Springer.

It has been argued by various authors that at high values of Q^2 the phenomenon of color transparency, i.e. a reduced NN cross section in the medium, might be observed. Color transparency is a consequence of the cancellation between various hadronic intermediate states of the produced ejectile. In [221] the vanishing of the FSI at high Q^2 has been produced by considering the finite formation time (FFT) the ejectile needs to reach its asymptotic form of a physical baryon. This has been implemented in Refs. [218,221–223] by explicitly considering the dependence of the NN scattering amplitude upon nucleon virtuality, leading to the replacement of $\theta(z_i - z_1)$ appearing in the Glauber profile with

$$J(z_i - z_1) = \theta(z_i - z_1) (1 - \exp[-(z_i - z_1)/l(Q^2)]) \quad (6.79)$$

where $l(Q^2) = Q^2/(x_B m_N M^2)$; here x_B is the Bjorken scaling variable and the quantity $l(Q^2)$ plays the role of the proton formation length, i.e. the length of the trajectory that the knocked out proton runs until it returns to its asymptotic form; the quantity M is related to the nucleon mass m_N and to an average resonance state of mass m^* by $M^2 = m^{*2} - m_N^2$. Since the formation length grows linearly with Q^2 , at higher Q^2 the strength of the Glauber-type FSI is reduced by the damping factor $(1 - \exp[-(z_i - z_1)/l(Q^2)])$; if $l(Q^2) = 0$, the usual Glauber operator is recovered. The results of calculations of the cross section of the process ${}^4\text{He}(e, e'p){}^3\text{H}$ in perpendicular kinematics taking into account FFT effects are presented in Fig. 65 (Right) (for calculations in parallel kinematics see [218]). It can be seen that at the JLAB kinematics ($Q^2 = 1.78 (\text{GeV}/c)^2$, $x \sim 1.8$) FFT effects, as expected, are too small to be detected, they can unambiguously be observed in the region $5 \leq Q^2 \leq 10 (\text{GeV}/c)^2$ and $x = 1.4$. Thus measuring the Q^2 dependence of the cross section of ${}^4\text{He}(e, e'p){}^3\text{H}$ process at $p_m \sim 430 \text{ MeV}/c$ and $Q^2 \sim 10 (\text{GeV}/c)^2$ would be extremely interesting. Similar conclusions have been reached in Ref. [224]. To complete this Section we show in Fig. 66 the results of calculations by Schiavilla and collaborators [207], who, besides the FSI effects treated by a Glauber approach similar to the one of Ref. [211], also include the effects of MEC. It can be seen that, as also stressed by the authors, the effects of the latter, although not negligible, are very small.

To sum up, the following remarks are in order: (i) an overall good agreement between the results of theoretical calculations and experimental data for both ${}^3\text{He}$ and ${}^4\text{He}$ is observed, which is very gratifying particularly in view of the lack of any adjustable parameter in theoretical calculations; (ii) the effects of the FSI are such that they systematically bring theoretical calculations in better agreement with the experimental data; for some quantities, FSI effects simply improve the agreement between theory and experiment, whereas for some other quantities, they play a dominant role; (iii) the 3bbu channel in ${}^3\text{He}$ provides evidence of NN correlations, in that the experimental values of p_m and E_m corresponding to the maximum values of the cross section satisfy, to a large extent, the relation predicted by the two-nucleon correlation mechanism, with FSI, however, largely affecting the magnitude of the cross section; (iv) the violation of the factorization approximation is appreciable at “negative” values ($\phi = 0$) of the missing momentum, whereas the non factorized and factorized predictions are in good agreement in the whole range of positive values ($\phi = \pi$) of $|\mathbf{p}_m|$. The realistic calculations have been performed with the AV18 interaction, but in view of the large effects of the FSI it is not clear whether softer

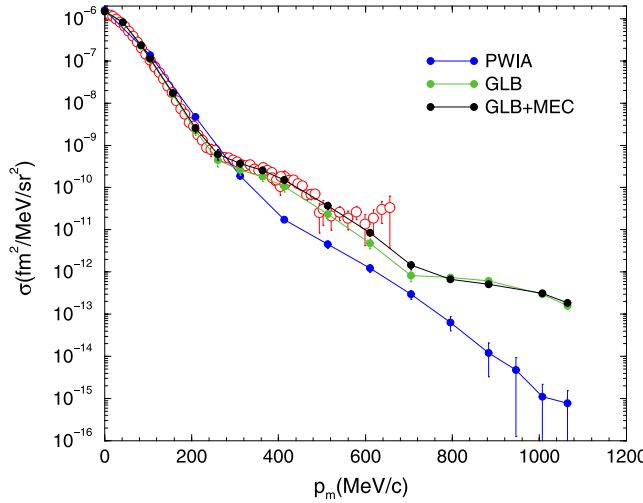


Fig. 66. The effects of MEC on the 2BBU channel of the process ${}^3\text{He}(e, e'p){}^2\text{H}$ at $\phi = 180^\circ$ (left side of Fig. 63) calculated in Ref. [207]. The experimental points are denoted by circles with error bars, the PWIA is shown by the blue line, the inclusion of Glauber FSI results in the green line and the inclusion of MECs leads to the black line. Ground-state wave functions of ${}^3\text{He}$ and ${}^2\text{H}$ from the Argonne AV18 interaction, as in Ref. [211]. (For interpretation of the references to color in this figure legend, the reader is referred to the web version of this article.)

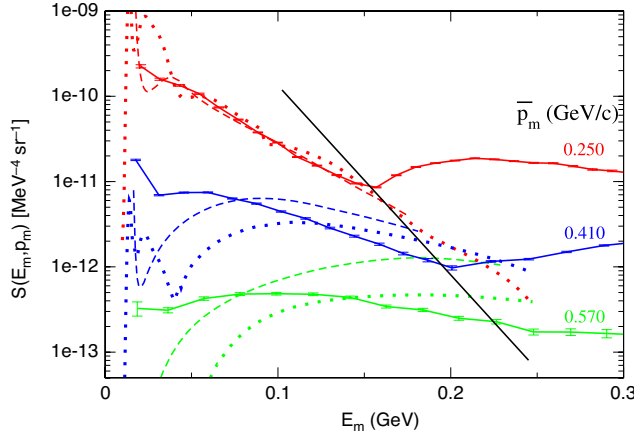


Fig. 67. The Spectral function S extracted from the experimental data on the process ${}^{12}\text{C}(e, e'p)X$ at high missing energy (E_m) and momentum (p_m) from the Jefferson Lab experiment E97/006 [225] (continuous lines with error bars) compared with model spectral functions for ${}^{12}\text{C}$ extrapolated from the nuclear matter spectral function of Ref. [228] (Bonn interaction) (dotted lines) and from the ${}^{16}\text{O}$ spectral function obtained from nuclear matter by the local density approximation (Urbana AV14 interaction) [112] (dashed lines). The black line separates the region governed by ground-state correlations from the region of nucleon resonance excitation.
Source: Reprinted from [225].

interaction would explain equally well the experimental data. Calculation based upon softer interaction would be very useful to answer this question.

6.6.1d The process ${}^{12}\text{C}(e, e'p)X$

As previously stressed, several experimental data on the $A(e, e'p)X$ on complex nuclei in the region of missing energy and momentum typical of a shell-model description ($E_m \lesssim 40\text{--}50$ MeV, $p_m \lesssim 1.5$ fm $^{-1}$), have been performed in the past which allowed one to obtain the single particle momentum distributions and energies of a large class of nuclei (see, e.g. Ref. [187]). Whereas a discussion of these experimental data and their theoretical interpretations is out of the scope of the present review, the first systematic attempt to investigate the correlation structure of nuclei, in particular ${}^{12}\text{C}$, by the $(e, e'p)$ process is worth being discussed. This is the E97-006 Jefferson Lab experiment [225] in which measurements performed in proper kinematics to reduce the effects of FSI (see a detailed discussion in [13] as well as in Refs. [226,227]) have been performed at relatively high values of missing momenta ($p_m \lesssim 600$ MeV/c) and removal energy ($E_m \lesssim 250$ MeV). The extracted spectral function of ${}^{12}\text{C}$ is shown in Fig. 67 where it is compared with model spectral functions. By integrating over the experimental range of removal energy the partial momentum distributions can be obtained; it can be seen from Fig. 31 that the experimental range in removal energy is too low to obtain the full momentum distributions which could be compared with available *ab initio* theoretical distributions. Nonetheless, these data, if really free from the effects of MEC

and final state interaction, can be very useful to check the validity of model spectral functions, as it clearly appears from the comparison shown in Fig. 67.

6.5.2. The process $A(e, e'N_1N_2)X$

The most direct process that in principle could provide information on two-nucleon dynamics, would be the process $A(e, e'N_1N_2)X$ when a pair of nucleons is detected in coincidence with the scattering electron. The differential cross section in one-photon exchange approximation will depend upon six response functions W_i as follows (see e.g. [229–232])

$$\frac{d^{12}\sigma}{d\epsilon_{e'} d\Omega_{e'} d\mathbf{p}_1 d\mathbf{p}_2 d\mathbf{p}_{A-2}} = \sigma_{Mott} \sum_{i=1}^6 V_i W_i(v, Q^2, p_1, p_2) \\ \times \delta \left(\mathbf{q} - \sum_{i=2}^2 \mathbf{p}_i - \mathbf{p}_{A-2} \right) \delta \left(v + M_A - \sum_{i=1}^2 (m_N^2 + \mathbf{p}_i^2)^{1/2} - (M_{A-2}^{2*} + \mathbf{p}_{A-2}^2)^{1/2} \right), \quad (6.80)$$

where V_i are known kinematical factors, and W_i the *response functions*, which have the following general form

$$W_i = \left| \langle \Psi_f^{(-)}(\mathbf{p}_1, \mathbf{p}_2, \mathbf{p}_{A-2}) | \hat{\phi}_i(\mathbf{q}) | \Psi_0(\mathbf{k}_1, \mathbf{k}_2, \mathbf{k}_{A-2}) \rangle \right|^2. \quad (6.81)$$

In Eq. (6.81) $\Psi_f^{(-)}$ and Ψ_0 are the continuum and ground-state wave functions of the target nucleus, respectively, and $\hat{\phi}_i(\mathbf{q})$ is a quantity depending on proper combinations of the components of the nucleon current operator \hat{j}^μ . In PWIA the nuclear part of the process depends upon the two-nucleon spectral function $P_A^{N_1N_2}(\mathbf{k}_1, \mathbf{k}_2, E^{(2)})$ defined by Eq. (5.48). If an experiment could be figured out which is sensitive to the two-nucleon spectral function, information on the two-nucleon momentum distribution could be in principle obtained. In the past intense theoretical [233–238] and experimental [239–245] activities have been produced aimed at investigating two-nucleon emission from nuclei at intermediate energies. Unfortunately, the experimental data, mainly involving low Q^2 regions, were dominated by MEC, FSI and other effects and no quantitative conclusive information on SRCs could be obtained (for a critical discussion of this topic see [13]). Recently, however, high momentum transfer experiments have been performed on ^{12}C and ^4He [246–252] that provided robust evidence of SRCs thanks to: (i) the high values of the momentum transfer ($Q^2 \simeq 2 (\text{GeV}/c)^2$), which, improving the resolution of the probe, allowed one to reduce the effects of FSI and MEC and to localize the interaction region at short inter-nucleon distances; (ii) the selection of kinematical regions with $x_B > 1$, i.e. the region where, as demonstrated in the previous sections, nucleon d.o.f are the dominant ones, and SRCs are expected to show up; (iii) the selection of the region of missing momentum and removal energy satisfying the relation $E_m \simeq [(A-1)p_m^2/(A-2)m_N]$, i.e. the region of the correlation peak exhibited by the nucleon spectral function. This mechanism has been checked for the first time via an experiment performed at Brookhaven National Laboratory [246,247] in the region of missing energy around the correlation peak i.e. $E_{mis} \approx \mathbf{p}_{mis}^2/(2m_N)$; in this experiment, whose basic mechanism is sketched in Fig. 68, the nucleus of ^{12}C was bombarded by a beam of protons with momentum in the range $5.9 < p_p < 9.0 \text{ GeV}/c$ and a leading proton, struck by the projectile, was detected in coincidence with neutrons with momentum in the range $0.05 < p_n < 0.55 \text{ GeV}/c$. By plotting the number of detected neutrons vs $\cos \gamma$, γ being the angle between $\mathbf{p}_{mis} = \mathbf{p}_1 - \mathbf{q}$ (equal to \mathbf{k}_1 in PWIA) and \mathbf{p}_n (equal to \mathbf{k}_2 in PWIA), the result shown in Fig. 69 has been obtained. It clearly appears that neutrons with low momentum (less than k_F), arising from a collective de-excitation of the nucleus, are emitted isotropically, without any directional correlation with \mathbf{p}_{mis} , whereas recoiling neutrons with momentum $p_n \simeq 2 - 2.5 \text{ fm}^{-1}$ were emitted in a backward cone in the direction of \mathbf{p}_{mis} , in agreement with the picture of the interaction of the incoming proton with a proton correlated with a neutron in a back-to-back configuration. An analysis of these experimental data performed within light cone kinematics in terms of a model spectral function and disregarding FSI [248] led to the results that $92_{-18}^{+8}\%$ of protons with momentum $p_{mis} > 275 \text{ MeV}/c$ were accompanied by a neutron emitted in the direction of \mathbf{p}_{mis} , with the conclusion that $92_{-18}^{+8}\%$ of protons in ^{12}C “are partners in np -SRC pairs”. In the BNL experiments only recoiling neutrons could be detected so that no information on pp SRCs could be obtained. These were investigated at Jlab [249–251] via the processes $^{12}\text{C}(e, e'p)X$ and $^{12}\text{C}(e, e'pp)X$, using electron beams of energy $\epsilon = 4.621 \text{ GeV}$ and a kinematics set-up such that $Q^2 = 2 (\text{GeV}/c)^2$, $|\mathbf{q}| = 1.65 \text{ GeV}/c$, $x_B \simeq 1.2$, as shown in Fig. 70 (Left) corresponding to $p_{mis} = 0.55 \text{ GeV}/c$. The evidence of short-range correlated pairs in ^{12}C has been first provided in the single arm experiment $^{12}\text{C}(e, e'p)X$, by detecting the SRC peak with its maximum located at $E_{mis} \simeq \mathbf{p}_{mis}^2/(2m_N) + E_{thr}^{(2)}$, as clearly shown in Fig. 70 (Right), where $p_m \simeq 0.31 \text{ GeV}/c$. In the following step the kinematics was fixed from the single arm experiment and recoiling protons emitted in the direction of \mathbf{p}_{mis} were detected in coincidence with the leading proton obtaining, by this way, the yield ratio $^{12}\text{C}(e, e'pp)X / ^{12}\text{C}(e, e'p)X$, where the counting rate of the single arm experiment $^{12}\text{C}(e, e'p)X$ includes the contribution from both pn and pp correlated pairs. The same experiment was performed by detecting recoiling neutrons [250]; by this way, assuming a correlation region defined by $0.3 \lesssim k_{rel} \lesssim 0.6 \text{ GeV}/c$, $0.0 \lesssim K_{c.m.} \lesssim 0.2 \text{ GeV}/c^{24}$ presented in Section 4, the yield ratio of the number of pn to pp pairs as

²⁴ Apparently in Ref [248] and subsequent papers, nucleon momentum components $\gtrsim 275 \text{ MeV}/c$ were considered to arise from SRCs. As shown by many-body realistic calculations a MF contribution to the momentum distributions at this value of the momentum should not be disregarded.

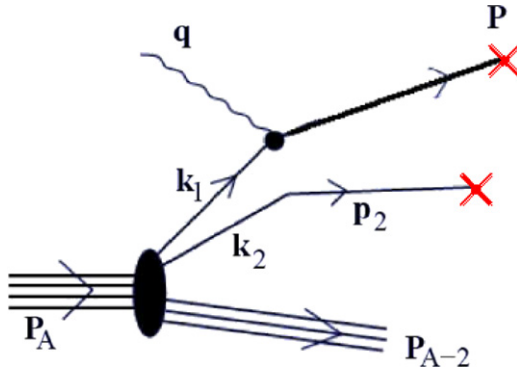


Fig. 68. A graphical representation of the basic mechanism of recent experiments on $A(e, e' pN)X$ investigating back-to-back correlated pairs of nucleons. The γ^* exchanged by the electron interacts with nucleon “1” (the *leading nucleon*) with momentum $\mathbf{k}_1 \simeq -\mathbf{k}_2$, which is ejected with momentum $\mathbf{P} = \mathbf{q} + \mathbf{k}_1 = \mathbf{p}_1$ and detected by the first spectrometer in coincidence with the recoiling partner emitted in the direction of $\mathbf{p}_m = \mathbf{q} - \mathbf{P} \simeq -\mathbf{k}_1 \simeq \mathbf{k}_2$.

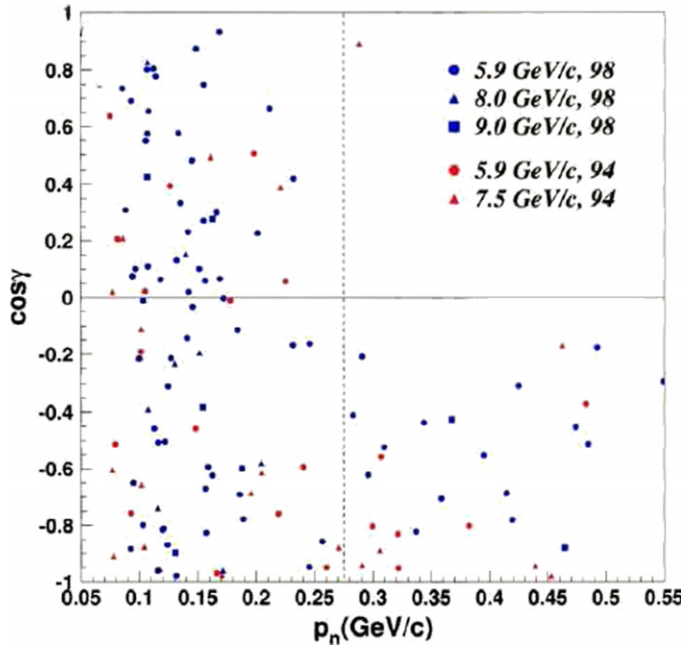


Fig. 69. The directional correlation between the magnitude of the recoil neutron momentum ($p_n = k_2$ in PWIA) and the angle γ between ($p_n = k_2$ in PWIA) and ($p_m = k_1$ in PWIA) in the process $A(p, p'pn)X$ (Note that in Ref. [247] the missing momentum has been defined as $\mathbf{p}_m = \mathbf{p}_1 - \mathbf{q} = \mathbf{k}_1$). The legend gives the initial proton beam momentum and year of the run, with hollow points (labeled 94) from Ref. [246] and solid points (labeled 98) from Ref. [247]. In all cases, no angular correlation is observed for neutron momenta less than the Fermi momentum k_F , while neutrons with larger momentum are produced preferably in the backward hemisphere of the reaction.

Source: Reprinted from [248].

© 2006, by APS.

well as the percent ratio of the pn pairs to the total numbers of correlated pairs in ^{12}C have been determined as follows (see Fig. 71).

$$\frac{\# np \text{ SRC pairs}}{\# pp \text{ SRC pairs}} = 18.0 \pm 5.0 \quad \frac{\# np \text{ SRC pairs}}{\text{Total}\#\text{SRC pairs}} = (84\text{--}92)\%. \quad (6.82)$$

The successful investigation of SRCs attained in the last few years was also due to new original ideas concerning the best way to proceed in their search. The basic idea of the experiments performed in Refs. [246–251] depicted in Fig. 68 is based upon the assumption of the existence in a nucleus of a back-to-back configuration of nucleons, “1” and “2”, with momenta $\mathbf{k}_1 \simeq -\mathbf{k}_2$, and $\mathbf{K}_{c.m.} = -\mathbf{P}_{A-2} \simeq 0$. The underlying mechanism of the process is assumed to be the one in which: (i) the incoming probe, a lepton or a hadron, interacts only with proton “1”, the “leading proton”, transferring to it the whole momentum $\mathbf{q} \gg \mathbf{k}_1$, (ii) the proton is emitted and detected with momentum $\mathbf{P} = \mathbf{k}_1 + \mathbf{q}$ in the direction not very different from the direction of the momentum transfer, (iii) because of momentum conservation nucleon “2”, which did not interact

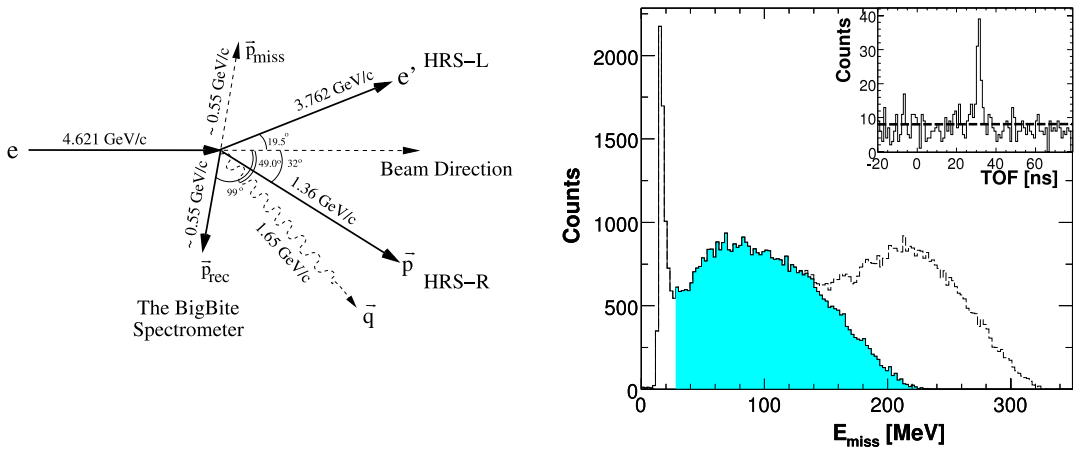


Fig. 70. (Left): the momentum vectors in the experiment of Ref. [249] on the process $^{12}\text{C}(e, e'pp)$ corresponding to the kinematics with the largest value of the missing momentum $p_m \equiv p_{\text{miss}} \simeq 0.55 \text{ GeV}/c$, e and e' denote the incoming and scattered electrons, respectively; \mathbf{p} denotes the leading (high momentum) detected proton and \mathbf{p}_{rec} the detected recoil proton; \mathbf{p} , and \mathbf{p}_{rec} are detected in the High Resolution Spectrometer (HRS) in coincidence with e' , detected in the BigBite Spectrometer. (Right): the measured $^{12}\text{C}(e, e'p)$ missing-energy spectrum in the experiment of Ref. [249] on the process $^{12}\text{C}(e, e'p)X$ corresponding to missing momentum $p_m \sim 0.31 \text{ GeV}/c$. The peak at 16 MeV is due to removal of p -shell protons leaving the ^{11}B nucleus in its ground state. The shaded region contains events with residual excited bound or continuum states. The space under the dashed line contains events with Δ excitation of the struck nucleon. Note that the peak of the shaded area is located at $E_m \simeq \mathbf{p}_m^2/(2m_N) + E_{\text{thr}} \simeq 70 \text{ MeV}$ in agreement with the SRC predictions. The random background is shown as a dashed line. (Note that in Ref. [249] the missing momentum has been defined as $\mathbf{p}_m = \mathbf{p}_1 - \mathbf{q} = \mathbf{k}_1$).
Source: Reprinted from [249].

© 2008, by the American Physical Society.

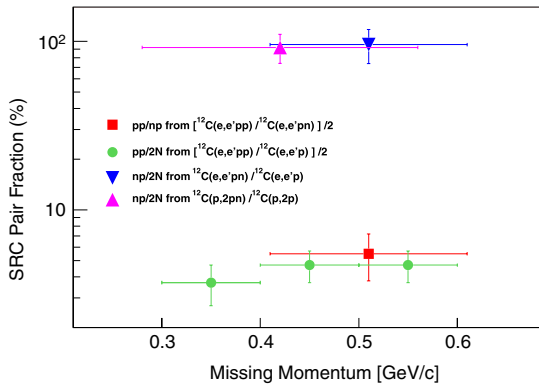


Fig. 71. The percent fraction of short range correlated pn and pp pair extracted from the $^{12}\text{C}(e, e'p)X$, $^{12}\text{C}(e, e'pp)X$ and $^{12}\text{C}(e, e'pn)X$ processes measured in Refs. [249] and [250]. In these ratios the yield of the $^{12}\text{C}(e, e'p)$ reaction represents the sum of the yield of $^{12}\text{C}(e, e'pp)X/2$ and $^{12}\text{C}(e, e'pn)X$.
Source: Reprinted from [250].

© 2008, by the American Physical Society.

with the incoming electron, is emitted by recoil and detected with momentum $\mathbf{p}_m = \mathbf{q} - \mathbf{P} = -\mathbf{k}_1 \simeq \mathbf{k}_2$ in coincidence with the leading proton, (iv) both nucleons leave the nucleus without any FSI. In reality, (i) the *c.m.* motion of the pair will spread the emission of the recoiling nucleon within a cone of small aperture, provided the convolution model of the spectral function of Ref. [114], discussed in Section 5.2.4, implying $\langle K_{\text{c.m.}} \rangle \ll \langle k_{\text{rel}} \rangle$, is valid and, (ii) the overall picture is expected to be distorted by FSI. The described model of two-nucleon emission due to SRCs is essentially an $A(e, e'p)X$ process with detection of a second nucleon, in the sense that the incoming electron interacted with one nucleon of a correlated pair and the second nucleon is emitted because of recoil.

Similar experiments have been performed on ^4He [251], extending the correlation region up to $k_{\text{rel}} \simeq 0.8 \text{ GeV}/c$ and assuming that the missing momentum p_m in the single arm experiment equals the relative momentum of the correlated pair, which can only occur in case of strict back-to-back nucleons with $K_{\text{c.m.}} = 0$; by this way the percent ratio of the yield of pp to pn correlated pairs vs $\mathbf{p}_m \simeq \mathbf{k}_{\text{rel}}$ has been determined and reported in the lowest panel of Fig. 72. A correct comparison of these results with theoretical calculations would require a full calculation of the cross section of the processes $A(e, e'p)X$

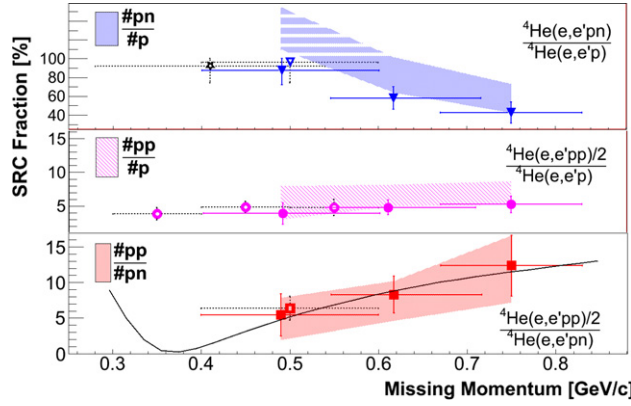


Fig. 72. Lower panel: the measured percent ratios [251] of SRC pp/pn pairs in ${}^4\text{He}$ (solid symbols) as a function of the missing momentum of the reaction ${}^4\text{He}(e, e'p)X$. The bands represent the data corrected for FSI to obtain the pair ratios (see [251] for details). The full curve is the theoretical calculations performed with two-body relative momentum distributions for pp and $p\bar{n}$ pairs in ${}^4\text{He}$ from Ref. [83]. The middle panel shows the measured and extracted $\#pp/\#p$ ratios. The upper panel shows the measured and extracted $\#pn/\#p$ ratios. Ratios for ${}^{12}\text{C}$ are shown as empty symbols with dashed bars. The empty star in the upper panel is the BNL result [247] ${}^{12}\text{C}$.

Source: Adapted from [251].

© 2014, by the American Physical Society.

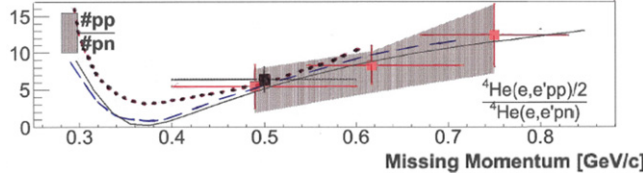


Fig. 73. The lower panel in Fig. 72 comparing the experimental results for the pp/pn ratio in ${}^4\text{He}$ (red squares) with theoretical calculations obtained within the VMC approach of Ref. [83] (full black line) and within the linked cluster expansion of Ref. [98] (dashed black line). Also shown by the black dotted line is the theoretical ratio for ${}^{12}\text{C}$ obtained within the linked cluster expansion of Ref. [98] compared with the experimental point at $\approx 0.5 \text{ GeV}/c$ denoted by the black square (the empty red square in Fig. 72).

Source: Adapted from [251].

© 2014, by the American Physical Society.

and $A(e, e'pN)X$ taking carefully into account FSI, which at the moment is not available. It is nevertheless gratifying, and to some extent surprising, that a reasonable explanation of the relative yields and ratios can be obtained by simply integrating the two-nucleon momentum distributions presented in Section 3, in the range of k_{rel} covered by the experiment. Using for ${}^4\text{He}$ the momentum distribution of Refs. [83,98], one obtains the results given by the full and dashed lines in Fig. 73 which nicely agree with the experimental data and also demonstrate the good agreement between the results of the VMC and the linked cluster expansion approaches, as it was expected from the results of the calculation of the momentum distributions presented in Section 4. In Fig. 73 also shown is the theoretical results for the pp/pn ratio in ${}^{12}\text{C}$ obtained in Ref. [98] and not yet available from the VMC approach; a good agreement between experimental data and theoretical calculations can again be seen. The surprising agreement obtained in terms of two-body momentum distributions can be reconciled with the basic properties of the spectral function in the region of SRCs, as described in this report in terms of *ab initio* few-nucleon wave functions, namely: (i) the factorization property, (ii) the small spin-isospin dependence of the pair *c.m.* momentum distributions, (iii) the minor role played by FSI in the spectator ($A - 2$) nucleus. Further evidence that the results of these experiments provide new and useful information on SRCs is provided by the experimental data related to the *c.m.* motion of the correlated pair. These are given in Fig. 74 which represents the distribution of the number of counts vs. the cosine of the opening angle γ between \mathbf{p}_{mis} and \mathbf{p}_{rec} (interpreted as the opening angle between \mathbf{k}_1 and \mathbf{k}_2). The two figures, referred, respectively, to ${}^{12}\text{C}$ and ${}^4\text{He}$, can indeed be explained by a simulation of the motion of a correlated pair whose *c.m.* momentum distribution is given by a Gaussian $n_{c.m.}^A(K_{c.m.}) = \exp(-\alpha_A K_{c.m.}^2)$ with the values of α_4 and α_{12} in full agreement with the prediction of the convolution model of the spectral function of Ref. [114].

Finally, an interesting experiment has been performed on the three-body disintegration of ${}^3\text{He}$, ${}^3\text{He}(e, e'p)p\bar{n}$ ${}^3\text{He}(e, e'n)pp$ [252], by isolating the process in which γ^* interacts with an uncorrelated nucleon with momentum $0 \lesssim K_{c.m.} \lesssim 2 \text{ fm}^{-1}$ and the nucleons of the correlated pair are emitted back-to-back, with the corresponding cross sections integrated over k_{rel} of the emitted pair, in the range $1.5 \lesssim k_{rel} \lesssim 2.5 \text{ fm}^{-1}$. The experimental results shown in Fig. 75 confirm the theoretical prediction shown in Figs. 21 and 22, namely that the dip in the pp distribution at $\mathbf{K}_{c.m.} \simeq 0$ is filled up with increasing values of $\mathbf{K}_{c.m..}$

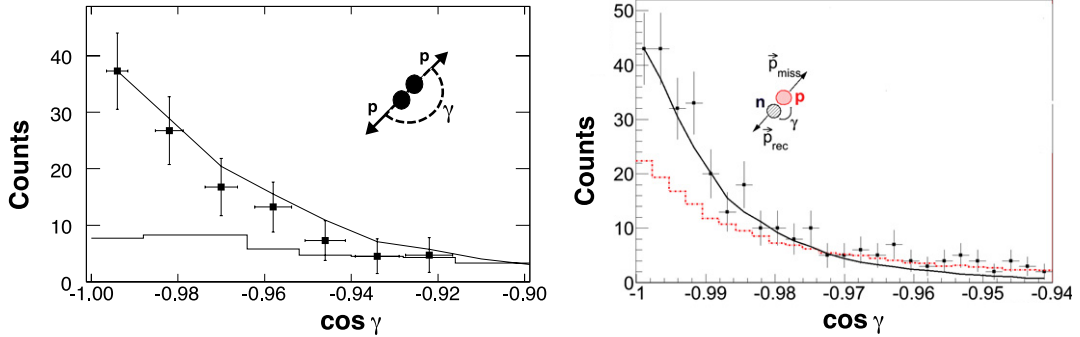


Fig. 74. (Left): the distribution of the cosine of the opening angle γ between the $\mathbf{p}_{\text{miss}} \equiv \mathbf{p}_m$ and \mathbf{p}_{rec} corresponding to $p_m = 0.55 \text{ GeV}/c$ in the process $^{12}\text{C}(e, e'\text{pp})$ at $Q^2 > 1 (\text{GeV}/c)^2$ [249]. The curve is a simulation of the scattering off a moving pair with center-of-mass motion described by a Gaussian with a width of $0.136 \text{ GeV}/c$. (Right): the same for the process $^4\text{He}(e, e'\text{pn})$ in correspondence of $p_m = 0.625 \text{ GeV}/c$ and $p_m = 0.75 \text{ GeV}/c$. The curve is a simulation of the scattering off a moving pair with the center-of-mass motion described by a Gaussian with a width of $0.100 \text{ GeV}/c$ [251]. The histograms show the distribution of random events. In both cases the widths of the Gaussian fully agree with the prediction of the convolution model of the spectral function [114] predicted on the basis of the mean kinetic energy of a shell-model description of both nuclei.
Source: Reprinted from [249] and [251]. © 2007 and 2014, by the American Physical Society.

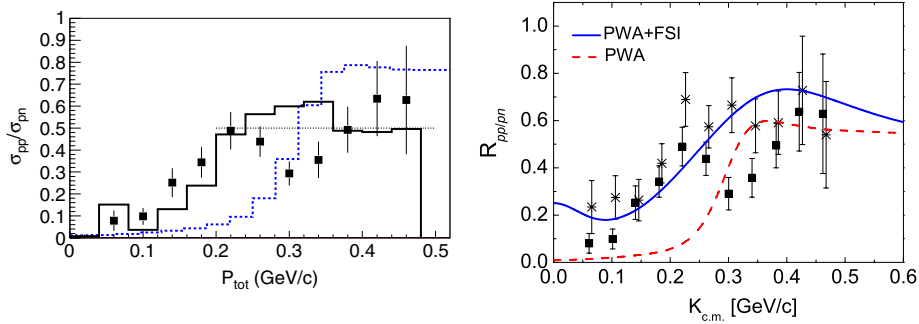


Fig. 75. Ratio of pp to pn spectator pair cross sections, integrated in the range $0.3 < p_{\text{rel}} < 0.5 \text{ GeV}/c$ vs the c.m. momentum $P_{\text{tot}} = K_{\text{c.m.}}$ of the spectator pair $pp(pn)$ obtained in Ref. [252] from the reaction $^3\text{He}(e, e'p)pn$. (Left): the points show the experimental data and the solid histogram shows the calculations of Ref. [253], based on *ab initio* three-nucleon Faddeev wave functions; the FSI between the spectator correlated nucleons is included and the one of the struck uncorrelated nucleon and the spectator pair is disregarded. The dashed histogram shows the ratio of the pp and pn bound state momentum distributions and the dotted line shows the ratio of the $pp/pn = 1/2$ pairs in ^3He . The data and the FSI calculation have been multiplied by 1.5 to approximately account for the ratio of the average ep and en elementary cross sections. (Right): the experimental data as in the (Left) panel compared with theoretical calculations of Ref. [97] based on *ab initio* three-nucleon wave functions of Ref. [48] using plane waves for the three-nucleon final state (PWA) and considering the FSI between the nucleons of the spectator pair (PWA + FSI).
Source: Reprinted from [252] and [97]. © 2008 and 2012, by the American Physical Society.

7. The relevance of short-range correlations in various fields

Whereas the previous chapters have been devoted to the theoretical predictions of SRCs and to the description of those experimental data that may provide information on them, here we will briefly describe several processes involving atomic nuclei where SRCs appear to play an important role.

7.1. Deep inelastic lepton–nucleus scattering and the EMC effect

It is well known that in 1983 CERN's European Muon Collaboration (EMC) investigating the parton structure of nucleons, by means of deep inelastic scattering of muons off ^2H and ^{56}Fe [254,255], found the unexpected result that the per nucleon ratio between the iron and deuteron structure functions

$$R_A(x_A, Q^2) = \frac{2}{A} \frac{F_2^A(x_A, Q^2)}{F_2^D(x_D, Q^2)}, \quad (7.1)$$

differed appreciably from one, in spite of the enormous differences in the energy scales of the incoming muons and of the target nuclei. This finding, called the EMC effect, was lately confirmed on a series of other experiments (see e.g. [256]),

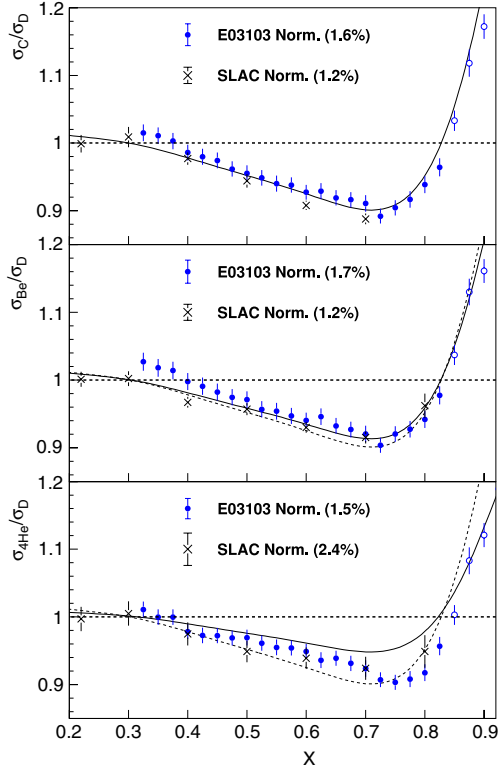


Fig. 76. (Color online) EMC ratios for ^{12}C , ^9Be , and ^4He , from Ref. [257] compared to SLAC data [256]. The ^9Be results include a correction for the neutron excess. The solid curve is the A-dependent fit to the SLAC data, while the dashed curve is the fit to ^{12}C . Normalization uncertainties are shown in parentheses for both measurements.

Source: Reprinted from [257].

© 2009, by the American Physical Society.

including the ones recently performed at Jlab shown in Fig. 76 [257].²⁵ The attempts to understand the origin of the EMC effect generated a plethora of possible theoretical explanations, ranging from the change of QCD scale in nuclei [259] to the effects of SRCs [260], but twenty years after the discovery of the effect its origin is still a matter of discussions (for an exhaustive recent list of experimental and theoretical review papers on the EMC effect see: [261–263]). It has been long ago demonstrated [264] that the slope of the ratio Eq. (7.1) at $x_A \lesssim 0.5$ is related to the mean nucleon's kinetic energy $\langle T \rangle$, and in Ref. [260] it has been shown, using *ab initio* spectral functions for few-nucleon systems and the 2N convolution model for complex nuclei, that SRCs, increasing nucleon's average kinetic and removal energies, lead indeed to a good agreement with the slope of the old EMC, being however unable alone to reproduce the entire x_A dependence of the effect. Recently, there was a renewal of interest in a possible connection between SRCs and the EMC effect, thanks to the new set of experimental data obtained at Jlab [257]. As a matter of fact, it has been illustrated in Ref. [265,266] that the slope of the EMC ratio at $x \leq 0.4$ and the value of the plateau $a_2(A)$ exhibited by the ratio of inclusive cross sections discussed in Section 6.3, are linearly related, as illustrated in Fig. 77. The microscopic origin of such a dependence has not been explained yet, but the correlation between the EMC effect and the values of a_2 might provide further evidence that the EMC effect should be a local short-range effect involving high momentum nucleons. The dependence of the structure function upon $\langle T \rangle$ can be shown by expanding F_2^A about $z = 1$ and by using the Koltun sum rule (see Section 5.1.2) obtaining [260]

$$F_2^A(x_A) \simeq F_2^N(x_A) + x_A F_2'^N \frac{2|\epsilon_A| + [(A-2)/(A-1)]\langle T \rangle}{m_N} + [2x_A F_2'^N + x_A^2 F_2''^N] \frac{2\langle T \rangle}{3m_N}, \quad (7.3)$$

where $F_2^{nN} \equiv \partial^n F_2'^N(x_A/z)/\partial z^n|_{z=1}$. Eq. (7.3) shows that the slope of the ratio Eq. (7.1) increases with increasing values of $\langle T \rangle$. Using typical values of the mean field average kinetics energies, $\langle T \rangle_{MF} \simeq 20$ MeV, lead to small slope of the EMC ratio [260].

²⁵ Note that in Eq. (7.1) the variable x_A is related to the Bjorken variable $x_B = Q^2/(2m_N v)$ by the following relation

$$x_A = \frac{Q^2}{2q \cdot P_A/A} = \frac{AQ^2}{2\nu m_A} = x_B \cdot \frac{Am_N}{M_A}, \quad (7.2)$$

resulting from the consideration of the structure function of a bound nucleon in the reference frame of the nucleus [258].

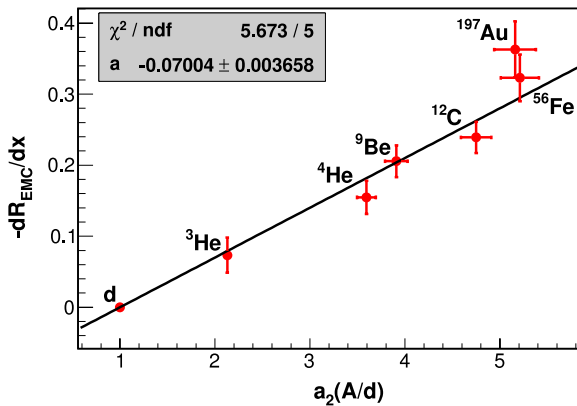


Fig. 77. The slope of the EMC effect for $0.35 \leq x_A \leq 0.7$ plotted vs. $a_2(A/d)$ (Eq. (6.49)), the constant ratio of the per-nucleon ratio of the quasi-elastic cross sections off nucleus A to the deuteron cross section discussed in Section 6.
Source: Reprinted from [266].

© 2012, by the American Physical Society.

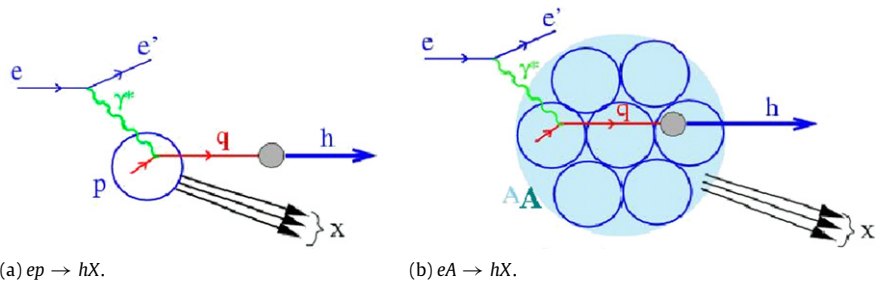


Fig. 78. Hadron production by DIS on a free nucleon (Left) and on a nucleus (Right). On a free nucleon hadronization, i.e. the production of hadrons by the hit quark, occurs on a microscopic scale, i.e. far from the detector, so that the latter detects only the produced colorless hadrons that have no memory of the initial stage of hadronization. In a nucleus the hit quark propagates in the medium and hadron production can be influenced by the FSI of the quark and the final hadron could be produced inside the nucleus, so that the detector will detect a number of hadrons with respect to the free case.
(Courtesy by Alberto Accardi).

SRCs, increasing the amount of high momentum components and, consequently the average value of $\langle T \rangle \gtrsim 40$ MeV brings theoretical calculations of the slope in better agreement with the experimental one. The calculation of the full x_B behavior of the EMC effect requires the knowledge of the full spectral function. A recent analysis, [262] based upon the 2N convolution model of the Spectral Function [114], aimed at understanding whether the experimental data requires, besides the effects of SRCs, also a modification of the free nucleon structure function, either in P_0 or in P_1 of Eq. (5.9), found that in the latter case the required modification of the structure function is only a few tenth percent. An increase of $\langle T \rangle$ would probably lead to the same conclusion. Understanding the EMC effect on a quantitative level is still an exciting challenge.

7.2. High energy diffractive hadron–nucleus and nucleus–nucleus scattering

The scattering of high energy hadrons off nuclei is providing important information on the properties of strong interactions. In the past nuclear targets in high energy physics were mainly used as generators of exotic particles and effective nucleon targets. Recently the role of the nucleus in high energy physics has been promoted to higher levels. As a matter of fact, it has been realized that nuclei can represent micro-detectors of several QCD effects that cannot be detected by the scattering between two free hadrons. Two important examples along this line are: (i) the phenomenon of *color transparency* (CT) [267,268], according to which hadrons produced in a nucleus at sufficiently high momentum transfer, behave as color neutral objects of reduced size, experiencing small interactions with other hadrons, and (ii) the phenomenon of *hadronization*, [269,270] describing the formation of a colorless hadron from a color object, like a quark, and providing basic information on the mechanism of confinement. The detailed investigation of both phenomena require the use of nuclear targets, because when a high energy probe hits a quark in a free nucleon, the created colored object, before forming the final hadron, travels a distance much higher than nuclear scales, so that only the formed colorless hadrons reach the detector, with no possibility to investigate the early stage of hadronization. If the color object is produced in a nucleus, it propagates in the medium by interacting with reduced final state interaction with the nuclear medium, affecting the formation time of the final hadrons, so that, by comparing the number of hadrons produced in nuclei of different sizes,

information on the hadron formation time could be obtained (see Fig. 78). Within such a picture, the effects of FSI is therefore playing a key, positive, role and a reliable theoretical approach to it is a prerequisite for obtaining unambiguous information on hadronization. At high energies FSI is usually treated within the Glauber approach, implemented by Gribov inelastic scattering. It is however a common practice in these treatments to approximate the nuclear density by a product of single nucleon densities ($|\Psi_0|^2 \rightarrow \prod \rho(i)$), disregarding by this way any type of short-range and statistical correlations (see Eq. (3.10) in Section 3). The role of SRCs in high energy scattering is being often advocated in recent years; let us illustrate it on the example of the total neutron–nucleus cross section σ_{tot}^{nA} , a quantity that: (i) has been experimentally measured with very high precision and in a wide kinematical range (see e.g. Ref. [271]), and (ii) has been the object of many theoretical analyzes and speculations, being very sensitive to various relevant phenomena, such as Glauber and Gribov diffractive scattering (see e.g. [271–275]). In terms of Glauber (Gl) elastic and Gribov inelastic scattering (IS) the total neutron–nucleus cross section is given by

$$\sigma_{tot}^{nA} = \sigma_A^{Gl} + \sigma_A^{IS} = \frac{4\pi}{k} \operatorname{Im} [F_{00}^{Gl}(0) + F_{00}^{IS}(0)], \quad (7.4)$$

where $F_{00}^{Gl(IS)}(0) = \frac{ik}{2\pi} \int d\mathbf{b}_n \Gamma_{00}^{Gl(IS)}(\mathbf{b}_n)$ is the forward elastic (inelastic) scattering amplitude, $\Gamma_{00}^{Gl(IS)}$ the nuclear elastic (inelastic) profile function and \mathbf{b}_n the impact parameter of the neutron moving along the z-axis. The scattering amplitude, within the Glauber approach, has the well-known form²⁶

$$\Gamma_{00}^{Gl}(\mathbf{b}_n) = 1 - \prod_{j=1}^A \langle \psi_0 | [1 - \Gamma_j^{NN}(\mathbf{b}_n - \mathbf{s}_j)] | \psi_0 \rangle \rightarrow 1 - e^{-T_A^{Gl}(\mathbf{b}_n)}, \quad (7.5)$$

where

$$T_A^{Gl}(\mathbf{b}_n) = A \int d\mathbf{s}_1 dz_1 \rho_1(\mathbf{s}_1, z_1) \Gamma(\mathbf{b}_n - \mathbf{s}_1), \quad (7.6)$$

is the *Glauber thickness function*. Here $\psi_0 \equiv \psi_0(\mathbf{r}_1, \mathbf{r}_2, \mathbf{r}_3, \dots, \mathbf{r}_A)$ ($\mathbf{r}_j = (\mathbf{s}_j, z_j)$) is the ground-state wave function of the target nucleus, and $\Gamma_j^{NN}(\mathbf{b}_n)$ the NN elastic profile function. It is well known that the total neutron–nucleus (nA) cross section at high energy is less than the sum of the total nucleon–nucleon cross sections $\sigma_{tot}^{NN}, \sigma_{tot}^{nA} \ll A \sigma_{tot}^{NN}$, the major mechanism for this effect being Glauber elastic shadowing, i.e. the shadow that a nucleon casts on other nucleons behind it, so that the incoming hadron impinging on the nucleus “sees” a number of nucleons less than A . It has been claimed in the past [271] that a quantitative agreement with the experimental data on the total nA cross section can only be achieved by the inclusion of Gribov inelastic shadowing, which increases the nuclear transparency, reducing by this way the total cross section. Such a statement has been object of criticism [272], arguing that nuclear radii used in Ref. [271] were too large by an appreciable (15%) quantity. In a recent paper [275] further criticism has been put forward, stressing that in Ref. [271], as in most calculations of the total nA cross section, the single-density approximation has been used, disregarding the higher order terms which include SRCs. In Ref. [275] a calculation of the total nA cross section has been undertaken introducing SRCs within the full expansion of the nuclear density given by Eq. (3.10). It should be recalled, in this connection, that Glauber in 1971 made a qualitative estimate of the effects of correlations on hadron–nucleus scattering, obtaining a total thickness function containing a correction term to Eq. (7.6) as follows

$$T_A^{Gl} \Rightarrow \tilde{T}_A^{Gl} = T_A^{Gl}(b) - \Delta T_A^{Gl}(b), \quad (7.7)$$

where

$$\Delta T_A^{Gl}(\mathbf{b}) = \left(\frac{2\pi A f(0)}{k} \right) \ell_c \int_{-\infty}^{+\infty} \rho^2(\mathbf{b}, z) dz, \quad (7.8)$$

where ℓ_c is a parameter measuring the “correlation length”. By assuming that the nuclear force has a range equal to \mathbf{a} , the leading approximation underlying the above equation is the following

$$\frac{\text{Range of NN force } \mathbf{a}}{\text{Range of correlations } \ell_c} \ll 1. \quad (7.9)$$

As warned by Glauber himself this can yield only a rough estimate of the effect of SRCs.²⁷ Qualitative calculations of SRCs employing more realistic $\Delta T_A(b)$ have been performed in several papers (see e.g., [274]), whereas a full quantitative calculations of σ_{tot}^{nA} has been performed in Ref. [275] using two-body contractions obtained from the fully-correlated wave function of Ref. [68] corresponding to the V8' interactions. By taking into account two-body correlations only, i.e. all terms

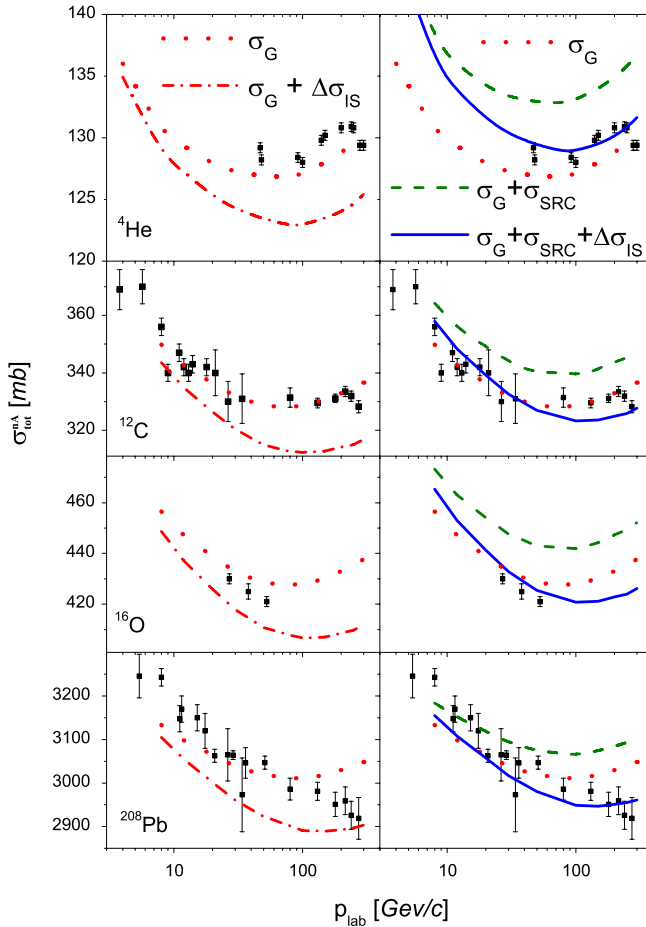


Fig. 79. The effect of SRCs on the total neutron–nucleus cross section at high energies [275]. The left panel shows the results which include Glauber scattering (dots) and Glauber plus Gribov inelastic scattering (dot-dash), whereas the right panel shows the effects of considering Glauber scattering plus SRCs (dash) and Glauber scattering plus SRCs plus Gribov inelastic scattering (full). The dotted line corresponds to the Glauber result shown in the left panel. Experimental data from Ref. [271].

Source: Reprinted from Ref. [275].

© 2008, by the American Physical Society.

of the expansion (3.10) containing all possible numbers of unlinked two-body contractions, one obtains

$$\Gamma_{00}^G(\mathbf{b}_n) \simeq 1 - e^{\left[-T_A^{GL}(\mathbf{b}_n) + \Delta T_A^{SRC}(\mathbf{b}_n) \right]}, \quad (7.10)$$

with T_A^{GL} given by Eq. (7.6) and the SRC term given by

$$\Delta T_A^{SRC}(\mathbf{b}_n) = \frac{A^2}{2} \int d\mathbf{s}_1 d\mathbf{s}_2 dz_1 dz_2 \Delta(\mathbf{s}_1, \mathbf{s}_2, z_1, z_2) \Gamma(\mathbf{b}_n - \mathbf{s}_1) \Gamma(\mathbf{b}_n - \mathbf{s}_2), \quad (7.11)$$

which vanishes when $\Delta = 0$. Concerning the inelastic profile Γ_{00}^{IS} , it can be reduced in the lowest order to an expression depending upon the total nucleon and diffractive cross sections σ_N and σ_r , respectively [273] whereas the inclusion of all higher order terms can be achieved within the so-called dipole approach [276]. The results of calculations of Ref. [275] in terms of contraction Δ including realistic SRCs and exactly satisfying the sum rule $\int d\mathbf{r}_1 \Delta(\mathbf{r}_1, \mathbf{r}_2) = 0$ are shown in Fig. 79 where the left panel shows the results obtained without correlations, and the results in the right panel include also the effects of two-nucleon correlations (for ${}^4\text{He}$ the cross section in Ref. [275] has been calculated to all orders of correlations finding

²⁶ To illustrate our arguments, we will use for ease of presentation the so called optical limit $(1+x)^A \simeq e^{-x/A}$ valid for large values of A .

²⁷ In Ref. [78] it is stated that: *Various types of correlations in positions and spin may exist between nucleons of an actual nucleus... If the system being considered is spatially uniform an idea of the magnitude and nature of the effects due to pair correlations may be obtained by assuming that the range of NN force \mathbf{a} is smaller than the range of correlations ℓ_c and the nuclear radius \mathbf{R} , $\ell_c \gg \mathbf{a}$ and $\mathbf{R} \gg \mathbf{a}$. Because \mathbf{R} is not vastly larger than \mathbf{a} , and the correlation length ℓ_c is not too different in magnitude from the force range, the approximations that follow from these conditions should only be used for rough estimates.*

that three- and four-nucleon correlations produce negligible effects). The results presented in Fig. 79 clearly show that: (i) when realistic one-body densities are considered the disagreement of the GA with the experimental data is not dramatic, which is at variance with the conclusions of Ref. [271]; (ii) within the one-body density approximation, inelastic shadowing corrections *increase* the nuclear transparency, which is a well-known result; (iii) NN correlations *decrease* the transparency (which is physically due to the reduction of the role of Glauber shadowing) and increase the total cross section (by an amount ranging from about 2% in ^{208}Pb up to about 5%–6% in ^4He) spoiling the agreement with the experimental data provided by the Glauber calculation; (iv) the simultaneous inclusion of inelastic shadowing and two-nucleon correlations brings back theoretical calculations in good agreement with experimental data. Thus if the correct values of nuclear radii are used, the interpretation of the experimental data would require the consideration of *both* NN correlations and inelastic shadowing. To sum up, SRCs, though being small in absolute value, appear to be of the same order as Gribov inelastic shadowing corrections and act in the opposite directions, a phenomenon that can naturally be explained in terms of the different effects produced on the nuclear transparency by SRCs and Glauber and Gribov shadowing. Following these results, the effects of SRCs have been included also in other high energy scattering process, like large rapidity gap processes [277] and the number of colliding nucleons [278], treating the inelastic shadowing corrections to all order by the dipole approach, finding again a contrasting effect between SRCs and Gribov inelastic corrections. The effects of realistic SRCs have been recently shown to produce effects also in heavy-ion collisions [279–281].

7.3. Neutrino physics

The three families of neutrinos, ν_e , ν_μ , and ν_τ , play a primary role in understanding several fundamental phenomena in different field of science [282], e.g.: (i) the energy production in the sun and the dynamics of core-collapse supernova, in astrophysics; (ii) the origin of the matter–antimatter asymmetry, in cosmology; (iii) the quark structure of hadrons and other properties of the standard model of electroweak interaction, in elementary particle physics. In spite of this important role played by neutrinos, information on their intrinsic properties have not been yet quantitatively fully collected. Because of their small interaction with matter, neutrinos can be detected only via the secondary particles that they produce interacting with protons and neutrons. Depending upon the type of boson they exchange with a hadron, neutrino interactions are classified in charged currents (CC) interactions, when a W^\pm boson is exchanged in the quasi elastic (q.e.) process

$$\nu + N \rightarrow \ell + X_N, \quad (7.12)$$

or neutral currents (NC) interactions, when a Z^0 boson is exchanged in the process

$$\nu + N \rightarrow \nu + X_N, \quad (7.13)$$

where ℓ stands for *lepton* and X_N denotes a nucleon in ground or resonance states. Recent experiments on solar and atmospheric neutrinos have eventually established that neutrinos have mass and oscillate between the three different flavors [283–287]. In these experiments neutrino reactions are identified by detecting secondary particles created by the interaction of neutrinos with nuclei like Carbon, Oxygen, Iron and Argon. A detailed accurate knowledge of neutrino–nucleus interaction is therefore a prerequisite for reaching the high precision which is necessary to extract reliable values of the neutrino mass and oscillation parameters. This has triggered a flourishing theoretical activity aimed at providing convincing and reliable treatments of neutrino–nucleus interaction. One of the main aims of such an activity concerns the description of the mechanism of production and propagation of the created hadron X_N in nuclear medium, which is required in order to understand quasi-elastic neutrino–nucleus scattering, particularly in the energy range 0.8–1 GeV. This is a range of energy where many experimental data and theoretical calculations have been produced on quasi-elastic electron scattering off nuclei, as illustrated in Section 6, where the importance of considering SRCs and FSI effects for a quantitative interpretation of the data has been demonstrated. Several theoretical groups are intensively working in the field of neutrino–nucleus scattering within a large spectrum of nuclear models.²⁸ In Ref. [288] a relativistic Fermi gas model is used to treat nuclear structure whereas in Ref. [289] the nuclear electro-weak structure functions are parametrized by directly fitting the response function to electron scattering data; the relativistic Green Function approach has been advocated in Ref. [290] to evaluate the effects of FSI within a Fermi gas treatment of the nucleus; a local Fermi gas plus the Random Phase Approximation (RPA) to account for multinucleon emission has been used in Refs. [291,292]; the work by [293,294] is based upon the Giessen–Boltzmann–Uehling–Uhlenbeck (GiBUU) transport theory which, besides q.e. scattering, includes also 2p–2h ground-state excitations, particle production, deep inelastic scattering and FSI; in Ref. [295] non-relativistic continuum RPA with effective NN interaction of the Skyrme type is the basis of the calculations. The work which is closer to the spirit of the present report is being performed by the Rome Group [296,297], which treats the nuclear ground state and the FSI of the produced hadrons in close analogy with electron scattering described in Section 6, i.e. in terms of realistic momentum distributions and spectral functions. Thus, in one boson exchange approximation, the cross section of the q.e. neutrino–nucleus inclusive cross section, in full analogy with electron scattering, is represented by

$$\frac{d^2\sigma_{IA}}{d\Omega dE_\ell} = \int d^3 k dE P_A(\mathbf{k}, E) \frac{d^2\sigma_{\text{elem}}}{d\Omega dE_\ell}, \quad (7.14)$$

²⁸ Due to the extensive production of papers in this field only the most recent ones will be quoted. There references to previous work can be found.

with the limits of integration and the expression of $\frac{d^2\sigma_{\text{elem}}}{d\Omega dk_\ell}$, obviously different from the ones pertaining to the exchange of a virtual photon γ^* , explicitly given in Ref. [297]. The use of a spectral function allows one to describe nucleon dynamics much better than the various forms of the Fermi gas that have been used in many papers. Nonetheless, it should however be remembered that the spectral function for complex nuclei is a model one, as described in Section 5; moreover another origin of model dependence is introduced by the FSI. How these influence the precision of the measurement should be probably checked by calculations using various models for the spectral functions and the FSI. It should also be pointed out that unlike electron–nucleus scattering data, for which the initial electron energy is exactly known, the νA and $\bar{\nu} A$ data are ν ($\bar{\nu}$)-flux integrated [298] so that additional difficulties arise from the reconstruction of the neutrino energy. Despite the enormous improvements in the experimental and theoretical understanding of (anti)neutrino–nucleus interactions in the few GeV region, the current experimental precision is of the order of 20–30% and the underlying processes on bound nucleons are not fully understood [298,299]. Coming back to the topic of SRCs, an interesting result has been recently reported by the MiniBooNE [300] and the Minerva [301] collaborations: measuring neutrino and antineutrino charge and neutral current scattering, an appreciable cross section exceeding the quasi-elastic predictions has been found and it has been suggested by the Minerva collaboration that this cross section could be due to two-nucleon correlation effects, specifically to the absorption of the neutrino by a nucleon of a correlated NN pair, followed by the recoil emission of the partner nucleon, namely

$$\bar{\nu}(np) \rightarrow \mu^+(nn) \quad (7.15)$$

$$\nu(np) \rightarrow \mu^-(pp), \quad (7.16)$$

i.e. with exactly the same mechanism leading to two nucleon emission in the $A(e, e'pp)X$ analyzed in Section 6.5.2. To test such a possibility and to rule out other mechanisms leading to two-nucleon emission, e.g. long-range two-nucleon effects like MEC, a semi-inclusive experiment measuring the directional correlation between the two nucleons in the final state, as it has been done in the case of the $A(e, e'N_1N_2)X$ process, would be necessary. Recently back-to-back protons with momenta higher than Fermi momentum were detected by the ArgoNeuT detector in the Main Injector neutrino beam at Fermilab [302]. Part of these events were compatible with the one-body quasi-elastic interaction of the neutrino with the neutron of a correlated pn pair in the Argon nucleus, with the proton recoiling in the back direction, i.e. the exactly the same mechanism occurring in the process $A(e, e'pp)X$.

The evidence and relevance of SRCs in a wider class of processes appears to rapidly increase.

8. Summary and outlook

We have reviewed recent theoretical and experimental progress in the long-standing and fundamental problem concerning the investigation of in-medium nucleon–nucleon short-range behavior, usually referred to as the problem of SRCs in nuclei. We have first of all emphasized the progress reached in the solution of the non relativistic Schrödinger equation for finite nuclei in terms of bare NN interactions as well as in the calculation of various kinds of density matrices (one- and two-body, diagonal and non diagonal, spin-isospin independent and dependent ones), that provide a detailed picture of in-medium NN distribution at short range and in particular on the universal character of the correlation hole at short internucleon distances. After that, we reviewed calculations by various groups of one- and two-nucleon momentum distributions illustrating several non trivial features of the high momentum part produced by the correlation hole. Concerning the one-nucleon momentum distribution, the following features have been stressed:

- the content of the high momentum components ($k \gtrsim 1.5\text{--}2 \text{ fm}^{-1}$), is very high representing about 20% of the total normalization, and it is such that in isoscalar nuclei the momentum distribution is, to a large extent, independent of A and overwhelms the mean-field distribution by orders of magnitude;
- the high momentum part is generated by nucleons which are members of correlated two-nucleon pairs with all possible values of the spin-isospin (ST) states (or, equivalently, of both even and odd values of the orbital momentum L), in particular the $(ST) = (10), (11), (01)$, contribute to generate the total momentum distributions;
- the shape of the high momentum part scales with A in that, apart from trivial normalization factors, it is almost independent of the nucleus mass;
- because of the contribution of all (ST) states and because of the center-of-mass motion of NN pairs in a nucleus, the momentum distributions in isoscalar nuclei cannot be quantitatively represented as a rescaled momentum distribution of the deuteron; on the contrary, in non isoscalar nuclei, like the mirror nuclei ${}^3\text{He}$ and ${}^3\text{H}$, the larger number of pn pairs makes the (normalized to one) momentum distribution of the minor component of nucleons (e.g. n in ${}^3\text{He}$ and p in ${}^3\text{H}$) more similar to the deuteron distribution, and higher than the one of the larger component.

As for the two-nucleon momentum distribution $n_A^{N_1N_2}(\mathbf{k}_1, \mathbf{k}_2) = n_A^{N_1N_2}(\mathbf{k}_{\text{rel}}, \mathbf{K}_{\text{c.m.}})$, the most interesting features at high relative momenta $k_{\text{rel}} \gtrsim 2 \text{ fm}^{-1}$ can be summarized as follows:

- the relative momentum distribution of pn pairs with back-to-back nucleons ($K_{\text{c.m.}} = 0$) in state $(ST) = (10)$, turned out to be nothing but the rescaled deuteron momentum distribution;

- due to the effects of the tensor force, the back-to-back pn relative momentum distribution in the region $1.5 < k_{rel} < 3 \text{ fm}^{-1}$ differs (is larger) from the back-to-back pp distribution by an appreciable amount, with the difference decreasing with increasing value of k_{rel} , when the core region is approached;
- the relative momentum distribution, which is obtained by integrating the two-nucleon distribution over the *c.m.* coordinate of the pair, does differ from the back-to-back relative distribution and, from the deuteron momentum distribution; in particular the integration over the *c.m.* coordinate fills in the dip exhibited in the region $1.5 \lesssim k_{rel} \lesssim 2.5 \text{ fm}^{-1}$ by the pp back-to-back distribution which does not get contribution from the tensor force;
- at high values of the relative momentum ($k_{rel} \geq 2 \text{ fm}^{-1}$) coupled with low values of the *c.m.* momentum ($K_{c.m.} \leq 1 \text{ fm}^{-1}$), the two-nucleon momentum distributions factorizes, to a large extent, as follows

$$n_A^{N_1 N_2}(\mathbf{k}_{rel}, \mathbf{K}_{c.m.}) \propto n^{N_1 N_2}(k_{rel}) n_A^{N_1 N_2}(K_{c.m.}) \quad (8.1)$$

with the A -dependent *c.m.* momentum distribution $n_A^{N_1 N_2}(K_{c.m.})$ associated to the shell-model average kinetic energy of the nucleus, and the A -independent relative momentum distribution, $n^{N_1 N_2}(k_{rel})$, associated, in the case of an pn pair, to the deuteron moment distribution. We have stressed that the factorization property appears to be a universal feature, being microscopically predicted in the wave function of few-nucleon systems and nuclear matter.

A fundamental quantity in the study of SRCs is the hole spectral function $P(k, E)$. The *ab initio* spectral functions of the three-nucleon systems and the microscopic spectral function of nuclear matter have been reviewed in detail, together with two widely used models for complex nuclei, namely: (i) the one in which the correlated part of the nuclear matter spectral function is used, via the local density approximation, in finite nuclei, and (ii) the one, called the convolution model, which, exploiting the factorization property of the nuclear wave function in momentum space is expressed in terms of a convolution integral of the relative and *c.m.* momentum distributions, two quantities that, nowadays, can be calculated *ab initio*. The two models agree very well in case of nuclear matter, but the degree of agreement in case of final nuclei is at present not completely known. To sum up, the message of the first part of the review was aimed at stressing that at present *ab initio* calculations of the details of in medium short-range NN dynamics generated by bare NN interactions, can be calculated with high degree of confidence, with the uncertainties related to the approximations used in the past to solve the Schrödinger equation drastically reduced. In view of these important theoretical achievement, the central issue is now whether the predictions of SRCs resulting from bare NN interactions, featuring strong short-range repulsive core, are supported or rejected by experimental evidences in complex nuclei. The second part of the report was therefore devoted to the analysis of available experimental data that could be related to in-medium NN short-range behavior. Keeping in mind the difficulties related to the fact that nucleon momentum distributions are not observable, but can only be extracted from proper cross sections within various approximations concerning the effects of FSI and MEC, a series of processes were reviewed that have been investigated in kinematical regions (high Q^2 and $x_B > 1$) where the dominant degrees of freedom are the nucleonic ones, and the effects of the FSI can reliably be treated within advanced parameter-free methods, based upon generalized Glauber-like multiple scattering approaches developed in recent years. The analyzed processes mainly include inclusive $A(e, e')X$, double-coincidence exclusive $A(e, e'p)X$ and triple coincidence exclusive $A(e, e'pN)X$ processes. Concerning the first process, we have reviewed the analysis of a wealth of experimental data performed in terms of the Y -scaling properties of the reduced cross sections and in terms of the x_B dependence of the cross section ratio. In the first case, the one-nucleon momentum distribution of several nuclei has been extracted by a method in which the effects of the FSI are partially removed by a proper extrapolation procedure of the experimental data to the asymptotic limit, and by removing the model dependence due to binding effects by the use of a proper scaling variable. Nonetheless at $k \gtrsim 1.5\text{--}2 \text{ fm}^{-1}$ the extracted momentum distributions are affected by large errors which do not allow the precise determination of different intensities of the short-range repulsion, but that, anyway, rule out any MF description. Moreover, from such an analysis it has been learned that though the FSI effects are large, they are apparently confined mainly within the correlated pair and are similar in a complex nucleus and in the deuteron. At the same time, the experimental data on the cross ratio vs x_B clearly show the constant behavior in the region $1.3 \lesssim x_B \lesssim 1.8$, signaling the effects from two-nucleon SRCs and providing further evidence about the similarity of FSI effects in nucleus A and in the deuteron. The theoretical treatment of FSI in inclusive scattering does not seem to us completely settled, unlike the case of exclusive double-coincidence process $A(e, e'p)X$, where important progress has been done in the treatment of the reaction mechanism, within parameter-free unfactorized cross sections, with FSI treated within improved Glauber-type approaches. Theoretical calculations based on *ab initio* ground-state wave functions corresponding to the AV18 interaction correctly reproduce available experimental data on few-nucleon system and confirm that the cross section at fixed value of high missing momentum p_m exhibits peaks at values of the missing energy $E_m \simeq (A - 2)p_m^2/[2(A - 1)m_N]$, as predicted by the basic mechanism of two-nucleon SRCs, but, at the same time, the experimental data are largely affected by FSI which overwhelm the fine details of SRCs like, e.g., the intensity of the short-range repulsion.

More reliable information on in medium short-range NN dynamics has been obtained from the very recent experimental data on triple coincidence experiments $A(e, e'pN)X$, performed mainly at JLab, but limited, so far, to the nuclei of ${}^4\text{He}$ and ${}^{12}\text{C}$ and, on a less extent, to the nucleus of ${}^3\text{He}$. These experimental data provide information on:

- the dominance of back-to-back correlated pairs in both nuclei, in that the emission of a high-momentum nucleon by the external probe is always accompanied by the emission of a recoiling high momentum nucleon directionally correlated with the first one, namely emitted in the opposite direction that the first nucleon had before being struck;

- the second nucleon is emitted within a cone generated by the *c.m.* motion of the correlated pair in the initial state, which can be associated to a Gaussian-like distribution with a width in agreement with the factorized configuration of the two-nucleon momentum distributions;
- the measured ratio of the pp/pn pairs in ${}^4\text{He}$ and ${}^{12}\text{C}$ in the region $1.5 < k_{rel} < 3 \text{ fm}^{-1}$, $K_{c.m.} \simeq 0$ is in full agreement with the ratio of pp and $p\bar{n}$ distributions $n_A^{N_1 N_2}(k_{rel}, K_{c.m.} \simeq 0)$ and reflects the leading role of the tensor force in the $p\bar{n}$ distributions;
- with increasing values of k_{rel} the pp/pn ratio appreciably increases since the effects of the repulsive core become more important;
- the pp/pn ratio in ${}^3\text{He}$ integrated in the range $1.5 < k_{rel} < 3 \text{ fm}^{-1}$ and plotted vs the common $K_{c.m.}$ of the pairs, increases with increasing values of $K_{c.m.}$ due to the filling in of the dip in the pp distributions, in full agreement with theoretical predictions.

All of the above experimental findings, can be reconciled with theoretical calculations based upon the GFMC or realistic linked-cluster expansion approaches, using the AV18 or AV8' interactions, agree with the behavior of the theoretical two-nucleon momentum distribution and confirm the factorization property of the wave function. It should however be stressed that being several experimental quantities related to cross section ratios it should not be excluded that a different, softer NN interaction with the same *central/tensor* strength would lead to similar results.

So far with the Summary. As for the Outlook, the following theoretical developments would be necessary for a better interpretation of the experimental data:

- a full microscopic calculation of the pp/pn ratio with the complete unfactorized cross section, taking explicitly into account FSIs, so as to fully understand the mechanism of the apparent similarity of FSI in complex nuclei and in the deuteron in the correlation region;
- a full microscopic calculation of the cross section ratio vs x_B including the effects of FSIs is necessary in order to fully understand the microscopic mechanism that leads to the plateaux;
- a microscopic calculation of the k_{rel} and $K_{c.m.}$ dependences of the two-nucleon momentum distributions in heavy nuclei with particular emphasis to the region $1.5 \lesssim k_{rel} \lesssim 4 \text{ fm}^{-1}$ $0 \lesssim k_{rel} \lesssim 1 \text{ fm}^{-1}$ should be performed to check whether the factorization property has a universal character; in this connection it would be desirable to perform an analysis of the high (low) $k_{rel}(K_{c.m.})$ structure of microscopic wave functions of the type that have been done in case of few-nucleon systems;
- the above calculations should be extended to non-isoscalar nuclei where, as it has been theoretically demonstrated in the case of the three-nucleon systems, proton and neutron distributions are differently affected by SRCs due to the dominance of SRCs in $p\bar{n}$ pairs;
- last, but not least microscopic calculations of the inclusive and exclusive cross sections in terms of NN interactions than the Argonne family ones, in particular chiral effective interactions, might represent a milestone in the study of in-medium short-range NN dynamics.

Concerning experimental developments it would be desirable:

- to extend the measurements in the deuteron to higher values of the momentum with the aim of extracting the $p\bar{n}$ momentum distribution in the core region;
- to extend the inclusive cross section ratios in order to reach the region of the onset of the three-nucleon correlation plateau at $x_B > 2$;
- to extend the triple coincidence experiments to other nuclei, in particular to isoscalar closed shell nuclei, like e.g. ${}^{16}\text{O}$ and ${}^{40}\text{Ca}$, for which all necessary kinds of momentum distributions have already been produced;
- to extend the inclusive, double coincidence and triple coincidence experiments to neutron reach nuclei, in order to study in more details the effects of deuteron-like $p\bar{n}$ SRC pairs on the momentum distributions and cross section ratio;
- to extend the triple coincidence experiments to higher values of k_{rel} to check the region of the core as it has been done in the case of ${}^4\text{He}$;

Data taking regarding several of these experimental developments have been already completed (see e.g. [303,304]) and new experiments are planned at 12 GeV upgraded Jlab (see e.g. [305]).

Acknowledgments

This work was partly supported by CONICYT (Comision Nacional de Investigacion Cientifica y Tecnica), Chile, under the project MEC 80122017. I thank Professors Ivan Schmidt and Boris Kopeliovich for warm hospitality at the Departamento de Física, Centro de Estudios Subatómicos, Universidad Técnica Federico Santa María, Valparaíso, Chile. Partial support from EPLANET (The European Particle physics Latin America NETwork) is gratefully acknowledged. This report contains large part of the work done together with my former Ph.D. students Massimiliano Alvioli, Simonetta Liuti, Chiara Benedetta Mezzetti, Giovanni Salme, Sergio Scopetta, Silvano Simula, and Veronica Palli, as well as with various friends and collaborators, in particular, Michail Braun, Leonid Frankfurt, Leonid Kaptari, Boris Kopeliovich, Hiko Morita, Emanuele Pace, Mark Strikman, and Daniele Treleani. To all of them I express my sincere gratitude.

References

- [1] Nuclear Science: A Long Range Plan, The DOE/NSF Nuclear Science Advisory Committee, USA, February 1996.
- [2] A. Deshalit, H. Feshbach, Theoretical Nuclear Physics: Nuclear Structure, John Wiley & Sons, 1974.
- [3] A. Bohr, B.R. Mottelson Bohr, Nuclear Structure, World Scientific, 1988.
- [4] R.J. Furnstahl, A. Schwenk, Focus issue on open problems in nuclear structure, *J. Phys. G* 6 (2010) 37.
- [5] R. Jastrow, *Phys. Rev.* 98 (1955) 1479.
- [6] K. Gottfried, *Ann. Phys.* 21 (1963) 29.
- [7] S.K. Bogner, R.J. Furnstahl, A. Schwenk, *Progr. Part. Nucl. Phys.* 65 (2010) 94.
- [8] S.K. Bogner, T.T.S. Kuo, A. Schwenk, *Phys. Rep.* 386 (2003) 1.
- [9] R.J. Furnstahl, K. Ebeler, *Rep. Progr. Phys.* 76 (2013) 126301.
- [10] E.R. Anderson, S.K. Bogner, R.J. Furnstahl, R.J. Perry, *Phys. Rev. C* 82 (2010) 054001.
- [11] S.K. Bogner, D. Roscher, *Phys. Rev. C* 86 (2012) 064304.
- [12] L. Frankfurt, M. Strikman, *Phys. Rep.* 76 (1981) 215;
L. Frankfurt, M. Strikman, *Phys. Rep.* 160 (1988) 235.
- [13] J. Arrington, D.W. Higinbotham, G. Rosner, M. Sargsian, *Prog. Part. Nucl. Phys.* 67 (2012) 898.
- [14] L. Frankfurt, M. Sargsian, M. Strikman, *Int. J. Mod. Phys. A* 23 (2008) 2991.
- [15] M. Alvioli, C. Ciofi degli Atti, L.P. Kaptari, C.B. Mezzetti, H. Morita, *Int. J. Mod. Phys. E* 22 (2013) 1330021.
- [16] C. Ciofi degli Atti, NN and 3N Interactions, Nova Science Publishers, 2014.
- [17] H. Primakoff, T. Holstein, *Phys. Rev.* 55 (1939) 1218.
- [18] A. Nogga, H. Kamada, W. Glöckle, *Phys. Rev. Lett.* 85 (2000) 944.
- [19] A. Kievsky, M. Viviani, L. Girlanda, L.E. Marcucci, *Phys. Rev. C* 81 (2010) 044003.
- [20] S.C. Pieper, R.B. Wiringa, *Annu. Rev. Nucl. Part. Sci.* 51 (2001) 53.
- [21] H.-W. Hammer, A. Nogga, A. Schwenk, *Rev. Mod. Phys.* 85 (2013) 197.
- [22] P. Sauer, *Int. J. Mod. Phys. E* 23 (2014) 1430015.
- [23] J.R. Bergerová, et al., *Phys. Rev. C* 41 (1990) 1435;
V.G.R. Stoks, R.A.M. Klomp, M.C.M. Rentmeester, J.J. de Swart, *Phys. Rev. C* 48 (1993) 792.
- [24] R.V. Reid, *Ann. Phys. N.Y.* 50 (1968) 411.
- [25] R. Machleidt, *Adv. Nucl. Phys.* 19 (1989) 189.
- [26] M. Lacombe, et al., *Phys. Rev. C* 21 (1980) 861.
- [27] M.M. Nagels, T. Arijsken, J.J. de Swart, *Phys. Rev. D* 17 (1978) 768.
- [28] B.S. Pudliner, V.R. Pandharipande, J. Carlson, S.C. Pieper, R.B. Wiringa, *Phys. Rev. C* 56 (1997) 1720.
- [29] R.B. Wiringa, R.A. Smith, T.A. Ainsworth, *Phys. Rev. C* 29 (1984) 974.
- [30] R.B. Wiringa, V.G.J. Stoks, R. Schiavilla, *Phys. Rev. C* 51 (1995) 38.
- [31] H. Yukawa, *Proc. Phys. Math. Soc. Jap.* 17 (1935) 48.
- [32] M. Taketani, S. Nakamura, M. Sasaki, *Progr. Theoret. Phys.* 6 (1951) 581.
- [33] W. Weise, *Nucl. Phys. A* 805 (2008) 115c.
- [34] D.R. Entem, R. Machleidt, *Phys. Rev. C* 68 (2003) 041001(R).
- [35] R. Machleidt, D.R. Entem, *Phys. Rep.* 503 (2011) 1.
- [36] E. Epelbaum, W. Glöckle, U.-G. Meißner, *Nucl. Phys. A* 747 (2012).
- [37] E. Epelbaum, H.-W. Hammer, U.-G. Meißner, *Rev. Mod. Phys.* 81 (2009) 1773.
- [38] K. Wendt, R.J. Furnstahl, S. Ramanan, *Phys. Rev. C* 68 (2003) 014003.
- [39] A.L. Walecka, J.D. Fetter, Quantum Theory of Many-Particle Systems, McGraw-Hill, New York, 1971.
- [40] J.-P. Blaizot, G. Ripka, Quantum Theory of Finite Systems, The MIT Press, Cambridge, Massachusetts, 1986.
- [41] W.H. Dickhoff, D. VanNeck, Many-Body Theory Exposed, World Scientific, 2010.
- [42] L.D. Faddeev, *Sov. Phys. JETP* 12 (1961) 101.
- [43] O.A. Yakubovsky, *Sov. J. Nucl. Phys.* 5 (1967) 93.
- [44] W. Glöckle, The Quantum Mechanical Few-Body Problem, Springer Verlag Berlin, 1983.
- [45] H. Kamada, A. Nogga, W. Glöckle, et al., *Phys. Rev. C* 64 (2001) 044001.
- [46] B.S. Pudliner, et al., *Phys. Rev. Lett.* 73 (1995) 4396.
- [47] W. Glöckle, H. Witala, D. Huber, H. Kamada, J. Golak, *Phys. Rep.* 274 (1996) 107.
- [48] A. Kievsky, S. Rosati, M. Viviani, *Nucl. Phys. A* 551 (1993) 241;
L.E. Marcucci, L. Girlanda, A. Kievsky, S. Rosati, M. Viviani, *Few-Body Syst.* 44 (2008) 227.
- [49] H. Morita, Y. Akaishi, H. Tanaka, *Progr. Theoret. Phys.* 79 (1988) 863.
- [50] R. Schiavilla, V.R. Pandharipande, R.B. Wiringa, *Nucl. Phys. A* 449 (1986) 219.
- [51] K. Varga, Y. Suzuki, Stochastic Variational Approach to Quantum-Mechanical Few-Body Problems, in: Lecture Notes in Physics, vol. 54, Springer, 1998.
- [52] K. Varga, Y. Suzuki, *Phys. Rev. C* 52 (1995) 2885.
- [53] Y. Suzuki, W. Horiuchi, M. Orabi, K. Arai, *Few Body Syst.* 42 (2008) 33.
- [54] Y. Suzuki, H. Horiuchi, *Nucl. Phys. A* 81 (2009) 188.
- [55] H. Feldmeier, W. Horiuchi, T. Neff, Y. Suzuki, *Phys. Rev. C* 84 (2011) 054003.
- [56] W. Leidemann, G. Orlandini, *Progr. Part. Nucl. Phys.* 68 (2013) 158.
- [57] B.R. Barrett, P. Navratil, J.P. Vary, *Progr. Part. Nucl. Phys.* 69 (2013) 131.
- [58] H. Bethe, *Annu. Rev. Nucl. Sci.* 21 (1971) 93.
- [59] B.D. Day, *Rev. Mod. Phys.* 50 (1978) 495.
- [60] C. Mahaux, R. Sartor, *Phys. Rep.* 211 (1992) 53.
- [61] M. Baldo, C. Maieron, *J. Phys. G* 34 (2007) R243.
- [62] F. Coester, *Nucl. Phys.* 7 (1958) 421;
F. Coester, H. Kümmel, *Nucl. Phys.* 17 (1960) 477.
- [63] R. Roth, T. Neff, H. Feldmeir, *Progr. Part. Nucl. Phys.* 65 (2010) 50.
- [64] G. Hagen, T. Poppenbrock, M. Hjorth-Jensen, D.J. Dean, *Rep. Progr. Phys.* 77 (2014) 096302.
- [65] J.W. Clark, *Progr. Part. Nucl. Phys.* 2 (1979) 89.
- [66] R. Jastrow, *Phys. Rev.* 98 (1955) 1479.
- [67] M. Gaudin, J. Gillespie, G. Ripka, *Nucl. Phys. A* 176 (1971) 237.
- [68] M. Alvioli, C. Ciofi degli Atti, H. Morita, *Phys. Rev. C* 72 (2005) 054310.
- [69] S. Fantoni, S. Rosati, *Nuovo Cimento A* 43 (1978) 413.
- [70] R. Guardiola, *Nucl. Phys. A* 39 (1979) 328.
- [71] O. Bohigas, S. Stringari, *Phys. Lett.* 95B (1980) 9.
- [72] F. Arias de Saavedra, C. Bisconti, G. Co', A. Fabrocini, *Phys. Rep.* 450 (2007) 1.
- [73] J.E. Mayer, M.G. Mayer, Statistical Mechanics, Wiley, New York and London, 1940.

- [74] S.C. Pieper, R.B. Wiringa, Annu. Rev. Nucl. Part. Sci. 51 (2001) 53.
- [75] S.C. Pieper, Nucl. Phys. A751 (2005) 516c.
- [76] R.B. Wiringa, S.C. Pieper, Riv. Nuovo Cimento 31 (2008) 709.
- [77] J.E. Lynn, J. Carlson, E. Epelbaum, S. Gandolfi, A. Gerlezis, A. Schwenk, Phys. Rev. Lett. 113 (2014) 192501.
- [78] R.J. Glauber, in: W.R. Brittin et al. (Eds.), Lectures in Theoretical Physics, New York, 1959.
- [79] L. Foldy, J.D. Walecka, Ann. Phys. (N.Y.) 54 (1969) 447.
- [80] M. Alvioli, C. Ciofi degli Atti, L.P. Kaptari, C.B. Mezzetti, H. Morita, Phys. Rev. C87 (2013) 034603.
- [81] R.B. Wiringa, Phys. Rev. C73 (2006) 034317.
- [82] J.L. Forest, V.R. Pandharipande, S.C. Pieper, R.B. Wiringa, R. Schiavilla, A. Arriaga, Phys. Rev. C54 (1996) 646.
- [83] R.B. Wiringa, R. Schiavilla, S.C. Pieper, J. Carlson, Phys. Rev. C89 (2014) 024305.
- [84] M. Vanhalst, W. Cosyn J. Ryckebusch, Phys. Rev. C84 (2011) 031302.
- [85] M. Vanhalst, W. Cosyn J. Ryckebusch, Phys. Rev. C86 (2012) 044619.
- [86] M. Alvioli, C. Ciofi degli Atti, H. Morita, arXiv:0709:3989 (2007).
- [87] S.C. Pieper, R.B. Wiringa, V.R. Pandharipande, Phys. Rev. C46 (1992) 1741.
- [88] J.G. Zabolitzky, W. Ey, Phys. Lett. 76 (1978) 527.
- [89] O. Benhar, C. Ciofi degli Atti, S. Liuti, G. Salmè, Phys. Lett. B177 (1986) 135.
- [90] J.W. Van Orden, W. Truex, M.K. Banerjee, Phys. Rev. C21 (1980) 2628.
- [91] X.-D. Ji, J. Engel, Phys. Rev. C40 (1989) 497.
- [92] C. Ciofi degli Atti, E. Pace, G. Salmè, Phys. Lett. 141B (1984) 14.
- [93] C. Ciofi degli Atti, S. Liuti, Phys. Lett. B225 (1989) 215.
- [94] R. Schiavilla, R.B. Wiringa, S.C. Pieper, J. Carlson, Phys. Rev. Lett. 98 (2007) 132501.
- [95] R.B. Wiringa, R. Schiavilla, S.C. Pieper, J. Carlson, Phys. Rev. C78 (2008) 021001(R).
- [96] M. Alvioli, C. Ciofi degli Atti, H. Morita, Phys. Rev. Lett. 100 (2008) 162503.
- [97] M. Alvioli, C. Ciofi degli Atti, L.P. Kaptari, C.B. Mezzetti, H. Morita, S. Scopetta, Phys. Rev. C85 (2012) 021001.
- [98] M. Alvioli, C. Ciofi degli Atti, H. Morita, to be published.
- [99] M.M. Sargsian, T.V. Abrahamyan, M.I. Strikman, L.L. Frankfurt, Phys. Rev. C71 (2005) 044615.
- [100] D.S. Koltun, Phys. Rev. Lett. 28 (1972) 182.
- [101] A.E.L. Dieperink, T. de Forest Jr., I. Sick, R.A. Brandenburg, Phys. Lett. 63B (1976) 261.
- [102] C. Ciofi degli Atti, E. Pace, G. Salmè, Phys. Rev. C21 (1980) 805.
- [103] H. Meier-Hajduk, Ch. Hajduk, P.E. Sauer, W. Thies, Nucl. Phys. A395 (1983) 332.
- [104] A. Kievsky, E. Pace, G. Salmè, M. Viviani, Phys. Rev. C56 (1997) 64.
- [105] C. Ciofi degli Atti, L.P. Kaptari, Phys. Rev. C71 (2005) 024005.
- [106] A. Ramos, A. Polls, W.H. Dickhoff, Nucl. Phys. A503 (1989) 1.
- [107] C. Mahaux, R. Sartor, Nucl. Phys. A50 (1989) 525; Nucl. Phys. A604 (1996) 429.
- [108] O. Benhar, A. Fabrocini, S. Fantoni, Nucl. Phys. A505 (1989) 267.
- [109] J. Lehr, H. Lenske, S. Leupold, U. Mosel, Nucl. Phys. A703 (2002) 393.
- [110] H. Morita, T. Suzuki, Progr. Theoret. Phys. 86 (1991) 671.
- [111] C. Ciofi degli Atti, S. Liuti, S. Simula, Phys. Rev. C41 (1990) R2474.
- [112] O. Benhar, A. Fabrocini, S. Fantoni, I. Sick, Nucl. Phys. A579 (1994) 493.
- [113] C. Ciofi degli Atti, L. Frankfurt, S. Simula, M. Strikman, Phys. Rev. C41 (1990) R2474.
- [114] C. Ciofi degli Atti, S. Simula, Phys. Rev. C53 (1996) 1689.
- [115] C. Ciofi degli Atti, S. Simula, Phys. Lett. B319 (1993) 23.
- [116] M. Baldo, M. Borromeo, C. Ciofi degli Atti, Nucl. Phys. A604 (1996) 429.
- [117] C. Ciofi degli Atti, L.P. Kaptari, H. Morita, S. Scopetta, Few-Body Syst. 50 (2011) 243.
- [118] O. Benhar, D. Meloni, arXiv:hep-ph/0610403v1.
- [119] C. Ciofi degli Atti, L.L. Frankfurt, L.P. Kaptari, M.I. Strikman, Phys. Rev. C76 (2007) 055206.
- [120] C. Ciofi degli Atti, C.B. Mezzetti, to be published.
- [121] W.J.W. Geurts, K. Allart, W.H. Dickhoff, H. Müther, Phys. Rev. C54 (1996) 1144.
- [122] O. Benhar, A. Fabrocini, Phys. Rev. C62 (2000) 034304.
- [123] S. Bjorken, S.D. Drell, Relativistic Quantum Mechanics, McGraw Hill, New York, 1964.
- [124] B. Povh, K. Ruth, C. Scholz, F. Zetsche, Particles and Nuclei: An Introduction to Physical Concepts, Springer, 2008.
- [125] V. Barone, E. Predazzi, High-Energy Particle Diffraction, Springer, 2002.
- [126] C. Ciofi degli Atti, Progr. Part. Nucl. Phys. 3 (1980) 163.
- [127] T.W. Donnelly, Progr. Part. Nucl. Phys. 13 (1985) 183.
- [128] S. Boffi, C. Giusti, F.D. Pacati, Phys. Rep. 226 (1993) 1.
- [129] J. Carlson, R.J. Schiavilla, Rev. Mod. Phys. 70 (1998) 743.
- [130] O. Benhar, A. Lovato, N. Rocco, arXiv:1312.1210.
- [131] A. Lovato, S. Gandolfi, J. Carlson, S.C. Pieper, R. Schiavilla, Phys. Rev. C91 (2015) 06250(R).
- [132] J.D. Bjorken, Phys. Rev. 179 (1969) 1547.
- [133] T. de Forest Jr., Nucl. Phys. A392 (1983) 232.
- [134] C. Ciofi degli Atti, D. Day, S. Liuti, Phys. Rev. C46 (1992) 1045.
- [135] C. Ciofi degli Atti, L. Kaptari, S. Scopetta, Eur. J. Phys. A5 (1999) 191.
- [136] A. Bodek, J.L. Ritchie, Phys. Rev. D23 (1981) 1070.
- [137] O. Benhar, D. Day, I. Sick, Rev. Mod. Phys. 80 (2008) 189.
- [138] B.D. Day, et al., Phys. Rev. Lett. 59 (1987) 427.
- [139] B.D. Day, et al., Phys. Rev. Lett. 43 (1979) 1143.
- [140] B.D. Day, et al., Phys. Rev. C40 (1989) 1011.
- [141] M. Anghinolfi, et al., Nucl. Phys. A602 (1996) 405.
- [142] S. Rock, et al., Phys. Rev. Lett. 49 (1982) 1139.
- [143] R.G. Arnold, et al., Phys. Rev. Lett. 61 (1988) 806.
- [144] S. Rock, et al., Phys. Rev. C26 (1982) 1592.
- [145] G.B. West, Phys. Rep. 18 (1975) 263.
- [146] E. Pace, G. Salmè, Phys. Lett. B110 (1982) 411.
- [147] C. Ciofi degli Atti, E. Pace, G.E. Salmè, Phys. Rev. C36 (1987) 1208.
- [148] C. Ciofi degli Atti, E. Pace, G.E. Salmè, Phys. Rev. C39 (1989) 259.
- [149] C. Ciofi degli Atti, E. Pace, G. Salmè, Phys. Rev. C43 (1991) 1155.
- [150] I. Sick, Progr. Part. Nucl. Phys. 13 (1984) 165; Nucl. Phys. A434 (1985) 677; Phys. Lett. B157 (1985) 13.
- [151] I. Sick, D. Day, J.S. McCarthy, Phys. Rev. Lett. 45 (1980) 871.
- [152] D. Day, T.W. Donnelly, I. Sick, Annu. Rev. Nucl. Sci. 40357 (1990) 357.
- [153] H. Arenhövel, Nucl. Phys. A384 (1982) 287;

W. Leidemarm, H. Arenhövel, private communication.

- [154] N. Fomin, et al., Phys. Rev. Lett. 108 (2012) 092502.
- [155] M. Bernheim, et al., Phys. Rev. Lett. 46 (1981) 402; Nucl. Phys. A365 (1981) 349.
- [156] P. Bosted, et al., Phys. Rev. Lett. 49 (1982) 1380.
- [157] W.P. Schultz, et al., Phys. Rev. Lett. 38 (1977) 259.
- [158] F. Coester, Nucl. Phys. A543 (1992) 427c.
- [159] S.A. Gurvitz, A.S. Rinat, R. Rosenfelder, Phys. Rev. C40 (1989) 1363.
- [160] E. Pace, G. Salmè, G.B. West, Phys. Lett. 273 (1997) 417.
- [161] E. Jans, et al., Phys. Rev. Lett. 49 (1982) 974;
E. Jans, et al., Nucl. Phys. A475 (1987) 687;
C. Marchand, et al., Phys. Rev. Lett. 60 (1988) 1703.
- [162] J.F.J. van den Brand, et al., Phys. Rev. Lett. 60 (1988) 2006.
- [163] A. Magnon, et al., Phys. Lett. B222 (1989) 352.
- [164] C. Ciofi degli Atti, G.B. West, Phys. Lett. B458 (1999) 447.
- [165] C. Ciofi degli Atti, D. Faralli, G.B. West, in: O. Benhar, A. Fabrocini, R. Schiavilla (Eds.), Proceedings of the Elba Workshop on Electron Nucleus Scattering, Edizioni ETS, Pisa, 1999.
- [166] C. Ciofi degli Atti, D. Faralli, G.B. West, in: S. Boffi, C. Ciofi degli Atti, M. Giannini (Eds.), Perspectives in Hadronic Physics, World Scientific, 2000, p. 75.
- [167] C. Ciofi degli Atti, C.B. Mezzetti, Phys. Rev. C79 (2009) 051302(R).
- [168] C.B. Mezzetti, Ph.D. thesis, University of Perugia, 2010, arXiv:1003.3650 [nucl-th].
- [169] C.B. Mezzetti, C. Ciofi degli Atti, arXiv:0906.5564 [nucl-th], 2009.
- [170] L.L. Frankfurt, M.I. Strikman, D.B. Day, M. Sargsian, Phys. Rev. C48 (1993) 2451.
- [171] K.S. Egyian, et al., Phys. Rev. Lett. 96 (2006) 082501.
- [172] N. Fomin, arXiv:0812.2144 [nucl-ex].
- [173] O. Benhar, A. Fabrocini, S. Fantoni, G.A. Miller, V.R. Pandharipande, I. Sick, Phys. Rev. 44 (1991) 2328.
- [174] O. Benhar, Phys. Rev. C87 (2013) 2.
- [175] C. Mahaux, R. Sartor, Nucl. Phys. A458 (1986) 25.
- [176] W. Heider, A.M. Kobos, J.R. Rook, Nucl. Phys. A438 (1985) 1.
- [177] T. Uchiyama, A.E.L. Dieperink, O. Scholten, Phys. Lett. B233 (1989) 31.
- [178] C. Ciofi degli Atti, L.P. Kaptari, D. Treleani, Phys. Rev. C63 (2001) 044601.
- [179] C. Ciofi degli Atti, S. Simula, Phys. Lett. B325 (1994) 276.
- [180] C. Ciofi degli Atti, S. Simula, Proceedings of the XIIth International Conference on Particles and Nuclei, Perugia, Italy, June 28–July 2, 1993, World Scientific, 1994, p. 448.
- [181] O. Benhar, A. Fabrocini, S. Fantoni, I. Sick, Phys. Lett. B343 (1995) 47.
- [182] C. Ciofi degli Atti, Contemporary issues in nuclear physics, in: Talk given at the Workshop High Density Nuclear Physics and QCD, Yerevan, October 6–10, 2008.
- [183] Ugo Amaldi jr., et al., Phys. Rev. Lett. 13 (1964) 341; Phys. Lett. 25B (1967) 24.
- [184] G. Van der Steenhoven, et al., Nucl. Phys. A480 (1988) 547.
- [185] S. Cohen, D. Kurath, Nucl. Phys. 73 (1965) 1.
- [186] A.G.M. Van Hees, P.W.M. Glaudemans, Z. Phys. A315 (1984) 223.
- [187] S. Frullani, J. Mougey, Adv. Nucl. Phys. 14 (1984) 1.
- [188] J. Kelly, Adv. Nucl. Phys. 23 (1966) 75.
- [189] N.N. Nikolaev, J. Speth, B.G. Zacharov, Nucl. Phys. A582 (1995) 665.
- [190] V.N. Gribov, Sov. Phys. JETP 30 (1970) 709.
- [191] L. Bertocchi, Nuovo Cimento 11A (1972) 45.
- [192] L.L. Frankfurt, W.R. Greenberg, G.A. Miller, M.M. Sargsian, M.I. Strikman, Z. Phys. A352 (1995) 97.
- [193] L.L. Frankfurt, M.M. Sargsian, M.I. Strikman, Phys. Rev. C56 (1997) 1124.
- [194] M.M. Sargsian, Int. J. Mod. Phys. E10 (2001) 405.
- [195] P.E. Ulmer, et al., Phys. Rev. Lett. 89 (2002) 062301.
- [196] W. Boeglin, et al., Phys. Rev. Lett. 107 (2011) 262501.
- [197] S. Jeschonnek, J.W. Van Orden, Phys. Rev. C 78 (2008) 014007.
- [198] M.M. Sargsian, Phys. Rev. C82 (2010) 014612.
- [199] W.P. Ford, S. Jeschonnek, J.W. Van Orden, arXiv:1411.3306 [nucl-th].
- [200] F. Gross, J. Van Orden, K. Holinde, Phys. Rev. C45 (1992) 2094.
- [201] F. Gross, A. Stadler, Few Body Syst. 44 (2008) 295.
- [202] V. Stoks, R. Klomp, C. Terheggen, J. de Swart, Phys. Rev. C49 (1994) 2950.
- [203] C. Marchand, et al., Phys. Rev. Lett. 60 (1988) 1703.
- [204] M.M. Rvachev, et al., Phys. Rev. Lett. 94 (2005) 192302.
- [205] F. Benmokhtar, et al., Phys. Rev. Lett. 94 (2005) 082305.
- [206] C. Ciofi degli Atti, L.P. Kaptari, Phys. Rev. Lett. 95 (2005) 052502.
- [207] R. Schiavilla, O. Benhar, A. Kievsky, L.E. Marcucci, M. Viviani, Phys. Rev. C 72 (2005) 064003.
- [208] W.P. Ford, R. Schiavilla, J.W. Van Orden, Phys. Rev. C 89 (2013) 034004.
- [209] C. Ciofi degli Atti, L.P. Kaptari, H. Morita, Nucl. Phys. A 782 (2007) 175.
- [210] C. Ciofi degli Atti, L.P. Kaptari, Phys. Rev. Lett. 100 (2005) 122301.
- [211] M. Alvioli, C. Ciofi degli Atti, L.P. Kaptari, Phys. Rev. C81 (2010) 021001(R).
- [212] C. Ciofi degli Atti, L.P. Kaptari, Phys. Rev. C66 (2002) 044004.
- [213] J.-M. Laget, Phys. Lett. B609 (2005) 49.
- [214] SAID: <http://pdg.lbl.gov/> and <http://said.phys.vt.edu/>.
- [215] C. Ciofi degli Atti, L.P. Kaptari, H. Morita, Nucl. Phys. A782 (2007) 191.
- [216] C. Ciofi degli Atti, L.P. Kaptari, H. Morita, Nucl. Phys. A805 (2008) 197.
- [217] C. Ciofi degli Atti, L.P. Kaptari, H. Morita, Few-Body Syst. 43 (2008) 39.
- [218] H. Morita, M. Braun, C. Ciofi degli Atti, D. Treleani, Nucl. Phys. A699 (2002) 328c.
- [219] M.A. Braun, C. Ciofi degli Atti, L.P. Kaptari, H. Morita, Nucl. Phys. A737 (2004) 3.
- [220] B. Reitz, et al., Eur. Phys. J. A619 (2004) 165.
- [221] M.A. Braun, C. Ciofi degli Atti, D. Treleani, Phys. Rev. C62 (2000) 034606.
- [222] M.A. Braun, C. Ciofi degli Atti, L.P. Kaptari, Phys. Rev. C60 (2000) 034003.
- [223] M. Braun, C. Ciofi degli Atti, L.P. Kaptari, Eur. J. Phys. A19 (2004) 143.
- [224] O. Benhar, N.N. Nikolaev, J. Speth, A.A. Usmani, B.G. Zakharov, Nucl. Phys. A673 (2000) 241.
- [225] D. Rohe, et al., Phys. Rev. Lett. 93 (2004) 182501.
- [226] D. Rohe, et al., Phys. Rev. C72 (2005) 054602.
- [227] C. Barbieri, D. Rohe, I. Sick, L. Lapikas, Phys. Lett. B608 (2005) 47.
- [228] H. Muther, G. Knehe, A. Polls, Phys. Rev. C52 (1955) 2955.
- [229] T. de Forest Jr., Ann. Phys. 45 (1967) 365.

- [230] C. Ciofi degli Atti, in: O. Benhar, A. Fabrocini (Eds.), Two Nucleon Emission Reactions, ETS Editrice, Pisa, 1990, p. 1.
- [231] O. Benhar, A. Fabrocini, S. Fantoni, in: O. Benhar, A. Fabrocini (Eds.), Two Nucleon Emission Reactions, ETS Editrice, Pisa, 1990.
- [232] S. Boffi, in: O. Benhar, A. Fabrocini (Eds.), Two Nucleon Emission Reactions, ETS Editrice, Pisa, 1999.
- [233] J.J. van Leeuwe, et al., Phys. Lett. B523 (2001) 6.
- [234] J. Ryckebusch, M. Vanderhaeghen, L. Machenil, M. Waroquier, Nucl. Phys. A568 (1994) 828.
- [235] J. Ryckebusch, L. Machenil, M. Vanderhaeghen, V. Van der Sluys, M. Waroquier, Phys. Rev. C49 (1994) 2704.
- [236] J. Ryckebusch, M. Vanderhaeghen, K. Heyde, M. Waroquier, Phys. Lett. B350 (1995) 1.
- [237] J. Ryckebusch, et al., Nucl. Phys. A624 (1997) 581.
- [238] C. Giusti, F.D. Pacati, M. Schwamb, S. Boffi, Eur. Phys. J. A33 (2007) 29.
- [239] E. Jans, in: S. Boffi, C. Ciofi degli Atti, M.M. Giannini (Eds.), 5th Workshop on Perspectives in Nuclear Physics at Intermediate Energies, World Scientific, 1992, p. 287.
- [240] G. Rosner, in: S. Boffi, C. Ciofi degli Atti, M. Giannini (Eds.), Proceedings of the Conference on Perspectives in Hadronic Physics, World Scientific, 1997, p. 185.
- [241] T. Hehl, Progr. Part. Nucl. Phys. 34 (1995) 385.
- [242] L.J.H.M. Kester, et al., Phys. Rev. Lett. 74 (1995) 1712.
- [243] K.I. Blomqvist, et al., Phys. Lett. B421 (1998) 71.
- [244] C.J.G. Onderwater, et al., Phys. Rev. Lett. 81 (1998) 2213.
- [245] D.L. Groep, et al., Phys. Rev. C63 (2001) 014005.
- [246] J.L. Aclander, J. Alster, D. Barton, G. Bounce, et al., Phys. Lett. B453 (1999) 211.
- [247] A. Tang, J.W. Watson, J.L.S. Aclander, J. Alster, G. Asryan, et al., Phys. Rev. Lett. 90 (2003) 042301.
- [248] E. Piasetzky, M. Sargsian, L. Frankfurt, M. Strikman, J.W. Watson, Phys. Rev. Lett. 97 (2006) 162504.
- [249] R. Shneor, et al., Phys. Rev. Lett. 99 (2007) 072501.
- [250] R. Subedi, et al., Science 320 (2008) 1476.
- [251] I. Korover, et al., Phys. Rev. Lett. 113 (2014) 022501.
- [252] H. Baghdasaryan, et al., [CLAS Collaboration], Phys. Rev. Lett. 105 (2010) 222501.
- [253] J. Golak, et al., Phys. Rev. C51 (1995) 1638.
- [254] A. Bodek, et al., Phys. Rev. Lett. 51 (1983) 534.
- [255] R. Arnold, P.E. Bosted, C. Chang, J. Gomez, A. Katramatou, et al., Phys. Rev. Lett. 52 (1984) 727.
- [256] J. Gomez, R. Arnold, P.E. Bosted, C. Chang, A. Katramatou, et al., Phys. Rev. D49 (1994) 4348.
- [257] J. Seely, A. Daniel, D. Gaskell, J. Arrington, N. Fomin, et al., Phys. Rev. Lett. 103 (2009) 202301.
- [258] L. Frankfurt, M. Strikman, Int. J. Mod. Phys. E21 (2012) 1230002.
- [259] G.V. Dunne, A.W. Thomas, Nucl. Phys. A455 (1986) 701.
- [260] C. Ciofi degli Atti, S. Liuti, Phys. Lett. B225 (1989) 215; Phys. Rev. C 41 (1990) 1100; Nucl. Phys. A532 (1991) 241.
- [261] P.R. Norton, Rep. Progr. Phys. 66 (2003) 1253.
- [262] O. En, D.F. Higinbotham, G.A. Miller, E. Piasetzky, L.B. Weinstein, Int. J. Mod. Phys. E22 (2013) 1330017.
- [263] S. Malace, D. Gaskell, D.H. Higinbotham, I. Kloet, Int. J. Mod. Phys. E 23 (2014) 1430013.
- [264] L.L. Frankfurt, M.I. Strikman, Nucl. Phys. B250 (1985) 147.
- [265] L.B. Weinstein, E. Piasetzky, D.W. Higinbotham, J. Gomez, O. Hen, R. Shneor, Phys. Rev. Lett. 106 (2011) 052301.
- [266] O. Hen, E. Piasetzky, L.B. Weinstein, Phys. Rev. C85 (2012) 047301.
- [267] A. Mueller, in: J. Tranh Thanh Van (Ed.), Proceedings of the 17th Rencontre de Moriond, Editions Frontieres, Gif-sur-Yvette, 1982, p. 13.
- [268] S. Brodsky, in: E.W. Kittel, W. Metzger, A. Stergiou (Eds.), Proceedings of the 13th International Symposium on Multiparticle Dynamics, World Scientific, Singapore, 1982, p. 964.
- [269] B.Z. Kopeliovich, J. Nemchik, E. Predazzi, A. Hayashigaki, Nucl. Phys. A740 (2004) 211.
- [270] A. Accardi, F. Arleo, W.K. Brooks, D. D'enterria, V. Muccifora, La Rivista del Nuovo Cimento 9–10 (2010) 439.
- [271] P.V.R. Murthy, et al., Nucl. Phys. B92 (1975) 269.
- [272] N.N. Nikolaev, Z. Phys. C32 (1986) 537.
- [273] B.K. Jenkins, G.A. Miller, Phys. Rev. C49 (1994) 2637.
- [274] E.J. Moniz, G.D. Nixon, Ann. Phys. (N.Y.) 67 (1971) 58.
- [275] M. Alvioli, C. Ciofi degli Atti, I. Marchino, H. Morita, V. Palli, Phys. Rev. C78 (2008) 031601(R).
- [276] B.Z. Kopeliovich, L.I. Lapidus, A.B. Zamolodchikov, JETP Lett. 33 (1981) 595. [Pisma Zh. Eksp. Teor. Fiz. 33 (1981) 612].
- [277] M. Alvioli, C. Ciofi degli Atti, B.Z. Kopeliovich, I.K. Potashnikova, I. Schmidt, Phys. Rev. C81 (2010) 025204.
- [278] C. Ciofi degli Atti, B.Z. Kopeliovich, C.B. Mezzetti, I.K. Potashnikova, I. Schmidt, Phys. Rev. C84 (2011) 025205.
- [279] M. Alvioli, M. Strikman, Phys. Rev. C83 (2011) 044905.
- [280] J.-P. Blaizot, W. Broniowski, J.-Y. Ollitrault, Phys. Rev. C 90 (2014) 034906.
- [281] G.S. Denicol, G. Gale, S. Jeon, J.-F. Paquet, H. Schenke, arXiv:1406.7792 [nucl-th].
- [282] A.B. Balantekin, Progr. Theoret. Phys. Suppl. 146 (2003) 227.
- [283] K. Abe, et al., T2K Collaboration, Phys. Rev. Lett. 107 (2011) 041801.
- [284] P. Adamson, et al., MINOS Collaboration, Phys. Rev. Lett. 110 (2013) 171801.
- [285] Y. Abe, et al., DOUBLE-CHOOZ Collaboration, Phys. Rev. Lett. 108 (2012) 131801.
- [286] F.P. An, et al., DAYA-BAY Collaboration, Phys. Rev. Lett. 108 (2012) 171803.
- [287] J.K. Ahn, et al., RENO Collaboration, Phys. Rev. Lett. 108 (2012) 191802.
- [288] M.V. Ivanov, R. González-Jiménez, J.A. Caballero, M.B. Barbaro, T.W. Donnelly, J.M. Udías, Phys. Lett. B727 (2013) 265.
- [289] J.E. Amaro, M.B. Barbaro, J.A. Caballero, T.W. Donnelly, Phys. Rev. Lett. 108 (2012) 153501.
- [290] A. Meucci, C. Giusti, Phys. Rev. D85 (2012) 093002.
- [291] M. Martini, M. Ericson, G. Chanfray, Phys. Rev. D87 (2013) 013009.
- [292] J. Nieves, I. Ruiz Simo, M.J. Vicente Vacas, Phys. Lett. B721 (2013) 90.
- [293] O. Lalakulich, U. Mosel, K. Gallmeister, Phys. Rev. C86 (2012) 054606.
- [294] O. Lalakulich, U. Mosel, K. Gallmeister, Phys. Rev. Lett. 112 (2014) 151802.
- [295] V. Pandey, N. Jachowicz, J. Ryckebusch, T. Van Cuyck, W. Cosyn, Phys. Rev. C89 (2014) 024601.
- [296] O. Benhar, P. Coletti, D. Meloni, Phys. Rev. Lett. 105 (2010) 132301.
- [297] O. Benhar, N. Rocco, arXiv:1310.3869 [nucl-th], 2013.
- [298] J.G. Morfin, J. Nieves, J.T. Sobczyk, Adv. High Energy Phys. 2012 (2012) 934597.
- [299] J.A. Formaggio, G.P. Zeller, Rev. Mod. Phys. 84 (2012) 1307.
- [300] A. Aguilar-Arevalo, et al., (MiniBooNE Collaboration), Phys. Rev. D83 (2012) 052009.
- [301] G.A. Fiorentini, et al., (MINERVA Collaboration), Phys. Rev. Lett. 111 (2013) 022502.
- [302] R. Acciari, et al., Phys. Rev. D90 (2014) 012008.
- [303] J. Arrington, et al. Jefferson Lab Experimental proposal E08-014, 2008.
- [304] J. Arrington, et al. Jefferson Lab Experimental proposal E12-11-112, 2006.
- [305] W. Boeglin, et al. Jefferson Lab Experimental proposal E12-10-003, 2010.